Collective Dynamics of Large Scale Multiagent Systems with Nonlocal Interactions

Kruk, Nikita

(2020)

DOI (TUprints): https://doi.org/10.25534/tuprints-00017368

TECHNISCHE
UNIVERSITÄT
DARMSTADT

COLLECTIVE DYNAMICS OF LARGE SCALE MULTIAGENT SYSTEMS WITH NONLOCAL INTERACTIONS

vom Fachbereich Elektrotechnik und Informationstechnik der
TECHNISCHEN UNIVERSITÄT DARMSTADT

zur Erlangung des Grades
Doktor rerum naturalium (Dr. rer. nat.)
Dissertation

von

NIKITA KRUK, M.SC.

Erstgutachter: Prof. Dr. techn. Heinz Köppl
Zweitgutachter: Prof. José A. Carrillo

Darmstadt 2020

Kruk, Nikita : *Collective Dynamics of Large Scale Multiagent Systems with Nonlocal Interactions*
Darmstadt, Technische Universität Darmstadt
Jahr der Veröffentlichung der Dissertation auf TUprints: 2020
Tag der mündlichen Prüfung: 01.12.2020

Dedicated to my grandmother.

ABSTRACT

The thesis investigates the emergence of collective behavior in large scale multiagent systems. Examples of such dynamics are ample. The most familiar of them are such macroscale phenomena as flocking of birds, schooling of fish, and swarming of insects. The other common macroscale manifestations of collective dynamics include herds of sheep, human crowds, and robotic swarms etc. On the microscale, we often find ordered motion in such living systems as bacterial suspensions and cell layers as well as in such nonliving systems as shaken granular rods and colloidal particles. One of the fascinating features of all the aforementioned systems is that they consist of constituents of completely different nature but still do produce qualitatively similar behavior as the whole. However, those constituents have one common characteristic, namely, they are able to propel themselves either by using an intrinsic source of energy or by consuming it from the surrounding environment. Such systems are generically referred to as active matter. Our approach to the study of active matter is primarily based on theories of nonlinear dynamical systems and statistical physics. In our research, we put particular emphasis on nonlocality of interactions. Namely, these are the interactions that are defined on intermediate ranges with respect to the system size, in contrast to closest-neighbor and all-to-all interactions.

The first part of the thesis is concerned with the analysis of active matter systems in terms of finite size particle models. Each particle serves as an abstraction for an underlying constituent, e.g., one of those described above, and it can be imagined as a collection of variables that describe the relevant information about it, e.g., a position, velocity, orientation etc. Then, the motion of a particle is described with nonlinear differential equations. At this point, the distinction should be made. First, the resulting collective behavior may be a consequence of intrinsic deterministic nonlinear dynamics themselves. In this case, particle's motion is described with ordinary differential equations and we employ the tools of nonlinear dynamical systems to characterize the resulting motion. It involves the description of fixed points, periodic orbits, and attractors, each of which corresponds to a specific collective motion pattern, as well as bifurcations that provide us with their stability. Second, collective phenomena in natural environment are inevitably subject to various internal and external perturbations. To take that into account, equations of particle motion are generalized to include stochastic forces. This way, particles are modeled as stochastic processes and their temporal evolution is described with stochastic differential equations. The important question in the theory of active matter is the stability of collective motion against noise and phase transitions between various collective motion patterns.

The second part of the thesis discusses the continuum description of large scale interacting multiparticle systems. Namely, when the number of particles becomes large, the description of their dynamics in terms of finite size particle models becomes inefficient. To find a more efficient system description in such cases, we observe that when the number of particles grows, they cover the domain of interest finer and under an appropriate scaling, they will cover all of it in the limit of infinite population size. We realize this by assuming a statistical approach according to which we determine the probability to find a particle at a particular point of the phase space at a particular time. In such a limit, the collective motion of interacting multiparticle systems is described with (probability) density functions or, more generally, with (probability) measures. Their temporal evolution is described with partial differential equations, which, in the context of interacting multiparticle systems, involve nonlinear integral terms. There are two types of continuum descriptions of active matter that we employ. The first one is the kinetic one. It is concerned with the description of a system in terms of a density function that depends on all phase space variables. The second type

of continuum description is the hydrodynamic one. This theory describes an active matter system with a set of a small number of fields that depend on spatial information only, in contrast to the kinetic theory. For example, one often considers fields that describe spatial distribution of particles, momenta, polar, or nematic orders.

The third part of the thesis is about the development of numerical schemes, dedicated to continuum limit equations of interacting multiparticle systems. These are nonlinear partial integro-differential equations that require dedicated analysis due to their complexity. The numerical schemes, we developed, consider such properties of the approximate solution as positivity preservation, physical conservations, and free energy dissipation. With such a numerical scheme at hand, we study true continuum limit behavior of original finite size particle models as well as related phase transitions without finite size effects.

The fourth part of the thesis covers the experimental work on the swarming of *B. subtilis* as a controlled system of *in vitro* active matter. This part includes preparation and execution of experiments, image processing, multitarget tracking, and mathematical modeling of a kind described above. We establish protocols for the swarming of *B. subtilis* in microfluidic polydimethylsiloxane channels as well as on agar plates, which are straightforward to reproduce. This results in a sequence of images per experiment, which we afterwards expose to multitarget tracking algorithms to retrieve each bacterium's trajectory. This knowledge allows us to construct models that provide collective behavior closer to the natural setup. Unlike the standard active matter models, the description of bacterial swarming in a confined environment requires the consideration of bacterium's physical shape. This is often achieved by modeling a bacterium as a self-propelled rod.

ZUSAMMENFASSUNG

Die Dissertation untersucht das Entstehen von kollektivem Verhalten in großzahligen Multiagentensystemen. Beispiele für solche Dynamik sind ubiquitär. Die bekanntesten darunter sind makroskopische Phänomene wie Vogelschwärme, Fischschwärme und Insektenschwärme. Zu anderen verbreiteten Manifestationen kollektiver Dynamik auf der Makroskala gehören Schafherden, Menschenmassen, Roboterschwärme usw. Auf der Mikroskala finden wir häufig geordnete Bewegung in biologischen Systemen wie etwa Bakteriensuspensionen und Zellschichten, sowie in nichtbiologischen Systemen wie etwa geschüttelte granulierte Stäbe und kolloidale Partikel. Eines der faszinierenden Merkmale aller genannten Systeme ist, dass sie aus Bestandteilen völlig unterschiedlicher Natur bestehen, aber dennoch ein qualitativ ähnliches Verhalten als Ganzes erzeugen. Diese Bestandteile haben eine gemeinsame Eigenschaft, nämlich dass sie in der Lage sind, sich selbst anzutreiben, indem sie entweder eine intrinsische Energiequelle nutzen oder diese aus der Umgebung verbrauchen. Solche Systeme werden allgemein als aktive Materie bezeichnet. Unsere Vorgehensweise zur Untersuchung von aktiven Materie basiert in erster Linie auf Theorien nichtlinearer dynamischer Systeme und der statistischen Physik. In unserer Forschung legen wir besonderen Wert auf die Nonlokalität der Interaktionen. Das sind nämlich die Interaktionen, die auf Zwischenbereichen in Bezug auf die Systemgröße definiert sind, im Gegensatz zu engsten Nachbar- und All-to-All-Interaktionen.

Der erste Teil dieser Dissertation befasst sich mit der Analyse von Aktive-Materie-Systemen im Hinblick auf Partikelmodelle finiter Größe. Jedes Teilchen dient als Abstraktion für einen zugrundeliegenden Bestandteil, z.B. einen der oben beschriebenen, und kann als eine Sammlung von Variablen verstanden werden, die die relevanten Informationen des Teilchen beschreiben, z.B. seine Position, Geschwindigkeit, Orientierung usw. Anschließend wird die Bewegung eines Teilchens mit nichtlinearen Differentialgleichungen beschrieben. An diesem Punkt wird eine Unterscheidung getroffen. Zunächst kann das resultierende kollektive Verhalten eine Folge der intrinsischen, deterministischen nichtlinearen Dynamik selbst sein. In diesem Fall wird die Bewegung eines Teilchens mit gewöhnlichen Differentialgleichungen beschrieben, und wir verwenden die Werkzeuge nichtlinearer dynamischer Systeme, um die resultierende Bewegung zu charakterisieren. Dazu gehört die Beschreibung von Fixpunkten, periodischen Bahnen und Attraktoren, von denen jeder einem bestimmten kollektiven Bewegungsmuster entspricht, sowie von Bifurkationen, die uns Einsicht in ihre Stabilität verleihen. Zweitens sind kollektive Phänomene in der natürlichen Umgebung zwangsläufig verschiedenen internen und externen Störungen unterworfen. Um dies zu berücksichtigen, werden Gleichungen der Teilchenbewegung verallgemeinert, um stochastische Kräfte einzubeziehen. Auf diese Weise werden die Teilchen als stochastische Prozesse modelliert und ihre zeitliche Entwicklung wird mit stochastischen Differentialgleichungen beschrieben. Die wichtige Frage in der Theorie von aktiven Materie ist die Stabilität der kollektiven Bewegung gegenüber Rauschen und Phasenübergänge zwischen verschiedenen kollektiven Bewegungsmustern.

Im zweiten Teil der Dissertation wird die Kontinuumsbeschreibung großskaliger interagierender Mehrteilchensysteme diskutiert. Wenn die Anzahl der Partikel groß wird, wird die Beschreibung ihrer Dynamik in Form von Partikelmodellen finiter Größe ineffizient. Um in solchen Fällen eine effizientere Systembeschreibung zu finden, beobachten wir, dass, wenn die Anzahl der Partikel zunimmt, sie die interessierende Domäne feiner abdecken und unter einer geeigneten Skalierung das gesamte Gebiet im Grenzfall der unendlichen Populationsgröße abdecken. Wir realisieren dies, indem wir von einem statistischen Ansatz ausgehen, in dem wir die Wahrscheinlichkeit bestimmen, ein Teilchen an einem bestimmten Punkt des Phasenraums zu einem bestimmten

Zeitpunkt zu finden. In einem solchen Grenzfall wird die kollektive Bewegung von wechselwirkenden Mehrteilchensystemen durch (Wahrscheinlichkeits-)Dichtefunktionen oder allgemeiner durch (Wahrscheinlichkeits-)Maße beschrieben. Ihre zeitliche Entwicklung wird durch partiellen Differentialgleichungen beschrieben, die im Zusammenhang mit wechselwirkenden Mehrteilchensystemen nichtlineare Integralterme beinhalten. Es existieren zwei Arten von Kontinuumsbeschreibungen der aktiver Materie, die wir verwenden. Die erste ist die kinetische. Sie befasst sich mit der Beschreibung eines Systems in Form einer Dichtefunktion, die von allen Phasenraumvariablen abhängt. Die zweite Art der Kontinuumsbeschreibung ist die hydrodynamische. Diese Theorie beschreibt ein Aktive-Materie-System mit einer Menge von einer kleinen Anzahl von Feldern, die im Gegensatz zur kinetischen Theorie nur von räumlichen Informationen abhängen. Beispielsweise berücksichtigt man oft Felder, die die räumliche Verteilung von Teilchen, Momenta, polaren oder nematischen Ordnungen beschreiben.

Der dritte Teil der Dissertation befasst sich mit der Entwicklung numerischer Schemata, die sich mit Kontinuum-Grenzgleichungen interagierender Mehrteilchensysteme befassen. Dabei handelt es sich um nichtlineare partielle Integro-Differentialgleichungen, die aufgrund ihrer Komplexität eine dedizierte Analyse erfordern. Die von uns entwickelten numerischen Schemata berücksichtigen Eigenschaften der Näherungslösung wie etwa Positivitätserhaltung, physikalische Erhaltungsgrößen und freie Energiedissipation. Mit einem solchen numerischen Schema untersuchen wir das wahre Kontinuum-Grenzverhalten der ursprünglichen Partikelmodelle endlicher Größe sowie die damit verbundenen Phasenübergänge ohne endliche Größeneffekte.

Der vierte Teil der Dissertation umfasst die experimentellen Arbeiten zum Schwärmen von *B. subtilis* als kontrolliertes System von *in vitro* aktiven Materie. Dieser Teil umfasst die Vorbereitung und Durchführung von Experimenten, Bildverarbeitung, Multitarget Tracking und mathematische Modellierung der oben beschriebenen Art. Wir erstellen Protokolle für das Schwärmen von *B. subtilis* in mikrofluidischen Polydimethylsiloxankanälen sowie auf Agarplatten, die einfach zu reproduzieren sind. Daraus ergibt sich eine Sequenz von Bildern pro Experiment, die wir anschließend Multitarget Tracking-Algorithmen aussetzen, um die Flugbahn jedes Bakteriums zu ermitteln. Dieses Wissen erlaubt es uns, Modelle zu konstruieren, die ein kollektives Verhalten ermöglichen, das dem natürlichen Aufbau näher kommt. Im Gegensatz zu den Standardmodellen für aktive Materie erfordert die Beschreibung von Bakterienschwärmen in einer begrenzten Umgebung die Berücksichtigung der physischen Form des Bakteriums. Dies wird oft durch die Modellierung eines Bakteriums als selbstangetriebener Stab erreicht.

ACKNOWLEDGMENTS

First, I would like to express my greatest thanks to Prof. Heinz Koeppl for letting me the opportunity to perform my doctoral studies and for patient guiding through all these years. I would like to especially thank my major collaborators Prof. José A. Carrillo, Prof. Yuri Maistrenko, and Prof. Arkady Pikovsky for their time and efforts in guiding me in my research.

All the past and present members of the BCS lab have been wonderful. Special thanks to Markus Baier and Christine Cramer for always helping with technical and administrative matters. Bastian Alt, Megan Bailey, Leo Bronstein, Özdemir Cetin, Kai Cui, Jascha Diemer, Nicolai Engelmann, Maleen Hanst, Kilian Heck, Christiane Hübner, Lukas Köhs, Alina Kuzembayeva, François-Xavier Lehr, Dominik Linzner, Hongfei Liu, Miloš Lješković, Melanie Mikosch-Wersching, Tim Prangemeier, Felix Reinhardt, Markus Röder, Michael Schmidt, Rogier Schoeman, Matthias Schultheis, Mark Sinzger, Adrian Šošić, Sofia Startceva, Anam Tahir, Klaus-Dieter Voss, Christian Wildner, Sikun Yang, Yujie Zhong; Hameer Abbasi, Volodymyr Volchenko, Tabea Treppmann, Sara Al-Sayed, Nurgazy Sulaimanov, Wasiur Rahman Khuda Bukhsh, Derya Altintan, Sunil Kumar, Sounak Kar, Yura Toma, Roman Yavorskyi, Alisa Cheburkova, Elizabeth Lemeshko, Viktoriia Petruk, Stanislav Stepaniuk, Bohdan Rozhko - thank you all very much.

I am deeply grateful to my family Svitlana, Mykola, and Ruslana Kruk as well as to my Ukrainian friends Ihor Oliinyk, Liubov Liashenko, Oleksii Drobot, and Serhii Brezetskyi for visiting me in Darmstadt. Finally, I dedicate this dissertation to my grandmother, Iraida Antropova, who has been supporting and keeping in constant touch with me all these years.

CONTENTS

LIST OF FIGURES

1

INTRODUCTION

1.1 THESIS OVERVIEW AND CONTRIBUTIONS

In this thesis, we investigate collective motion of nonlocally interacting active particle systems. We need to clarify several points of this statement. First, a particle can generally be any living or nonliving entity that changes its states over time but we are primarily concerned with particles whose description involves physical coordinates in two or three dimensions, such as birds, fish, robots, bacteria, or colloids. This allows us to consider interactions between particles on qualitatively different scales, i.e., global, local, or nonlocal, by introducing a relevant distance measure. Note that we usually call interactions on intermediate scales ’nonlocal’ but one might come across the formulation ’nonglobal’ when it should be contrasted to the global ones. Second, active matter theory considers any particles that convert some energy source into motion but we will consider only those particles that are able to perform self-propulsion, i.e., correlated directed motion. The class of such models is known as self-propelled particle (SPP) models. As a last remark, collective motion itself encompasses many qualitatively different types of spatio-temporal behavior in SPP systems. This includes spatially homogeneous polar or nematic motion as well as spatially inhomogeneous traveling bands, vortical arrays, number density fluctuations, and so on. Therefore, by collective motion, we generally mean any correlated motion of a subset of particles in space or time.

The key moment in the development of active matter was the introduction of the Vicsek model (VM). It is a simplistic discrete-time SPP model that captures the emergence of polar order. According to this model, each particle moves with a constant speed and adjusts its orientation to the one averaged across its neighborhood. Later, it was shown that under an appropriate scaling, this model was able to be written in a time-continuous form. We have noticed that by writing the differential equations for the velocity direction and omitting particle coordinates (which can be done without loss of generality for spatially homogeneous configurations), one obtains a model that is well-known in the theory of oscillatory networks as the Kuramoto model (KM). One of the recent achievements for this model was the discovery of novel kind of spatio-temporal dynamics that was called chimera states. This dynamics is characterized by simultaneous existence of synchronized and chaotic subpopulations of oscillators despite their identical nature. In order to observe such chimera states, one has to introduce a phase lag into the coupling between oscillators as well as consider only nonlocal interactions. By following this idea, we have generalized a time-continuous version of the VM and obtained a model capable of yielding the novel types of SPP motion which we call self-propelled chimera states due to their qualitative resemblance to chimera states from the KM if considering only particle’s direction of motion. The detailed description of this class of collective motion from the point of view of the nonlinear dynamics theory is presented in Chapter 2.

Until recent times, the study of active matter primarily considered the motion of linear swimmers, i.e., particles that exhibit self-propulsion without rotations. For such models, many spatially inhomogeneous collective motion have been found, e.g., traveling bands, high-density clouds, vortex arrays, to name a few. One of the recent activity in the theory of active matter has been towards similar development for chiral particles, i.e., the ones that are able to self-rotate. However, the amount of spatially inhomogeneous dynamics, exhibited in such models, was not as rich as for the linear active matter. This gave us an idea that if we consider our aforementioned model as an active particle model, it would be of chiral type due to implicit rotations that particles undertake upon interactions influenced by the phase lag. Indeed, this formulation eventually allowed us to discover a wide range of new spatially inhomogeneous chiral active matter patterns such as traveling bands, clouds, and vortices that consist of constantly rotating particles. Unlike the previous work on self-propelled chimera states, here we investigated the finite size particle model in a purely stochastic setup, which is discussed in Chapter 2. However, in order to reveal all those patterns in the first place, we needed to consider the continuum limit formulation of interacting particle systems. Its derivation from a particle model as well as related spatially homogeneous analytic solutions are presented in Chapter 3 from the point of view of the kinetic theory and in Chapter 4 from the point of view of the hydrodynamic theory. Based on the knowledge of such analytic solutions, we were able to perform linear stability analyses against spatially inhomogeneous perturbations that allowed us to find parameter domains where spatially inhomogeneous patterns arise. We discuss such an analysis in Chapter 5. The hydrodynamic theory, resulted from applying a large diffusion approximation, did not yield much insight into pattern formation mechanisms for the particle system under consideration. As such, we turned to an alternative approach to formulate the hydrodynamic equation by applying the Ott-Antonsen (OA) ansatz, which proved useful in the investigation of oscillatory dynamics in the Kuramoto model. Formulation of hydrodynamic description using the OA reduction can be found in Chapter 5.

Recent developments in the theory of network oscillators revealed yet another interesting phenomenon. Under second order rules of motion, some oscillators might detach from a completely synchronized group and assemble in a new group, which is internally also synchronized. This kind of dynamics became known as a solitary state. Continuing our work on chimera states, we generalize our self-propelled particle model to the second order for orientation and investigate the resulting dynamics. As a first step in that direction, we primarily concentrate on a regime of spatially homogeneous distribution of particles. Thereby, we combine theories of active matter and network oscillators. Our analysis shows how solitary states with arbitrary numbers of particles arise, how they behave under the influence of noise, and how they manifest themselves in the mean-field limit, i.e., with interactions kept global. We discuss these matters in Chapter 2.

The continuum limit of interacting active particles is described in terms of nonlinear partial integro-differential equations. The efficient numerical analysis of such equations requires integration schemes specifically dedicated to the problem at hand. Therefore, in order to be able to proceed with the investigation of our active matter models, we derived particular finite volume methods (FVMs) that allowed us to observe the aforementioned particle dynamics in the continuum limit without finite size effects. The main ideas behind these methods were positivity preservation of solutions, conservation of mass, and the dissipation of free energy. The details on our FVMs are presented in Chapter 6.

As part of this thesis, we conducted experiments with bacterial swarming in microfluidic environments. Our end goal is to apply the developed theories of interacting particles to a system of natural origin. We established a protocol to observe the swarming of *B. subtilis* in polydimethylsiloxane channels of $1 \mu m$ height. This setup was chosen to restrict bacteria to two-dimensional motion in order to perform meaningful image acquisition with positions of all bacteria observable. The experiments provide us with sequences of images representing bacterial cultures in consecutive time points. By developing a multitarget tracking procedure with data association, we can extract trajectories of each single bacterium during the run of an experiment. For modeling of bacterial swarming, we formulated a self-propelled rods model, commonly applied to such systems. This part belongs to the ongoing research and its discussion is presented in Chapter 7.

1.2 PUBLICATIONS

The contents of this thesis have partially been published in the following articles:

1. N. Kruk, Y. Maistrenko, and H. Koeppl (Sept. 2018). "Self-propelled chimeras". *Phys. Rev. E* 98 (3), p. 032219
2. N. Kruk, J. A. Carrillo, and H. Koeppl (Aug. 2020). "Traveling bands, clouds, and vortices of chiral active matter". *Phys. Rev. E* 102 (2), p. 022604
3. N. Kruk, J. A. Carrillo, and H. Koeppl (preprint). "A finite volume method for continuum limit equations of nonlocally interacting active chiral particles". *Submitted to Journal of Computational Physics. Preprint is available at https://arxiv.org/abs/2008.08493*
4. N. Kruk, Y. Maistrenko, and H. Koeppl (Nov. 2020). "Solitary states in the mean-field limit". *Chaos: An Interdisciplinary Journal of Nonlinear Science* 30.11, p. 111104

1.3 PRELIMINARIES

1.3.1 *Nonlinear Dynamical Systems*

When we describe motion of interacting particles, we prescribe a specific rule according to which every particle moves. In general, in the theory of nonlinear dynamics, dynamical systems can be divided in two classes. The first one considers ordinary differential equations (ODEs) where time is continuous and the second one considers discrete maps where time is discrete. For a beautiful introduction to this theory please refer to (S. Strogatz 2007) and for more advanced topics see (Coddington and Levinson 1955; Guckenheimer and Holmes 2002; Hale 2009; Izhikevich 2007; Jordan et al. 1999; Katok and Hasselblatt 1997; Kuznetsov 1998; Robert L. Devaney et al. 2004; Wiggins 2003). In this thesis, we will discuss interacting particle systems that evolve in continuous time.

Let us proceed by an example. We consider a system with N particles, each of which is described as an S-dimensional function of time. For example, we will regularly consider particles moving in two dimensions with constant velocity magnitude but varying orientation. Therefore, it is sufficient to describe a particle as a $S = 3$-dimensional vector $p_i \in \Omega, i = 1, \dots, N$ whose components denote two spatial coordinates and one angular coordinate and where Ω denotes some three-dimensional space. Temporal evolution of such a particle system is defined by

$$\frac{\mathrm{d}}{\mathrm{d}t} p_i = q_i(p_1, \dots, p_N),\ i = 1, \dots, N, \tag{1.3.1}$$

where $q_i : \Omega^N \to \Omega, i = 1, \dots, N$ are velocities, together with an initial condition

$$p_i(0) = p_{i,0},\ i = 1, \dots, N, \tag{1.3.2}$$

where values $p_{i,0}, i = 1, \dots, N$ are known. The problem of solving Eq. (1.3.1) with a given initial condition Eq. (1.3.2) is called an initial value problem or a Cauchy problem for (1.3.1). The space Ω constitutes the phase space of one particle whereas the space Ω^N constitutes the phase space of the whole particle ensemble. Note that for an interacting particle system, each function $q_i, i = 1, \dots, N$ depends on the information about other particles which makes the ODE coupled. In general, the right hand side of Eq. (1.3.1) may depend on time but our discussion will not consider such cases.

In the theory of differential equations, the existence and uniqueness of solutions for (1.3.1) is guaranteed if the velocity functions $q_i, i = 1, \dots, N$ are continuously differentiable, i.e., they are continuous and their partial derivatives with respect to all particles' state variables are continuous on some open connected set $D \subset \Omega^N$. There are other existence and uniqueness theorems (Guckenheimer and Holmes 2002; Robert L. Devaney et al. 2004) that are less restrictive than continuous differentiability but for our purposes, this is sufficient. In most cases, interacting particle systems such as (1.3.1) are nonlinear and we cannot find its analytical solutions. Instead, a lot of our knowledge of how particles behave comes from numerical analysis. The most common scheme that we will use is the Runge-Kutta method (E. Wanner et al. 2002).

From the practical point of view, particles in natural environments are always subject to external perturbations. To account for that we consider particles to be stochastic processes and reformulate the interacting particle system (1.3.1) as a system of stochastic differential equation (SDE)

$$\mathrm{d}p_i = q_i(p_1, \dots, p_N)\,\mathrm{d}t + D\mathrm{d}W_i,\ i = 1, \dots, N, \tag{1.3.3}$$

where stochastic forces are accounted for by a family of independent Wiener processes $(W_i(t))_{t\geq 0}$ and D is a matrix that accounts for noise strength acting in different phase space domains. Note that $W_i, i = 1, \dots, N$ are vector-valued quantities since they generate perturbations that generally act on all components of $p_i, i = 1, \dots, N$. For an introduction to the theory of stochastic processes, please refer to (Øksendal 2003; Särkkä and Solin 2019). However, our interest in this theory is practical. The reader interested in numerical analysis of such systems may refer to (Platen and Bruti-Liberati 2010).

1.3.2 *Partial Differential Equations*

Let us consider a function f that depends of several variables, which we will denote as an N-dimensional vector $p \in \mathbb{R}^N$. If this function changes with respect to at least two of them, we deal with partial differential equations (PDEs). PDEs are equations that involve partial derivative terms and the order of the highest derivative n is the order of the PDE. In this thesis, we will consider PDEs of first and second orders. For the comprehensive theory on general PDEs, please refer to (G. Evans, Blackledge, and Yardley 1999; L. Evans and Society 1998; Zauderer 2011). Therefore, let us first consider the first-order case, i.e., $n = 1$. For simplicity, let us also set the number of independent variables $N = 3 + 1$ so that we can expand $p = (x_1, x_2, x_3, t) \in \mathbb{R}^3 \times \mathbb{R}_+$. Note that we often separate the time variable from the rest of the independent variables and this covers most of the cases covered in this thesis. Thereby, we consider a first-order PDE of four variables that in a general form reads

$$A_0 \partial_t f(x_1, x_2, x_3, t) + \sum_{i=1}^{3} A_i \partial_{x_i} f(x_1, x_2, x_3, t) + A_4 = 0,$$

where functions $A_i, i = 0, \dots, 4$ are given and we assume that they are nonzero. Note that if all these coefficients do not depend on the function f and its partial derivatives, such a PDE is called linear. Otherwise, we will call it nonlinear. It is not convenient to have a multiplier in front of the time derivative so that we eliminate it to obtain

$$\partial_t f(x_1, x_2, x_3, t) + \sum_{i=1}^{3} a_i \partial_{x_i} f(x_1, x_2, x_3, t) + a_4 = 0, \tag{1.3.4}$$

where $a_i = A_i/A_0, i = 1, \dots, 4$. In this thesis, we will prefer the vector notation for the above summation. Namely, let $x := (x_1, x_2, x_3)$, $a := (a_1, a_2, a_3)$, and $\nabla_x := (\partial_{x_1}, \partial_{x_2}, \partial_{x_3})$. Thus, we can write Eq. (1.3.4) as

$$\partial_t f(x_1, x_2, x_3, t) + a \cdot \nabla_x f(x_1, x_2, x_3) + a_4 = 0, \tag{1.3.5}$$

This equation is called the transport equation. The coefficients in front of the partial derivative terms function as vector components in respective dimensions. One can show that with $a_4 = 0$, the transport Eq. (1.3.5) has a solution of the form

$$f(x,t) = f_0(x - at), \tag{1.3.6}$$

where f_0 is a known initial condition. Solutions of this type are called traveling waves solutions where the velocity vector a defines its propagation front. They will be encountered during our analysis of continuum limit equations for spatially homogeneous particle configurations.

Now let us consider a second-order PDE which in a general form reads

$$\sum_{i=0}^{3}\sum_{j=0}^{3} A_{ij}\partial_{x_i x_j} f(x_1,x_2,x_3,x_0) + \sum_{i=0}^{3} B_i \partial_{x_i} f(x_1,x_2,x_3,x_0) + C = 0, \tag{1.3.7}$$

where $A_{ij}, i,j = 0,\dots,3$, $B_i, i = 0,\dots,3$ and C are given. Note that for the sake of notation, we have denoted time as $x_0 := t$. The classification of second-order PDEs considers equations of elliptic, parabolic, and hyperbolic types. Depending on the type, the qualitative behavior of resulting solutions is different and this behavior is dependent on the higher-order derivative terms. In order to establish the type of a given PDE, one considers a matrix composed of the coefficients A_{ij} in front of the second-order partial derivatives. Namely, let the matrix read $A = (A_{ij})_{i,j=0,\dots,3}$. We compute its eigenvalues $\lambda_i, i = 0,\dots,3$. If all eigenvalues are of the same sign, i.e., $\forall i\ \lambda_i > 0$ or $\forall i\ \lambda_i < 0$, Eq. (1.3.7) is of elliptic type. If at least one of the eigenvalues is zero, i.e., $\exists i\ \lambda_i = 0$, Eq. (1.3.7) is of parabolic type. If one of the eigenvalues differs in sign from the rest, i.e., $\exists i\ \lambda < 0$ or $\lambda < 0$ with $\lambda_j > 0$ or $\lambda_j < 0, j \neq i$, respectively, then Eq. (1.3.7) is of hyperbolic type. Note that for high-dimensional systems, it is possible that several eigenvalue have the opposite sign from the rest. In such cases, one often refers to Eq. (1.3.7) as of ultrahyperbolic type (Zauderer 2011). The distinctive feature of hyperbolic equations is that their solution can experience shocks even though the equation itself does not contain discontinuous terms. On the opposite, elliptic and parabolic equations are more regular so that given sufficiently regular conditions on $A_{ij}, i,j = 0,\dots,3$, $B_i, i = 0,\dots,3$ and C, their solutions will also be regular, except at the initial time (Zauderer 2011). All of this can be shown using the theory of characteristic which are defined as the lines across which shocks can propagate. However, in this thesis, we do not consider it in any detail and the interested reader may refer to (L. Evans and Society 1998; Zauderer 2011) for sufficient discussion. Note that in general, the matrix coefficients are not constant but depend on $x_i, i = 1,\dots,3$. This results in that a PDE can be of different type in different domains. The continuum limit equations discussed in this thesis are of parabolic type.

It is not convenient to have multipliers in front of the highest order time derivative. Moreover, we do not encounter PDEs with mixed partial derivatives of time and space. Therefore, we normalize the above equation by A_0 and put $A_{i,0} = A_{0,i} = 0, i = 1,\dots,3$. This leads to

$$\partial_{x_0 x_0} f(x_1,x_2,x_3,x_0) + \sum_{i=1}^{3}\sum_{j=1}^{3} a_{ij}\partial_{x_i x_j} f(x_1,x_2,x_3,x_0) + \sum_{i=0}^{3} b_i \partial_{x_i} f(x_1,x_2,x_3,x_0) + c = 0,$$

where $a_{ij} = A_{ij}/A_{00}, i,j = 1,\dots,3$, $b_i = B_i/A_{00}, i = 0,\dots,3$, and $c = C/A_{00}$. Let us consider several canonical examples. First, if we disregard all temporal information and put $a_{ij} = 0, i \neq j$, $a_{ii} = 1, i = 1,\dots,3$, $b_i = 0, i = 0,\dots,3$, and $c = 0$, we obtain the Laplace equation

$$\Delta f(x_1,x_2,x_3) := \sum_{i=1}^{3} \partial_{x_i x_i} f(x_1,x_2,x_3) = 0,$$

which is an equation of elliptic type and where Δ is known as the Laplace operator. Second, if we omit the first term and put $a_{ij} = 0, i \neq j$, $a_{ii} = -1, i = 1, \ldots, 3$, $b_0 = 1$, $b_i = 0, i = 1, \ldots, 3$ and $c = 0$, we obtain the heat (or diffusion) equation

$$-\Delta f(x_1, x_2, x_3, x_0) + \partial_{x_0} f(x_1, x_2, x_3, x_0) = 0,$$

which is an equation of parabolic type. Third, if we put $a_{ij} = 0, i \neq j$, $a_{ii} = -1$, $b_i = 0, i = 0, \ldots, 3$, and $c = 0$, we obtain the wave equation

$$\partial_{x_0 x_0} f(x_1, x_2, x_3, x_0) - \Delta f(x_1, x_2, x_3, x_4) = 0,$$

which is an equation of hyperbolic type.

In this thesis, we discuss systems that consist of interacting particles. Each particle is described with a position and an orientation. These are the variables that determine $x_i, i = 1, \ldots, 3$, described above. Namely, it will often be the case that x_1 and x_2 denote coordinates from a spatial domain and x_3 denotes orientational (sometimes also called directional, angular) domain. We will mostly treat the unknown function f as a probability density function. Thereby, f will quantify the probability to encounter a particle at position (x_1, x_2) moving in the direction x_3 at time t. In a general form, it is governed by

$$a_{33} \partial_{x_3 x_3} f(x_1, x_2, x_3, x_0) + \sum_{i=0}^{3} b_i \partial_{x_i} f(x_1, x_2, x_3, x_0) + c = 0,$$

which is an equation of parabolic type.

Nonlinear PDEs rarely have analytic solutions in the domain of interest. Therefore, for the most interesting dynamics, we perform their numerical integration. For the purposes of this thesis, we developed dedicated finite volume methods for the continuum limit equations discussed in Chapter 6. For the reader interested in the theory on numerical analysis for PDEs, please refer to (Anderson 1995; C. Hirsch 2006; Laney 1998; Moukalled, Mangani, and Darwish 2015; Schäfer 2006).

2

ACTIVE PARTICLE DYNAMICS

2.1 REPRESENTATION OF ACTIVE MATTER AS SELF-PROPELLED PARTICLE SYSTEMS

Synchronized motion of collectives of agents is a widespread phenomenon that can be encountered both in nature and in artificially manufactured systems. The most remarkable examples include bacterial swarming, flocking of birds, schooling of fish, human crowds, and robotic swarms (Gompper et al. 2020; Vicsek and Zafeiris 2012). It is remarkable that all these systems can exhibit similar synchronized behavior despite the inherent diversity of the constituent agents. In order to understand what defines such behavior, we study minimal models of collective motion. Such models often describe systems that are far from equilibrium and are referred to as active matter. It has become a standard approach to analyze such systems with the Vicsek model (VM) (Vicsek, Czirók, et al. 1995) in discrete time or ABP models in continuous time (Romanczuk et al. 2012). Models of this type have been extensively analyzed and a number of spatially nonhomogeneous structures like large scale traveling bands or irregular high density clouds have been reported (Chaté et al. 2008; Farrell et al. 2012; Mishra, Baskaran, and Marchetti 2010; Nagai et al. 2015; O'Keeffe, Hong, and S. H. Strogatz 2017; Solon, Chaté, and Tailleur 2015).

In this section, we start our discussion with the Vicsek model as the most simple model for collective motion of active matter. However, we are interested in the study of time continuous processes and, thus, derive a time continuous version of the Vicsek model. By constraining particle motion to two dimensions, we obtain a model known as the Kuramoto-Vicsek model. That will be the starting point for our generalizations.

2.1.1 *The Vicsek model*

The intensive study of active matter started after the introduction of the standard Vicsek model. It is the model for polar particles interacting via polar alignment. It reads

$$r_i(t+\Delta t) = r_i(t) + v_0 v_i(t)\Delta t \tag{2.1.1a}$$

$$v_i(t+\Delta t) = \bar{v}_i(t) + \sqrt{2D\Delta t}\,\eta_i(t), \tag{2.1.1b}$$

where $\bar{v}_i(t) = \frac{\sum_{j\in B_\varrho^i} v_j(t)}{\|\sum_{j\in B_\varrho^i} v_j(t)\|}$ is the mean velocity field generated by a neighborhood of radius ϱ, which we define as

$$B_\rho^i(t) := \{j \in \{1,\dots,N\}\backslash i \mid \|r_j(t) - r_i(t)\| \le \rho\}.$$

Generally, the neighborhood of each particle is time dependent but we write $B_\varrho^i = B_\varrho^i(t)$ for brevity. By the formulation of the model, we have $|v_i(t)| = |v_i(t+\Delta t)|$, which implies

$$(v_i(t+\Delta t) - v_i(t)) \cdot (v_i(t+\Delta t) + v_i(t)) = 0.$$

Let us consider a projection operator $P(v) = I - v \otimes v$ based on any $v \in \mathbb{R}^d$, where I is the identity matrix and $\otimes$ denotes an outer product of two vectors. It's application to another vector can be written as $P(v)w = w - (w \cdot v)v$ for any $v, w \in \mathbb{R}^d$. Using this identity and subtracting $v_i(t)$ from Eq. (2.1.1b), one obtains

$$v_i(t + \Delta t) - v_i(t) = P\left(v_i\left(t + \frac{\Delta t}{2}\right)\right)\left(\bar{v}_i(t) + \sqrt{2D\Delta t}\eta_i(t)\right),$$

where $v_i(t + \frac{\Delta t}{2}) = \frac{1}{2}(v_i(t) + v_i(t + \Delta t))$. By dividing both sides by Δt and taking the limit $\Delta t \to 0$, the left hand side converges to $\frac{\partial v_i(t)}{\partial t}$. However, the right hand side does not seem to have a well-defined limit. This is due to the fact that the time scale in the Vicsek model Eq. (2.1.1) is not set. In fact, if one considers a two times smaller time step, particles would interact two times more often; as a result, if one directs $\Delta t \to 0$, particles would interact infinite number of times. This gives us an idea that we must replace the frequency factor Δt^{-1} in front of the interaction term with an appropriate one, which would stay finite in the limit. Let us denote it with σ. Thus, we formally obtain in the limit

$$\begin{aligned} \mathrm{d}r_i(t) &= v_0 v_i(t)\, \mathrm{d}t \\ \mathrm{d}v_i(t) &= P(v_i(t))\left(\sigma\bar{v}_i(t)\, \mathrm{d}t + \sqrt{2D}\mathrm{d}W_i(t)\right), \end{aligned}$$

where W_i is the family of independent d-dimensional Wiener processes. In this formulation, if the system of particles becomes less synchronized, the denominator of $\bar{v}_i(t)$ decreases and particles begin to interact faster in order to preserve the synchrony. However, we are interested in the dynamics where particles influence equally one another. We can do that by changing $\sigma\frac{\sum_{j\in B_\varrho^i} v_j(t)}{\|\sum_{j\in B_\varrho^i} v_j(t)\|}$ by $\sigma\frac{1}{|B_\varrho^i|}\sum_{j\in B_\varrho^i} v_j(t)$. As a result, we obtain the following time continuous version of the Vicsek model Eq. (2.1.1):

$$\mathrm{d}r_i(t) = v_0 v_i(t)\, \mathrm{d}t \tag{2.1.2a}$$

$$\mathrm{d}v_i(t) = P(v_i(t))\left(\frac{\sigma}{\mid B_\varrho^i \mid}\sum_{j\in B_\varrho^i} v_j(t)\, \mathrm{d}t + \sqrt{2D}\mathrm{d}W_i(t)\right). \tag{2.1.2b}$$

If one considers a general particle interaction rule instead of the alignment in Eq. (2.1.2b) and possibly relieves the restriction of constant particle speed, one usually refers to such a model as an ABP one.

2.1.2 *The Kuramoto-Vicsek model*

The development of the previous section is valid for particles in a d-dimensional space. In the theory of active matter, two- and three-dimensional problems are the ones with most importance. First, we are going to concentrate on two-dimensional systems. Under the assumption that particle velocities change only in direction, we can write $v_i(t) = (\cos\varphi_i(t), \sin\varphi_i(t)) \in \mathbb{S}^1 \subset \mathbb{R}^2$, where $\varphi_i \in \mathbb{T}$ is particle's orientation. The description of particle dynamics in terms of Eq. (2.1.2) is therefore redundant and we will seek for its representation in terms of φ_i. We note the following. Since each particle changes its velocity only in direction, at each time point, its velocity vector v_i rotates around some axis ω_i in the direction of $\mathrm{d}v_i$

$$\omega_i(t) = v_i(t) \times \mathrm{d}v_i(t).$$

If we multiply Eq. (2.1.2b) by v_i from the left using a vector product and use $P(v)w = w - (w \cdot v)v$, we find

$$\omega_i(t) = \frac{\sigma}{\mid B_\varrho^i \mid}\sum_{j\in B_\varrho^i} v_i(t) \times v_j(t) + \sqrt{2D}v_i(t) \times \mathrm{d}W_i(t).$$

Since we constrain particles to move on a two-dimensional plane, $\omega_i = (0, 0, \mathrm{d}\varphi_i)$. By taking the absolute value of the above expression, we obtain

$$\begin{aligned} \mathrm{d}r_i(t) &= v_0 v_i(t)\ \mathrm{d}t \\ \mathrm{d}\varphi_i(t) &= \frac{\sigma}{\mid B_\varrho^i \mid} \sum_{j \in B_\varrho^i} \sin(\varphi_j - \varphi_i)\ \mathrm{d}t + \sqrt{2D}\mathrm{d}W_i(t), \end{aligned} \tag{2.1.3}$$

where $W_i, i = 1, \ldots, N$ now denotes the family of 1-dimensional Wiener processes. This model is known in the literature as the Kuramoto-Vicsek model due to the fact that the second equation in Eq. (2.1.3) defines the well-known Kuramoto model for networks of phase oscillators (Kuramoto 1984).

According to this model, the system either converges to complete alignment or remains in a disordered state. However, many of experimentally observed collective dynamics do not fall into these two categories. More specifically, regular coherent and irregular disordered dynamics are seen to be present simultaneously. Such coexistence of two disparate dynamical regimes is indicated, for instance, in the milling of a small group of fish within a large school (Calovi et al. 2014) or in the vortexing of microtubuli within a large collection of meandering microtubuli (Sumino et al. 2012) or in the rotation of energized ferromagnetic colloids (Geyer, Morin, and Bartolo 2018; Kaiser, Snezhko, and Aranson 2017). Related complex dynamics, such as rotating chains or moving bands (Chaté et al. 2008), can only be reproduced in SPP models in the presence of a strong stochastic driving term. A genuine coexistence of dynamical regimes in the absence of any stochastic forcing has recently been found in networks of nonlocally coupled oscillators and termed chimera states. In such a chimera state, groups of oscillators are synchronized while other oscillators undergo chaotic dynamics. This regime was first observed in the Kuramoto-Sakaguchi model (Abrams and S. H. Strogatz 2004; Kuramoto and Battogtokh 2002) of coupled phase oscillators that can be derived from the complex Ginzburg-Landau equation (Kuramoto 1984). The existence of chimera states has also been experimentally confirmed in optical (Hagerstrom et al. 2012; Larger, Penkovsky, and Maistrenko 2015), chemical (Schmidt et al. 2014; Tinsley, Nkomo, and Showalter 2012; Totz et al. 2020) and mechanical (Kapitaniak et al. 2014; Martens et al. 2013) systems. In the next section, we present how to obtain such states in the framework of two-dimensional SPP systems, starting from Eq. (2.1.3).

2.2 SELF-PROPELLED CHIMERA STATES

ABP models usually describe the motion of linear swimmers. This implies that particles prefer to move in a straightforward way rather than perform circular motion. Due to the lack of possibility for a particle to deliberately undertake circular motion in such models, there has recently been an increase of interest in a new class of models now known as chiral active matter (Bäuerle, Löffler, and Bechinger 2020; Chen et al. 2017; Degond, Dimarco, and Mac 2014; Denk et al. 2016; Han et al. 2017; Lei, Ciamarra, and Ni 2019; Levis, Pagonabarraga, and Liebchen 2019; Liebchen and Levis 2017; Narinder, Bechinger, and Gomez-Solano 2018; Nourhani, Crespi, and Lammert 2015; Souslov et al. 2017; Tociu et al. 2019). The most prominent examples of such motion are bacterial swarming close to boundaries of a substrate (Lauga et al. 2006; Lemelle et al. 2010), irregular vortex structures in dense suspensions of swimming bacteria (Sumino et al. 2012), swarming of magnetotactic bacteria in a rotating magnetic field (Ērglis et al. 2007), swimming of sperm cells (Friedrich and Jülicher 2007; Riedel, Kruse, and Howard 2005), and shimmering behavior of giant honeybees against predatory wasps (Kastberger, Schmelzer, and Kranner 2008).

2.2.1 *Model*

That said, we consider the following minimal extension of the Kuramoto-Vicsek model Eq. (2.1.3) that allows us to generate chimera states. As before, we consider a system of N particles moving with a constant speed in a unit square domain with periodic boundary conditions, according to the equations of motion given by

$$\dot{r}_i = v(\varphi_i), \quad \dot{\varphi}_i = \frac{\sigma}{\left|B^i_\rho\right|} \sum_{j \in B^i_\rho} \sin(\varphi_j - \varphi_i - \alpha) \tag{2.2.4}$$

with $r_i = (x_i, y_i)$ and $v(\varphi_i) = (\cos\varphi_i, \sin\varphi_i)$, and the particles are assumed to have unit mass and unit speed, without loss of generality. Each particle i interacts with all of its neighbors j within a finite interaction range ρ, i.e., with all particles falling in the disk

$$B^i_\rho := \{j \mid (x_i - x_j)^2 + (y_i - y_j)^2 \leq \rho^2\}.$$

The alignment is controlled by the coupling coefficient σ and the size of neighborhood $\left|B^i_\rho\right|$. We can consider equation Eq. (2.2.4) as a generalization of the Kuramoto model in the sense that oscillators are augmented to be motile (Leonard et al. 2012; O'Keeffe, Hong, and S. H. Strogatz 2017). Following this idea, we introduce the additional phase lag parameter α that originally allowed to observe chimera states in the Kuramoto-Sakaguchi model. In the context of SPPs, this parameter eventually induces a circular motion for the aligned group of particles. When $\alpha = 0$, the dynamics reduces to the Vicsek model in polar coordinates (A. A. Chepizhko and V. L. Kulinskii 2009; Degond and Motsch 2008). As mentioned earlier, the uniqueness of our model is that it admits the coexistence of aligned and nonaligned collectives of particles. We call such a behavior a self-propelled chimera state.

It has been shown that in the presence of noise the standard Vicsek model exhibits the formation of localized, traveling, high-density, and high-order structures, such as bands and sheets, or even blobs due to hydrodynamic interactions but at sufficiently large noise amplitudes (Chaté et al. 2008; Nagai et al. 2015). We emphasize that our situation is different: coherent localized structures due to Eq. (2.2.4) arise solely because of internal nonlinear interactions imposed by nonlocal coupling in the complete absence of noise. It should be mentioned that interesting patterns such as traffic jams, gliders, and static bands can be found for a simple swarming model with ferromagnetic alignment mechanism and volume exclusion (Peruani et al. 2011); however, these patterns do not constitute chimera states since such a model does not introduce phase synchronization. Moreover, if the alignment and antialignment are controlled depending on the range of interaction, coherent structures such as periodic vortex arrays may be produced (Großmann, Romanczuk, et al. 2014).

2.2.2 *Behavior*

Results of direct numerical simulation in the two-parameter plane of coupling radius ϱ and phase lag α are presented in the phase diagram in Fig. 2.1 obtained with the help of the continuation method (see the details of its implementation in (Kruk, Maistrenko, and Koeppl 2018)). The diagram reveals the existence of different chimera states in a considerable domain at intermediate radii ϱ and at phase lags α close to $\pi/2$. For smaller α or larger ϱ (the top left region), complete phase synchronization occurs, which is an analog to the standard Vicsek model. On the contrary, for α close to $\pi/2$ and very small ϱ, as well as for $\alpha \geq \pi/2$ the behavior of the system is chaotic (the region on the right).

We observe two types of chimera states (see videos S1 and S2 under (`https://www.youtube.com/playlist?list=PLjL7stT6PH4x1qpj_fFa2Rx5bI6EygOuw` n.d.)

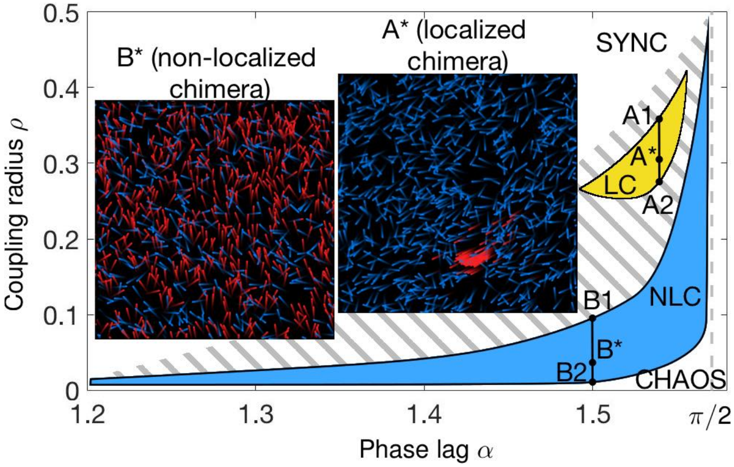

Figure 2.1: Phase diagram for model Eq. (2.2.4) in the (α, ϱ) parameter plane. Localized (LC) and nonlocalized (NLC) chimeras exist in yellow (light gray) and blue (dark gray) regions, respectively. Snapshots demonstrate typical chimera regimes, i.e., A*=$(1.54, 0.3)$, B*=$(1.5, 0.03)$, respectively. Particles are colored with respect to averaged phase velocity $\langle\dot{\varphi}\rangle$ (cf. Fig. 2.2(a) and (c); averaging time is $t = 5$ time units; see videos S1 and S2 under (`https://www.youtube.com/playlist?list=PLjL7stT6PH4x1qpj_fFa2Rx5bI6EygOuw` n.d.)) subject to binary thresholding. Intermittent behavior is characteristic for the neighboring region (oblique hatching). The region to the left leads to complete phase synchronization (SYNC) and the region to the right leads to full disorder (CHAOS). The lines A1-A2 and B1-B2 are used in Fig. 2.5 for order parameter description. Other parameters are $\sigma = 1.0$, $N = 1000$.

for their temporal dynamics). Both types are classified as chimeras since they possess the partial synchronization property with respect to the direction of motion $\varphi \in \mathbb{T}$. This property is similar to phase synchronization of the Kuramoto-Sakaguchi model. However, the addition of the spatial equations reveals new possibilities for the group behavior. The first chimera type is characterized by the formation of a peculiar coherent and localized group. We call it a localized chimera (see the inset $A*$ in Fig. 2.1 and Fig. 2.2(a),(b)). Notably, this regime exists for a parameter region of only an intermediate interaction range ϱ (Fig. 2.1, yellow (light gray) region). The second type of chimeras is characterized by partial phase synchronization but without any spatial localization. We call it a nonlocalized chimera (see the inset $B*$ in Fig. 2.1 and Fig. 2.2(c)). It can be obtained for a distinct parameter domain of relatively larger size (blue (dark gray) region). In addition to the above two, the oblique hatched region corresponds to an intermittent system behavior between other states. Interestingly, at the center of this domain, multiheaded chimeras, which comprise two or more separate coherent groups, can be found. However, such multiclustered structures are unstable and always disintegrate in the current setup. Thus, we do not focus on them further.

In all the simulations, the initial positions and directions of particles were drawn from uniform distribution if not mentioned otherwise. First, we describe the evolution scenario for the localized chimera case. In the initial stage (Fig. 2.2(a),(b) at t_1), while the system tries to synchronize, none of the particles show any considerable increase in phase velocity (a flat $\langle\dot{\varphi}\rangle$ profile), there is no visible group having the same traveling direction (a scattered $\langle\varphi\rangle$ profile), and there is no *a priori* benchmark point to calculate the localization measure (a profile in Fig. 2.2(b)). Meanwhile, particles gradually polarize and when the polarization is sufficiently large, the particles try to form a huge disk-shaped group, whose radius corresponds to the radius of interaction ϱ. That group consists of the majority of particles. The profiles in Fig. 2.2(a) at t_2 reveal its emergence. All

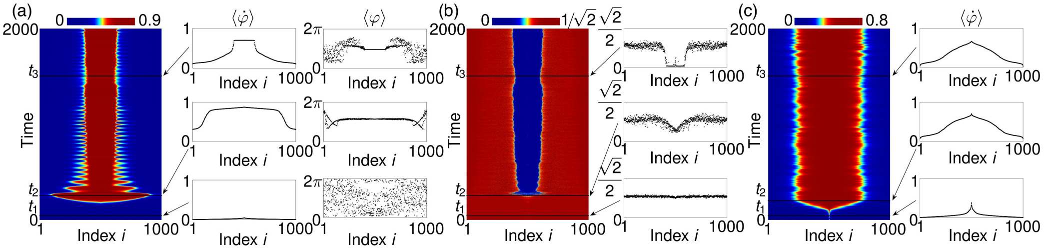

Figure 2.2: Emergence of chimeras. (a) Space-time plot for a localized chimera, based on the averaged phase velocity. Along with it, profiles of averaged phase velocity $\langle\dot\varphi\rangle$ and averaged phase $\langle\varphi\rangle$ are provided for time points from characteristic periods of formation. (b) Space-time plot for a localized chimera, based on the averaged value of distance from a particle position to a point of maximum density. Along with it, the corresponding profiles are provided at the same times as in (a). (c) Space-time plot for a nonlocalized chimera in the same manner as in (a). Particles are reordered identically at every time step with respect to the value of averaged angular velocity from (a) or (c), (b) is ordered according to (a). Temporal averaging is $t = 10$. Time points for (a) and (b) are $t_1 = 50$, $t_2 = 255$, and $t_3 = 1500$; time points for (c) are $t_1 = 50$, $t_2 = 210$, and $t_3 = 1500$. Parameters: (a),(b) $\sigma = 1.0, \varrho = 0.3, \alpha = 1.54$; (c) $\sigma = 1.0, \varrho = 0.03, \alpha = 1.5$.

particles in that group are directed similarly and are synchronized (flattened regions in the middle of the profiles). It appears that the group can not be maintained for a long time and many particles leave it until a smaller highly dense spot remains. That spot is stable and it is well distinguished from the other particles by the plateaus in each profile of Fig. 2.2(a),(b) at t_3.

The evolution of a nonlocalized chimera is qualitatively similar till the so-called point of maximum synchronization (see the definition in the next section). After that point (Fig. 2.2(c) at t_2), the dense disk-shaped group does not emerge. The system stalls in such a situation and the synchronized but scattered group remains.

In the case of the scenario with localization, when the dense spot of synchronized particles appears, particles from that spot follow a quasicircular trajectory while others fill the rest of the space uniformly (cf. Fig. 2.3(a),(b)). In such a setup, the phase dynamics in that synchronized group can be approximated as a combination of coherent and incoherent terms. A coherent term is imposed by all the particles which constitute the group. An incoherent term is imposed by all other desynchronized particles. Thus, we have

$$\dot\varphi_i = -\sigma\gamma_i \sin\alpha + \frac{\sigma}{\mid B_\varrho^i \mid} \sum_{j\in B_\varrho^i \setminus N_c} \sin(\varphi_j - \varphi_i - \alpha),$$

where $\gamma_i = \mid N_c^i \mid / \mid B_\varrho^i \mid$ is the fraction of coherent particles N_c^i in the neighborhood B_ϱ^i of the particle i. Since every synchronized particle moves approximately along a circular trajectory, its velocity vector can be assumed to have only a tangential component. The tangential component of a particle on a circle is equal to $\xi_i\dot\varphi_i$, where ξ_i is the radius of rotation of that particle. Thus, $\|v_i\| = \xi_i\dot\varphi_i$.

Throughout the paper, we assume that particles have unit speed. Therefore, the radius for the coherent group can be estimated approximately as

$$\xi(\sigma) \approx (\sigma\gamma\sin\alpha)^{-1}, \tag{2.2.5}$$

where $\gamma = \langle\gamma\rangle_{N_c,t}$ is the average of γ_i with respect to the group of coherent particles N_c and with respect to one rotational cycle of that group. The dependence of ξ on σ can be seen from Fig. 2.3(c) obtained directly from simulations and also obtained by the given approximation. We

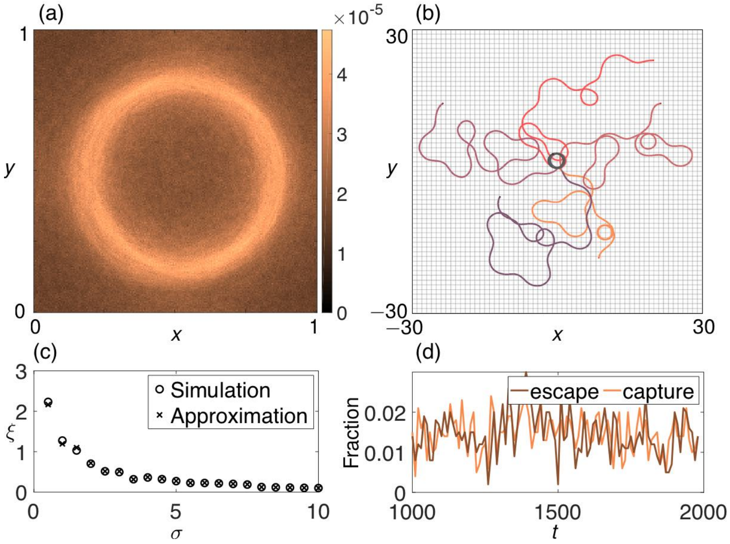

Figure 2.3: Localization traits of a localized chimera. (a) Traces of all particles over time ($t = 100$). Light circular trajectories indicate the motion of particles from a synchronized group whilst the dark background of considerable nonzero mass indicates the uniform spreading of the rest of chaotic particles. The color code corresponds to the number of particles at a particular position, normalized by the number of particles N and by the averaging time. Coupling strength is $\sigma = 4$ in order to keep the whole circular trajectory inside a simulation box. (b) Image of trajectories for one particle from a localized cluster (black circle in the middle) and for five different particles from the chaotic cluster (here $\sigma = 1$) for unrolled periodic boundary conditions. The tracking time is $t = 100$. (c) Radius of rotation ξ for particles from a localized group as a function of the coupling strength σ. (d) Number of particles, which leave and join the synchronized cluster, per cluster cycle (≈ 10 time units) per population size. Other parameters are $\varrho = 0.3, \alpha = 1.54, N = 1000$.

see an agreement of both these methods, which supports the validity of the approximation. It should be indicated that the averaged parameter γ is not a constant in Eq. (2.2.5) but depends on σ itself. It is because the coupling strength σ influences the shape and size of the localized group, thus, controlling N_c^i and γ_i of each particle.

Particles that are not in the coherent group are uniformly distributed over the whole space (Fig. 2.3(a), dark uniform background) exhibiting a kind of chaotic itinerancy (Fig. 2.3(b)). Such particles periodically try to follow the circular rotations of the coherent group but generally fall off after some time and continue wandering around. It appears that the synchronized group does not consist of the same set of particles all the time. Chaotic particles influence that group in a destabilizing manner (its explanation can be found in (Kruk, Maistrenko, and Koeppl 2018)), forcing some particles to leave it. But in addition, the chaotic cluster as a whole tries to synchronize, thus introducing new particles into the coherent group. As a result, over time, there are particles that leave and join that group (Fig. 2.3(d)). This behavior leads to small fluctuations in the group size. The fine balance between escape and capture phenomena enables existence of chimeras for an indefinite time.

We computed the local Lyapunov spectra Λ_x,Λ_y, and Λ_φ for both chimera types (Fig. 2.4(a) for a localized chimera, Fig. 2.4(b) for a nonlocalized chimera) to confirm that such dynamics are truly chaotic. Particles' indexes are ordered with respect to $\langle\dot{\varphi}\rangle$ in accordance with Fig. 2.2(a),(c), respectively. In case of the localized chimera, the values of Λ_x and Λ_y for the synchronized particles remain around 0 and the values of Λ_φ are slightly negative. For the rest of the particles, first two

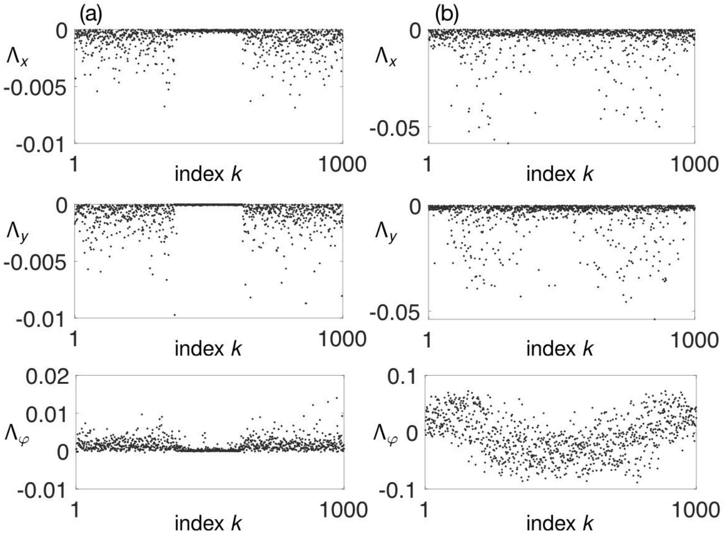

Figure 2.4: Local Lyapunov exponents. (a) Local Lyapunov spectra Λ_x,Λ_y, and Λ_φ in a localized chimera case for all particles for x,y,φ variables, respectively. The exponents were computed after 100 time units after the chimera has been formed. Particles are ordered with respect to $\langle\dot{\varphi}\rangle$ in the same manner as in Fig. 2.2(a). Other parameters are $\sigma = 1.0$, $\varrho = 0.3$, $\alpha = 1.54$. (b) Local Lyapunov spectra Λ_x,Λ_y, and Λ_φ in a nonlocalized chimera case for all particles for x,y,φ variables, respectively. The exponents were computed after 10 time units after the chimera has been formed. Particles are ordered with respect to $\langle\dot{\varphi}\rangle$ in the same manner as in Fig. 2.2(c). Other parameters are $\sigma = 1.0$, $\varrho = 0.03$, $\alpha = 1.5$.

spectra are negative while the third one is mostly positive. Thus, since the spectrum contains positive exponents, the nature of the system is chaotic. In case of the nonlocalized chimera, Λ_x and Λ_y hardly show any distinction between synchronized and desynchronized groups of particles. The directional spectrum Λ_φ clearly shows negative values for the synchronized cluster and positive values for the chaotic cluster but it has a high variation. Such a high variation can be explained by the fact that both clusters occupy all the space and influence mutual dynamics to a great extent. By the same reasoning, the system is chaotic in this regime too.

2.2.3 *Summary statistics*

One of the important characteristics to describe collective motion in coupled systems is the complex order parameter (Pikovsky, Rosenblum, and Kurths 2003a)

$$Z(t) = R(t)e^{i\Theta(t)} = \frac{1}{N}\sum_{j=1}^{N} e^{i\varphi_j(t)},$$

where $R(t)$ and $\Theta(t)$ can be considered to represent the magnitude and phase of the averaged particle velocity, respectively. The magnitude allows to learn the extent of polarization in the system.

Starting from random initial conditions, particles always begin to synchronize. This behavior is well observable from the evolution of $R(t)$ (cf. Fig. 2.5(a),(b)). The polarization of the system continues till a certain point after which it either decreases or remains at the same level approximately. The time point when it occurs is called the point of maximum synchronization t_{max}. The stages of

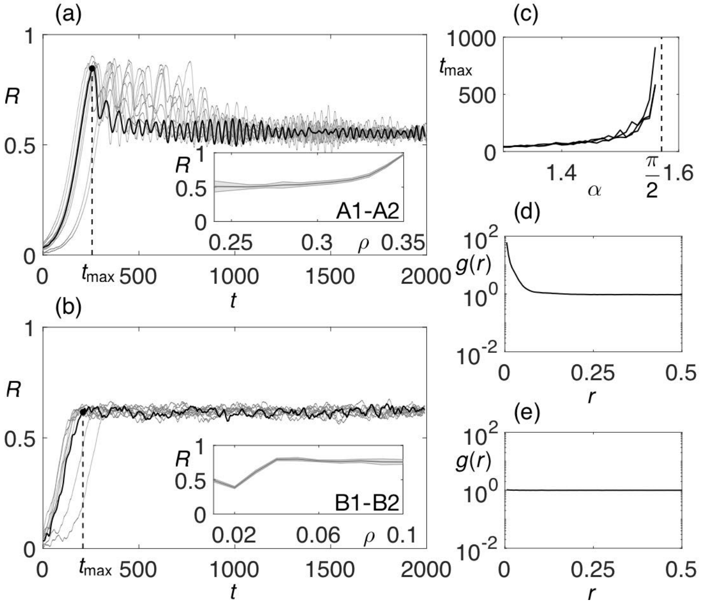

Figure 2.5: Summary statistics for chimera states. Evolution of the order parameter magnitude R over time for (a) localized and (b) nonlocalized chimeras. Temporal averaging of $t = 10$ is applied. Insets indicate changes in the synchronization level along the lines A1-A2 and B1-B2 from Fig. 2.1. (c) The time of maximum synchronization quantified through R versus phase lag α, for different radii $\varrho \in \{0.1, 0.3, 0.5\}$. (d),(e) Pair distribution functions for the localized and nonlocalized chimeras, respectively. Other parameters are the same as in Fig. 2.2.

the system evolution for both chimera types, described in the previous section, can be observed here additionally, with $t_2 = t_{\text{max}}$.

The qualitative difference of the order parameter dynamics between the two scenarios is the following. For a localized chimera, there is always a pronounced peak at t_{max}. But shortly afterwards, it drops. This happens when the big disk-shaped group shrinks into a dense spot. It can be seen that it is not the case with a nonlocalized chimera where the maximum synchronization is preserved at the same level approximately. It is also worthwhile to notice that when either chimera reaches its stationarity, it is subsequently impossible to differentiate them just by considering the order parameter $Z(t)$ (the insets of Fig. 2.5(a),(b) additionally show that the ranges of order parameter magnitudes at stationarity for both chimera types intersect).

A more detailed description to resolve this problem would be to introduce a local complex mean field (Xie, Knobloch, and Kao 2014)

$$Z_k(t) = R_k(t) e^{i\Theta_k(t)} = \frac{1}{\mid B_\varrho^k \mid} \sum_{j \in B_\varrho^k} e^{i\varphi_j(t)},$$

which is now space-dependent (cf. Fig. 2.6). To distinguish the dynamics is now easy. The local complex mean field for a localized chimera shows explicitly that a synchronized group exists and its presence gives the extreme polarization around itself (the plateau in Fig. 2.6(a)). Since a nonlocalized chimera does not possess any localization properties by definition, such a plateau is not possible by considering $Z_k(t)$ in this case. The drawback of the local complex mean field as

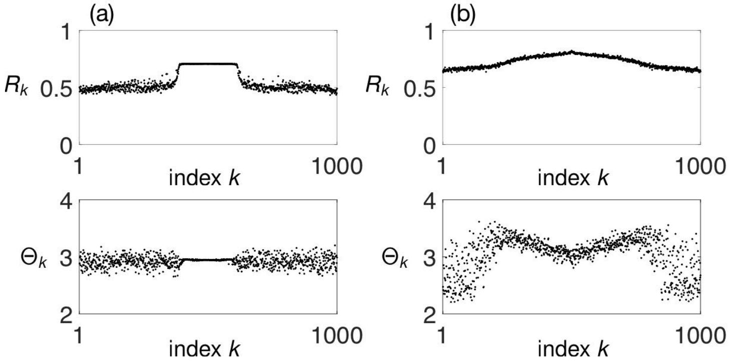

Figure 2.6: Local complex mean field $Z_k(t) = R_k(t)\exp(i\Theta_k(t))$ at $t = 1000$ for (a) localized and (b) nonlocalized chimeras. The ordering of particles is the same as in Fig. 2.2(a),(c), respectively. Parameters: (a) $\sigma = 1.0, \varrho = 0.3, \alpha = 1.54$; (b) $\sigma = 1.0, \varrho = 0.03, \alpha = 1.5$.

a summary statistic is that it contains information about all particle positions and, thus, does not effectively reduce the state space of the problem.

Now, we want to delve deeper into what role each parameter in the model Eq. (2.2.4) plays. First, as it has been seen, the coupling strength σ regulates the speed of particle rotations and consequently the radius of such rotations (cf. Eq. (2.2.5)). Its increase facilitates faster system polarization and, thus, smaller t_{max}. Second, an increase in the radius of interaction ϱ leads to an amplification of polarization as more and more particles are engaged into a synchronous group. It is noticeable that for different chimeras the functional dependence $R(\varrho)$ differs (see insets in Fig. 2.5(a),(b)). We did not observe a considerable influence of ϱ upon t_{max}. Third, an increase of the phase lag α prolongs t_{max} in an exponential way independently of ϱ (Fig. 2.5(c)), with $t_{\text{max}} \to \infty$ as $\alpha \to \pi/2$. Not surprisingly, its increase also decreases system polarization. This looks natural if we look at both chimeras as transient phenomena between complete synchronization (Fig. 2.1, region on the left) and chaos (region on the right).

From the definition of both chimera types, the basic difference between localized and nonlocalized chimeras is the degree of homogeneity of the system on a small scale. An appropriate function that captures the spatial structure of a system is the pair distribution function $g(r)$ for $r \in \mathbb{U}$. It is a measure of local spatial ordering. It is defined as

$$g(r) = \frac{1}{\pi r^2 \rho} \left\langle \sum_{\substack{j=1 \\ j \neq i}}^{N} \delta(r - r_{ij}) \right\rangle_i ,$$

where r is the distance at which the density is to be computed, r_{ij} is the distance between particles i and j, $\rho = N/L^2$ is the average number density of N particles in the system, $\langle \dots \rangle_i$ denotes taking average over all particles. In Fig. 2.5(d),(e), we show the shape of $g(r)$ for both chimeras. For the localized one, it has a very high peak at small r which reflects the fact that there is a localized dense group of particles. For the nonlocalized one, the peak is absent implying the lack of any localization.

2.2.4 *Generalizations*

The presented chimera states obtained from integrating Eq. (2.2.4) are not restricted only to that model. To show this, we have also investigated extended versions of the model.

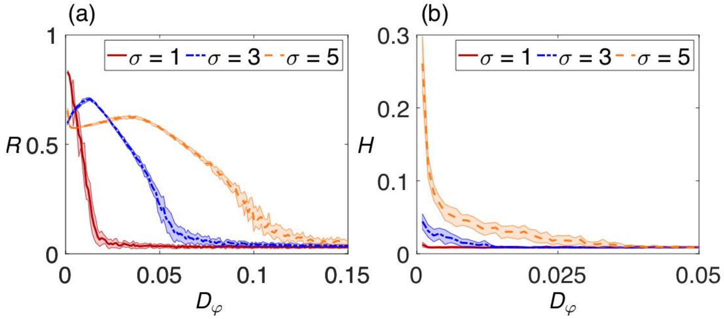

Figure 2.7: Summary statistics for chimera states under noise. (a) Values of global order parameter magnitude R versus noise intensity D_φ for solutions of equation Eq. (2.3.13). Different colors (line styles) correspond to different coupling coefficients σ; (b) Localization measure H versus noise intensity D_φ. A shaded region shows the standard deviation along a curve. Other parameters are $\varrho = 0.3, \alpha = 1.54, N = 1000$.

The first important generalization of the chimera model in the context of SPP systems is to introduce noise (Yates et al. 2009). Let the particles obey the Langevin equation

$$\mathrm{d}r_i(t) = v_i(t)\ \mathrm{d}t \tag{2.2.6a}$$

$$\mathrm{d}\varphi_i(t) = \frac{\sigma}{\mid B_\varrho^i \mid} \sum_{j \in B_\varrho^i} \sin(\varphi_j(t) - \varphi_i(t) - \alpha)\ \mathrm{d}t + \sqrt{2D_\varphi} \mathrm{d}W_i(t), \tag{2.2.6b}$$

where the last additional term represents the noise; W_i and W_j are independent Wiener processes for $i \neq j,\ \ i, j \in \{1, ..., N\}$, and D_φ is the noise intensity.

The summary of system's dynamics is presented in Fig. 2.7 through the magnitude R of the order parameter as a measure of polarization and through $H = \int |g(r) - 1|\, \mathrm{d}r$ as a global measure of localization. The addition of noise prevents particles from gathering into dense formations for small σ (cf. Fig. 2.7, $\sigma = 1$) but does not prevent the partial synchronization (i.e., a localized chimera turns into a nonlocalized one). As σ is increased, we recover again localized chimera states ($\sigma = 5$, intermediate R and high H). There is another interesting phenomenon. If D_φ increases, the order parameter magnitude R initially grows. This occurs because the higher the value of D_φ is, the more spacious the localized group becomes. The process continues till the point at which the order parameter is maximized and the localization measure reaches a minimal possible value. At this point, the system can again be described as a nonlocalized chimera. Further increase of D_φ merely destroys the remaining phase synchronization.

In order to confirm that the reported self-propelled chimera states are not the result of applying only the piecewise constant interaction kernel in Eq. (2.2.4), we have considered two other types of couplings commonly applied for the Kuramoto model, i.e., the cosine and exponential couplings.

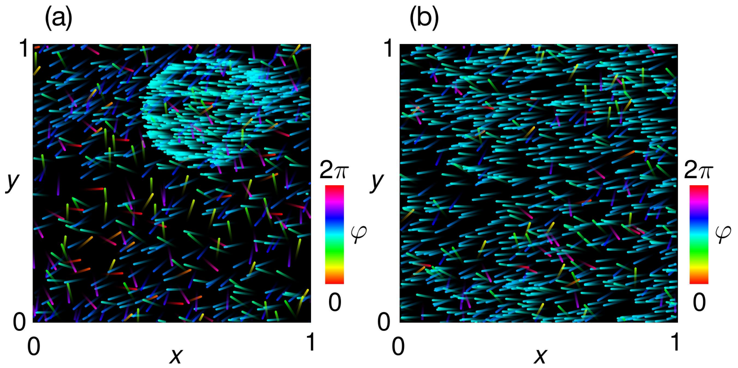

Figure 2.8: Chimera states due to the generalized model Eq. (2.2.7) with the cosine kernel Eq. (2.2.8). (a) A localized chimera state with parameters $\sigma = 1.0$, $\alpha = 1.53$, $A = 1.0$; (b) A nonlocalized chimera state with parameters $\sigma = 1.0$, $\alpha = 1.56$, $A = 1.0$.

However, in order to embed such a coupling function into our system, we need to rewrite it the following way:

$$\begin{aligned}\dot{r}_i(t) &= v_i(t)\\ \dot{\varphi}_i(t) &= \frac{\sigma}{\mid B_\varrho^i \mid}\sum_{j\in B_\varrho^i}\sin(\varphi_j(t)-\varphi_i(t)-\alpha)\\ &= \sigma\frac{\sum\limits_{j=1}^{N} H(\varrho - \|r_j(t)-r_i(t)\|)\sin(\varphi_j(t)-\varphi_i(t)-\alpha)}{\sum\limits_{j=1}^{N} H(\varrho - \|r_j(t)-r_i(t)\|)},\end{aligned}$$

where H is a Heaviside step function such that $H(x) = \begin{cases}0, & x<0\\ 1, & x\geq 0\end{cases}$ for $x \in \mathbb{R}$. This model is an equivalent representation of Eq. (2.2.4). Now we replace the piecewise constant Heaviside step function with a general kernel function which leads to the following model:

$$\begin{aligned}\dot{r}_i(t) &= v_i(t)\\ \dot{\varphi}_i(t) &= \sigma\frac{\sum_{j=1}^{N} G(\|r_j(t)-r_i(t)\|)\sin(\varphi_j(t)-\varphi_i(t)-\alpha)}{\sum_{j=1}^{N} G(\|r_j(t)-r_i(t)\|)},\end{aligned} \tag{2.2.7}$$

where G is a distance-dependent kernel function that provides nonlocal coupling between particles.

One common choice for the kernel function in the systems of coupled oscillators is

$$G(r) = 1 + A\cos(2\pi r), \tag{2.2.8}$$

where $0 \leq A \leq 1$ (Abrams and S. H. Strogatz 2004) is a tunable parameter.

It appears that the modified system Eq. (2.2.7) also produces various chimeric patterns (cf. Fig. 2.8). We have found that in a localized chimera case, synchronized particles form a localized structure but it has a form of a ball rather than a spot. The dynamics in a nonlocalized chimera case is qualitatively similar to the corresponding behavior due to equation Eq. (2.2.4).

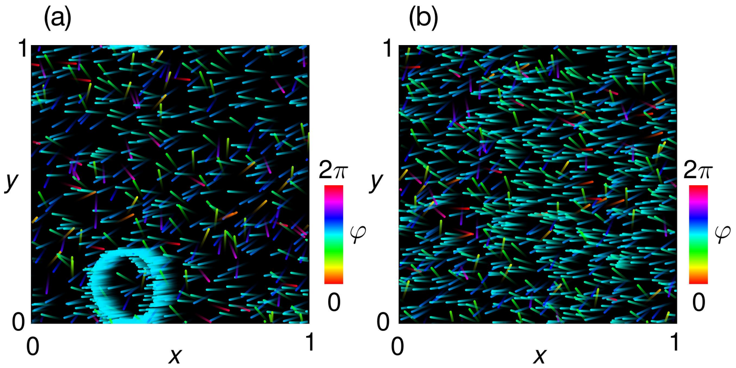

Figure 2.9: Chimera states due to the generalized model Eq. (2.2.7) with the exponential kernel Eq. (2.2.9). (a) A localized chimera state with parameters $\sigma = 1.0$, $\alpha = 1.54$, $k = 4.0$; (b) A nonlocalized chimera state with parameters $\sigma = 1.0$, $\alpha = 1.54$, $k = 20.0$.

Another common choice for the kernel function is

$$G(r) = \frac{k}{2} e^{-kr}, \tag{2.2.9}$$

where k is a tunable parameter (Kuramoto and Battogtokh 2002). Considering the inclusion of the exponential coupling into the extended system Eq. (2.2.7), two different states of chimeras can again be observed (cf. Fig. 2.9). Remarkably, due to the global connection of the particles, a localized chimera state gains additional peculiarity. As soon as the localized group has appeared, it also synchronizes particles outside of the group, thus creating a subsequently synchronized scattered group. The resulting coherent cluster consists of both localized and nonlocalized particles. The change of α leads to the alteration of the shape of the localized group, e.g., the higher it is the less concentrated and convex-shaped the group becomes. With increase of the tuning parameter k, the size of the localized cluster decreases and as a result, the number of scattered but synchronized particles grows. Again, the dynamics in a nonlocalized chimera case is qualitatively similar to the corresponding behavior due to Eq. (2.2.4).

2.2.5 *Continuum limit*

In this section we discuss the continuum limit for the Langevin equation Eq. (2.3.13) and show by numerical integration of the resulting 3+1-dimensional PDE that chimeras discussed so far are also preserved in this limit.

In this subsection, we follow the approach of (Dean 1996), which was also used in (Großmann, Romanczuk, et al. 2014) for the derivation of the Fokker-Planck equation from a system of self-propelled particles and which is alternative to the approach presented in Section 3. For the details of this approach, we refer the reader to (Kruk, Maistrenko, and Koeppl 2018). We define the microscopic density function for N particles $f^N(r,\varphi,t) = 1/N \sum_{i=1}^{N} \delta(r_i(t) - r)\delta(\varphi_i(t) - \varphi)$, which includes all the particle state variables. Using Ito's calculus, we obtain the following closed-form equation for the time evolution of the density function

$$\begin{aligned} \partial_t f^N(r,\varphi,t) = -\nabla_r \cdot (f^N(r,\varphi,t)\dot{r}(\varphi,t)) - \\ \partial_\varphi (f^N(r,\varphi,t)\dot{\varphi}(r,\varphi,t)) + D_\varphi \partial_{\varphi\varphi} f^N(r,\varphi,t), \end{aligned} \tag{2.2.10}$$

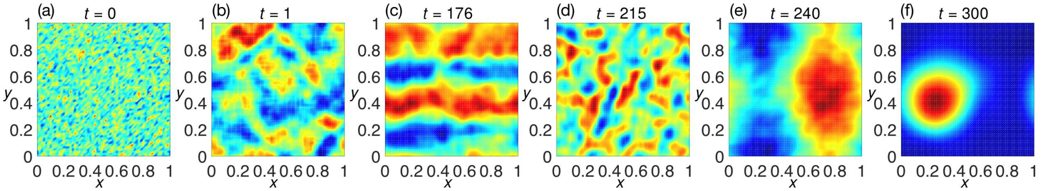

Figure 2.10: Solution for the 3+1-dimensional density function from the continuum limit Eq. (2.2.11), projected into spatial coordinates (x, y). The projection was done so as to ensure $f(x, y, t) = \int_0^{2\pi} f(x, y, \varphi, t) \mathrm{d}\varphi$. The color corresponds to the density value, normalized per each frame, so that all dynamical variations are captured. The solution here is shown as a sequence of characteristic phases that the system passes (see their description in the text).

where $f^N \dot{r}$ is the flux due to the motion of particles and $f^N \dot{\varphi}$ is the angular flux resulting from the alignment mechanism. Since f^N contains the information of all the particles' state variables, equation (2.2.10) is of the Klimontovich type (Nicholson 1983).

Under the molecular chaos assumption (Spohn 1991), which corresponds to neglecting all pre-collisional particle correlations, we arrive at the mean-field limit (O. Chepizhko and V. Kulinskii 2014) as the number of particles N goes to infinity. In this limit, the microscopic density function converges to a one-particle density function $f = f(r, \varphi, t) = \lim_{N\to\infty} f^N(r, \varphi, t)$ (J. A. Carrillo, Choi, and Hauray 2014a; Spohn 1991), which is finally independent of the explicit particle information. If we express variables x, y, φ explicitly, we finally proceed to the following Fokker-Planck equation with non-local coupling term

$$\begin{aligned} \partial_t f = {} & -\partial_x (f \cos\varphi) - \partial_y (f \sin\varphi) - \\ & \partial_\varphi \left(f \frac{\sigma}{|B_\rho|} \iint\limits_{B_\rho} \int\limits_0^{2\pi} f' \sin(\varphi' - \varphi - \alpha) \, \mathrm{d}x' \mathrm{d}y' \mathrm{d}\varphi' \right) + D_\varphi \partial_{\varphi\varphi} f, \end{aligned} \tag{2.2.11}$$

where $|B_\rho|$ represents the normalization term in the form of the neighborhood mass and $f' = f(x', y', \varphi')$.

Despite the fact that the dynamics of Eq. (2.2.11) depends on x, y, and φ, here we present only the projections of the solution into (x, y) because it allows simpler representation while still keeping the key aspects of the dynamics (the corresponding complete dynamics is described in Appendix C; see videos S4 and S5 under `https://www.youtube.com/playlist?list=PLjL7stT6PH4x1qpj_fFa2Rx5bI6EygOuw` n.d. for the temporal dynamics). Although our emphasis is primarily on the most fascinating regime that is equivalent to the LC state of the model Eq. (2.2.4), the other regimes also exist in the continuum limit.

At the beginning of a simulation, each grid point is initialized uniformly with small perturbation and then rescaled so as to keep the overall system density normalized (cf. Fig. 2.10(a)). As the system starts to move, many patches of high density appear and propagate according to the given velocity field (cf. Fig. 2.10(b)). Those patches first merge into tubes of high density, which, in turn, agglomerate into a thick layer, uniform in (x, y). The layer moves along the φ direction for a considerable amount of time, slowly shrinking. At some point, the layer shrinks rapidly and wavy structures appear in front of it (cf. Fig. 2.10(c)). Soon, those structures become irregular (cf. Fig. 2.10(d)) and the layer transforms into an elongated object of high density (cf. Fig. 2.10(e)). Eventually the object condenses into a small ellipsoidal shape that moves along a helical trajectory (cf. Fig. 2.10(f)). Also note that the final localized high-density shape coexists with the surrounding

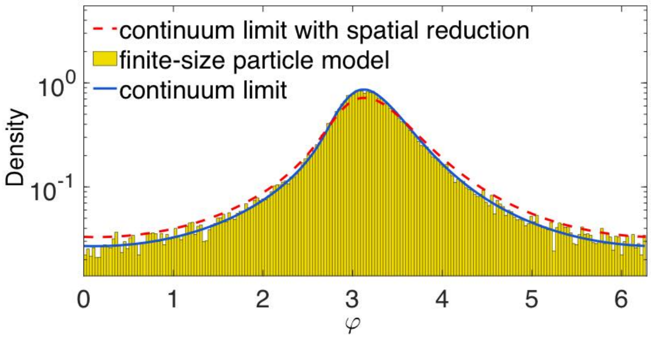

Figure 2.11: Comparison of the dynamics in the case of the nonlocalized chimera state from different models: (i) yellow histogram of particles' directions is given by the solution of a finite-size particle model Eq. (2.3.13) with the number of particles $N = 5 \cdot 10^4$; (ii) solid blue curve represents the projection of the solution for a 3+1-dimensional partial differential equation Eq. (2.2.11) into φ coordinates; (iii) dashed red curve represents the solution of a reduced partial differential equation Eq. (2.2.12). Parameters for the three models are $\sigma = 1.0, \rho = 0.03, \alpha = 1.5, D_\varphi = 0.01$.

of non-zero mass. Because of that, the system state resembles the motion of a coherent group of particles through an incoherent surrounding, i.e., the LC.

If we consider the NLC behavior, the final solution consists of a thin layer, which moves along the φ direction and which is uniform in x, y. In this case, we can employ the spatial homogeneity that is expressed as $f(x, y, \varphi, t) = \hat{f}(\varphi, t)$ for the considered unit square domain. Since $\hat{f}$ does not depend on x, y anymore, we can drop the first two terms on the right hand side of Eq. (2.2.11). Integration of the remaining equation over the unit square domain yields

$$\partial_t \hat{f}(\varphi, t) = -\partial_\varphi \left(\hat{f}(\varphi, t) \frac{\sigma}{|B_\rho|} \int_0^{2\pi} \hat{f}(\varphi', t) \sin(\varphi' - \varphi - \alpha) \mathrm{d}\varphi' \right) + D_\varphi \partial_{\varphi\varphi} \hat{f}(\varphi, t), \quad (2.2.12)$$

where the normalization term reads

$$|B_\rho| = \int_0^{2\pi} \hat{f}(\varphi', t) \mathrm{d}\varphi'.$$

The solution to this equation exhibits a pronounced peak for a certain phase and significant non-zero mass at other phases (cf. Fig. 2.11, the dashed red curve). Such a form corresponds to the NLC solution of the finite-size particle model Eq. (2.3.13) in such a way that there is a cluster of synchronized particles but at the same time there is still a cluster of chaotically moving particles. Moreover, as it has been assumed, both clusters are uniformly distributed in space.

Even though the reduced equation does recover the partial synchronization property needed for the system to be described as a chimera, the form of the solution to this reduced equation is not entirely similar than that one from the original 3+1-dimensional continuum limit Eq. (2.2.11), projected into the φ-coordinates (cf. Fig. 2.11, the solid blue curve). The figure shows that the solution to Eq. (2.2.11) fits well the phase histogram, which is obtained from particles' directions due to the Langevin equation Eq. (2.3.13). At the same time, the solution to (2.2.12) smooths out the pronounced peak to a higher extent than the original continuum limit density function. It can be explained by the fact that in this case we ignore all the spatial inhomogeneity during the formation of the chimera.

2.3 OTHER SPATIALLY NONHOMOGENEOUS DYNAMICS

Despite rich diversity of patterns in linear swimmer models, their chiral counterparts have not yet been shown to possess the same variety of nonequilibrium dynamics. Inspired by results on the Kuramoto-Sakaguchi model (Abrams and S. H. Strogatz 2004; Kuramoto and Battogtokh 2002; Omel'chenko 2018; Omel'chenko, Wolfrum, et al. 2012) for networks of phase oscillators, which we might regard as stationary particles, we generalized it to a self-propelled particle model and reported the existence of chimeric structures, i.e., the coexistence of synchronized and chaotic interacting particle groups even for a zero noise level (Kruk, Maistrenko, and Koeppl 2018). However, we believe that as an ABP model, it might exhibit a much wider class of nonequilibrium behavior (Kruk, J. A. Carrillo, and Koeppl 2020).

Let $\mathbb{U} := \mathbb{R}/(L\mathbb{Z})$ and $\mathbb{T} := \mathbb{R}/(2\pi\mathbb{Z})$ be one-dimensional spaces with periodic boundaries extending from $[0, L]$ and $[0, 2\pi]$, respectively. We again consider a system of N particles moving in a two-dimensional space $\mathbb{U}^2$ of fixed size L with periodic boundaries such that the coordinates of a particle $i = 1, \dots, N$ are given by $r_i = (x_i, y_i) \in \mathbb{U}^2$. Unlike the previous discussion, the speed of each particle is now assumed to be an arbitrary constant $v_0 \in \mathbb{R}_+$ and its velocity is determined by its directional phase $\varphi_i \in \mathbb{T}$. Particles interact with each other within a radius ϱ. Therefore, the set of all neighbors for a particle i is defined as

$$B_\varrho^i := \{j \mid j \in \{1, \dots, N\} \backslash i,\ (x_i - x_j)^2 + (y_i - y_j)^2 \le \varrho^2\}.$$

Particles evolve according to the following system of coupled stochastic differential equations (SDEs):

$$\begin{aligned} \mathrm{d}x_i &= v_0 \cos\varphi_i \, \mathrm{d}t \\ \mathrm{d}y_i &= v_0 \sin\varphi_i \, \mathrm{d}t \\ \mathrm{d}\varphi_i &= \frac{\sigma}{|B_\varrho^i|} \sum_{j \in B_\varrho^i} \sin(\varphi_j - \varphi_i - \alpha) \, \mathrm{d}t + \sqrt{2D_\varphi} \, \mathrm{d}W_i. \end{aligned} \tag{2.3.13}$$

According to the third equation, each particle adjusts its direction of motion to the average one over its nonlocal neighborhood B_ϱ^i, with $|B_\varrho^i|$ denoting the cardinality of the set of all neighbors. Particle interaction is controlled by a coupling strength parameter $\sigma \in \mathbb{R}_+$ and is additionally generalized by adding a phase lag parameter $\alpha \in \mathbb{T}$, which allows for rotation upon particle interaction. Note that this implicitly defines Eq. (2.3.13) as a chiral active particle model as long as $\alpha \neq 0$. Particles are subject to the external source of randomness with intensity $D_\varphi \in \mathbb{R}_+$, modeled by a family of independent Wiener processes. Our interest is to investigate the stochastic dynamics in the large N limit by preserving nonlocality of particle interactions.

To reduce the number of independent parameters, we choose time and space units as $1/\sigma$ and L, respectively. Thus, the model has four control parameters, e.g., the particle velocity $\hat{v}_0 = v_0/(L\sigma)$, the radius of interaction ϱ, the phase lag α, and the rotational diffusion rate relative to the coupling strength $\hat{D}_\varphi = D_\varphi/\sigma$. We will study a continuum limit of Eq. (2.3.13), where each particle is considered to be a point mass. In this case, we can find a limit with $N \to \infty$ with the system size fixed $L = \text{const}$. Therefore, we put $L = 1$ without loss of generality. Similar limits for weakly interacting particle systems with a large radius of interaction are known in kinetic theory as Vlasov limits (Dobrushin 1979; Lancellotti 2005). Note that a particle density, usually defined as $\rho_0 = N/L^2$, which plays an important role in the standard VM (Vicsek, Czirók, et al. 1995), does not arise here as an independent parameter due to the probabilistic interpretation of the density function in this setup (therefore, it is now fixed as $\rho_0 \equiv 1$). It should be treated as the average number of particles per unit length in the system of fixed size $L \times L = 1$ (Kipnis and Landim 1998a) divided into $\sqrt{N} \times \sqrt{N}$ units in two dimensions.

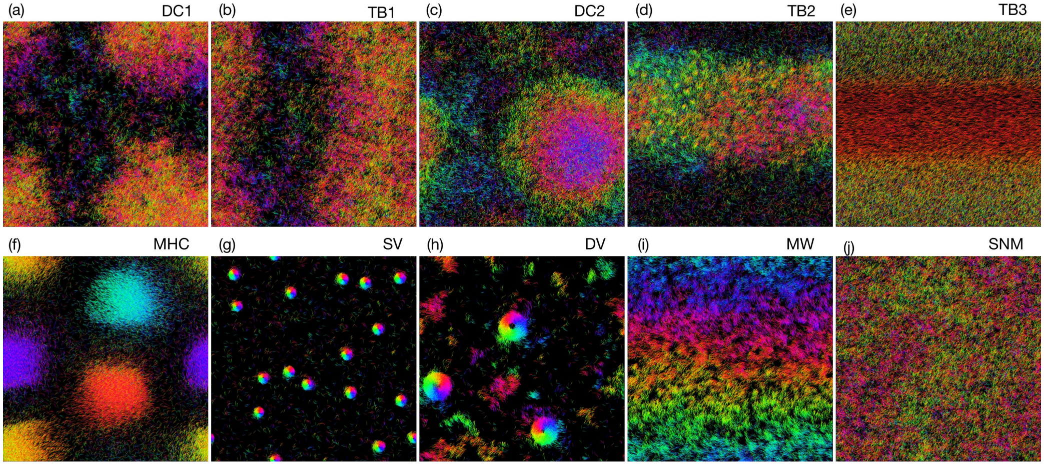

Figure 2.12: Particle dynamics according to Eq. (2.3.13) (see (`https://www.youtube.com/playlist?list=PLjL7stT6PH4xdc4X5Ee7xAr2vm49uIHvW` n.d.) for corresponding movies). Abbreviations stand for a dense cloud (DC), a traveling band (TB), a multiheaded chimera (MHC), a stationary vortex (SV), a dynamic vortex (DV), a momentum wave (MW), and a spatially nonhomogeneous momentum (SNM). Color indicates the direction of motion in the HSV color map. Each particle is represented as an elongated object over several time points. Parameter values correspond to those marked on the phase diagrams in Fig. 2.1. Parameters: $N = 5 \cdot 10^4$, $L = 1$, $\tilde{\varrho} = 1$, $\hat{v}_0 = 0.01$, (a) $\varrho = 0.01, \alpha = 0.78, \hat{D}_\varphi = 0.2075$, (b) $\varrho = 0.01, \alpha = 0.9, \hat{D}_\varphi = 0.18$, (c) $\varrho = 0.01, \alpha = 1.3, \hat{D}_\varphi = 0.06$, (d) $\varrho = 0.01, \alpha = 1.45, \hat{D}_\varphi = 0.01$, (e) $\varrho = 0.4, \alpha = 1.45, \hat{D}_\varphi = 0.005$, (f) $\varrho = 0.2, \alpha = 1.36, \hat{D}_\varphi = 0.005$, (g) $\varrho = 0.01, \alpha = 1.3, \hat{D}_\varphi = 0.02$, (h) $\varrho = 0.01, \alpha = 1.0, \hat{D}_\varphi = 0.0375$, (i) $\varrho = 0.01, \alpha = 1.0, \hat{D}_\varphi = 0.0575$, and (j) $\varrho = 0.01, \alpha = 1.07, \hat{D}_\varphi = 0.145$.

Exemplary particle dynamics can be found in Fig. 2.12 and respective movies can be found in (`https://figshare.com/projects/Traveling_Bands_Clouds_and_Vortices_of_Chiral_Active_Matter/82163` n.d.; `https://www.youtube.com/playlist?list=PLjL7stT6PH4xdc4X5Ee7xAr2vm49uIHvW` n.d.). We do not go into the details of analyzing each of those states because it extends beyond the scope of the paper. We only comment on their key features. One of the states is a cloud of high density (DC1 and DC2). In both cases, particles self-organize into circular shapes of high density (cf. Fig. 2.13), which we call clouds. While a momentum field is quite homogeneous for DC1, it has a clear radial structure for DC2. The same holds true for traveling bands TB1 and TB2. The dense part of TB1 is characterized with a uniform momentum field while TB2 has points with the radial change of a momentum field. Moreover, we have found a traveling band of low density TB3 for large $\tilde{\varrho}$ values only. The other dynamics include (i) a multiheaded chimera state (cf. Fig. 2.12(f)) characterized by the formation of several synchronized and spatially localized groups that rotate with constant frequency. This state is the generalization of a localized chimera state reported in (Kruk, Maistrenko, and Koeppl 2018). By decreasing $\tilde{\varrho}$, one increases the number of chimeric heads. By increasing α, the chaotic background becomes more pronounced until the heads become unstable and one observes giant number fluctuations in the density field. (ii) There are vortical structures where each one is either static (cf. Fig. 2.12(g)) in shape or periodically expands and shrinks (cf. Fig. 2.12(h)). By changing $\tilde{\varrho}$, one can control the number of vortices appearing. (iv) Particles may organize in structures of uniform density but with the direction of a momentum field

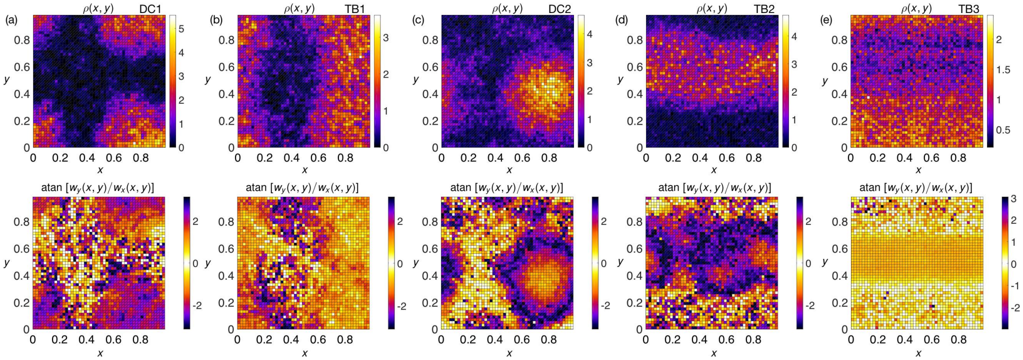

Figure 2.13: Coarse grained marginal density function $\rho(r, t)$ (the upper row) and the direction of a momentum field $w(r, t)$ (the lower row). Parameters: $N = 5 \cdot 10^4$, $\tilde{\varrho} = 1$, $v_0 = 0.01$, (a) $\varrho = 0.01, \alpha = 0.78, D_\varphi = 0.2075$, (b) $\varrho = 0.01, \alpha = 0.9, D_\varphi = 0.18$, (c) $\varrho = 0.01, \alpha = 1.3, D_\varphi = 0.06$, (d) $\varrho = 0.01, \alpha = 1.45, D_\varphi = 0.01$, and (e) $\varrho = 0.4, \alpha = 1.45, D_\varphi = 0.005$.

uniformly distributed horizontally or vertically (cf. Fig. 2.12(i)). (v) We also find a configuration with a spatially homogeneous density but a nonhomogeneous momentum field (cf. Fig. 2.12(j)).

Let us describe in more detail the differences in collective behavior for pairs of solutions having qualitatively similar macroscopic structure by looking at their coarse grained hydrodynamic description in terms of $\rho(r, t)$ and $w(r, t)$.

First, we find two types of solutions where particles accumulate into clouds of high density (DC1 and DC2 in Fig. 2.12(a) and (c), respectively). Inside both such clouds, particles are distributed quite uniformly with respect to r but the momentum fields structurally differ (cf. Fig. 2.13(a) and (c), respectively). For DC1, the mean direction $\arg(w(r, t))$ is also quite uniform. Therefore, on average, particles inside the cloud are oriented similarly but due to the small microscopic velocity v_0 they stay in the cloud for a long time. For DC2, the momentum field clearly possesses a radial structure. During such motion, central particles first define the orientation which later (in time) is assumed by particles further away from the center.

Second, we observe three types of traveling bands (TB1, TB2, and TB3 in Fig. 2.12(b),(d), and (e), respectively). TB1 and TB2 are characterized by the formation of bands of high density, which align horizontally or vertically depending on initial conditions. The hydrodynamic structure inside these bands follows the description of DC1 and DC2 with the hydrodynamic field illustrated in Fig. 2.13(b) and (d), respectively. We also observe TB3 where particles, which become synchronized, form a band that does not comprise most of the population. However, the other particles not inside this band do not become completely disordered. Due to the large interaction radius $\varrho = 0.4$, they are significantly influenced by the synchronized group and follow their orientation with some lag in time (cf. Fig. 2.13(e)).

Third, we find two vortical structures (SV and DV in Fig. 2.12(g) and (h), respectively). For SV, when particles are entrained into one of the vortexes, they begin to rotate on average around a common center and do not deviate from it much. For DV, particles periodically approach the center of a vortex but then rotate away from it. Thus, these vortexes remind a ’breathing’ shape.

Last, we would like to comment on localized (self-propelled) chimera structures, introduced in (Kruk, Maistrenko, and Koeppl 2018), and generalized here to multiple ’heads’ (cf. Fig. 2.12(f)). A localized chimera state is a solution of Eq. (2.3.13) in which a particle system splits into two distinct populations. Particles in the first population synchronize and additionally gather into a compact rotating cloud (sometimes called a ’head’). The rest of the particles remain disordered and are uniformly distributed across the domain. In (Kruk, Maistrenko, and Koeppl 2018), we reported the existence of a localized chimera state with one 'head'. In Fig. 2.12(f), one can observe a four-headed localized chimera state. Moreover, by changing $\tilde{\varrho}$, one can obtain such chimera states with a different number of compact clouds.

The integration of the SDEs Eq. (2.3.13) was performed using the strong order 1.5 Taylor scheme (Platen and Bruti-Liberati 2010). The movies representing these exemplary particle dynamics can be found in `https://figshare.com/projects/Traveling_Bands_Clouds_and_Vortices_of_Chiral_Active_Matter/82163` n.d.; `https://www.youtube.com/playlist?list=PLjL7stT6PH4xdc4X5Ee7xAr2vm49uIHvW` n.d.

2.4 SELF-PROPELLED SOLITARY STATES

We have shown that under an appropriate scaling, the Vicsek model can be recast into a continuous time form, where the temporal update for the direction of motion is effectively the same as the Kuramoto model for networks of coupled oscillators (Kuramoto 1984). As a result, in situations where the spatial information about collective dynamics is negligible, the study of a particle model coincides with the study of an oscillator model. In the view of recent increase of attention to the Kuramoto model with inertia, we are interested in analyzing how a similar modification would influence self-propelled particle motion (Kruk, Maistrenko, and Koeppl 2020).

To be more precise, let us consider a system of N particles moving in a two-dimensional space with periodic boundaries of size L with constant velocity magnitude $v_0 \in \mathbb{R}$. The state of a particle is given by a position $r_i \in \mathbb{U}^2, \mathbb{U} := \mathbb{R}/(L\mathbb{Z})$, orientation $\varphi_i \in \mathbb{T}, \mathbb{T} := \mathbb{R}/(2\pi\mathbb{Z})$, and angular velocity $\omega_i \in \mathbb{R}$. We describe particles' motion with the following system of ordinary differential equations (ODEs):

$$\begin{aligned}
\dot{r}_i(t) &= v_0 e_i(t), \\
\dot{\varphi}_i(t) &= \omega_i(t), \\
\dot{\omega}_i(t) &= -\xi\omega_i(t) + \frac{\sigma}{|B^i_\varrho|} \sum_{j \in B^i_\varrho} \sin(\varphi_j(t) - \varphi_i(t) - \alpha),
\end{aligned} \tag{2.4.14}$$

where $e_i = (\cos\varphi_i, \sin\varphi_i)$ denotes particle's orientation; $\xi \in \mathbb{R}_+$ is a rotational friction coefficient; $\sigma \in \mathbb{R}_+$ controls the strength of alignment within a neighborhood

$$B^i_\varrho := \{j = 1, \ldots, N \mid \|r_i - r_j\| \leq \varrho\}$$

of radius $\varrho \in \mathbb{U}$; $\alpha \in \mathbb{T}$ is a phase lag. By nondimensionalization, we find that $\frac{\xi B}{A} \gg 1$, where A and B are time and phase scales, respectively, defines the overdamped limit for orientational dynamics. In this limit, which implies $\dot{\omega}_i \approx 0$, with symmetric interaction potential, i.e., $\alpha = 0$, Eq. 2.4.14 becomes the known continuous time formulation of the Vicsek model (Degond and Motsch 2008). We remark that it has been shown that an alternative second order model in phase proves relevant in explaining oscillations in bacterial swarming (Chen et al. 2017).

Eq. (2.4.14) becomes the Kuramoto model with inertia in situations where the dynamics of position variables r_i become negligible. Namely, in the context of active matter theory, this arises in the following situations. First, if we consider global interactions between particles, i.e., $\varrho \geq \frac{L}{2}$, spatial inhomogeneity of the last term in Eq. (2.4.14) becomes irrelevant. Second, it is a common phenomenon for active matter systems that in the hydrodynamic limit $\varrho \to 0_+$, particle dynamics may become spatially homogeneous. Therefore, as the first step towards understanding general dynamics of Eq. (2.4.14), we will restrict ourselves to its spatially homogeneous formulation.

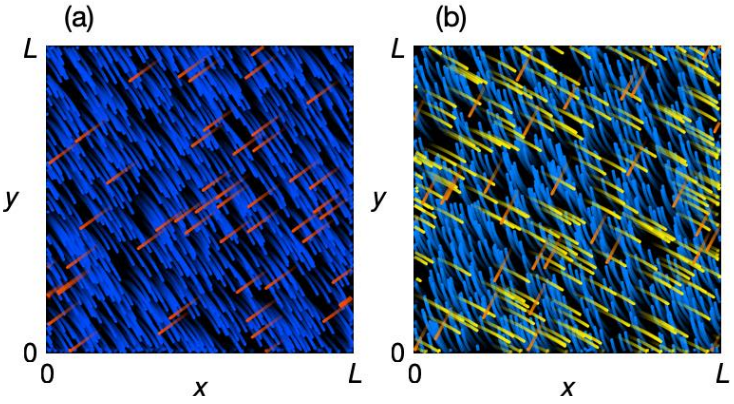

Figure 2.14: Examples of spatially homogeneous particle dynamics generated by Eq. (2.4.14) with $N = 10^3$ (see corresponding movies in (`https://www.youtube.com/playlist?list=PLjL7stT6PH4z3MFm3uyJFBfduO_yqHLbx` n.d.)) where particles self-organize into (a) two and (b) three frequency groups. Particle color denotes instantaneous angular velocity. Background is shown in black. Particles are represented as stripes with transparency increasing backward in time. Other parameters are the same as in Fig. 2.15(a) and (d), respectively.

Examples of such particle motion, which results from second-order angular dynamics only, are presented in Fig. 2.14.

The Kuramoto model (Kuramoto 1984) has gained a lot of attention in the last two decades due to the discovery of the striking coexistence of synchronized and desynchronized groups in networks of coupled oscillators, which became known as *chimera states* (Abrams and S. H. Strogatz 2004; Kuramoto and Battogtokh 2002). Since that, chimera states where obtained in very different fields (see recent review papers (Omel'chenko and Knobloch 2019; Panaggio and Abrams 2015; Schöll 2016)) including self-propelled systems (Kruk, Maistrenko, and Koeppl 2018). Subsequent studies on the Kuramoto model with inertia have revealed the appearance of yet another collective oscillatory motion termed *solitary states* (Berner et al. 2019; Jaros, Brezetsky, et al. 2018; Jaros, Maistrenko, and Kapitaniak 2015; Maistrenko, Penkovsky, and Rosenblum 2014). They satisfy the definition of *weak chimera states* (Ashwin and Burylko 2015) but, nevertheless, reflect a qualitatively distinct situation where only a single oscillator or a relatively small group of oscillators splits off from the main synchronized cluster and starts to rotate with a different averaged frequency, i.e., Poincaré rotation number (cf. Fig. 2.14 and movies in (`https://www.youtube.com/playlist?list=PLjL7stT6PH4z3MFm3uyJFBfduO_yqHLbx` n.d.) for examples of such motion in a self-propelled particle context Eq. (2.4.14)). An importance of this kind of behavior follows from the fact that solitary states naturally arise in realistic networks with inertia, such as coupled pendula (Kapitaniak et al. 2014) and power grids (Hellmann et al. 2020; Taher, Olmi, and Schöll 2019) but they are not possible in the paradigmatic standard Kuramoto model without inertia.

2.4.1 *Solitary phenomena*

Let us consider a spatially homogeneous formulation of particle dynamics Eq. (2.4.14), which we now refer to as oscillators. The state of each oscillator is given by a phase $\varphi_i \in \mathbb{T}$ and a frequency

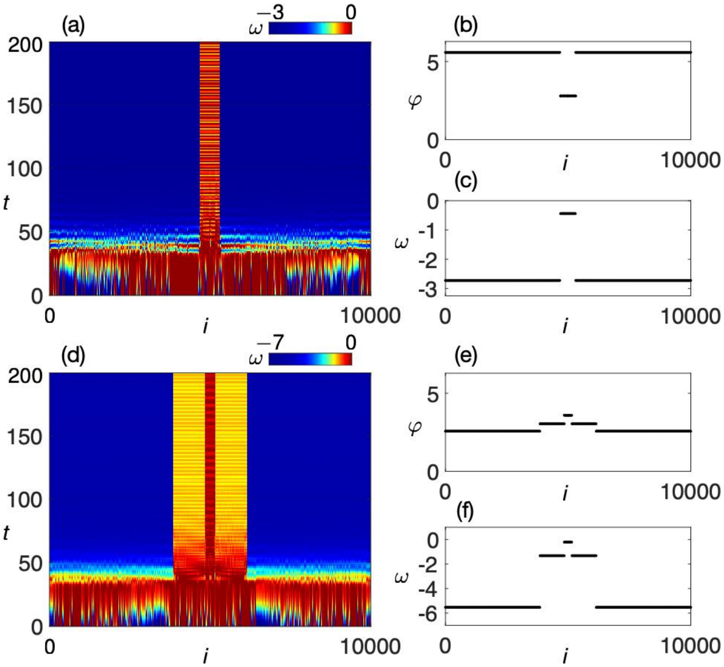

Figure 2.15: Temporal evolution towards a solitary state with (a) one frequency cluster ($\alpha = 0.3$) and (d) two frequency clusters ($\alpha = 0.8$) starting from random initial conditions as space-time plots. Color corresponds to instantaneous frequency ω. (b,c) and (e,f) Respective profiles of instantaneous phase φ and instantaneous frequency ω. Frequency profiles correspond to respective horizontal intersections of space-time plots at $t = 200$. Oscillators are reordered according to the value of instantaneous frequency at $t = 200$ from (c) and (f), respectively. Other parameters are $\xi = 0.1$, $\sigma = 1$, $N = 10^4$.

$\omega_i \in \mathbb{R}$. To study oscillatory dynamics without the influence of spatial distribution, we assume that oscillators are globally coupled and obey the following system of ODEs:

$$\begin{aligned} \dot{\varphi}_i(t) &= \omega_i(t), \\ \dot{\omega}_i(t) &= -\xi\omega_i(t) + \frac{\sigma}{N}\sum_{j=1}^{N} \sin(\varphi_j(t) - \varphi_i(t) - \alpha), \end{aligned} \tag{2.4.15}$$

where $\xi \in \mathbb{R}_+$ is a friction coefficient, $\sigma \in \mathbb{R}_+$ controls the strength of coupling, and $\alpha \in \mathbb{T}$ is a phase lag. The last term in Eq. (2.4.15) favors synchronization between oscillators. The presence of the phase lag α induces additional rotation of the oscillators with respect to the average orientation of all neighbors. Eq. (2.4.15) contains three parameters ξ, σ, and α, one of which can be eliminated by appropriate time scaling. For convenience, we put $\xi = 0.1$ (Jaros, Brezetsky, et al. 2018) for the rest of the paper and consider $\alpha \geq 0$.

Numerical investigation of Eq. 2.4.15 reveals the following. First, in the absence of the phase lag, i.e., when $\alpha = 0$, all oscillators are stationary and completely synchronized. For small $\alpha > 0$, the oscillators remain synchronized but rotating with the angular frequency $\omega^* = -\frac{\sigma}{\xi}\sin\alpha$. Upon a further increase of α (cf. Fig. 2.16(a)) (and as long as $\xi < 2\sqrt{\sigma\cos\alpha}$, see Appendix B in (Kruk, Maistrenko, and Koeppl 2020) and subsequent discussion), a group of oscillators split off from the majority and begins to rotate with a separate frequency. This type of dynamics has been termed as a *solitary state* (Jaros, Brezetsky, et al. 2018).

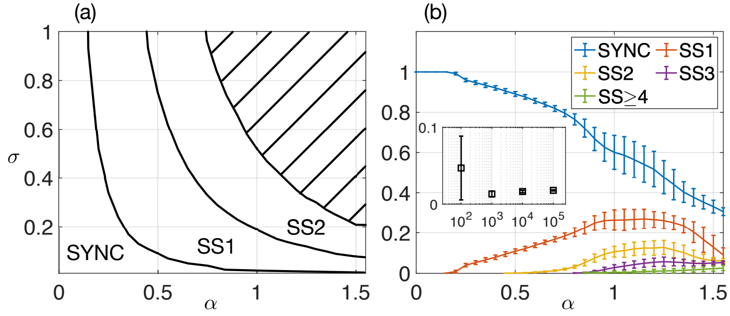

Figure 2.16: (a) Phase diagram of oscillatory dynamics due to 2.4.15. The synchronized motion (SYNC) is stable in all of the displayed domain. SS1 and SS2 denote regions where one and two groups of solitary oscillators emerge, respectively. Oblique hatching denotes a region where three and more solitary groups as well as chimeras appear. The phase diagram has been obtained with a continuation method for $N = 10^3$. (b) Fraction of oscillators from different groups versus the phase lag α out of 200 experiments per parameter tuple. Error bar indicates standard deviation with respect to different initial configurations. The inset shows the fraction of solitary oscillators in SS1 versus different population sizes ($\alpha = 0.3$). Other parameters are $\xi = 0.1$, $\sigma = 1$.

The formation of solitary states starting from random initial conditions is illustrated in Fig. 2.15(a)). At the beginning, the oscillators are disordered each pointing in its own direction and with its own frequency. Soon after, they gradually synchronize with respect to both phase φ and frequency ω (cf. Fig. 2.15(a), $t \lessapprox 50$). At this point, one can already observe the formation of the second group of oscillators that are not in sync with the majority. Subsequently, the division between two groups becomes more pronounced and the variations of φ and ω inside each of them tend to minimize (cf. Fig. 2.15(b,c)).

Our simulations confirm that at further increase of the coupling strength σ or the phase lag α, the second solitary cluster emerges (cf. Fig. 2.15(d-f) and Fig. 2.16(a)). The temporal evolution of a system towards such a state starting from random initial conditions is initially the same as described above for the solitary state with the only one frequency cluster. As it can be seen from Fig. 2.15(d), during the initial stage, the first solitary cluster develops and soon after, at some point ($t \approx 50$), the second smaller solitary group starts to rotate with their own distinctive frequencies. As time advances, this latter group synchronizes and rotates with a frequency different from frequencies of the other two clusters (cf. Fig. 2.15(e,f)). Continuing in this way, we observe a cascade of solitary states with an increasing number of frequency clusters (cf. Fig. 2.16(b)). For $N = 10^3$, we observe up to four additional such frequency clusters. Upon the further increase of the phase lag ($\alpha \gtrapprox 1.3$ for $\sigma = 1$), all solitary clusters merge and their averaged frequencies are continuously distributed over some range. In this paper, we primarily concentrate on the solitary states with one solitary group and will not discuss the rest of the cascade.

The number of solitary oscillators in frequency clusters depends essentially on initial conditions (cf. the inset in Fig. 2.16(b)). For small population sizes $N \sim 10^2$, this dependence is strong. However, upon the increase of the system size N, these fluctuations decrease and the total fraction of oscillators in a solitary group tends to a certain limit. One can see that for population sizes $N \sim 10^3$ and larger, the variance in the size drops drastically.

It has been shown (Jaros, Brezetsky, et al. 2018) that the mechanism for one solitary oscillator to emerge is a homoclinic bifurcation of a saddle at some $\alpha = \alpha_1(\sigma)$. After the bifurcation, oscillators are separated into two populations, each with their own phase and frequency (φ_0, ω_0) and (φ_1, ω_1), respectively. System's dynamics evolves on a two-dimensional cylinder Ω^2, $\Omega := \mathbb{T} \times \mathbb{R}$. It can easily be reduced to a one-dimensional cylinder for the difference variables $\Delta\varphi = \varphi_1 - \varphi_0$ and $\Delta\omega = \omega_1 - \omega_0$. Analyzing the dynamics of these difference variables (Maistrenko, Popovych, et al. 2004) (see the details in Appendix B in (Kruk, Maistrenko, and Koeppl 2020)), we find two equilibria: a sink $O = (0, 0)$ and a saddle $S = (\pi - 2\beta, 0)$ with $\beta = \arctan[(1 - 2/N)\tan\alpha]$. The origin O corresponds to complete synchronization and is a stable focus for $\xi < 2\sqrt{\sigma\cos\alpha}$ (otherwise, it is a stable node). The second equilibrium S is a saddle. At $\alpha = \alpha_1$, a homoclinic orbit γ_1 is created in the moment when the unstable manifold of S spans the phase space and comes back to S as its stable manifold. It signifies the appearance of a solitary oscillator in Eq. (2.4.15). For $\alpha > \alpha_1$ the phase portrait contains a stable limit cycle that coexists with the stable focus O. Note that if the coupling strength σ is kept constant and the friction coefficient is considerably increased, i.e, $\xi > 2\sqrt{\sigma\cos\alpha}$, O becomes a stable node and solitary oscillators do not emerge.

As the next step, we want to understand how two solitary oscillators appear given the aforementioned mechanism for the emergence of one such oscillator. Suppose that the system consists of $N - 2$ synchronized oscillators and two solitary ones. The fraction of each of the solitary oscillators equals $w = 1/N$ of the whole population. Let (φ_0, ω_0) denote phase and frequency of each synchronized oscillator and (φ_1, ω_1) and (φ_2, ω_2) denote the same variables of two solitary oscillators. In terms of difference variables (Maistrenko, Popovych, et al. 2004) $\Delta\varphi_{1,2} = \varphi_{1,2} - \varphi_0$ and $\Delta\omega_{1,2} = \omega_{1,2} - \omega_0$, system's dynamics are completely governed by (see Appendix C in (Kruk, Maistrenko, and Koeppl 2020))

$$\begin{aligned}
\Delta\dot{\varphi}_1 &= \Delta\omega_1, \\
\Delta\dot{\omega}_1 &= -\xi\Delta\omega_1 - \sigma R\sin(\Delta\varphi_1 + \beta) + \sigma B \\
&\quad + \sigma w\sin(\Delta\varphi_2 - \Delta\varphi_1 - \alpha) - \sigma w\sin(\Delta\varphi_2 - \alpha), \\
\Delta\dot{\varphi}_2 &= \Delta\omega_2, \\
\Delta\dot{\omega}_2 &= -\xi\Delta\omega_2 - \sigma R\sin(\Delta\varphi_2 + \beta) + \sigma B \\
&\quad + \sigma w\sin(\Delta\varphi_1 - \Delta\varphi_2 - \alpha) - \sigma w\sin(\Delta\varphi_1 - \alpha),
\end{aligned} \tag{2.4.16}$$

where $A = (1 - w)\cos\alpha$, $B = (1 - 3w)\sin\alpha$, $R = \sqrt{A^2 + B^2}$, and $\beta = \arctan(B/A)$. This system defines a flow on a two-dimensional cylinder Ω^2. Note that Eq. (2.4.16) are symmetric with respect to the diagonal plane

$$D := \left\{(\Delta\varphi_1, \Delta\omega_1, \Delta\varphi_2, \Delta\omega_2) \in \Omega^2 \mid \Delta\varphi_1 = \Delta\varphi_2, \Delta\omega_1 = \Delta\omega_2\right\}. \tag{2.4.17}$$

The system Eq. (2.4.16) has four equilibria $O = (0, 0, 0, 0)$, $S_1 = (\pi - 2\beta', 0, 0, 0)$, $S_2 = (0, 0, \pi - 2\beta', 0)$, and $S_{12} = (\pi - 2\beta'', 0, \pi - 2\beta'', 0)$, where we have denoted $A' = \cos\alpha$, $B' = (1 - 2w)\sin\alpha$, $R' = \sqrt{A'^2 + B'^2}$, and $\beta' = \arctan(B'/A')$; $A'' = \cos\alpha$, $B'' = (1 - 4w)\sin\alpha$, $R'' = \sqrt{A''^2 + B''^2}$, and $\beta'' = \arctan(B''/A'')$. O is a stable focus as long as $\xi < 2\sqrt{\sigma\cos\alpha}$; otherwise, it is a stable node. It corresponds to the synchronization of both oscillators with the main group. The fixed points S_1 and S_2 are of a saddle type. Two of their eigenvalues $\lambda_1 > 0$ and $\lambda_2 < 0$ are the same as in the previously discussed one-dimensional case; two remaining eigenvalues are equal $\lambda_{3,4} = \frac{1}{2}(-\xi \pm \sqrt{\xi^2 - 4\sigma\cos\alpha(1 - 2w)/R'^2})$. Since we keep $w = 1/N$, with $N \to \infty$, $\lambda_{3,4} \in \mathbb{C}$ with Re $\lambda_{3,4} < 0$ so that S_1 and S_2 are saddle-foci. The last fixed point S_{12}, which lies on the diagonal plane D, has two eigenvalues $\lambda_1 > 0$ and $\lambda_2 < 0$, as well. The other two read $\lambda_{3,4} = \frac{1}{2}(-\xi \pm \sqrt{\xi^2 + 4\sigma(1 - 4w)\cos\alpha/R''^2})$. With $N \to \infty$, we have $\lambda_3 > 0$ and $\lambda_4 < 0$. Therefore, S_{12} is a saddle with two stable and two unstable manifolds.

The homoclinic bifurcation discussed previously leads to the creation of two periodic orbits γ_1 and γ_2 which lie in the respective two-dimensional subspaces

$$P_1 := \left\{(\Delta\varphi_1, \Delta\omega_1, \Delta\varphi_2, \Delta\omega_2) \in \Omega^2 \mid \Delta\varphi_2 = 0, \Delta\omega_2 = 0\right\} \tag{2.4.18}$$

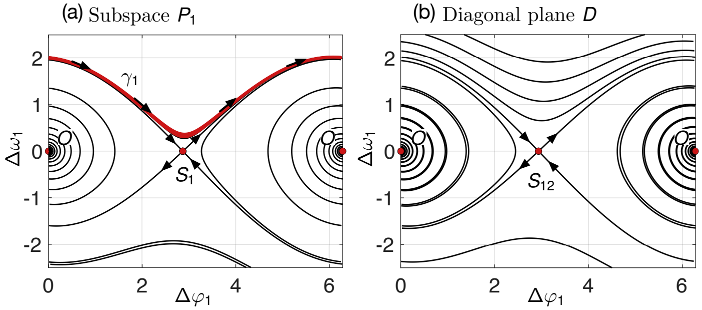
(a) Subspace P_1 (b) Diagonal plane D

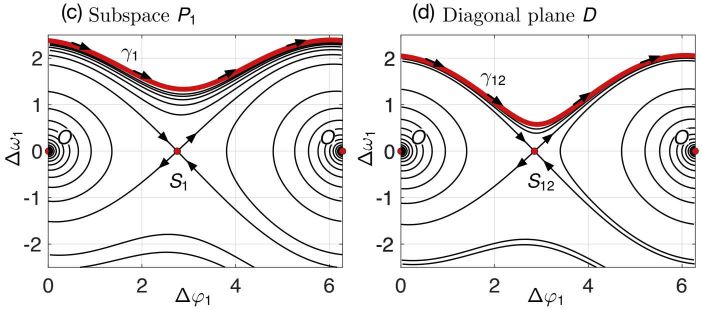
(c) Subspace P_1 (d) Diagonal plane D

Figure 2.17: Subspaces of phase portraits of Eq. (2.4.16) for different values of the phase lag α. (a) The plane P_1 Eq. (2.4.18) and (b) the diagonal plane D Eq. (2.4.17) of the first solitary oscillator, respectively, after appearance of a periodic orbit $\gamma_1 \subset P_1$, i.e., $\alpha_1 < \alpha < \alpha_2$. (c) The plane P_1 and (d) the diagonal plane D of the first solitary oscillator, respectively, after appearance of a periodic orbit $\gamma_{12} \subset D$, i.e., $\alpha > \alpha_2$. Black arrows around saddle points indicate their respective stable and unstable manifolds. Black arrows along periodic orbits indicate the direction of motion along them.

and $P_2 := \{(\Delta\varphi_1, \Delta\omega_1, \Delta\varphi_2, \Delta\omega_2) \in \Omega^2 \mid \Delta\varphi_1 = 0, \Delta\omega_1 = 0\}$. The phase portrait in P_1 is shown in Fig. 2.17(a) (in P_2, it is similar due the symmetry of Eq. (2.4.16)). At this point, all trajectories on the diagonal plane D, where the saddle point S_{12} exists, converge to the focus O (except for the saddle itself and its stable manifolds) (cf. Fig. 2.17(b)). With a subsequent increase of the phase lag till some $\alpha = \alpha_2$, the next homoclinic orbit γ_{12} is created, belonging to the diagonal plane D. It occurs in the moment when the unstable manifold of the saddle S_{12} merges with its stable manifold. With $\alpha > \alpha_2$, the phase portrait on the diagonal plane contains two equilibria O and S_{12} and a limit cycle (cf. Fig. 2.17(d)) that signifies existence of two solitary oscillators, which rotate in-phase and with the same frequency.

With a subsequent increase of α, we observe a cascade of homoclinic bifurcations appearing on diagonals defined by $(\Delta\varphi_1, \Delta\omega_1) = (\Delta\varphi_2, \Delta\omega_2)$, $(\Delta\varphi_1, \Delta\omega_1) = (\Delta\varphi_2, \Delta\omega_2) = (\Delta\varphi_3, \Delta\omega_3)$, and so on. This behavior depends on the fraction w of solitary oscillators. Therefore, with the increase of the population size, the maximum allowed size of a solitary group increases linearly. However, in the large population size limit $N \to \infty$, the probability to observe any finite *number* of solitary oscillators out of the whole population tends to zero and we become interested in observing a finite *fraction* of solitary oscillators, which will consist of an infinite subpopulation. In this limit, since $w \to 0_+$, all homoclinic bifurcation boundaries, described above, collapse into one that signifies the appearance of the whole solitary group (cf. Fig. 2.16(a)).

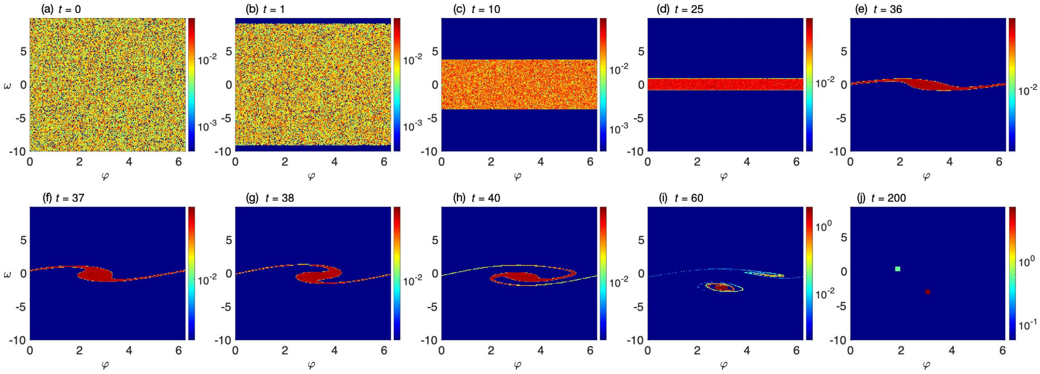

Figure 2.18: Snapshots of coarse-grained representation Eq. (2.4.22) of oscillatory dynamics, obtained by integrating Eq. (2.4.15), that evolve towards a solitary state with one frequency cluster for the large but finite population size. Color represents the value of a coarse-grained density function Eq. (2.4.22). The discretization in (φ, ω) is 256×200 for (a)-(i) and 32×30 for (j) for better visibility. Other parameters are $\xi = 0.1$, $\sigma = 1.0$, $\alpha = 0.3$, $N = 10^5$.

2.4.2 *Langevin dynamics*

In the context of active matter and in general in systems where global polar order emerges, it is convenient to introduce a respective order parameter that characterizes large scale oscillatory ensembles in low dimension. The classical macroscopic characteristic for such systems is a global polar order parameter defined as a complex valued function as

$$R(t)e^{i\Theta(t)} = \frac{1}{N}\sum_{j=1}^{N} e^{i\varphi_j(t)}, \tag{2.4.19}$$

where $e^{i\varphi_j(t)}$ can be interpreted as an active rotor on the unit circle $\mathbb{S}^1$ (J. A. Carrillo, Choi, and Pareschi 2019) and this operation evolves computing the average orientation among them. If we consider phases as orientations of self-propelled particles, this operation is equivalent to computing the average direction of motion of all population. The magnitude shows how strongly the system is synchronized. If $R = 0$, it is disordered, and if $R = 1$, it is completely synchronized. Otherwise, $R \in (0, 1)$ indicates a partial level of orientational order. Note that one can rewrite the interaction term in Eq. (2.4.15) in terms of this order parameter, i.e., $\frac{1}{N}\sum_{j=1}^{N}\sin(\varphi_j - \varphi_i - \alpha) = R_i \sin(\Theta_i - \varphi_i - \alpha)$, $i = 1, \ldots, N$. Namely, the dynamics of one oscillator are defined in terms of a mean field. This mean field is in turn generated by the whole population of oscillators. This formulation will prove useful for our subsequent study of the mean-field limit behavior.

From the natural and application point of view, we must take into account that oscillators are generally subject to some external perturbations which we consider to be of stochastic origins. Therefore, we now regard oscillators as interacting stochastic processes and reformulate ODEs Eq. (2.4.15) as stochastic differential equations (SDEs)

$$\begin{aligned} \mathrm{d}\varphi_i(t) &= \omega_i(t)\,\mathrm{d}t, \\ \mathrm{d}\omega_i(t) &= -\xi\omega_i(t)\,\mathrm{d}t + \sigma R_i(t)\sin(\Theta_i(t) - \varphi_i(t) - \alpha)\,\mathrm{d}t + \sqrt{2D_\varphi}\,\mathrm{d}W_i(t), \end{aligned} \tag{2.4.20}$$

where interactions between oscillators are expressed in terms of the mean field as previously discussed. Oscillators are subject to external stochastic forces accounted for by families of independent

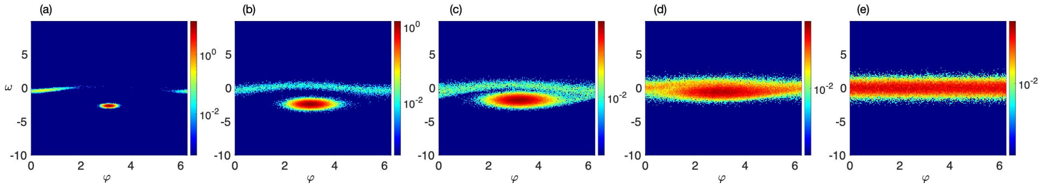

Figure 2.19: Coarse-grained PDFs for stochastic dynamics Eq. (2.4.20) manifesting a solitary state with one frequency cluster for different noise levels: (a) $D_\varphi = 0.001$, (b) $D_\varphi = 0.01$, (c) $D_\varphi = 0.02$, (d) $D_\varphi = 0.04$, and $D_\varphi = 0.05$, which are taken along the order-disorder phase transition route in Fig. 7(b) in the main text. Color denotes values of the density function. The number of particles used for coarse graining is $N = 10^5$. The discretization in (φ, ω) is 256×200. Other parameters are $\xi = 0.1$, $\sigma = 1.0$, $\alpha = 0.3$.

Wiener processes $(W_i(t))_{t\geq 0}$, $i = 1, \ldots, N$ with $D_\varphi > 0$ as the noise strength. The resulting dynamics under noise are determined through the interplay of alignment and stochastic forces. Namely, if the first one prevails, we observe the emergence of ordered motion; otherwise, the motion remains disordered. All our Langevin simulations of Eq. (2.4.20) are performed using the strong order 1.5 Taylor scheme (Platen and Bruti-Liberati 2010).

The temporal evolution of a network of oscillators towards a solitary state with one frequency cluster under noise is qualitatively similar as in a deterministic setup (cf. Fig. 2.15). Starting from random initial conditions (with compact support for frequencies), oscillators synchronize in frequency first with phases remaining disordered. At some later point, oscillators start to synchronize in phases. However, each frequency cluster is no longer characterized with a single averaged value. Instead, each cluster is now characterized with a distribution over ω. For partial synchronization, this distribution is skewed and unimodal. For solitary states, it is multimodal, where the number of peaks corresponds to the number of frequency clusters with the highest peak representing the largest synchronized group. For small D_φ, averaged frequencies of all groups are less than zero (for $\alpha > 0$). With the increase of D_φ, they shift towards zero until all modes coalesce and the distribution for the whole population becomes Gaussian for ω and uniform for φ (compare to Eq. (2.4.26)).

2.4.3 *Coarse-grained representation of an oscillatory ensemble with large population size*

To better understand the dynamics of a large (but finite) population of oscillators governed by the system of ODEs Eq. (2.4.14) we assume a probabilistic approach and describe it in terms of an appropriate probability density function (PDF). Thereby, we introduce an empirical PDF

$$f^{[N]}(\varphi, \omega, t) = \frac{1}{N} \sum_{i=1}^{N} \delta[\varphi - \varphi_i(t)] \delta[\omega - \omega_i(t)], \tag{2.4.21}$$

where the superscript N indicates the implicit dependence of the function on all of oscillators' states and δ is the generalized Dirac delta function. This function gives the fraction of oscillators that have phase φ and frequency ω at time t. If the number of oscillators were infinite, it would have a nonzero value anywhere in its support. However, since Eq. (2.4.21) is an approximation to such a continuum description, it is nonzero only on the points (φ, ω) where oscillators are located. Since N is finite, this set is of measure zero with respect to the Lebesgue measure. In order to make use of this approximation, we consider a coarse-grained formulation of the density function defined as a convolution between Eq. (2.4.21) and a suitable piecewise constant kernel function K as

$$\bar{f}^{[N]}(\varphi,\omega,t) = \int_{\Omega} f^{[N]}(\varphi',\omega',t) K(\varphi-\varphi',\omega-\omega')\, \mathrm{d}\varphi' \mathrm{d}\omega', \tag{2.4.22}$$

where $K(\varphi,\omega) = H(h_\varphi/2 - |\varphi|)H(h_\omega/2 - |\omega|)$ is a product of two Heaviside step functions, with the support $\{(\varphi,\omega) \in \Omega \mid |\varphi| < h_\varphi/2, |\omega| < h_\omega/2\}$. In other words, $\bar{f}^{[N]}$ gives the fraction of oscillators whose states fall into the differential area of size $h_\varphi h_\omega$ around (φ,ω) at time t.

The typical evolution of a large scale system of oscillators towards a solitary state with one additional frequency cluster starting from random initial conditions is depicted in Fig. 2.18. To facilitate the compact support of the PDF, we draw phases $\varphi_i \sim \mathcal{U}(0, 2\pi)$ and $\omega_i \sim \mathcal{U}(-\sigma/\xi, \sigma/\xi)$ for each $i = 1, \ldots, N$ (cf. Fig. 2.18(a)). We have solved Eq. (2.4.15) with a Runge-Kutta method with adaptive step size and absolute and relative tolerances set to 10^{-10}. Since the interactions in Eq. (2.4.15) between oscillators are defined for frequencies, they begin to gradually synchronize in frequency first, with phases remaining uniformly distributed (cf. Fig. 2.18(b)-(d)). When the synchronization with respect to frequency is large enough, oscillators have approached a respective higher-order diagonal in the phase space (see the main text for the description of phase portrait dynamics) and start to follow an unstable manifold that leads to solitary behavior along a periodic orbit for a smaller group and for synchronized behavior towards a stable focus O for the majority (cf. Fig. 2.18(e)-(h)). After the oscillators have separated into two distinct groups (cf. Fig. 2.18(i)), each of them gradually contracts to a point mass that exhibits oscillatory motion itself (cf. Fig. 2.18(j)).

When oscillators are subject to noise, their motion is governed by the system of SDEs Eq. (2.4.20). The temporal evolution of a network of oscillators towards a solitary state with one frequency cluster is qualitatively similar to the deterministic setup described above. Starting from random initial conditions (with compact support for frequencies), oscillators synchronize in frequency first with phases remaining disordered. In terms of a PDF, this continues until the ω-marginal of the corresponding PDF shrinks to a Gaussian density. Afterwards, oscillators' phases start to synchronize and one observes similar spiral-like behavior of high-density stripes (cf. Fig. 2.18(e-h)) until the formation of two high-density regions. The difference from the deterministic motion is that here, it is eventually described by a bimodal PDF with the highest peak representing the largest synchronized group and with solitary oscillators being distributed along closed orbits they follow (cf. Fig. 2.19(a)). Examples of solitary states with one frequency cluster for different noise levels are represented in Fig. 2.19. For small D_φ, averaged frequencies of both groups are less than zero (for $\alpha > 0$). We observe that with the increase of D_φ, they shift towards zero until both modes coalesce and the PDF becomes Gaussian for ω and uniform for φ (cf. Fig. 2.19(e)).

2.4.4 *Mean-field limit*

To understand the dynamics of solitary states without finite size effects, we turn to the mean-field description of interacting particle systems, i.e., the limit $N \to \infty$ (Cañizo, J. A. Carrillo, and Rosado 2011; J. Carrillo et al. 2014; Kipnis and Landim 1998b; Lancellotti 2005; Neunzert 1984). This description is commonly provided by a one-particle probability density function (PDF) $f(\varphi,\omega,t) : \Omega \times \mathbb{R}_+ \to \mathbb{R}_+$ with $\Omega = \mathbb{T} \times \mathbb{R}$, which quantifies the probability to find an oscillator having phase φ and rotating with frequency ω at time t. Our first goal in this section is to find a partial differential equation (PDE) that governs its evolution. We start by considering an empirical PDF Eq. (2.4.21) as a particle approximation to the mean-field PDF. This function gives the fraction of oscillators that have phase φ and frequency ω at time t. Using the framework of Fokker-Planck equations (Risken and Frank 1996), we look for an ensemble-averaged representation of the empirical PDF Eq. (2.4.21) (Archer and Rauscher 2004a). This

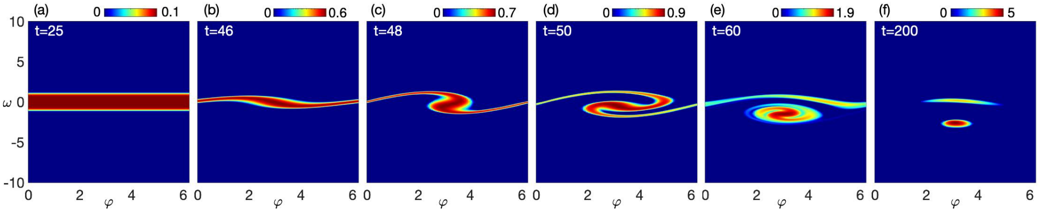

Figure 2.20: Temporal evolution of a PDF as a solution to the continuum Kuramoto model with inertia Eq. (2.4.23) towards a solitary state with one frequency cluster starting from irregular initial conditions. Snapshots are taken at (a) $t = 25$, (b) $t = 46$, (c) $t = 48$, (d) $t = 50$, (e) $t = 60$, and (f) $t = 200$. Color denotes values of the PDF. The discretization in (φ, ω) is 128×1000. Other parameters are $\xi = 0.1$, $\sigma = 1.0$, $\alpha = 0.3$, $D_\varphi = 0.001$.

way, one obtains an infinite hierarchy of n-particle density functions and assumes a mean-field approximation $f(\varphi_1, \omega_1, \varphi_2, \omega_2, t) \approx f(\varphi_1, \omega_1, t) f(\varphi_2, \omega_2, t)$ in order to close the hierarchy at the first order. As a result, we obtain a nonlinear Fokker-Planck-Kolmogorov PDE for a one-particle PDF $f = f(\varphi, \omega, t)$

$$\partial_t f = -\omega \partial_\varphi f - \partial_\omega \left\{ f \left[-\xi\omega + \sigma R \sin(\Theta - \varphi - \alpha) \right] \right\} + D_\varphi \partial_{\omega\omega} f, \tag{2.4.23}$$

where the polar order parameter Eq. (2.4.19) becomes

$$R(t) e^{i\Theta(t)} = \int_\Omega e^{i\varphi} f(\varphi, \omega, t) \, \mathrm{d}\varphi \mathrm{d}\omega. \tag{2.4.24}$$

An example of how the mean-field dynamics evolves towards a solitary state with one frequency cluster is presented in Fig. 2.20 (see a corresponding movie in (`https://www.youtube.com/playlist?list=PLjL7stT6PH4z3MFm3uyJFBfduO_yqHLbx` n.d.)). One observes qualitatively similar evolution of a PDF $f(\varphi, \omega, t)$ and a finite-size oscillator ensemble represented in terms of a coarse-grained PDF (cf. Fig. 2.20 and Appendix D in (Kruk, Maistrenko, and Koeppl 2020)). Namely, starting from a sufficiently irregular initial condition with compact support, the solution rapidly becomes uniform in φ and unimodal in ω. This signifies the tendency of oscillators to synchronize via frequency (cf. Fig. 2.20(a)). When such synchronization is large enough, the high-density stripe starts to bend and rotate (cf. Fig. 2.20(b-d)). This means that oscillators begin to synchronize in phase, which is updated via frequency. Therefore, the probability mass that lies above the $\omega = 0$ line, warps one way while the lower part warps the opposite way. The direction of rotation depends on the sign of α. Such rotational motion is also contracting. If α is large enough, a part of probability mass separates and follows its own oscillating trajectory (cf. Fig. 2.20(e)). Eventually, both peaks become more compact (cf. Fig. 2.20(f)), the level of which depends on a diffusion constant D_φ. By varying α, one observes partial synchronization or a solitary state with two frequency clusters, respectively (cf. Fig. 2.21 and (`https://www.youtube.com/playlist?list=PLjL7stT6PH4z3MFm3uyJFBfduO_yqHLbx` n.d.) for corresponding movies). For all numerical studies of Eq. (2.4.23), we have implemented a finite volume method (Kruk, J. A. Carrillo, and Koeppl preprint) with boundary conditions being periodic for φ and zero flux for ω.

From the stochastic dynamics Eq. (2.4.20), we know that oscillators can synchronize in one group or in several groups, i.e., a solitary state, or remain disordered, i.e., $R = 0$. The latter case is described with a stationary distribution in the mean-field limit. To find its analytical expression, we first note that due to periodic boundaries, the PDF in terms of φ is uniform. Therefore, it should

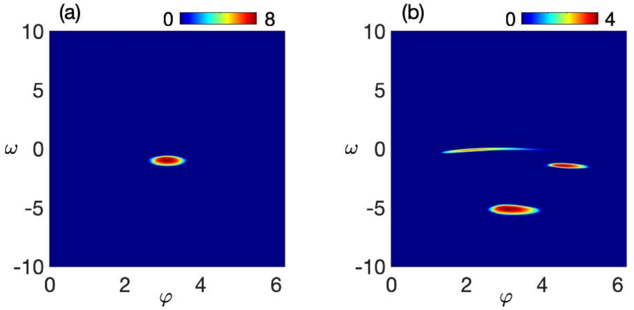

Figure 2.21: Snapshots of solutions of the continuum Kuramoto model with inertia Eq. (2.4.23) representing (a) nonstationary partial synchronization ($\alpha = 0.1$, $D_\varphi = 0.001$) and (b) a solitary state with two frequency clusters ($\alpha = 0.8$, $D_\varphi = 0.0001$). Color denotes values of a density function $f(\varphi, \omega, t)$. Grid discretization in (φ, ω) is 128 by 1000. Other parameters are $\xi = 0.1$, $\sigma = 1.0$.

only depend on frequency ω, over which it has unbounded support. Second, we require that the PDF is sufficiently regular, i.e., $f(\omega) \to 0$ and $f'(\omega) \to 0$ as $\omega \to \pm\infty$. Under such assumptions, one can show that disordered oscillatory motion in the mean-field limit is described by (cf. Fig. 2.22, the right insets)

$$f(\varphi, \omega) = \frac{1}{2\pi}\Phi_G(\omega), \tag{2.4.25}$$

where a prefactor $1/(2\pi)$ arises due to normalization with respect to φ and Φ_G is a Gaussian PDF

$$\Phi_G(\omega) = \frac{1}{\sqrt{2\pi s^2}} e^{-\frac{\omega^2}{2s^2}} \tag{2.4.26}$$

with zero mean and standard deviation $s = \sqrt{D_\varphi/\xi}$. Note that this solution is valid for any phase lag value α.

In the absence of the phase lag and for sufficiently small noise, oscillators exhibit partial synchronization. A PDF that corresponds to this behavior is symmetric with respect to both φ and ω. In fact, the ω-marginal has qualitatively the same form as Eq. Eq. (2.4.26). Therefore, we look for a stationary solution of the form $f(\varphi, \omega) = \Phi(\varphi)\Phi_G(\omega)$, where Φ is to be determined. Substituting f into Eq. Eq. (2.4.23), we find

$$f(\varphi, \omega) = \Phi_{VM}(\varphi)\Phi_G(\omega), \tag{2.4.27}$$

where Φ_{VM} is a von Mises PDF

$$\Phi_{VM}(\varphi) = \frac{1}{2\pi I_0(\gamma)} e^{\gamma \cos(\varphi - \Theta)}$$

with $\gamma = \sigma\xi R/D_\varphi$ denoting system's relative synchronization level and I_0 is the modified Bessel function of the first kind. This PDF depends on R which in turn depends on the PDF itself. Thereby, we can determine R implicitly from

$$R = \frac{I_1[\gamma(R)]}{I_0[\gamma(R)]}$$

and put $\Theta \equiv 0$ without loss of generality due to the translation invariance of Eq. (2.4.23). Analyzing this expression around the onset of orientational order at $R = 0$ (Kruk, J. A. Carrillo, and Koeppl 2020), we find the order-disorder transition line

$$D_\varphi = \frac{\sigma\xi}{2}. \tag{2.4.28}$$

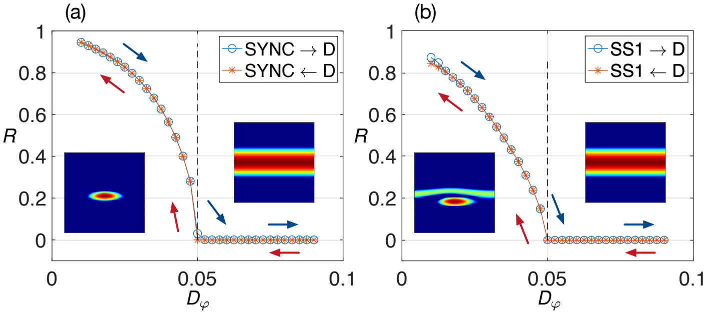

Figure 2.22: Phase transitions between disordered motion (D) and (a) partial synchronization (SYNC) and (b) a solitary state with one frequency cluster (SS1). The transitions are quantified in terms of a polar order parameter magnitude R Eq. (2.4.24). Routes from SYNC and SS1 towards D are depicted with blue circles. Routes from D to SYNC and SS1 are depicted with red stars. Black dashed lines denote order-disorder transition points $D_\varphi = \frac{1}{2}\sigma\xi\cos(\frac{1}{2}\alpha)$ Eq. (2.4.29). Insets show PDFs at respective endpoints of bifurcation curves. Colored arrows indicate directions of bifurcation paths. Other parameters are $\xi = 0.1$, $\sigma = 1$, (a) $\alpha = 0.1$, (b) $\alpha = 0.3$.

For noise levels higher than this critical value, oscillatory motion remains disordered, i.e., $R = 0$ for all t, while for lower values of D_φ, one observes the emergence of polar order described by Eq. (2.4.27). The transition across this line is of second order and it corresponds to supercritical pitchfork bifurcation in terms of R. This is reminiscent of the continuum Kuramoto model with noise (J. A. Carrillo, Choi, and Pareschi 2019).

For the more interesting collective motion of polar order with rotation, i.e., $\alpha > 0$, and solitary states, we cannot find analytical solutions to Eq. (2.4.23). These are composed of one or several skewed bivariate peaks (cf. Figs. 2.20 and 2.21). But since we know the representation of disordered motion for any α, we perform linear stability analysis of it against perturbations in Fourier space (see the details in Appendix E in (Kruk, Maistrenko, and Koeppl 2020)). As a result, we obtain stability diagrams for Eq. (2.4.25) in the parameter domain of D_φ and α. We find that the transition line where this solution becomes unstable is well described by

$$D_\varphi = \frac{\sigma\xi}{2}\cos\left(\frac{\alpha}{2}\right), \tag{2.4.29}$$

which is consistent with Eq. (2.4.28). In particular, we see that in the deterministic case $D_\varphi \to 0_+$, oscillators never stay disordered, as mentioned before. The knowledge of the general order-disorder transition line Eq. (2.4.29) allows us to study phase transitions between disordered motion and partial synchronization or solitary states. We find that in both cases, the transition is of second order (cf. Fig. 2.22) which is similar to the results for the continuum Kuramoto model with noise for identical oscillators (J. A. Carrillo, Choi, and Pareschi 2019; Kruk, J. A. Carrillo, and Koeppl preprint). We note that for the continuum Kuramoto model with inertia for nonidentical oscillators (cf. Appendix F in (Kruk, Maistrenko, and Koeppl 2020)) and in the absence of the phase lag (Munyaev et al. 2020; Olmi et al. 2014; Tanaka, Lichtenberg, and Oishi 1997a,b) first order transitions accompanied by hysteresis effects were reported.

3 CONTINUUM LIMIT DESCRIPTION OF INTERACTING PARTICLE SYSTEMS

3.1 TRANSITION FROM PARTICLE TO CONTINUUM DESCRIPTION

In this section, we present how to obtain the equations that describe the dynamics of an ensemble of particles in the continuum limit $N \to \infty$ within the framework of FPEs. The continuum limit is understood in such a way that for each fixed N, a two-dimensional system domain is divided into $\sqrt{N}$ units (Kipnis and Landim 1998a) Fig. 3.1. The approach we follow here is different from the one discussed in (Kruk, Maistrenko, and Koeppl 2018), and it eventually provides us with a hierarchy of evolution equations for density functions that incorporate inter-particle interactions of any order. For two-dimensional systems in Section 2.2, we nondimensionalized the particle model by introducing dimensionless quantities such as a particle velocity $\hat{v}_0$ and a phase diffusion intensity $\hat{D}_\varphi$. In this section, we use the same variables but omit the $\hat{}$ symbol hereafter for the sake of simplicity.

In Section 2.2, the system size L is assumed to be equal to one, but throughout this section we keep it arbitrary but constant. We will denote a three-dimensional state space of each particle by $\Omega = \mathbb{U} \times \mathbb{U} \times \mathbb{T}$. We introduce new variables to keep notation more compact. We will denote a spatial position of each particle with index $i \in \{1, \dots, N\}$ by $r_i = (x_i, y_i) \in \mathbb{U}^2$. We will also denote a state of each particle by $p_i = (x_i, y_i, \varphi_i) \in \Omega$. First, let's define a empirical probability density function as

$$\begin{aligned} \hat{f}(p, t; p_1, \dots, p_N) &= \frac{1}{N} \sum_{i=1}^{N} \delta(p_i(t) - p) \\ &= \frac{1}{N} \sum_{i=1}^{N} \delta(x_i(t) - x)\delta(y_i(t) - y)\delta(\varphi_i(t) - \varphi). \end{aligned} \tag{3.1.1}$$

This function should be treated the following way. For a given solution of the particle SDE, we compute the value of an integral of $\hat{f}$ against some sufficiently smooth test function ϕ. As the

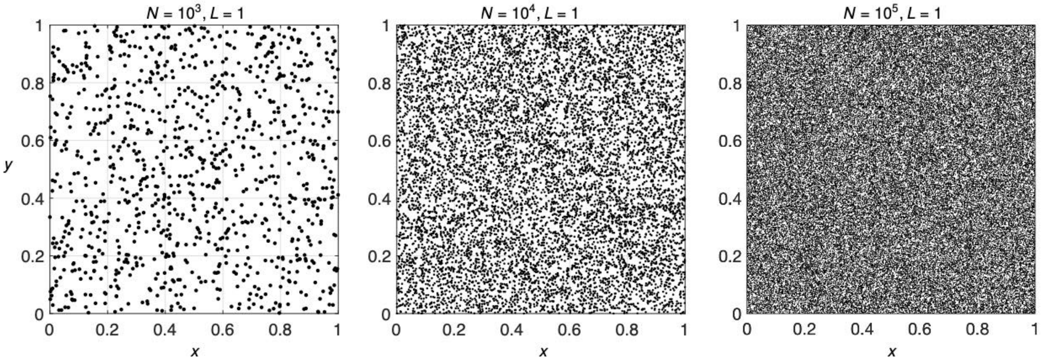

Figure 3.1: Limiting procedure $N \to \infty$ with the volume of the domain kept fixed.

next step, we consider a probability of finding particles with coordinates $\{p_i\}_{i=1,\dots,N}$ at time t, and denote its probability density function by $w = w(p_1, \dots, p_N, t)$. The time evolution of such a probability density function is given by the FPE (Risken and Frank 1996) and it reads

$$\begin{aligned}\partial_t w = -\sum_{i=1}^{N} \Bigg(& v_0 \cos\varphi_i \partial_{x_i} w + v_0 \sin\varphi_i \partial_{y_i} w \\ & + \partial_{\varphi_i} \Bigg(\frac{1}{|B_\varrho^i|} \sum_{j \in B_\varrho^i} \sin(\varphi_j - \varphi_i - \alpha) w \Bigg) - D_\varphi \partial_{\varphi_i \varphi_i} w \Bigg).\end{aligned} \tag{3.1.2}$$

This equation requires information about each particle, the fact of which is prohibitive in practice. Therefore, we define an ensemble averaged probability density function $f = f(p, t)$ as the microscopic density $\hat{f}$ averaged with respect to the configuration probability w:

$$f(p, t) = \int_{\Omega^N} \hat{f}(p, t; p_1, \dots, p_N) w(p_1, \dots, p_N, t) \, \mathrm{d}p_1 \dots \mathrm{d}p_N,$$

where $\mathrm{d}p_i = \mathrm{d}x_i \mathrm{d}y_i \mathrm{d}\varphi_i$ is a three dimensional volume element in Ω. Since the particles are considered to be identical, the probability of the system configuration w is symmetric with respect to permutations of particles. We can rewrite the ensemble averaged microscopic density as (Archer and Rauscher 2004b)

$$f(p, t) = \int_{\Omega^{N-1}} w(p, p_2, \dots, p_N) \, \mathrm{d}p_2 \dots \mathrm{d}p_N.$$

We can now use the FPE Eq. (3.1.2) to obtain the time evolution for the one-particle density function. Namely, we integrate out $N-1$ particles in Eq. (3.1.2). The first terms are transformed as follows

$$\int_{\Omega^{N-1}} \partial_t w \, \mathrm{d}p_2 \dots \mathrm{d}p_N = \partial_t f(p_1, t),$$

$$\int_{\Omega^{N-1}} \sum_{i=1}^{N} v_0 \cos\varphi_i \partial_{x_i} w \, \mathrm{d}p_2 \dots \mathrm{d}p_N = v_0 \cos\varphi_1 \partial_{x_1} f(p_1, t),$$

$$\int_{\Omega^{N-1}} \sum_{i=1}^{N} v_0 \sin\varphi_i \partial_{y_i} w \, \mathrm{d}p_2 \dots \mathrm{d}p_N = v_0 \sin\varphi_1 \partial_{y_1} f(p_1, t).$$

We have used the fact that surface terms, which appear in integrals with partial derivatives, vanish due to periodic boundary conditions. For the interaction term, we have

$$\begin{aligned}& \int\limits_{\Omega^{N-1}} \sum_{i=1}^{N} \partial_{\varphi_i} \Bigg(\frac{1}{|B_\varrho^i|} \sum_{j \in B_\varrho^i} \sin(\varphi_j - \varphi_i - \alpha) w \Bigg) \mathrm{d}p_2 \dots \mathrm{d}p_N \\ & = \int\limits_{\Omega^{N-1}} \sum_{i=1}^{N} \partial_{\varphi_i} \Bigg(\frac{1}{\sum_{\substack{j=1 \\ j \neq i}}^{N} H(\varrho - \|r_{ji}\|)} \sum_{\substack{j=1 \\ j \neq i}}^{N} \sin(\varphi_j - \varphi_i - \alpha) H(\varrho - \|r_{ji}\|) w \Bigg) \mathrm{d}p_2 \dots \mathrm{d}p_N,\end{aligned} \tag{3.1.3}$$

where H is a Heaviside step function. We have rewritten the summation term and the neighborhood cardinality using the definition of particle's neighborhood B_ϱ^i, defined for the particle model. The interparticle distance is computed with respect to $L^2(\mathbb{U}^2)$-norm. All the integrand terms except for the first particle cancel out because of periodic boundaries, and we write Eq. (3.1.3) as

$$\begin{aligned}
&\partial_{\varphi_1} \int_{\Omega^{N-1}} \frac{1}{\sum_{j=2}^{N} H(\varrho - \|r_{j1}\|)} \sum_{j=2}^{N} \sin(\varphi_j - \varphi_1 - \alpha) H(\varrho - \|r_{j1}\|) w \,\mathrm{d}p_2 \ldots \mathrm{d}p_N \\
&= (N-1)\partial_{\varphi_1} \int_{\Omega} \sin(\varphi_2 - \varphi_1 - \alpha) H(\varrho - \|r_{21}\|) \left(\int_{\Omega^{N-2}} \frac{w \,\mathrm{d}p_3 \ldots \mathrm{d}p_N}{\sum_{j=2}^{N} H(\varrho - \|r_{j1}\|)} \right) \mathrm{d}p_2.
\end{aligned} \tag{3.1.4}$$

The denominator in the last expression does not allow to integrate w out straightforwardly. However, we are interested in the continuum limit $N \to \infty$. In this limit, by the law of large numbers

$$\begin{aligned}
\lim_{N\to\infty} \frac{1}{N-1} \sum_{j=2}^{N} H(\varrho - \|r_{j1}\|) &= \iint_{\mathbb{U}^2} H(\varrho - \|r_2 - r_1\|) \tilde{f}(x_2, y_2, t) \mathrm{d}x_2 \mathrm{d}y_2 \\
&= \iiint_{\Omega} H(\varrho - \|r_2 - r_1\|) f(x_2, y_2, \varphi_2, t) \mathrm{d}x_2 \mathrm{d}y_2 \mathrm{d}\varphi_2,
\end{aligned}$$

where in the intermediate step, $\tilde{f}$ denotes a marginal density function of spatial variables. We use this fact to rewrite the right hand side of Eq. (3.1.4) further as

$$\partial_{\varphi_1} \int_{\Omega} \sin(\varphi_2 - \varphi_1 - \alpha) H(\varrho - \|r_2 - r_1\|) \left(\frac{f^{(2)}(p_1, p_2, t)}{\int_{\Omega} H(\varrho - \|r_2 - r_1\|) f(p_2, t) \,\mathrm{d}p_2} \right) \mathrm{d}p_2, \tag{3.1.5}$$

where $f^{(2)}(p_1, p_2, t) = \lim\limits_{N\to\infty} \int_{\Omega^{N-2}} w \,\mathrm{d}p_3 \ldots \mathrm{d}p_N$ is a two-particle density function. Similarly to how we expressed the one-particle density function by averaging the microscopic density function, we can obtain the two-particle density function in the limit of infinitely many particles (Gupta, Campa, and Ruffo 2014b) in the following way:

$$\begin{aligned}
&\lim_{N\to\infty} \int_{\Omega^N} \hat{f}(p, t; p_1, \ldots, p_N) \hat{f}(p', t; p_1, \ldots, p_N) w(p_1, \ldots, p_N, t) \,\mathrm{d}p_1 \ldots \mathrm{d}p_N \\
&= \lim_{N\to\infty} \frac{N-1}{N} \int_{\Omega^{N-2}} w(p, p', p_3, \ldots, p_N) \mathrm{d}p_3 \ldots \mathrm{d}p_N + \frac{1}{N} \delta(p - p') f(p, t) = f^{(2)}(p, p', t),
\end{aligned}$$

where the first transition has been performed using the definition Eq. (3.1.1) and the symmetry of w under permutations.

Lastly, we integrate the diffusion term in the FPE Eq. (3.1.2) and obtain

$$\int_{\Omega^{N-1}} D_{\varphi} \sum_{i=1}^{N} \partial_{\varphi_i \varphi_i} w \,\mathrm{d}p_2 \ldots \mathrm{d}p_N = D_{\varphi} \partial_{\varphi_1 \varphi_1} f(p_1, t).$$

As a result, the time evolution of the one-particle density function $f = f(p_1, t) = f(r_1, \varphi_1, t)$ reads

$$\begin{aligned}
\partial_t f = &-v_0 e(\varphi_1) \cdot \nabla_{r_1} f + D_{\varphi} \partial_{\varphi_1 \varphi_1} f \\
&- \frac{1}{\mid C(r_1; \varrho) \mid} \partial_{\varphi_1} \int_{C(r_1; \varrho)} \sin(\varphi_2 - \varphi_1 - \alpha) f^{(2)}(p_1, p_2, t) \,\mathrm{d}p_2,
\end{aligned}$$

where $e(\varphi_1) = (\cos \varphi_1, \sin \varphi_1) \in \mathbb{S}^1 \subset \mathbb{R}^2$ is a unit velocity vector, $\nabla_{r_1} = (\partial_{x_1}, \partial_{y_1})$ is a spatial gradient, and

$$\mid C(r_1; \varrho) \mid = \int_{C(r_1; \varrho)} f(p_2, t) \,\mathrm{d}p_2 = \int_{\Omega} f(r_2, \varphi_2, t) H(\varrho - \|r_2 - r_1\|) \,\mathrm{d}r_2 \mathrm{d}\varphi_2$$

is a neighborhood mass. The neighborhood domain $C(r;\varrho)$ is itself defined as

$$C(r;\varrho) = \left\{(r',\varphi') \in \mathbb{U}^2 \times \mathbb{T} \mid \|r'-r\| \leq \varrho\right\}. \tag{3.1.6}$$

We hereafter use $C(r)$ instead of $C(r;\varrho)$ for shorter notation. We see that for an interacting particle system, the time evolution of a one-particle density function is not a closed equation since it depends on a two-particle density function. In order to obtain a closure, one often admits the simplest mean field approximation known as a molecular chaos assumption (Laney 1998). It postulates that particle correlations are negligible and the following factorization of the two-particle density function is possible:

$$f^{(2)}(p_1,p_2,t) \approx f(p_1,t)f(p_2,t).$$

Under that assumption, the time evolution of f is given by

$$\begin{aligned}\partial_t f &= -v_0 e(\varphi_1)\cdot\nabla_{r_1} f + D_\varphi \partial_{\varphi_1\varphi_1} f\\ &\quad - \frac{1}{\mid C(r_1)\mid}\partial_{\varphi_1}\left(f\int_{C(r_1)} \sin(\varphi_2-\varphi_1-\alpha) f(p_2,t)\,\mathrm{d}p_2\right).\end{aligned} \tag{3.1.7}$$

This is the main equation that we will work with in the next sections.

3.1.1 *Two-particle Density Function*

In the case that the closure at the first order is not sufficient, we may proceed in the same manner and next define a three-particle density function. In the limit of infinitely many particles, we have

$$f^{(3)}(p,p',p'',t) = \lim_{N\to\infty}\int_{\Omega^{N-3}} w(p,p',p'',p_4,\ldots,p_N,t)\,\mathrm{d}p_4\ldots\mathrm{d}p_N.$$

If we integrate out $N-2$ particles from the FPE Eq. (3.1.2), we derive the equation for the time evolution of the two-particle density function $f^{(2)} = f^{(2)}(p_1,p_2,t) = f^{(2)}(r_1,\varphi_1,r_2,\varphi_2,t)$. It reads

$$\begin{aligned}\partial_t f^{(2)} &= -v_0 e(\varphi_1)\cdot\nabla_{r_1} f^{(2)} + D_\varphi\partial_{\varphi_1\varphi_1} f^{(2)}\\ &\quad - \frac{1}{\mid C(r_1)\mid}\partial_{\varphi_1}\int_{C(r_1)} \sin(\varphi_3-\varphi_1-\alpha) f^{(3)}(p_1,p_2,p_3,t)\,\mathrm{d}p_3\\ &\quad - v_0 e(\varphi_2)\cdot\nabla_{r_2} f^{(2)} + D_\varphi\partial_{\varphi_2\varphi_2} f^{(2)}\\ &\quad - \frac{1}{\mid C(r_2)\mid}\partial_{\varphi_2}\int_{C(r_2)} \sin(\varphi_3-\varphi_2-\alpha) f^{(3)}(p_1,p_2,p_3,t)\,\mathrm{d}p_3,\end{aligned}$$

where the neighborhood domain $C(r)$ is defined in Eq. (3.1.6). The time evolution of the two-particle density function $f^{(2)}$ now depends on the three-particle density function $f^{(3)}$. If we continue further, we can derive a corresponding equation for an n-particle density function which will further depend on an $n+1$-particle density function. This infinite hierarchy of integro-differential equations is similar to the Born-Bogolubov-Green-Kirkwood-Yvon (BBGKY) or Vlasov hierarchies in statistical physics (Braun and Hepp 1977; Spohn 1991). We could theoretically close the hierarchy at any level provided that we have a required closure. Besides the molecular chaos assumption that closes it at the first order, the so-called Kirkwood superposition approximation can be used to obtain the second order closure. It assumes that the three-particle density function is factorized as a product of two-particle density functions as

$$f^{(3)}(p_1,p_2,p_3,t) \approx \frac{f^{(2)}(p_1,p_2,t)f^{(2)}(p_1,p_3,t)f^{(2)}(p_2,p_3,t)}{f(p_1,t)f(p_2,t)f(p_3,t)}.$$

The time evolution of the two-particle density function under this approximation reads

$$
\begin{aligned}
\partial_t f^{(2)} &= -v_0 e(\varphi_1)\cdot\nabla_{r_1} f^{(2)} - v_0 e(\varphi_2)\cdot\nabla_{r_2} f^{(2)} + D_\varphi \partial_{\varphi_1\varphi_1} f^{(2)} + D_\varphi \partial_{\varphi_2\varphi_2} f^{(2)} \\
&- \frac{1}{\mid C(r_1)\mid}\partial_{\varphi_1}\left[\frac{f^{(2)}(p_1,p_2,t)}{f(p_1,t)f(p_2,t)}\int_{C(r_1)}\sin(\varphi_3-\varphi_1-\alpha)\frac{f^{(2)}(p_1,p_3,t)f^{(2)}(p_2,p_3,t)}{f(p_3,t)}\mathrm{d}p_3\right] \\
&- \frac{1}{\mid C(r_2)\mid}\partial_{\varphi_2}\left[\frac{f^{(2)}(p_1,p_2,t)}{f(p_1,t)f(p_2,t)}\int_{C(r_2)}\sin(\varphi_3-\varphi_2-\alpha)\frac{f^{(2)}(p_1,p_3,t)f^{(2)}(p_2,p_3,t)}{f(p_3,t)}\mathrm{d}p_3\right].
\end{aligned}
$$

The approximation is usually required when the dynamics due to a self-propelled particle system involves hard-core repulsion interactions (Marconi and Tarazona 1999). Since our model does not contain such terms, we limit ourselves to subsequently work with the one particle density function, whose dynamics is described by Eq. (3.1.7).

3.2 ANALYTIC SOLUTIONS TO CONTINUUM LIMIT EQUATIONS

From now on, we do not use p as particle's state variable. Instead, we split it up into position $r = (x, y) \in \mathbb{U}^2$ and phase φ variables. The easiest solution to Eq. (3.1.7) (and to all of its variations) is the uniform probability density function, i.e.,

$$f(r,\varphi,t) = \frac{1}{2\pi}.$$

It corresponds to the chaotic behavior of the particle system, for which the continuum limit has been derived. One also says that this solution represents a globally disordered state.

The model Eq. (3.1.7) admits a major simplification if we assume that solutions are spatially homogeneous. Based on the results from (Kruk, Maistrenko, and Koeppl 2018), we know that a subset of chimeric solutions are of such a form. Under such an assumption of spatial homogeneity, we obtain a $1+1$-dimensional PDE, which we can also consider as the continuum Kuramoto-Sakaguchi model:

$$\partial_t f(\varphi,t) = D_\varphi \partial_{\varphi\varphi} f(\varphi,t) - \partial_\varphi\left(f(\varphi,t)\,\frac{\int_{\mathbb{T}} f(\varphi',t)\sin(\varphi'-\varphi-\alpha)\mathrm{d}\varphi'}{\int_{\mathbb{T}} f(\varphi',t)\mathrm{d}\varphi'}\right).$$

Since we treat the function $f(\varphi,t)$ as a probability density function, we have that $\int_{\mathbb{T}} f(\varphi,t)\mathrm{d}\varphi = 1$. The time evolution of the density function then becomes

$$\partial_t f(\varphi,t) = D_\varphi \partial_{\varphi\varphi} f(\varphi,t) - \partial_\varphi\left(f(\varphi,t)\,\int_{\mathbb{T}} f(\varphi',t)\sin(\varphi'-\varphi-\alpha)\mathrm{d}\varphi'\right). \qquad (3.2.8)$$

This model have certain symmetries. Generally, we could rescale $f(\varphi,t)\mapsto cf(\varphi,t), c\in\mathbb{R}$ but since we treat f as a probability density function, this symmetry is of no importance to us. The equation is also invariant under the phase translation $f(\varphi,t)\mapsto f(\varphi+\varphi_0,t) \quad \forall\varphi_0\in\mathbb{T}$. This means that we can shift the distribution by any φ_0 and obtain another solution. This is particularly important in the stability analysis conducted later. The third symmetry is due to the invariance under the reflection of phase $f(\varphi,t)\mapsto f(-\varphi,t)$ if $\alpha\mapsto-\alpha$. Thus, we see that we can obtain another solution by flipping the signs of phases and the parameter α simultaneously. Given that, we will subsequently consider $\alpha\in[0,\pi/2]$ only. We also see that the solution will be symmetric with respect to some φ_0 only if $\alpha = 0$. Thus, we will first look for solutions of Eq. (3.2.8) without a phase lag.

3.2.1 *Stationary Solutions*

To find a nontrivial stationary solution to Eq. (3.2.8), we put $\partial_t f(\varphi, t) = 0$. This gives us a second order ordinary differential equation (ODE) of the form:

$$D_\varphi \frac{\mathrm{d}^2 f(\varphi)}{\mathrm{d}\varphi^2} - \frac{\mathrm{d}}{\mathrm{d}\varphi}\left(f(\varphi) \int_{\mathbb{T}} f(\varphi') \sin(\varphi' - \varphi - \alpha) \mathrm{d}\varphi' \right) = 0.$$

In terms of the order parameter, we can write it as

$$D_\varphi \frac{\mathrm{d}^2 f(\varphi)}{\mathrm{d}\varphi^2} - \frac{\mathrm{d}}{\mathrm{d}\varphi}\left[f(\varphi) R \sin(\Theta - \varphi - \alpha) \right] = 0.$$

To solve this equation, we integrate it once and then look for the solution of the form

$$f(\varphi) = c(\varphi) e^{\gamma \cos(\Theta - \varphi - \alpha)},$$

where the function $c(\varphi)$ is to be determined from the ODE, and $\gamma = R/D_\varphi$. It can be shown that eventually the solution is of the form

$$f(\varphi) = c_1 e^{\gamma \cos(\Theta - \varphi - \alpha)} \left(1 + c_2 \int e^{-\gamma \cos(\Theta - \varphi - \alpha)} \mathrm{d}\varphi \right),$$

where c_1, c_2 are the constants to be determined. We are interested in smooth solutions to Eq. (3.2.8), so we require that $f \in C(\mathbb{T})$. This implies that $f(0) = f(2\pi)$, which can be shown to hold if and only if $c_2 = 0$. From the normalization condition, we find that $c_1 = (2\pi I_0(\gamma))^{-1}$, where $I_0(\gamma) = 1/(2\pi) \int_{\mathbb{T}} \exp(\gamma \cos\varphi) \mathrm{d}\varphi$ denotes the modified Bessel function of the first kind (Olver et al. 2010). As a result, we have the nontrivial stationary solution of the form:

$$f(\varphi) = \frac{e^{\gamma \cos(\Theta - \varphi - \alpha)}}{2\pi I_0(\gamma)}.$$

Due to the translational invariance of Eq. (3.2.8) with respect to the phase φ, we can put $\Theta = 0$ without loss of generality. This simplifies the solution to

$$f(\varphi) = \frac{e^{\gamma \cos(\varphi + \alpha)}}{2\pi I_0(\gamma)}. \tag{3.2.9}$$

In this form, the solution is not particularly useful since the density function is recursively contained in the definition of the order parameter. However, we are able to determine the latter the other way. If we multiply Eq. (3.2.9) by $\cos\varphi$ and integrate over the domain $\mathbb{T}$, we find that

$$R = \frac{1}{2\pi I_0(\gamma)} \int_{\mathbb{T}} e^{\gamma \cos(\varphi + \alpha)} e^{i\varphi} \mathrm{d}\varphi = e^{-i\alpha} \frac{I_1(\gamma)}{I_0(\gamma)}.$$

From the equation for the imaginary part, we have that either $\alpha = 0$ or $I_1(\gamma) = 0$. The latter case is true for $\gamma = R/D_\varphi = 0$. But if the order parameter magnitude is zero, the density function Eq. (3.2.9) becomes just a constant and the phase lag α does not play any role. Therefore, we conclude that the system Eq. (3.2.8) is solved by Eq. (3.2.9) only when $\alpha = 0$:

$$f(\varphi) = \frac{e^{\gamma \cos\varphi}}{2\pi I_0(\gamma)}, \tag{3.2.10}$$

for which the order parameter magnitude is determined from

$$R = \frac{I_1\left(\frac{R}{D_\varphi}\right)}{I_0\left(\frac{R}{D_\varphi}\right)}. \tag{3.2.11}$$

3.2.1.1 *The Onset of Orientational Order*

Even though we do not have a closed form solution for the density function f that solves Eq. (3.2.8), we can extract the information on what relation the model parameters should satisfy in order to allow the existence of this nontrivial solution. It was shown in (Pearce 1981) that for positive values of R, the relation Eq. (3.2.11) has a unique solution. That solution allows us to find a condition where the nonconstant density function of the form Eq. (3.2.10) appears. We should search for parameters for which the slope on the right hand side of Eq. (3.2.11) is greater than the slope on the left hand side at $R = 0$. Namely, we consider $\frac{\mathrm{d}}{\mathrm{d}R}[I_1(\gamma)/I_0(\gamma)] \geq 1$, where we denote $\gamma = R/D_\varphi$. Using the properties (Olver et al. 2010) of the Bessel function $\frac{\mathrm{d}}{\mathrm{d}R}I_0(\gamma) = \frac{\sigma}{D_\varphi}I_1(\gamma)$ and $\frac{\mathrm{d}}{\mathrm{d}R}I_1(\gamma) = \frac{\sigma}{2D_\varphi}[I_0(\gamma) + I_2(\gamma)]$, we rewrite the above inequality as

$$\frac{1}{2D_\varphi} + \frac{1}{2D_\varphi}\frac{I_2(\gamma)}{I_0(\gamma)} - \frac{1}{D_\varphi}\frac{I_1^2(\gamma)}{I_0^2(\gamma)} \geq 1.$$

Using the property (Joshi and Bissu 1991) $I_0(\gamma) - I_2(\gamma) = \frac{2}{\gamma}I_1(\gamma)$, we obtain the desired inequality for the order parameter magnitude

$$\frac{1}{D_\varphi}R^2 - \frac{1}{D_\varphi} + 2 \leq 0.$$

Since we are interested in the value of the slope at $R = 0$, we derive the following condition for the existence of the nontrivial stationary solution to Eq. (3.2.8):

$$D_\varphi \leq \frac{1}{2}. \tag{3.2.12}$$

We also see from Eq. (3.2.10) and Eq. (3.2.11) that when $D_\varphi \to 0$, the order parameter approaches 1 and we have the completely synchronous stationary state, namely,

$$f(\varphi, t) = \delta(\varphi - \varphi_0),$$

where the phase φ_0 is determined from the initial condition.

3.2.2 *Traveling Wave Solutions*

Our next step is to investigate the solution to Eq. (3.2.8) in the presence of a nonzero phase lag α. We know, when $\alpha \neq 0$ the density $f(\varphi, t)$ is no longer a symmetric function. It moves to the left if $\alpha > 0$ and to the right if $\alpha < 0$ with some constant speed v. This fact allows us to look for a solution in the form of a traveling wave. Thus, we introduce an ansatz $f(\varphi, t) = g(\varphi - vt) = g(\omega)$, where v is the speed of the traveling wave, which is also to be determined. After the substitution, we obtain the following second order ODE:

$$D_\varphi \frac{\mathrm{d}^2}{\mathrm{d}\omega^2}g(\omega) + \frac{\mathrm{d}}{\mathrm{d}\omega}\left\{[v - R\sin(\Theta - \omega - \alpha)]\, g(\omega)\right\} = 0, \tag{3.2.13}$$

where R and Θ are now constants. We trivially integrate it with respect to ω and get

$$D_\varphi \frac{\mathrm{d}}{\mathrm{d}\omega}g(\omega) + [v - R\sin(\Theta - \omega - \alpha)]\, g(\omega) = c_1,$$

where $c_1 \in \mathbb{R}$ is some constant. The method to solve such an equation is again to look for a solution of the form

$$g(\omega) = c(\omega)\exp\left(-\int\left[\frac{v}{D_\varphi} - \frac{R}{D_\varphi}\sin(\Theta - \omega - \alpha)\right]\mathrm{d}\omega\right),$$

where the function $c(\omega)$ is to be determined. After we substitute the function of this form into the above differential equation, we find the following solution:

$$g(\omega) = E_1(\omega)\left(c_1 \int E_1^{-1}(\omega')\mathrm{d}\omega' + c_2\right),$$

where we have denoted $E_1(\omega) = \exp\left[-\frac{v}{D_\varphi}\omega + \frac{R}{D_\varphi}\cos(\Theta - \omega - \alpha)\right]$ and $c_2 \in \mathbb{R}$ is some constant. One of the constants can be found by recalling that we are looking for a periodic and continuous solution, i.e., $g(0) = g(2\pi)$. The other constant is determined from the normalization condition of the probability density function. Eventually, we arrive at the following solution (compare to the form of the solution in the case of the Kuramoto model with frequency distribution and zero phase lag (Gupta, Campa, and Ruffo 2014a)):

$$g(\omega) = c_0 E_1(\omega)\left(1 + c_1 \frac{\int_0^\omega E_1^{-1}(\omega')\mathrm{d}\omega'}{\int_{\mathbb{T}} E_1^{-1}(\omega')\mathrm{d}\omega'}\right),$$

where $c_0 \in \mathbb{R}$ is a normalization constant and $c_1 = \left(e^{2\pi \frac{v}{D_\varphi}} - 1\right)$ comes form a periodicity constraint.

One may notice that due to the translational invariance of Eq. (3.2.8), by the suitable shift of $\omega - \Theta \mapsto \omega$, we have the system where the order parameter phase can be put equal to zero without loss of generality. In other words, we could initially have introduced an ansatz $f(\varphi, t) = g(\varphi - vt - \Theta_0) = g(\omega)$, with v to be determined and where $\Theta_0 = \Theta(0)$. The density function, expressed in terms of new ω, can be shown to read

$$g(\omega) = c_0 E_2(\omega)\left(1 + c_1 \frac{\int_0^\omega E_2^{-1}(\omega')\mathrm{d}\omega'}{\int_{\mathbb{T}} E_2^{-1}(\omega')\mathrm{d}\omega'}\right), \tag{3.2.14}$$

where the exponential function is redefined as $E_2(\omega) = \exp\left[-\frac{v}{D_\varphi}\omega + \frac{R}{D_\varphi}\cos(\omega + \alpha)\right]$.

The above solution Eq. (3.2.14) is expressed in terms of the traveling wave variable ω, and we now want to return to the original variables φ and t. Inserting them back, we find the solution of the traveling wave form to be

$$f(\varphi, t) = c_0 E(\varphi, t)\left(1 + c_1 \frac{\int_{vt}^{\varphi_0 + vt} E^{-1}(\varphi', t)\mathrm{d}\varphi'}{\int_{vt}^{2\pi + vt} E^{-1}(\varphi', t)\mathrm{d}\varphi'}\right)$$

with $\varphi \in [vt, 2\pi + vt)$, $E(\varphi, t) = \exp\left[-\frac{v}{D_\varphi}\varphi + \frac{R}{D_\varphi}\cos(\varphi - vt + \alpha)\right]$, and $\varphi_0 = \varphi|_{t=0} = \varphi - vt$ is the initial reference frame. For the computational purposes, it is better to perform the change of variables $\varphi_0 = \varphi - vt$ in the integrals so that they are independent of time, giving

$$f(\varphi, t) = c_0 E(\varphi, t)\left(1 + c_1 \frac{\int_0^{\varphi_0} E^{-1}(\varphi_0, 0)\mathrm{d}\varphi_0}{\int_{\mathbb{T}} E^{-1}(\varphi_0, 0)\mathrm{d}\varphi_0}\right) \quad \text{with } \varphi \in [vt, 2\pi + vt). \tag{3.2.15}$$

3.2.2.1 *The Onset of Orientational Order*

To learn the behavior of the order parameter, corresponding to Eq. (3.2.15), it is enough to study its profile $g(\omega)$. The global order parameter is defined as

$$R = \int_{\mathbb{T}} e^{i\omega} g(\omega)\mathrm{d}\omega, \tag{3.2.16}$$

where the average direction is shifted to the origin so that $\Theta \equiv 0$ without loss of generality. Thus, the order parameter must satisfy the following set of self-consistency equations:

$$R = \int_{\mathbb{T}} g(\omega) \cos \omega \mathrm{d}\omega, \tag{3.2.17a}$$

$$0 = \int_{\mathbb{T}} g(\omega) \sin \omega \mathrm{d}\omega, \tag{3.2.17b}$$

where g is given by Eq. (3.2.14). This system does not have an analytical solution but can be solved numerically for R and v, assuming that $\Theta \equiv 0$. Note that in order to obtain them, one has to use multiprecision arithmetic. For parameter values away from the order-disorder transition line, the exponents in Eq. (3.2.14) assume values not valid for the double precision format.

As before, we can use the set of self-consistent equations to determine conditions on the model parameters that lead to the existence of the nontrivial solution g. If we substitute Eq. (3.2.14) into Eq. (3.2.17a), expand the right hand side of Eq. (3.2.17a) in powers of $\gamma := R/D_\varphi$, and take the limit $\gamma \to 0+0$ (Gupta, Campa, and Ruffo 2014a), we find the following equality:

$$R = -\frac{\cos\alpha}{2} \frac{\gamma}{\frac{v^2}{D_\varphi^2}+1} \frac{v^2}{D_\varphi^2} - \frac{\sin\alpha}{2} \frac{\gamma}{\frac{v^2}{D_\varphi^2}+1} \frac{v}{D_\varphi} + \frac{\cos\alpha}{2}\gamma + O\left(\gamma^2\right).$$

If we divide both sides by the order parameter magnitude R, we obtain the relation between the critical coupling strength, the diffusion constant D_φ, and the phase lag α expressed as

$$1 = \frac{2(D_\varphi^2 + v^2)}{D_\varphi \cos\alpha - v \sin\alpha}.$$

The drawback is that it also involves the unknown parameter v. But fortunately as we have mentioned, we must simultaneously satisfy Eq. (3.2.17b). Thus, we substitute Eq. (3.2.14) into Eq. (3.2.17b) and perform the expansion again. We find the condition for the critical velocity as $v = -D_\varphi \tan\alpha$. Combining it with the last expression, we obtain the value for the critical coupling strength in terms of the known system parameters as

$$\frac{1}{2}\cos\alpha = D_\varphi.$$

We thus deduce that the condition to completely desynchronize the system is $D_\varphi \geq \frac{1}{2}\cos\alpha$. Note that if we let $\alpha \to 0$, we obtain the same condition as given by Eq. (3.2.12) for the case of zero phase lag.

4

HYDRODYNAMIC THEORY FOR INTERACTING PARTICLE SYSTEMS

4.1 LARGE DIFFUSION APPROXIMATION AND RELATED SOLUTIONS

The stability analysis from the point of view of the kinetic theory is effective when using the numerical methods, thus, providing us with the quantitative information about the instability mechanisms that act on a solution. If we want to have the qualitative description of the system behavior with respect to the microscopic parameters of the model, we must restrict the consideration of the infinite hierarchy of the Fourier modes Eq. (5.1.4) to the first several ones. The common strategy to pursue is the following. The expansion of the density function that solves the original spatially nonhomogeneous PDE Eq. (5.1.1) into Fourier series transforms the problem of solving the temporal dynamics of the $3+1$-dimensional density function into the problem of solving the temporal dynamics of the infinite system of $2+1$-dimensional density functions. The first modes from that hierarchy can be given a reasonable interpretation. Namely, the integration of $f(r,\varphi,t)$ over the phase variable gives a marginal density function of spatial coordinates $r=(x,y)\in\mathbb{U}^2$:

$$\rho(r,t)=\int_{\mathbb{T}} f(r,\varphi,t)\mathrm{d}\varphi = 2\pi f_0(r,t).$$

This definition also establishes the connection of the marginal density function to the zeroth Fourier mode defined in Eq. (5.1.2). Furthermore, we consider an arbitrary unit velocity vector $e(\varphi)=(\cos\varphi,\sin\varphi)\in\mathbb{S}^1\subset\mathbb{R}^2$ and find its expectation with respect to the one-particle density function $f(r,\varphi,t)$. The result of this operation is known to be a momentum field $w(r,t) = (w_x(r,t),w_y(r,t))\in\mathbb{R}^2$, which is defined in the relation to the Fourier modes as

$$\begin{aligned} w_x(r,t) &= \int_{\mathbb{T}} \cos\varphi f(r,\varphi,t)\mathrm{d}\varphi = \pi[f_1(r,t)+f_{-1}(r,t)],\\ w_y(r,t) &= \int_{\mathbb{T}} \sin\varphi f(r,\varphi,t)\mathrm{d}\varphi = -i\pi[f_1(r,t)-f_{-1}(r,t)]. \end{aligned}$$

The marginal density function and the momentum field constitute a hydrodynamic description of a system of interacting particles.

The momentum field, divided by the marginal density function, is isomorphic to the order parameter we introduced earlier Eq. (3.2.16), i.e., we could associate $\dfrac{w_x(r,t)}{\rho(r,t)} = R(r,t)\cos\Theta(r,t)$ and $\dfrac{w_y(r,t)}{\rho(r,t)} = R(r,t)\sin\Theta(r,t)$. Thus, the knowledge of the hydrodynamic variables $\rho(r,t)$ and $w(r,t)$ automatically allows us to evaluate the degree of polarization in the particle flow.

4.1.1 *Stationary Solutions*

We are interested in the time evolution of the marginal density function and the momenta. They are obtained directly from the above definitions using the differential equations of the respective Fourier coefficients. Since the temporal dynamics of each Fourier mode is coupled to the neighboring modes, we cannot derive the required equations immediately. Namely, we see that the first Fourier mode couples to the second one through the convective terms and through the nonlinear interaction terms Eq. (5.1.4). In order to obtain the closure, we adopt the approach of (Bertin, Droz, and Grégoire 2009). We assume that the temporal evolution of the nematic order field, which is related to the second Fourier modes, is a small quantity, giving $\partial_t f_{\pm 2} \approx 0$. Furthermore, we assume that the higher order fields are negligible $f_n \approx 0, |n| \geq 3$. This is appropriate for sufficiently high diffusion levels since $\partial_t f_n \propto -n^2 D_\varphi$. As a result, the second Fourier mode is approximated by

$$f_2(r,t) \approx -\frac{v_0}{8D_\varphi}[\partial_x f_1(r,t) + i\partial_y f_1(r,t)] + \frac{f_1(r,t)}{4D_\varphi}\frac{\iint_{B(r)} f_1(r',t)\mathrm{d}r'}{\iint_{B(r)} f_0(r',t)\mathrm{d}r'}e^{-i\alpha}. \tag{4.1.1}$$

Using the closure relation Eq. (4.1.1), we find the following system of differential equations for the marginal density $\rho = \rho(r,t)$ and the momentum field $w = w(r,t)$:

$$\begin{aligned}
\partial_t \rho &= -v_0 \nabla \cdot w, \\
\partial_t w &= -\frac{v_0}{2}\nabla\rho - D_\varphi w + \frac{v_0^2}{16D_\varphi}\Delta w + \frac{\rho}{2}Q_{-\alpha}W \\
&+ \frac{1}{8D_\varphi}\Big\{\frac{v_0}{2}Q_\alpha\left[(W\cdot\nabla)w + (W_\perp\cdot\nabla)w_\perp\right] \\
&- w\|W\|^2 + v_0 Q_{-\alpha}\Big[\nabla(w\cdot W) - (W\cdot\nabla)w \\
&- (\nabla\cdot W)w - W(\nabla\cdot w) - (w\cdot\nabla)W\Big]\Big\}.
\end{aligned} \tag{4.1.2}$$

where $w_\perp = (-w_y, w_x)^T$ and $W_\perp = (-W_y, W_x)^T$. We have denoted the spatially averaged momentum field as

$$W = W(r,t) = \frac{\iint_{B(r)} w(r',t)\mathrm{d}r'}{\iint_{B(r)} \rho(r',t)\mathrm{d}r'}$$

by analogy with the interaction terms in Eq. (3.1.7). Note that the neighborhood domain $B(r)$ implicitly depends on the radius of interaction ϱ, as defined previously by Eq. (5.1.5). The matrix $Q_\alpha = \begin{pmatrix} \cos\alpha & -\sin\alpha \\ \sin\alpha & \cos\alpha \end{pmatrix}$ represents anticlockwise rotation by α radians.

We begin our analysis by looking for the solutions of Eq. (4.1.2). As usual for such models, Eq. (4.1.2) has two stationary spatially homogeneous solutions. The first one $(\rho, w) = (1, 0, 0)$ represents a spatially uniform disordered state of the system. The second one is best found using the polar representation for the momentum field. Note that due to the approach we used to derive the continuum limit, the particle density $\rho_0 \equiv 1$ since we are bound to work only with PDFs, and as a result the marginal density function $\rho = 1$. Assuming the temporal and spatial independence of the solutions, we have $W = (\pi\varrho^2 w_x, \pi\varrho^2 w_y)^T$. We find the second solution, which represents the partially synchronized flocking, to be $(\rho, w) = (1, \|w^*\|\cos\varphi_0, \|w^*\|\sin\varphi_0)$, where the degree of polarization is

$$\|w^*\| = 2\sqrt{D_\varphi(\cos\alpha - 2D_\varphi)} \tag{4.1.3}$$

and $\varphi_0 \in \mathbb{T}$ is an arbitrary direction subject to initial conditions. One of the assumptions that we have used to obtain the closure relation Eq. (4.1.1) is that the diffusion level is high enough to justify the negligence of the higher order Fourier modes. We can now see from Eq. (4.1.3) the limitations of those assumptions. Namely, it shows that the polarization level goes to zero with the diffusion value going to zero which is definitely not correct. From our previous study we know that the polarization level goes up to one with the decrease of D_φ. But at the onset of the flocking $D_\varphi = 1/2$, the answer is correct. By analyzing Eq. (4.1.3), we find that the maximum polarization level could be $\frac{\sqrt{2}}{2}\cos\alpha$ and it is attained at $D_\varphi = \frac{1}{4}\cos\alpha$. Thus, the hydrodynamic equations Eq. (4.1.2) are correct for the range $\frac{1}{4}\cos\alpha \leq D_\varphi \leq \frac{1}{2}\cos\alpha$, the later of which is the order-disorder transition line as we already know and it is also the existence condition for Eq. (4.1.3).

4.1.2 *The Traveling Wave Solution*

As it was the case for the kinetic theory, the stability analysis of the traveling wave solutions cannot be carried out using Eq. (4.1.2) because it has been developed under the assumption of the stationarity of the solutions. Therefore, we need to rederive the corresponding hydrodynamic equations for the traveling wave solutions anew, starting from the Fourier modes Eq. (5.1.16). Since the most of the derivations are straightforward generalizations of the ones from the previous section, we provide only the key steps here.

The assumptions made to obtain the closure relation Eq. (4.1.1) are the same as for the stationary solutions, except that we additionally assume that the spatial variation of the nematic order field is negligible $\nabla h_{\pm 2} \approx 0$. This is appropriate for sufficiently high diffusion levels, which we have also assumed previously in the context of the hydrodynamic theory. The hydrodynamic equations describing the evolution of the marginal density function $\rho = \rho(r,t)$ and the momentum field $w = w(r,t)$ read

$$\begin{aligned}
\partial_t \rho &= -v_0 \nabla \cdot w + v(r \times \nabla)\rho, \\
\partial_t w &= -\frac{v_0}{2}\nabla\rho - C_1 w + v(r \times \nabla) w + \frac{v_0^2}{8} C_2 \Delta w \\
&\quad + \frac{\rho}{2} Q_{-\alpha} W + \frac{1}{4} C_2 \Bigg\{ \frac{v_0}{2} Q_\alpha \left[(W \cdot \nabla) w + (W_\perp \cdot \nabla) w_\perp \right] \\
&\quad - w\|W\|^2 + v_0 Q_{-\alpha} \Big[\nabla(w \cdot W) - (W \cdot \nabla) w \\
&\quad - (\nabla \cdot W) w - W(\nabla \cdot w) - (w \cdot \nabla) W \Big] \Bigg\},
\end{aligned} \tag{4.1.4}$$

where the matrix $Q_\alpha = \begin{pmatrix} \cos\alpha & -\sin\alpha \\ \sin\alpha & \cos\alpha \end{pmatrix}$ represents anticlockwise rotation by α radians; the matrix $C_1 = \begin{pmatrix} D_\varphi & -v \\ v & D_\varphi \end{pmatrix}$ arises due to the coupling between the longitudinal and transversal length scales; the matrix $C_2 = \frac{1}{4D_\varphi^2 + v^2} \begin{pmatrix} 2D_\varphi & v \\ -v & 2D_\varphi \end{pmatrix}$ arises due to the coupling between the first and second Fourier modes.

The system has two stationary spatially homogeneous solutions. The first one $(\rho, w) = (1, 0, 0)$ represents a spatially homogeneous disordered state of the system. The second one, which represents the partially synchronized flocking, is $(\rho, w) = (1, \|w^*\|\cos\varphi_0, \|w^*\|\sin\varphi_0)$, where the degree of polarization is

$$\|w^*\| = \sqrt{\frac{1}{D_\varphi}(4D_\varphi^2 + v^2)(\cos\alpha - 2D_\varphi)} \tag{4.1.5}$$

and $\varphi_0 \in \mathbb{T}$ is an arbitrary direction subject to initial conditions. The group velocity v is not a parameter of choice here but implicitly depends on other microscopic parameters of the Langevin dynamics. Generally, it can be estimated from the self-consistent system of equations Eq. (3.2.17a).

But we have shown that near the order-disorder transition line the group velocity is equal $v = -\frac{1}{2}\sin\alpha$. Thus, the degree of polarization Eq. (4.1.5) next to that transition line is

$$\|w^*\| = \sqrt{\left(4D_\varphi + \frac{\sin^2\alpha}{4D_\varphi}\right)(\cos\alpha - 2D_\varphi)}.$$

4.2 OTT-ANTONSEN REDUCTION

4.2.1 *General derivation for particles with persistent rotation and noise*

Let us formulate equations of self-propelled particle motion with the orientational dynamics rewritten in a different formulation suited for our subsequent purpose. The equations of motion read

$$\begin{aligned} \mathrm{d}x_i &= \cos\varphi_i \,\mathrm{d}t, \\ \mathrm{d}y_i &= \sin\varphi_i \,\mathrm{d}t, \\ \mathrm{d}\varphi_i &= \omega + \frac{1}{2i}(H_i e^{-i\varphi_i} - H_i^* e^{i\varphi_i}) \,\mathrm{d}t + D_\varphi \mathrm{d}W_i(t), \end{aligned}$$

where ω denotes particle's internal orientational frequency and we denote the nonlocal polar order parameter as a complex-valued variable as

$$H_i(t) = R_i(t)e^{i\Theta_i(t)} = \frac{1}{|B_\varrho^i|}\sum_{j\in B_\varrho^i} e^{i\varphi_i}.$$

Here, we put the velocity of particles to be 1, which fixes one relation between the spatial and temporal scales. Each particle experiences stochastic perturbations, accounted for by families of independent Wiener processes $(W_i(t))_{t\geq 0}, i = 1, \ldots, N$.

By following the same procedure for the derivation of continuum limit equations Section 3.1, we find the Fokker-Planck equation that describes temporal evolution for the PDF

$$\begin{aligned} &\frac{\partial}{\partial t}f + \frac{\partial}{\partial x}(\cos\varphi f) + \frac{\partial}{\partial y}(\sin\varphi f) \\ &\quad + \frac{\partial}{\partial\varphi}\left(\left[\omega + \frac{1}{2i}(He^{-i\varphi} - H^* e^{i\varphi})\right] f\right) - D_\varphi \frac{\partial^2}{\partial\varphi^2} f = 0. \end{aligned} \tag{4.2.6}$$

This equation constitutes the kinetic description for the interacting particle system Section 4.2.1.

In order to apply the Ott-Antonsen reduction procedure, we need to find a respective hydrodynamic description. First, we set a Fourier transform in φ:

$$f(x, y, \varphi, , \omega, t) = F_0(t, x, y, \omega) + \sum_{n=1}^{\infty} F_n(t, x, y, \omega)e^{-in\varphi} + \sum_{n=1}^{\infty} F_n^*(t, x, y, \omega)e^{in\varphi}$$

We apply the transform to each term in Eq. (4.2.6). For the first one, we have

$$\frac{\partial}{\partial x}(\cos\varphi f) = \frac{e^{i\varphi}+e^{-i\varphi}}{2}\left[\frac{\partial}{\partial x}F_0 + \sum_{n=1}^{\infty}\frac{\partial}{\partial x}F_n e^{-in\varphi} + \sum_{n=1}^{\infty}\frac{\partial}{\partial x}F_n^* e^{in\varphi}\right] =$$
$$= \frac{1}{2}\left[\frac{\partial}{\partial x}F_0 e^{i\varphi} + \sum_{k=2}^{\infty}\frac{\partial}{\partial x}F_{k+1}e^{-ik\varphi} + \frac{\partial}{\partial x}F_1 + \frac{\partial}{\partial x}F_2 e^{-i\varphi} + \sum_{k=2}^{\infty}\frac{\partial}{\partial x}F_{k-1}^* e^{ik\varphi}\right] +$$
$$+\frac{1}{2}\left[\frac{\partial}{\partial x}F_0 e^{-i\varphi} + \sum_{k=2}^{\infty}\frac{\partial}{\partial x}F_{k-1}e^{-ik\varphi} + \sum_{k=2}^{\infty}\frac{\partial}{\partial x}F_{k+1}^* e^{ik\varphi} + \frac{\partial}{\partial x}F_1^* + \frac{\partial}{\partial x}F_2^* e^{i\varphi}\right].$$

The second terms is transformed as

$$\frac{\partial}{\partial y}(\sin\varphi f) = \frac{e^{i\varphi}-e^{-i\varphi}}{2i}\left[\frac{\partial}{\partial y}F_0 + \sum_{n=1}^{\infty}\frac{\partial}{\partial y}F_n e^{-in\varphi} + \sum_{n=1}^{\infty}\frac{\partial}{\partial y}F_n^* e^{in\varphi}\right] =$$
$$= \frac{1}{2i}\left[\frac{\partial}{\partial y}F_0 e^{i\varphi} + \sum_{k=2}^{\infty}\frac{\partial}{\partial y}F_{k+1}e^{-ik\varphi} + \frac{\partial}{\partial y}F_1 + \frac{\partial}{\partial y}F_2 e^{-i\varphi} + \sum_{k=2}^{\infty}\frac{\partial}{\partial y}F_{k-1}^* e^{ik\varphi}\right] -$$
$$-\frac{1}{2i}\left[\frac{\partial}{\partial y}F_0 e^{-i\varphi} + \sum_{k=2}^{\infty}\frac{\partial}{\partial y}F_{k-1}e^{-ik\varphi} + \frac{\partial}{\partial y}F_1^* + \frac{\partial}{\partial y}F_2^* e^{i\varphi} + \sum_{k=2}^{\infty}\frac{\partial}{\partial y}F_{k+1}^* e^{ik\varphi}\right].$$

The terms with particle interaction can be shown to transform as

$$\frac{\partial}{\partial\varphi}(\omega + \frac{1}{2i}(He^{-i\varphi} - H^* e^{i\varphi})f) =$$
$$= -i\omega\sum_{k=1}^{\infty}kF_k e^{-ik\varphi} + i\omega\sum_{k=1}^{\infty}kF_k^* e^{ik\varphi} +$$
$$+\frac{H}{2i}\left(-iF_0 e^{-i\varphi} + \sum_{k=2}^{\infty}F_{k-1}(-ik)e^{-ik\varphi} + \sum_{k=2}^{\infty}F_{k+1}^*(ik)e^{ik\varphi} + iF_2^* e^{i\varphi}\right) -$$
$$-\frac{H^*}{2i}\left(F_0 ie^{i\varphi} + \sum_{k=2}^{\infty}F_{k+1}(-ik)e^{-ik\varphi} - iF_2 e^{-i\varphi} + \sum_{k=2}^{\infty}F_{k-1}^*(ik)e^{ik\varphi}\right).$$

The last diffusion term becomes

$$D_\varphi\frac{\partial^2}{\partial\varphi^2}f = D_\varphi\left(\sum_{k=1}^{\infty}(-k^2)F_k e^{-ik\varphi} + \sum_{k=1}^{\infty}(-k^2)F_k^* e^{ik\varphi}\right).$$

The Fourier-transformed version of Eq. (4.2.6) results into an infinite hierarchy of PDEs for the Fourier modes, as before. In practice, we are interested in the evolution of the zeroth and the first modes. By substituting all above transformed terms into Eq. (4.2.6), we gather the resulting equation with respect to the powers of the complex exponent. The resulting equation for the zeroth order reads

$$\frac{\partial}{\partial t}F_0 + \frac{1}{2}\frac{\partial}{\partial x}F_1 + \frac{1}{2}\frac{\partial}{\partial x}F_1^* + \frac{1}{2i}[\frac{\partial}{\partial y}F_1 - \frac{\partial}{\partial y}F_1^*] =$$
$$\frac{\partial}{\partial t}F_0 + \frac{\partial}{\partial x}\mathrm{Re}(F_1) + \frac{\partial}{\partial y}\mathrm{Im}(F_1) = 0$$

The equation for the first order in front of $e^{-i\varphi}$ reads

$$\frac{\partial}{\partial t}F_1 + \frac{1}{2}\left[\frac{\partial}{\partial x}F_0 + \frac{\partial}{\partial x}F_2\right] - \frac{1}{2i}\left[\frac{\partial}{\partial y}F_0 - \frac{\partial}{\partial y}F_2\right] - i\omega F_1 + \frac{H}{2i}(-iF_0) + \frac{H^*}{2i}(iF_2) + D_\varphi F_1$$

$$\frac{\partial}{\partial t}F_1 + \frac{1}{2}\frac{\partial}{\partial x}\left[F_0 + F_2\right] - \frac{1}{2i}\frac{\partial}{\partial y}\left[F_0 - F_2\right] - i\omega F_1 - \frac{H}{2}(F_0) + \frac{H^*}{2}(F_2) + D_\varphi F_1 = 0.$$

One finds the rest of the equations with $e^{-ik\varphi}$, $k \geq 2$ to be

$$\begin{gathered}\frac{\partial}{\partial t}F_k + \frac{1}{2}[\frac{\partial}{\partial x}F_{k+1} + \frac{\partial}{\partial x}F_{k-1}] + \frac{1}{2i}[\frac{\partial}{\partial y}F_{k+1} - \frac{\partial}{\partial y}F_{k-1}] - i\omega kF_k + \\ + \frac{H}{2i}(-ik)F_{k-1} - \frac{H^*}{2i}(-ik)F_{k+1} + D_\varphi k^2 F_k = \\ \frac{\partial}{\partial t}F_k + \frac{1}{2}\frac{\partial}{\partial x}\left[F_{k+1} + F_{k-1}\right] + \frac{1}{2i}\frac{\partial}{\partial y}\left[F_{k+1} - F_{k-1}\right] - i\omega kF_k - \\ - \frac{H}{2}kF_{k-1} + \frac{H^*}{2}kF_{k+1} + D_\varphi k^2 F_k = 0,\end{gathered}$$

where $F_k = F_k(t, x, y, \omega)$. Note that equations for the modes with negative indices are conjugate to these equations.

4.2.2 *Identical oscillators with noise: OA ansatz*

For simplicity, we now assume no distribution of "frequencies" ω for particles and set $\omega = 0$. The Ott-Antonsen ansatz (Ott and Antonsen 2008) reads $F_k = \rho Z^k$. By applying it to the PDEs for Fourier modes, we have for the equation of zeroth order

$$\frac{\partial}{\partial t}\rho + \frac{\partial}{\partial x}\left[\rho \mathrm{Re}(Z)\right] + \frac{\partial}{\partial y}\left[\rho \mathrm{Im}(Z)\right] = 0.$$

The equation for the first order wit $e^{-i\varphi}$ becomes

$$\frac{\partial}{\partial t}\left[\rho Z\right] + \frac{1}{2}\frac{\partial}{\partial x}\left[\rho + \rho Z^2\right] - \frac{1}{2i}\frac{\partial}{\partial y}\left[\rho - \rho Z^2\right] - \frac{H}{2}(\rho) + \frac{H^*}{2}(\rho Z^2) + D_\varphi \rho Z = 0,$$

which can be rewritten using the previously obtained zeroth order equation as

$$\begin{gathered}\rho\frac{\partial}{\partial t}Z + \frac{1}{2}\frac{\partial}{\partial x}\left[\rho + \rho Z^2\right] - \frac{1}{2i}\frac{\partial}{\partial y}\left[\rho - \rho Z^2\right] - \\ - \frac{H}{2}(\rho) + \frac{H^*}{2}(\rho Z^2) + D_\varphi \rho Z - Z\left(\frac{\partial}{\partial x}\left[\rho \mathrm{Re}(Z)\right] + \frac{\partial}{\partial y}\left[\rho \mathrm{Im}(Z)\right]\right) = 0.\end{gathered}$$

The rest of the hierarchy with $e^{-ik\varphi}$, $k \geq 2$ are transformed as

$$\begin{gathered}\frac{\partial}{\partial t}\left[\rho Z^k\right] + \frac{1}{2}\frac{\partial}{\partial x}\rho\left[Z^{k+1} + Z^{k-1}\right] + \frac{1}{2i}\frac{\partial}{\partial y}\rho\left[Z^{k+1} - Z^{k-1}\right] - \\ - \frac{H}{2}k\rho Z^{k-1} + \frac{H^*}{2}k\rho Z^{k+1} + D_\varphi k^2 \rho Z^k = 0,\end{gathered}$$

which can also be rewritten using the zeroth order equation as

$$\begin{gathered}\rho\frac{\partial}{\partial t}Z^k + \frac{1}{2}\frac{\partial}{\partial x}\rho\left[Z^{k+1} + Z^{k-1}\right] + \frac{1}{2i}\frac{\partial}{\partial y}\rho\left[Z^{k+1} - Z^{k-1}\right] - \\ - \frac{H}{2}k\rho Z^{k-1} + \frac{H^*}{2}k\rho Z^{k+1} + D_\varphi k^2 \rho Z^k - Z^k\left(\frac{\partial}{\partial x}\left[\rho \mathrm{Re}(Z)\right] + \frac{\partial}{\partial y}\left[\rho \mathrm{Im}(Z)\right]\right) = 0.\end{gathered}$$

This equation can further be simplified into

$$k\rho\frac{\partial}{\partial t}Z+\frac{1}{2Z^{k-1}}\frac{\partial}{\partial x}\rho\left[Z^{k+1}+Z^{k-1}\right]+\frac{1}{2iZ^{k-1}}\frac{\partial}{\partial y}\rho\left[Z^{k+1}-Z^{k-1}\right]-$$
$$-\frac{H}{2}k\rho+\frac{H^*}{2}k\rho Z^2+D_\varphi k^2\rho Z-Z\left(\frac{\partial}{\partial x}\left[\rho\mathrm{Re}(Z)\right]+\frac{\partial}{\partial y}\left[\rho\mathrm{Im}(Z)\right]\right)=0.$$

The equation for the zeroth term imposes conservation of probability mass in the system. By comparing equations in orders 1 and k, we observe

$$\rho\frac{\partial}{\partial t}Z+\frac{1}{2}\frac{\partial}{\partial x}\left[\rho+\rho Z^2\right]-\frac{1}{2i}\frac{\partial}{\partial y}\left[\rho-\rho Z^2\right]-$$
$$-\frac{H}{2}(\rho)+\frac{H^*}{2}(\rho Z^2)+D_\varphi\rho Z-Z\left(\frac{\partial}{\partial x}\left[\rho\mathrm{Re}(Z)\right]+\frac{\partial}{\partial y}\left[\rho\mathrm{Im}(Z)\right]\right)=0;$$

$$\rho\frac{\partial}{\partial t}Z+\frac{1}{2kZ^{k-1}}\frac{\partial}{\partial x}\rho\left[Z^{k+1}+Z^{k-1}\right]+\frac{1}{2ikZ^{k-1}}\frac{\partial}{\partial y}\rho\left[Z^{k+1}-Z^{k-1}\right]-$$
$$-\frac{H}{2}\rho+\frac{H^*}{2}\rho Z^2+D_\varphi k\rho Z-\frac{Z}{k}\left(\frac{\partial}{\partial x}\left[\rho\mathrm{Re}(Z)\right]+\frac{\partial}{\partial y}\left[\rho\mathrm{Im}(Z)\right]\right)=0.$$

One can see that the OA ansatz gives correct equations only for a homogeneous field without noise.

The above procedure allowed us to formulate another hydrodynamic description of interacting particle systems that includes the scalar density field $\rho(t,x,y):\mathbb{R}_+\times\mathbb{R}^2\to\mathbb{R}$, i.e., the local density of the particles, and the complex field $Z(t,x,y):\mathbb{R}_+\times\mathbb{R}^2\to\mathbb{C}$ which accounts for the local mean velocity of the particles. The equation for the density is

$$\frac{\partial}{\partial t}\rho+\rho\frac{\partial}{\partial x}\mathrm{Re}(Z)+\rho\frac{\partial}{\partial y}\mathrm{Im}(Z)+\mathrm{Re}(Z)\frac{\partial}{\partial x}\rho+\mathrm{Im}(Z)\frac{\partial}{\partial y}\rho=0.$$

Potentially, to include local collisions of the particles, one can impose a diffusion term $\sim D_r$ for spatial distribution

$$\frac{\partial}{\partial t}\rho+\rho\frac{\partial}{\partial x}\mathrm{Re}(Z)+\rho\frac{\partial}{\partial y}\mathrm{Im}(Z)+\mathrm{Re}(Z)\frac{\partial}{\partial x}\rho+\mathrm{Im}(Z)\frac{\partial}{\partial y}\rho=D_r\left(\frac{\partial^2}{\partial x^2}\rho+\frac{\partial^2}{\partial y^2}\rho\right).$$

The equation for the mean velocity can be written as

$$\rho\frac{\partial}{\partial t}Z+\frac{\rho}{2}\frac{\partial}{\partial x}\left[1+Z^2\right]-\frac{\rho}{2i}\frac{\partial}{\partial y}\left[1-Z^2\right]+\frac{1+Z^2}{2}\frac{\partial}{\partial x}\rho-\frac{1-Z^2}{2i}\frac{\partial}{\partial y}\rho-$$
$$-Z\rho\left(\frac{\partial}{\partial x}\mathrm{Re}(Z)+\frac{\partial}{\partial y}\mathrm{Im}(Z)\right)-Z\mathrm{Re}(Z)\frac{\partial}{\partial x}\rho-Z\mathrm{Im}(Z)\frac{\partial}{\partial y}\rho=$$
$$=\frac{H}{2}(\rho)-\frac{H^*}{2}(\rho Z^2)-D_\varphi\rho Z.$$

Dividing by the density field ρ, we obtain

$$\frac{\partial}{\partial t}Z+\frac{1}{2}\frac{\partial}{\partial x}\left[1+Z^2\right]-\frac{1}{2i}\frac{\partial}{\partial y}\left[1-Z^2\right]+\frac{1+Z^2}{2\rho}\frac{\partial}{\partial x}\rho-\frac{1-Z^2}{2i\rho}\frac{\partial}{\partial y}\rho-$$
$$-Z\left(\frac{\partial}{\partial x}\mathrm{Re}(Z)+\frac{\partial}{\partial y}\mathrm{Im}(Z)\right)-Z\mathrm{Re}(Z)\frac{1}{\rho}\frac{\partial}{\partial x}\rho-Z\mathrm{Im}(Z)\frac{1}{\rho}\frac{\partial}{\partial y}\rho=$$
$$=\frac{H}{2}-\frac{H^*}{2}Z^2-D_\varphi Z.$$

Alternative way to define nonlocal coupling is to write an extra PDE for the field $H(t, x, y)$

$$\tau \frac{\partial}{\partial t} H = \kappa^2 \left(\frac{\partial^2}{\partial x^2} + \frac{\partial^2}{\partial y^2} \right) H - H + \sigma e^{i\alpha} Z$$

Here α is the Kuramoto-Sakaguchi phase shift, σ is the strength of interactions, and κ defines the spatial scale of coupling, and the parameter τ defines inertia in the coupling. In the limit $\tau \to 0_+$, we have

$$0 = \kappa^2 \left(\frac{\partial^2}{\partial x^2} + \frac{\partial^2}{\partial y^2} \right) H - H + \sigma e^{i\alpha} Z,$$

which in an infinite medium has a solution (Shima and Kuramoto 2004)

$$H(t, \mathrm{r}) = \frac{\sigma e^{i\alpha}}{2\pi\kappa^2} \iint K_0(\kappa^{-1}|\mathrm{r} - \mathrm{r}'|) Z(t, \mathrm{r}')\, d^2\mathrm{r}',$$

where K_0 is the Bessel function of the second kind. Asymptotically, for large arguments $K_0(r) \sim \exp(-r\kappa^{-1})$ so one could cut this function for finite domains. As an alternative, one could use a two-dimensional Gaussian function.

One has still a freedom to fix one scale (spatial or temporal) in the system. It might be convenient to fix the system size L to one. Then the coupling strength σ will be a relevant parameter, together with κ, D_φ, and D_r. Another way could be to fix $\kappa = 1$ and to use the system size L as a parameter.

5

LINEAR STABILITY ANALYSIS OF INTERACTING PARTICLE SYSTEMS

5.1 KINETIC THEORY APPROACH

Now that we have derived several spatially homogeneous solutions for the original problem Eq. (3.1.7), we want to know parameter regions, where these solutions become unstable and spatially nonhomogeneous structures appear. In order to do that, we perform linear stability analysis of the solutions in Fourier space from the point of view of the kinetic theory first.

5.1.1 *Stationary Solutions*

First, let us provide the version of the nonhomogeneous continuum limit PDE, we will build our further analysis upon. We start with Eq. (3.1.7) for a one-particle density function $f = f(p,t) = f(r,\varphi,t)$, which we state here one more time for the easier reference:

$$\partial_t f = -v_0 e(\varphi)\cdot\nabla_r f - \partial_\varphi\left(f\frac{\int_{C(r)} f(r',\varphi',t)\sin(\varphi'-\varphi-\alpha)\mathrm{d}r'\mathrm{d}\varphi'}{\int_{C(r)} f(r',\varphi',t)\mathrm{d}r'\mathrm{d}\varphi'}\right) + D_\varphi\partial_{\varphi\varphi} f, \tag{5.1.1}$$

where we have explicitly separated the combined variable p into the position vector r and the phase φ. Note that the neighborhood domain $C(r)$ implicitly depends on the radius of interaction ϱ according to Eq. (3.1.6). We are interested in the solutions that are periodic in spatial and phase variables. We can generally represent it in a Fourier series as

$$f(r,\varphi,t) = \sum_{k\in\mathbb{Z}^2}\sum_{n\in\mathbb{Z}} f_{n,k}(t)e^{-in\varphi-i\frac{2\pi}{L}k\cdot r}.$$

Since spatial and phase scales have different periodicities, we will perform the two corresponding transforms separately.

Our first step is to transform Eq. (5.1.1) into the Fourier space with respect to the phase variable φ. The density function can be represented as

$$f(r,\varphi,t) = \sum_{n\in\mathbb{Z}} f_n e^{-in\varphi}, \tag{5.1.2}$$

where each Fourier mode is defined as

$$f_n(r,t) = \frac{1}{2\pi}\int_{\mathbb{T}} f(r,\varphi,t)e^{in\varphi}\mathrm{d}\varphi. \tag{5.1.3}$$

Using the above decomposition, each term of Eq. (5.1.1) can be rewritten as

$$\partial_t f(r,\varphi,t) = \sum_{n\in\mathbb{Z}}\partial_t f_n(r,t)e^{-in\varphi},$$

$$\begin{aligned} v_0 e(\varphi)\cdot\nabla_r f(r,\varphi,t) = &-\frac{v_0\partial_x}{2}\sum_{n\in\mathbb{Z}}(f_n e^{-i(n-1)\varphi} + f_n e^{-i(n+1)\varphi}) \\ &+\frac{iv_0\partial_y}{2}\sum_{n\in\mathbb{Z}}(f_n e^{-i(n-1)\varphi} - f_n e^{-i(n+1)\varphi}), \end{aligned}$$

$$\begin{aligned}\partial_\varphi\left(f(r,\varphi,t)\frac{\iiint_{C(r)} f(r',\varphi',t)\sin(\varphi'-\varphi-\alpha)\mathrm{d}r'\mathrm{d}\varphi'}{\iiint_{C(r)} f(r',\varphi',t)\mathrm{d}r'\mathrm{d}\varphi'}\right)\\ =\frac{1}{2}\sum_{n\in\mathbb{Z}} f_n\Bigg[(n-1)e^{-i(n-1)\varphi}\frac{\iint_{B(r)} f_{-1}(r',t)\mathrm{d}r'}{\iint_{B(r)} f_0(r',t)\mathrm{d}r'}e^{i\alpha}\\ -(n+1)e^{-i(n+1)\varphi}\frac{\iint_{B(r)} f_1(r',t)\mathrm{d}r'}{\iint_{B(r)} f_0(r',t)\mathrm{d}r'}e^{-i\alpha}\Bigg],\end{aligned}$$

$$\partial_{\varphi\varphi}f(r,\varphi,t)=-\sum_{n\in\mathbb{Z}} n^2 f_n e^{-in\varphi}.$$

Gathering the terms corresponding to each Fourier mode $e^{-in\varphi}$, the evolution equation for each mode $f_n=f_n(r,t), n\in\mathbb{Z}$ becomes

$$\begin{aligned}\partial_t f_n=&-n^2D_\varphi f_n-\frac{v_0}{2}\partial_x(f_{n+1}+f_{n-1})+\frac{iv_0}{2}\partial_y(f_{n+1}-f_{n-1})\\ &+\frac{n}{2}\left(f_{n-1}\frac{\iint_{B(r)} f_1(r',t)\mathrm{d}r'}{\iint_{B(r)} f_0(r',t)\mathrm{d}r'}e^{-i\alpha}-f_{n+1}\frac{\iint_{B(r)} f_{-1}(r',t)\mathrm{d}r'}{\iint_{B(r)} f_0(r',t)\mathrm{d}r'}e^{i\alpha}\right).\end{aligned}\tag{5.1.4}$$

The integration over the cylinder $C(r)=C(r;\varrho)$ becomes the integration over the disk $B(r)=B(r;\varrho)$, which is defined as

$$B(r;\varrho)=\left\{r'\in\mathbb{U}^2 \mid \|r'-r\|\le\varrho\right\}.\tag{5.1.5}$$

As before, we usually suppress the explicit dependence of the circular neighborhood $B(r)$ on the parameter ϱ for the sake of brevity.

Next, we perform the Fourier transform of Eq. (5.1.4) with respect to spatial coordinates r. Each Fourier mode $f_n(r,t)$ can be decomposed into a series as

$$f_n(r,t)=\sum_{k\in\mathbb{Z}^2} g_n(k,t)e^{-i\frac{2\pi}{L}k\cdot r},$$

where its coefficients are defined as

$$g_n(k,t)=\mathcal{F}\{f_n(r,t)\}(k,t)=\frac{1}{L^2}\iint_{\mathbb{U}^2} f_n(r,t)e^{i\frac{2\pi}{L}k\cdot r}\mathrm{d}r.\tag{5.1.6}$$

Our next goal is to obtain the differential equations for each mode $g_n(k,t)$ in the Fourier space with respect to the spatial variables, with the subsequent goal of deriving its linearized dynamics. With that regard, all terms in Eq. (5.1.4) except for the nonlinear interaction one are easily transformed as

$$\mathcal{F}\left\{\partial_t f_n(r,t)\right\}(k,t)=\partial_t g_n(k,t),$$

$$\mathcal{F}\left\{\partial_x[f_{n+1}(r,t)+f_{n-1}(r,t)]\right\}(k,t)=-i\frac{2\pi}{L}k_x[g_{n+1}(k,t)+g_{n-1}(k,t)],$$

$$\mathcal{F}\left\{\partial_y[f_{n+1}(r,t)-f_{n-1}(r,t)]\right\}(k,t)=-i\frac{2\pi}{L}k_y[g_{n+1}(k,t)-g_{n-1}(k,t)].$$

As to the interaction terms (the ones with the integrals), we will consider the derivation only for the first one of them. In order to find its transformation, we first represent it as

$$\begin{aligned}&\frac{1}{L^2}\iint_{\mathbb{U}^2} f_{n-1}(r,t)\frac{\iint_{B(r)} f_1(r',t)\mathrm{d}r'}{\iint_{B(r)} f_0(r',t)\mathrm{d}r'}e^{i\frac{2\pi}{L}k\cdot r}\mathrm{d}r\\&=\sum_{q\in\mathbb{Z}^2} g_{n-1}(q,t)\frac{1}{L^2}\iint_{\mathbb{U}^2}\frac{\iint_{B(r)} f_1(r',t)\mathrm{d}r'}{\iint_{B(r)} f_0(r',t)\mathrm{d}r'}e^{i\frac{2\pi}{L}(k-q)\cdot r}\mathrm{d}r=\sum_{q\in\mathbb{Z}^2} g_{n-1}(q,t)K_1(k-q,t),\end{aligned}$$

where K_1 denotes the Fourier transform Eq. (5.1.6) of one of the interaction force terms. The other appears as K_{-1} and inherently depends on f_{-1}. To obtain the representation of the interaction kernel K_1 in the Fourier space solely, i.e., via the wave vectors, we need to transform the integrals involving the primed variables (Großmann, Schimansky-Geier, and Romanczuk 2013). Generally, we consider

$$\begin{aligned}\iint_{B(r)} f_n(r',t)\mathrm{d}r' &= \sum_{k\in\mathbb{Z}^2}\iint_{B(r)} g_n(k,t)e^{-i\frac{2\pi}{L}k\cdot r'}\mathrm{d}r'\\&=\sum_{k\in\mathbb{Z}^2} g_n(k,t)e^{-i\frac{2\pi}{L}k\cdot r}\iint_{B(0)} e^{-i\frac{2\pi}{L}k\cdot z}\mathrm{d}z\\&=\sum_{k\in\mathbb{Z}^2} g_n(k,t)e^{-i\frac{2\pi}{L}k\cdot r}\int_0^{\varrho}\int_{\mathbb{T}}\|z\|e^{-i\frac{2\pi}{L}\|z\|\|k\|\cos(\zeta-\chi)}\mathrm{d}\|z\|\mathrm{d}\zeta\\&=2\pi\sum_{k\in\mathbb{Z}^2} g_n(k,t)e^{-i\frac{2\pi}{L}k\cdot r}\int_0^{\varrho}\|z\|J_0\left(\frac{2\pi}{L}\|z\|\|k\|\right)\mathrm{d}\|z\|\\&=L\varrho\sum_{k\in\mathbb{Z}^2} g_n(k,t)e^{-i\frac{2\pi}{L}k\cdot r}\frac{J_1\left(\frac{2\pi}{L}\varrho\|k\|\right)}{\|k\|}.\end{aligned}$$

In the above derivation, we have made use of the polar representation of $z=\|z\|(\cos\zeta,\sin\zeta)^T$ and $k=\|k\|(\cos\chi,\sin\chi)^T$. The functions J_0 and J_1 denote the Bessel functions of the first kind. The transition between these functions was performed using the identity $\int_0^R sJ_0(s)\mathrm{d}s=RJ_1(R), R\in\mathbb{R}_+$. Note that the last transition of the above chain is valid as long as $k\neq(0,0)^T$. Otherwise, in the zero wave number regime, one has $\int_0^{\varrho}\|z\|J_0(0)\mathrm{d}\|z\|=\varrho^2/2$.

The last sum of the above chain of equations is the Fourier series with the coefficients containing the Bessel function. To simplify the further notation, we will denote

$$j_{\varrho}(k)=\frac{J_1\left(\frac{2\pi}{L}\varrho\|k\|\right)}{\|k\|}.$$

Note that despite of the division by the norm of a wave vector, it is possible to consider the dynamics in the hydrodynamic limit, since $\lim\limits_{x\to 0+0}\frac{1}{x}J_1(x)=\frac{1}{2}$. With the new notation, we can write the interaction kernel as

$$K_{\pm 1}(k-q,t)=\mathcal{F}\left\{\frac{\sum_{p\in\mathbb{Z}^2} g_{\pm 1}(p,t)j_{\varrho}(p)e^{-i\frac{2\pi}{L}p\cdot r}}{\sum_{p\in\mathbb{Z}^2} g_0(p,t)j_{\varrho}(p)e^{-i\frac{2\pi}{L}p\cdot r}}\right\}(k-q,t). \tag{5.1.7}$$

The kernel in this representation still depends on the Fourier coefficients in a nonlinear way but further decomposition of the kernel in a linear combination requires the knowledge of g_n.

We see that after the Fourier transform with respect to spatial variables, the coefficient $\frac{2\pi}{L}$ exclusively appears in front of v_0 and ϱ. Thus, we introduce $v_0^* = \frac{2\pi}{L} v_0$ and $\varrho^* = \frac{2\pi}{L}\varrho$ to shorten the further notation. The auxiliary function $j_\varrho(k)$ becomes $j_\varrho(k) = \frac{J_1(\varrho^* \|k\|)}{\|k\|}$.

With the current representation of the interaction kernels, the time evolution of the Fourier coefficients $g_n = g_n(k,t)$ reads

$$\begin{aligned}\partial_t g_n(k,t) &= -n^2 D_\varphi g_n + \frac{i v_0^*}{2} k_x (g_{n+1} + g_{n-1}) + \frac{v_0^*}{2} k_y (g_{n+1} - g_{n-1}) \\ &\quad + \frac{n}{2}\left(e^{-i\alpha} \sum_{q \in \mathbb{Z}^2} g_{n-1}(q,t) K_1(k-q,t) - e^{i\alpha} \sum_{q \in \mathbb{Z}^2} g_{n+1}(q,t) K_{-1}(k-q,t) \right),\end{aligned} \tag{5.1.8}$$

where the Fourier transforms $K_{\pm 1}$ of the interaction kernels are defined in Eq. (5.1.7). As an outline, we mention that since we are going to test only the spatially homogeneous solutions on the matter of stability, their Fourier transforms with respect to x, y will contain Kronecker delta functions. Upon the substitution of such transforms into the above expression, the sums over the wave numbers q will be resolved.

For convenience, we denote

$$\mathcal{L}[g_0, g_{\pm 1}, g_{n \mp 1}](q,k,t) = g_{n \mp 1}(q,t) K_{\pm 1}(k-q,t),$$

where the dependence on g_0 and $g_{\pm 1}$ comes through $K_{\pm 1}$. We will use this expression in the linearization procedure described next.

Let the stationary spatially homogeneous solution of Eq. (5.1.1), transformed to the Fourier space with respect to the spatial variables, be $g_n^*(k)$. We denote the components of a small perturbation to the solution as

$$\delta g_n(k,t) = g_n(k,t) - g_n^*(k). \tag{5.1.9}$$

To see how those perturbations behave over time, we need to derive differential equations for δg_n. To do that, we linearize Eq. (5.1.8) around $g_n^*(k)$. Since the right hand side of Eq. (5.1.8) depends on several δg_n, by Taylor series expansion we find

$$\begin{aligned}\partial_t \delta g_n(k,t) &= \frac{i v_0^*}{2} k_x [\delta g_{n+1}(k,t) \\ &\quad + \delta g_{n-1}(k,t)] + \frac{v_0^*}{2} k_y [\delta g_{n+1}(k,t) - \delta g_{n-1}(k,t)] - n^2 D_\varphi \delta g_n(k,t) \\ &\quad + \frac{n}{2} e^{-i\alpha} \sum_{m \in \{0,1,n-1\}} \sum_{q \in \mathbb{Z}^2} \frac{\partial \mathcal{L}[g_0, g_1, g_{n-1}]}{\partial g_m}(q,k,t) \Bigg|_{g_0^*, g_1^*, g_{n-1}^*} \delta g_m(q,t) \\ &\quad - \frac{n}{2} e^{i\alpha} \sum_{m \in \{0,-1,n+1\}} \sum_{q \in \mathbb{Z}^2} \frac{\partial \mathcal{L}[g_0, g_{-1}, g_{n+1}]}{\partial g_m}(q,k,t) \Bigg|_{g_0^*, g_{-1}^*, g_{n+1}^*} \delta g_m(q,t).\end{aligned} \tag{5.1.10}$$

One can show that the derivatives of the functional $\mathcal{L}$ are

$$\begin{aligned}\frac{\partial \mathcal{L}[g_0, g_1, g_{n-1}]}{\partial g_0}(q,k,t) &= -j_\varrho(q) \sum_{p \in \mathbb{Z}^2} g_{n-1}(p,t) \times \\ &\times \mathcal{F}\left\{ \frac{\sum_{s \in \mathbb{Z}^2} g_1(s,t) j_\varrho(s) e^{-i \frac{2\pi}{L} s \cdot r}}{[\sum_{s \in \mathbb{Z}^2} g_0(s,t) j_\varrho(s) e^{-i \frac{2\pi}{L} s \cdot r}]^2} \right\}(k-p-q),\end{aligned}$$

$$
\begin{aligned}
\frac{\partial \mathcal{L}[g_0, g_1, g_{n-1}]}{\partial g_1}(q,k,t) &= j_\varrho(q) \sum_{p\in\mathbb{Z}^2} g_{n-1}(p,t)\times \\
&\times \mathcal{F}\left\{ \frac{1}{\sum_{s\in\mathbb{Z}^2} g_0(s,t) j_\varrho(s) e^{-i\frac{2\pi}{L}s\cdot r}} \right\}(k-p-q), \\
\frac{\partial \mathcal{L}[g_0, g_1, g_{n-1}]}{\partial g_{n-1}}(q,k,t) &= K_1(k-q,t),
\end{aligned}
$$

and the other three derivatives are determined similarly. In the derivation of the above derivatives, one needs to take particular care so as to ensure that the perturbed variables depend on the same variables as the functions, with respect to which the differentiation is performed.

As we have already mentioned, we are interested here in stationary spatially homogeneous solutions of Eq. (5.1.1), i.e., $f^*(r,\varphi,t) = f^*(\varphi)$. This property results in the fact that its Fourier coefficients f_n^* in Fourier space with respect to the spatial variables are factorized as $g_n^*(k) = \delta_{k,0} f_n^*$ with $\delta_{k,0} = \delta_{k_x,0}\delta_{k_y,0}$ as a product of two Kronecker delta functions. Plugging the found expressions for all the functional derivatives into Eq. (5.1.10) and evaluating them at the fixed points by using the factorization property, we obtain

$$
\begin{aligned}
\partial_t \delta g_n(k,t) &= -n^2 D_\varphi \delta g_n(k,t) \\
&+ \frac{i v_0^*}{2} k_x [\delta g_{n+1}(k,t) + \delta g_{n-1}(k,t)] + \frac{v_0^*}{2} k_y [\delta g_{n+1}(k,t) - \delta g_{n-1}(k,t)] \\
&- \frac{n}{2 f_0^*}\left[\frac{f_1^* f_{n-1}^*}{f_0^*} j_1(k) \delta g_0(k,t) - f_{n-1}^* j_1(k) \delta g_1(k,t) - f_1^* \delta g_{n-1}(k,t) \right] e^{-i\alpha} \\
&+ \frac{n}{2 f_0^*}\left[\frac{f_{-1}^* f_{n+1}^*}{f_0^*} j_1(k) \delta g_0(k,t) - f_{n+1}^* j_1(k) \delta g_{-1}(k,t) - f_{-1}^* \delta g_{n+1}(k,t) \right] e^{i\alpha},
\end{aligned}
$$

where we have denoted $j_1(k) = j_\varrho(k)/j_\varrho(0) = 2J_1(\varrho^* \|k\|)/(\varrho^*\|k\|)$.

Since $n \in \mathbb{Z}$, we have obtained an infinite linear system of ODEs, which we can write more compactly as

$$
\partial_t \delta g_n(k,t) = \sum_{m=-\infty}^{\infty} M_{n,m}(k) \delta g_m(k,t), \tag{5.1.11}
$$

where the matrix coefficients are given by

$$
\begin{aligned}
M_{n,m} &= -n^2 D_\varphi \delta_{n,m} + \frac{v_0^*}{2}(ik_x - k_y)\delta_{n-1,m} + \frac{v_0^*}{2}(ik_x + k_y)\delta_{n+1,m} \\
&- \frac{n}{2 f_0^*}\left(\frac{f_1^* f_{n-1}^*}{f_0^*} j_1(k) \delta_{0,m} - f_{n-1}^* j_1(k) \delta_{1,m} - f_1^* \delta_{n-1,m} \right) e^{-i\alpha} \\
&+ \frac{n}{2 f_0^*}\left(\frac{f_{-1}^* f_{n+1}^*}{f_0^*} j_1(k) \delta_{0,m} - f_{n+1}^* j_1(k) \delta_{-1,m} - f_{-1}^* \delta_{n+1,m} \right) e^{i\alpha},
\end{aligned} \tag{5.1.12}
$$

where $\delta_{n,m}$ is the Kronecker delta symbol for $n,m \in \mathbb{Z}$. This system is the linearization of Eq. (5.1.8) around a stationary spatially homogeneous solution as postulated by Eq. (5.1.9).

The further stability analysis for the spatially homogeneous solutions proceeds as follows. One needs to calculate the eigenvalues λ of the stability matrix $M = (M_{n,m})_{n,m\in\mathbb{Z}}$, each of which is a function of the wave vector k, from the characteristic equation

$$
\det(M - \lambda(k) I) = 0,
$$

where I is the identity matrix. The relationship $\lambda = \lambda(k)$ is known as a dispersion relation and it defines the stability of a solution with respect to a given wave vector k. If the real part of all eigenvalues $\lambda_n, n \in \mathbb{Z}$ for all values of the wave vector is negative, then the solution is stable. If there exists an eigenvalue such that for a range of k its real part becomes positive, the solution is unstable. Additionally, in the latter case, if the imaginary part of the eigenvalue is zero, we should expect another stationary pattern for that parameter set. Otherwise, we expect a nonstationary behavior of the system.

In the following, we apply the developed stability analysis framework to the known stationary spatially homogeneous solutions. Namely, a uniform density function and a von Misés density function Eq. (3.2.10).

5.1.1.1 *The Uniform Solution*

We are first interested in the stability analysis of the simplest solution that satisfies Eq. (3.1.7), i.e., a uniform density function $f^*(r, \varphi, t) = \frac{1}{2\pi}$. Its Fourier transform with respect to the phase variable is $f_n^* = \frac{1}{2\pi}\delta_{n,0}$. Subsequently, its Fourier transform with respect to spatial r and angular φ variables is $g_n(k,t) = \delta_{n,0}\delta_{k,0}$. We have constructed everything we need for the linear stability analysis of this solution so far. We substitute the Fourier modes of this fixed point into Eq. (5.1.12) and obtain the linearized system of ODEs described by the following matrix:

$$\begin{aligned} M_{n,m} = & -n^2 D_\varphi \delta_{n,m} + \frac{v_0^*}{2}(ik_x - k_y)\delta_{n-1,m} + \frac{v_0^*}{2}(ik_x + k_y)\delta_{n+1,m} \\ & + \frac{n}{2} j_1(k)\left(\delta_{n,1}e^{-i\alpha} - \delta_{n,-1}e^{i\alpha}\right)\delta_{n,m}. \end{aligned}$$

If we consider the spatially homogeneous system Eq. (3.2.8), the above matrix simplifies by setting $k = (0,0)^T$:

$$M_{n,m} = -n^2 D_\varphi \delta_{n,m} + \frac{n}{2}\left(\delta_{n,1}e^{-i\alpha} - \delta_{n,-1}e^{i\alpha}\right)\delta_{n,m}.$$

Since this is a diagonal matrix, we find the eigenvalues straightforwardly. They are

$$\lambda_0 = 0, \quad \lambda_{\pm 1} = \frac{1}{2}\cos\alpha - D_\varphi \mp \frac{i}{2}\sin\alpha, \quad \lambda_n = -n^2 D_\varphi, |n| \geq 2.$$

The zeroth eigenvalue is always neutrally stable and the eigenvalues with $|n| \geq 2$ are always stable since $\mathrm{Re}(\lambda_n) < 0$. The only instability may arise for $\lambda_{\pm 1}$. The uniform solution $f(r, \varphi, t) = \frac{1}{2\pi}$ is stable, if $\mathrm{Re}(\lambda_{\pm 1}) < 0$, i.e., if $D_\varphi > \frac{1}{2}\cos\alpha$. As a result, the line

$$D_\varphi = \frac{1}{2}\cos\alpha$$

is the transition line for the onset of polar order. This is in accordance with the result that we had when we analyzed the traveling wave solution Eq. (3.2.14). The numerical investigations of this solution against both the parallel and transversal perturbations does not reveal any new instability mechanisms for $D_\varphi > \frac{1}{2}\cos\alpha$.

5.1.1.2 *The Zero Phase Lag Case*

We have showed that the other stationary solution to the spatially homogeneous system Eq. (3.2.8) in the absence of phase lag α is

$$f^*(\varphi) = \frac{e^{\gamma\cos\varphi}}{2\pi I_0(\gamma)},$$

where $\gamma = R/D_\varphi$. The Fourier modes in the series expansion of this solution with respect to the phase variable φ read

$$f_n^* = \frac{I_n(\gamma)}{2\pi I_0(\gamma)}.$$

For completeness, we here provide the stability matrix Eq. (5.1.12) for the linearized dynamics of the perturbations to this solution:

$$\begin{aligned} M_{n,m} = {} & -n^2 D_\varphi \delta_{n,m} + \frac{v_0^*}{2}(ik_x - k_y)\delta_{n-1,m} + \frac{v_0^*}{2}(ik_x + k_y)\delta_{n+1,m} \\ & - \frac{n}{2}\left(j_1(k)\frac{I_1(\gamma)I_{n-1}(\gamma)}{I_0^2(\gamma)}\delta_{0,m} - j_1(k)\frac{I_{n-1}(\gamma)}{I_0(\gamma)}\delta_{1,m} - \frac{I_1(\gamma)}{I_0(\gamma)}\delta_{n-1,m} \right) \\ & + \frac{n}{2}\left(j_1(k)\frac{I_{-1}(\gamma)I_{n+1}(\gamma)}{I_0^2(\gamma)}\delta_{0,m} - j_1(k)\frac{I_{n+1}(\gamma)}{I_0(\gamma)}\delta_{-1,m} - \frac{I_{-1}(\gamma)}{I_0(\gamma)}\delta_{n+1,m} \right). \end{aligned}$$

Because of its form, we cannot solve an eigenvalue problem for this stability matrix in the spatially nonhomogeneous case analytically. Thus, we solve it numerically. As a result, it appears that the von Misés density function is always stable for $D_\varphi < \frac{1}{2}$ (see its further analysis in the next section on the hydrodynamic theory approach).

5.1.2 *Traveling Wave Solutions*

Inside the region of partial polar order, we have shown that the solution to Eq. (3.2.8) in the presence of the phase lag is given by Eq. (3.2.14). If we use the ansatz $\omega = \varphi - vt$, we find that Eq. (3.2.15) solves Eq. (3.2.8) as well as Eq. (5.1.1). The stability analysis framework, developed so far, is valid only for the stationary solutions of Eq. (5.1.1), which was stated by Eq. (5.1.9). In order to make the same framework be applicable to Eq. (3.2.15), we introduce the following ansatz being an extension to the traveling wave ansatz used before:

$$\begin{aligned} \xi &= \cos(vt)x + \sin(vt)y, \\ \eta &= -\sin(vt)x + \cos(vt)y, \\ \omega &= \varphi - vt, \\ h(\xi, \eta, \omega, t) &= f(x, y, \varphi, t). \end{aligned} \tag{5.1.13}$$

Leaving alone the spatial variables for the moment, the previous substitution of the form $f(\varphi, t) = g(\omega)$ transforms the PDE of two variables into the ODE. Instead, if we consider the substitution like $f(\varphi, t) = h(\omega, t)$, we transform the PDE to the moving frame $\varphi - vt$, which has the solution Eq. (3.2.14) as its stationary solution. Now, in order to perform the stability analysis of Eq. (5.1.1) instead of Eq. (3.2.8), one also needs to take into account that with the substitution $\omega = \varphi - vt$, the spatial advection terms become dependent on time and the stability analysis is again not applicable. In order to circumvent that, we introduce the ansatz Eq. (5.1.13). After its application, the PDE becomes

$$\begin{aligned} \partial_t h = {} & -(v_0 \cos\omega + v\eta)\partial_\xi h - (v_0 \sin\omega - v\xi)\partial_\eta h \\ & + D_\varphi \partial_{\omega\omega} h + v\partial_\omega h - \partial_\omega \left(h \frac{\int_{C(r)} h(r', \omega', t)\sin(\omega' - \omega - \alpha)\mathrm{d}r'\mathrm{d}\omega'}{\int_{C(r)} h(r', \omega', t)\mathrm{d}r'\mathrm{d}\omega'} \right), \end{aligned} \tag{5.1.14}$$

where we now denote the spatial vector as $r = (\xi, \eta) \in \mathbb{U}^2$.

This equation admits the profile of the spatially homogeneous traveling wave solution Eq. (3.2.14) as its stationary solution:

$$h(\omega) = c_0 E(\omega) \left(1 + c_1 \frac{\int_0^{\omega} E^{-1}(\omega')\mathrm{d}\omega'}{\int_{\mathbb{T}} E^{-1}(\omega')\mathrm{d}\omega'} \right). \tag{5.1.15}$$

where $E(\omega) = \exp\left[-\frac{v}{D_\varphi}\omega + \frac{R}{D_\varphi}\cos(\omega+\alpha)\right]$, c_0 is a normalization constant, and $c_1 = (\exp(2\pi v/D_\varphi) - 1)$ comes from a periodicity constraint.

Due to that fact, we can proceed in the same manner as we did for the stationary solutions. First, we expand the new density function h into a Fourier series with respect to the phase ω and substitute the expansion into Eq. (5.1.14). If we gather the terms of each Fourier mode together, we obtain

$$\begin{aligned}
\partial_t h_n(r,t) = {} & v(r \times \nabla)h_n - \frac{v_0}{2}\partial_\xi(h_{n+1} + h_{n-1}) + \frac{iv_0}{2}\partial_\eta(h_{n+1} - h_{n-1}) \\
& - n^2 D_\varphi h_n - invh_n \\
& + \frac{n}{2}\left(h_{n-1}\frac{\iint_{B(r)} h_1(r',t)\mathrm{d}r'}{\iint_{B(r)} h_0(r',t)\mathrm{d}r'} e^{-i\alpha} - h_{n+1}\frac{\iint_{B(r)} h_{-1}(r',t)\mathrm{d}r'}{\iint_{B(r)} h_0(r',t)\mathrm{d}r'} e^{i\alpha} \right),
\end{aligned} \tag{5.1.16}$$

where $\times$ denotes the third component of a cross product, i.e., $r \times \nabla = \xi\partial_\eta - \eta\partial_\xi$.

Next, we need to transform this hierarchy of position dependent Fourier modes into the Fourier space with respect to the spatial variables using Eq. (5.1.6). Most of the terms are transformed as described in the previous section, except for

$$\begin{aligned}
\mathcal{F}\{v(r \times \nabla)h_n\}(k,t) &= iv\frac{2\pi}{L}\mathcal{F}\left\{(k \times r)h_n(r,t)\right\}(k,t) \\
&= iv\pi(k_x - k_y)g_n(k_x,k_y,t) + \sum_{\substack{q_y \in \mathbb{Z} \\ k_y \neq q_y}} \frac{vk_x}{k_y - q_y} g_n(k_x,q_y,t) - \sum_{\substack{q_x \in \mathbb{Z} \\ k_x \neq q_x}} \frac{vk_y}{k_x - q_x} g_n(q_x,k_y,t).
\end{aligned}$$

The appearance of the couplings between $g_n(k)$ and $g_n(k')$ with $k \neq k'$, i.e., to the function values at the wave vectors other than k, makes the subsequent linear stability analysis convoluted and computationally unfeasible. We could map three Fourier indices n, k_x, and k_y into one index and perform the stability analysis of all the perturbations together but the solution to the eigenvalue problem would lose the spatial dependence, and we would not be able to obtain the dispersion relations and draw necessary conclusions. But note that if we rescale the spatial dimension in Eq. (5.1.17) as $k' = v_0 k$ (see the detailed example about the rescaling of the marginal density function in the section S4.4), we see that the above Fourier transform is mainly determined by the first term in the limit of small particle velocities v_0 so that we may assume

$$\mathcal{F}\{v(r \times \nabla)h_n\}(k,t) \approx iv\pi(k_x - k_y)g_n(k_x,k_y,t).$$

As a result, the PDE Eq. (5.1.16) for the Fourier modes of the traveling wave solution in the Fourier space with respect to the spatial variables becomes

$$\begin{aligned}
\partial_t g_n(k,t) = {} & -(n^2 D_\varphi + inv)g_n + iv\pi(k_x - k_y)g_n(k,t) \\
& + \frac{iv_0^*}{2}k_x(g_{n+1} + g_{n-1}) + \frac{v_0^*}{2}k_y(g_{n+1} - g_{n-1}) \\
& + \frac{n}{2}\left[e^{-i\alpha}\sum_{q \in \mathbb{Z}^2} g_{n-1}(q,t)K_1(k-q,t) - e^{i\alpha}\sum_{q \in \mathbb{Z}^2} g_{n+1}(q,t)K_{-1}(k-q,t) \right],
\end{aligned} \tag{5.1.17}$$

where we have again denoted $v_0^* = \frac{2\pi}{L}v_0$ and we will also use $\varrho^* = \frac{2\pi}{L}\varrho$.

At this point, we postulate again that in order to proceed further in the derivation of the linearized differential equations for the perturbations, we use the fact that the solutions, we are interested in, are stationary solutions of Eq. (5.1.14), i.e., their Fourier transforms with respect to the spatial variables are $g_n^*(k) = \delta_{k,0}h_n^*$. Under such assumptions, the perturbations have the form Eq. (5.1.9) and we need to linearize Eq. (5.1.17) around $g_n^*, n \in \mathbb{Z}$.

Following the same procedure as for the stationary solutions, we find the time evolution of the linearized dynamics of small spatially dependent perturbations to be

$$\begin{aligned}\partial_t \delta g_n(k,t) &= -(n^2 D_\varphi + inv)\delta g_n + iv\pi(k_x - k_y)\delta g_n \\ &+ \frac{iv_0^*}{2}k_x(\delta g_{n+1} + \delta g_{n-1}) + \frac{v_0^*}{2}k_y(\delta g_{n+1} - \delta g_{n-1}) \\ &- \frac{n}{2h_0^*}\left[\frac{h_1^* h_{n-1}^*}{h_0^*}j_1(k)\delta g_0(k,t) - h_{n-1}^* j_1(k)\delta g_1(k,t) - h_1^*\delta g_{n-1}(k,t)\right]e^{-i\alpha} \\ &+ \frac{n}{2h_0^*}\left[\frac{h_{-1}^* h_{n+1}^*}{h_0^*}j_1(k)\delta g_0(k,t) - h_{n+1}^* j_1(k)\delta g_{-1}(k,t) - h_{-1}^*\delta g_{n+1}(k,t)\right]e^{i\alpha}.\end{aligned} \tag{5.1.18}$$

The corresponding stability matrix coefficients Eq. (5.1.11) read

$$\begin{aligned}M_{n,m} &= -(n^2 D_\varphi + inv)\delta_{n,m} + iv\pi(k_x - k_y)\delta_{n,m} \\ &+ \frac{v_0^*}{2}(ik_x - k_y)\delta_{n-1,m} + \frac{v_0^*}{2}(ik_x + k_y)\delta_{n+1,m} \\ &- \frac{n}{2h_0^*}\left(\frac{h_1^* h_{n-1}^*}{h_0^*}j_1(k)\delta_{0,m} - h_{n-1}^* j_1(k)\delta_{1,m} - h_1^*\delta_{n-1,m}\right)e^{-i\alpha} \\ &+ \frac{n}{2h_0^*}\left(\frac{h_{-1}^* h_{n+1}^*}{h_0^*}j_1(k)\delta_{0,m} - h_{n+1}^* j_1(k)\delta_{-1,m} - h_{-1}^*\delta_{n+1,m}\right)e^{i\alpha}.\end{aligned} \tag{5.1.19}$$

5.1.2.1 *The Nonzero Phase Lag Case*

In order to perform the stability analysis of the traveling wave solution, we need to transform it first into the Fourier space with respect to the phase variable φ. However, one cannot straightforwardly integrate it using Eq. (5.1.3) as required by the definition of Fourier modes. We first make use of the following decomposition of an exponential function into a series containing the modified Bessel functions of the first kind:

$$e^{\gamma\cos\varphi} = I_0(\gamma) + 2\sum_{\nu=1}^{\infty} I_\nu(\gamma)\cos(\nu\varphi), \quad \gamma \in \mathbb{R}, \varphi \in \mathbb{T}.$$

in order to rewrite the corresponding terms in the density function. Such a decomposition makes it possible to integrate Eq. (5.1.15) when applying Eq. (5.1.3). Performing the lengthy integration, one can show that the Fourier modes take the following form:

$$\begin{aligned}f_n(t) = c_0\Big\{&c_1(n)I_0(\gamma)I_n(-\gamma) \\ &+ \sum_{\nu=1}^{\infty} I_\nu(\gamma)\big[c_1(n+\nu)I_{n+\nu}(-\gamma) + c_1(n-\nu)I_{n-\nu}(-\gamma)\big]\Big\}e^{-in\alpha},\end{aligned} \tag{5.1.20}$$

where as previous $\gamma = R/D_\varphi$ and the normalization constant can be shown to be

$$c_0 = \frac{1}{2\pi}\left\{c_1(0)I_0^2(\gamma) + \sum_{\nu=1}^{\infty} I_\nu(\gamma)I_\nu(-\gamma)\left[c_1(\nu) + \bar{c}_1(\nu)\right]\right\}^{-1},$$

where $\bar{c}_1$ denotes a complex conjugate. We have also denoted for brevity

$$c_1(\nu) = \frac{v/D_\varphi + i\nu}{(v/D_\varphi)^2 + \nu^2}.$$

Given such a representation of the solution Eq. (5.1.15) and even more complicated form of the stability matrix than it was for the zero phase lag case, the only way to study stability properties here is using the numerical methods. For spatially homogeneous perturbations, we find that Eq. (5.1.15) is always stable for $D_\varphi < \frac{1}{2}\cos\alpha$. However, we are interested in the development of small spatially dependent perturbations to the solution Eq. (5.1.15). The dynamics of such perturbations is governed by the linearized system Eq. (5.1.18). It depends on the Fourier modes $f_n, n \in \mathbb{Z}$ of the solution, which are given by Eq. (5.1.20).

5.2 HYDRODYNAMIC THEORY APPROACH

5.2.1 *Stationary Solutions*

Now that we have the solutions of the model, we proceed with the analysis of their stability. As previously, we first transform the equations to the Fourier space with respect to the spatial variables. Since we work in the space with periodic boundaries, we may expand the marginal density function as

$$\rho(r,t) = \sum_{k\in\mathbb{Z}^2} \hat{\rho}(k,t)e^{-i\frac{2\pi}{L}k\cdot r},$$

where the coefficients of each mode are defined as

$$\hat{\rho}(k,t) = \mathcal{F}\{\rho(r,t)\}(k,t) = \frac{1}{L^2}\iint_{\mathbb{U}^2} \rho(r,t)e^{i\frac{2\pi}{L}k\cdot r}\mathrm{d}r.$$

The expansion for the momentum field is defined similarly.

The transformation of Eq. (4.1.2) into the Fourier space with respect to the spatial variables is then performed the same way as we did it in the kinetic theory. Thus, we do not delve into all the details here but mention several key points. Namely, the transforms of all functionally different terms can be found to be

$$\mathcal{F}\{\nabla\cdot w(r,t)\}(k,t) = -i\frac{2\pi}{L}(\hat{w}(k,t)\cdot k),$$

$$\mathcal{F}\{\nabla\rho(r,t)\}(k,t) = -i\frac{2\pi}{L}\hat{\rho}(k,t)k,$$

$$\mathcal{F}\{\Delta w(r,t)\}(k,t) = -\left(\frac{2\pi}{L}\right)^2|k|^2\hat{w}(k,t),$$

$$\mathcal{F}\{\rho(r,t)W(r,t)\}(k,t) = \sum_{q\in\mathbb{Z}^2}\hat{\rho}(q,t)K_1(k-q,t),$$

$$\mathcal{F}\{\nabla[w(r,t)\cdot W(r,t)]\}(k,t) = -i\frac{2\pi}{L}k\sum_{q\in\mathbb{Z}^2}[\hat{w}(q,t)\cdot K_1(k-q,t)],$$

$$\mathcal{F}\{w(r,t)[\nabla\cdot W(r,t)]\}(k,t) = -i\frac{2\pi}{L}\sum_{q\in\mathbb{Z}^2}\hat{w}(q,t)[(k-q)\cdot K_1(k-q,t)],$$

$$\mathcal{F}\{[w(r,t)\cdot\nabla]W(r,t)\}(k,t) = -i\frac{2\pi}{L}\sum_{q\in\mathbb{Z}^2}[(k-q)\cdot\hat{w}(q,t)]K_1(k-q,t),$$

$$\mathcal{F}\{W(r,t)[\nabla\cdot w(r,t)]\}(k,t) = -i\frac{2\pi}{L}\sum_{q\in\mathbb{Z}^2}[q\cdot\hat{w}(q,t)]K_1(k-q,t),$$

$$\mathcal{F}\{[W(r,t)\cdot\nabla]w(r,t)\}(k,t) = -i\frac{2\pi}{L}\sum_{q\in\mathbb{Z}^2}\hat{w}(q,t)[q\cdot K_1(k-q,t)],$$

$$\mathcal{F}\{w(r,t)\|W(r,t)\|^2\}(k,t) = \sum_{q\in\mathbb{Z}^2}\hat{w}(q,t)K_2(k-q,t),$$

where we have introduced two kernel functions in comparison with the ones from the previous chapter:

$$K_1(k-q,t) = \frac{1}{L^2}\iint_{\mathbb{U}^2} W(r,t)e^{i\frac{2\pi}{L}(k-q)\cdot r}\mathrm{d}r,$$
$$K_2(k-q,t) = \frac{1}{L^2}\iint_{\mathbb{U}^2} \|W(r,t)\|^2 e^{i\frac{2\pi}{L}(k-q)\cdot r}\mathrm{d}r.$$

Note that the spatially averaged momentum field can be written in terms of the wave vectors as

$$W(r,t) = \frac{\sum_{p\in\mathbb{Z}^2}\hat{w}(p,t)j_\varrho(p)e^{-i\frac{2\pi}{L}p\cdot r}}{\sum_{p\in\mathbb{Z}^2}\hat{\rho}(p)j_\varrho(p)e^{-i\frac{2\pi}{L}p\cdot r}},$$

where $j_\varrho(p) = J_1\left(\frac{2\pi}{L}\varrho\|p\|\right)/\|p\|$ as before.

The hydrodynamic equations in the Fourier space with respect to the spatial variables read

$$\begin{aligned}
&\partial_t\hat{\rho}(k) = iv_0^*[k\cdot\hat{w}(k)],\\
&\partial_t\hat{w}(k) = \frac{iv_0^*}{2}k\hat{\rho}(k) - D_\varphi\hat{w}(k) - \frac{(v_0^*)^2}{16D_\varphi}|k|^2\hat{w}(k)\\
&\quad + \sum_{q\in\mathbb{Z}^2}\Bigg\{\frac{1}{2}Q_{-\alpha}\hat{\rho}(q)K_1(k-q) - \frac{1}{8D_\varphi}\hat{w}(q)K_2(k-q)\\
&\quad - \frac{iv_0^*}{16D_\varphi}Q_\alpha\left\{\hat{w}(q)[q\cdot K_1(k-q)] + \hat{w}_\perp(q)[q\cdot K_{1,\perp}(k-q)]\right\}\\
&\quad - \frac{iv_0^*}{8D_\varphi}Q_{-\alpha}\{k[\hat{w}(q)\cdot K_1(k-q)] - \hat{w}(q)[k\cdot K_1(k-q)] - [k\cdot\hat{w}(q)]K_1(k-q)\}\Bigg\},
\end{aligned} \tag{5.2.21}$$

where $K_{1,\perp} = (-K_{1,y}, K_{1,x})^T$ and we use $v_0^* = \frac{2\pi}{L}v_0$ and $\varrho^* = \frac{2\pi}{L}\varrho$ as before. Note that we suppressed the explicit time dependence of $\hat{\rho}$, $\hat{w}$, K_1, and K_2 for compactness.

Let a stationary spatially homogeneous solution to Eq. (4.1.2) be $\rho(r,t) = 1$ (since we are allowed to work only with probability density functions) and $w(r,t) = w^*$. Due to its spatial homogeneity, the Fourier transform of such a solution is $\hat{\rho}(k,t) = \hat{\rho}^*(k) = \delta_{k,0}$, $\hat{w}(k,t) = \hat{w}^*(k) = w^*\delta_{k,0}$ with $\delta_{k,0} = \delta_{k_x,0}\delta_{k_y,0}$. We consider the infinitesimal deviations from such a solution as

$$\begin{aligned} \delta\hat{\rho}(k,t) &= \hat{\rho}(k,t) - \hat{\rho}^*(k), \\ \delta\hat{w}(k,t) &= \hat{w}(k,t) - \hat{w}^*(k) \end{aligned}$$

and we want to derive the linearized dynamics for these perturbations if they evolve according to Eq. (5.2.21). Note that the kernels $K_{1,2}$ implicitly depend on the marginal density $\hat{\rho}$ and the momentum field $\hat{w}$.

The complete procedure how the linearization is done is the same as it was previously for the kinetic equations. For that reason, we do not go into the details here. One can show that the linearized dynamics of the perturbations around a stationary solution follow

$$\begin{aligned} \partial_t\delta\hat{\rho}(k,t) &= iv_0^*[k\cdot\delta\hat{w}(k,t)], \\ \partial_t\delta\hat{w}(k,t) &= \bigg\{ \frac{iv_0^*}{2}k + \frac{1}{2}[1-j_1(k)]Q_{-\alpha}w^* + \frac{1}{4D_\varphi}j_1(k)\|w^*\|^2 w^* \\ &\qquad + \frac{iv_0^*}{8D_\varphi}Q_{-\alpha}j_1(k)\left(\|w^*\|^2 k - 2(k\cdot w^*)w^*\right)\bigg\}\,\delta\hat{\rho}(k,t) \\ &\quad + \bigg\{ -D_\varphi - \frac{(v_0^*)^2}{16D_\varphi}|k|^2 + \frac{1}{2}j_1(k)Q_{-\alpha} - \frac{1}{8D_\varphi}\|w^*\|^2 I - \frac{1}{4D_\varphi}j_1(k)(w^*\otimes w^*) \\ &\qquad - \frac{iv_0^*}{16D_\varphi}Q_\alpha\left[(k\cdot w^*)I + (k\cdot w_\perp^*)Q_{\frac{\pi}{2}}\right] \\ &\qquad - \frac{iv_0^*}{8D_\varphi}[1+j_1(k)]Q_{-\alpha}\left[(k\otimes w^*) - (w^*\otimes k) - (k\cdot w^*)I\right]\bigg\}\,\delta\hat{w}(k,t), \end{aligned}$$

where $\otimes$ denotes the outer product. As before, we have denoted $j_1(k) = 2J_1\left(\varrho^*|k|\right)/\left(\varrho^*|k|\right)$.

For the further analysis, it would be helpful to rewrite this linearized system in a matrix form as

$$\partial_t \begin{pmatrix} \delta\hat{\rho} \\ \delta\hat{w}_x \\ \delta\hat{w}_y \end{pmatrix} = M \begin{pmatrix} \delta\hat{\rho} \\ \delta\hat{w}_x \\ \delta\hat{w}_y \end{pmatrix},$$

where $M = (M_{n,m})_{n,m=1,2,3}$ is the stability matrix with the coefficients

$$\begin{aligned} M_{11} &= 0, \quad M_{12} = iv_0^* k_x, \quad M_{13} = iv_0^* k_y, \\ M_{21} &= \frac{iv_0^*}{2}k_x + \frac{1}{2}[1-j_1(k)](w^*\cdot n_\alpha) + \frac{1}{4D_\varphi}j_1(k)\|w^*\|^2 w_x^* \\ &\quad + \frac{iv_0^*}{8D_\varphi}j_1(k)\left[\|w^*\|^2(k\cdot n_\alpha) - 2(k\cdot w^*)(w^*\cdot n_\alpha)\right], \\ M_{22} &= \frac{iv_0^*}{8D_\varphi}\bigg\{[1+j_1(k)][(w^*\cdot n_\alpha)k_x - w_x^*(k\cdot n_\alpha)] + \left[\frac{1}{2}+j_1(k)\right](k\cdot w^*)\cos\alpha \\ &\quad + \frac{1}{2}(k\cdot w_\perp^*)\sin\alpha\bigg\} - D_\varphi - \frac{(v_0^*)^2}{16D_\varphi}|k|^2 + \frac{1}{2}j_1(k)\left(\cos\alpha - \frac{(w_x^*)^2}{2D_\varphi}\right) - \frac{\|w^*\|^2}{8D_\varphi}, \\ M_{23} &= \frac{iv_0^*}{8D_\varphi}\bigg\{[1+j_1(k)][(w^*\cdot n_\alpha)k_y - w_y^*(k\cdot n_\alpha)] + \left[\frac{3}{2}+j_1(k)\right](k\cdot w^*)\sin\alpha \\ &\quad + \frac{1}{2}(k\cdot w_\perp^*)\cos\alpha\bigg\} + \frac{1}{2}j_1(k)\left(\sin\alpha - \frac{w_x^* w_y^*}{2D_\varphi}\right), \end{aligned}$$

$$\begin{aligned} M_{31} = {} & \frac{iv_0^* k_y}{2} - \frac{1}{2}[1 - j_1(k)](n_\alpha \cdot w_\perp^*) + \frac{1}{4D_\varphi} j_1(k) \|w^*\|^2 w_y^* \\ & + \frac{iv_0^*}{8D_\varphi} j_1(k) \left[2(k \cdot w^*)(n_\alpha \cdot w_\perp^*) - \|w^*\|^2 (n_\alpha \cdot k_\perp)\right], \end{aligned}$$

$$\begin{aligned} M_{32} = {} & \frac{iv_0^*}{8D_\varphi} \Bigg\{ [1 + j_1(k)][w_x^*(k_\perp \cdot n_\alpha) - (w_\perp^* \cdot n_\alpha) k_x] - \left[\frac{3}{2} + j_1(k)\right] (k \cdot w^*) \sin\alpha \\ & - \frac{1}{2}(k \cdot w_\perp^*) \cos\alpha \Bigg\} - \frac{1}{2} j_1(k) \left(\sin\alpha + \frac{w_x^* w_y^*}{2D_\varphi}\right), \end{aligned}$$

$$\begin{aligned} M_{33} = {} & \frac{iv_0^*}{8D_\varphi} \Bigg\{ [1 + j_1(k)][w_y^*(k_\perp \cdot n_\alpha) - (w_\perp^* \cdot n_\alpha) k_y] + \left[\frac{1}{2} + j_1(k)\right] (k \cdot w^*) \cos\alpha \\ & + \frac{1}{2}(k \cdot w_\perp^*) \sin\alpha \Bigg\} - D_\varphi - \frac{(v_0^*)^2}{16 D_\varphi} |k|^2 + \frac{1}{2} j_1(k) \left(\cos\alpha - \frac{(w_y^*)^2}{2D_\varphi}\right) - \frac{\|w^*\|^2}{8D_\varphi}, \end{aligned}$$

where $n_\alpha = (\cos\alpha, \sin\alpha)^T$ and $k_\perp = (-k_y, k_x)^T$.

The general form of the linearized matrix is not particularly informative and we need to instantiate the solutions to Eq. (4.1.2) as well as impose various assumptions on the parameters in order to simplify the above expressions and draw any conclusions. Still, there are some useful observations from the form of the linearized dynamics. First, the phase lag α and the noise strength D_φ appear nontrivially in most of the matrix coefficients, so they are definitely the parameters that determine the linear stability of the system. Second, the particle velocity v_0 and the interaction range ϱ both appear only as multipliers of the wave vector k. Thus, they both influence the spatial scale of the perturbations. But they do so separately, i.e., ϱ only appears inside $j_1(k)$. As a result, by rescaling $\tilde{k} = v_0^* k$, we have $j_1(k) = 2J_1\left(\frac{\varrho^*}{v_0^*}|\tilde{k}|\right) / \left(\frac{\varrho^*}{v_0^*}|\tilde{k}|\right)$, which signifies that the third independent parameter that is important for the stability of the solutions is ϱ^*/v_0^* ratio. For this reason, the length scale of the patterns that result from the instability of the partially synchronized solution, scales proportionally to ϱ^*/v_0^*. However, since the radius of interaction is restricted to be in $[0, \frac{1}{2}]$ range, we will keep these two parameters separately in the subsequent derivations. Note also that in the view of the fact that the wave numbers are integers, v_0^* and ϱ^* would determine whether the instabilities are detected at all.

5.2.2 *The Uniform Solution*

The uniform solution, which signifies the disordered motion of particles, is

$$(\rho, w_x, w_y) = (1, 0, 0).$$

The stability matrix M for this solution simplifies to

$$\begin{pmatrix} 0 & iv_0^* k_x & iv_0^* k_y \\ \frac{iv_0^*}{2} k_x & \frac{1}{2} j_1(k)\cos\alpha - D_\varphi - \frac{(v_0^*)^2}{16D_\varphi}|k|^2 & \frac{1}{2} j_1(k) \sin\alpha \\ \frac{iv_0^*}{2} k_y & -\frac{1}{2} j_1(k)\sin\alpha & \frac{1}{2} j_1(k)\cos\alpha - D_\varphi - \frac{(v_0^*)^2}{16D_\varphi}|k|^2 \end{pmatrix}$$

In the presence of a phase lag, the characteristic equation to the above matrix is a third degree polynomial and the explicit solutions of it are not particularly informative. In order to gain insight whether the long wavelength instability is possible for this solution, we expand the eigenvalues up to the second order both in the wave number k_x around $k_x = 0$ and in the diffusion constant around the order-disorder transition line $D_\varphi = \frac{1}{2}$. The resulting expansions read

$$\begin{aligned}\lambda_1(|k|, D_\varphi) &\approx -\frac{4\sqrt{3}}{9|\sin\alpha|}\left(D_\varphi - \frac{1}{2}\cos\alpha\right)^2,\\ \lambda_{2,3}(|k|, D_\varphi) &\approx \pm\frac{i}{2}|\sin\alpha| - \frac{4}{3}\left(D_\varphi - \frac{1}{2}\cos\alpha\right)\\ &\quad -\frac{1}{2}\left(\frac{(v_0^*)^2}{4\cos\alpha} + \frac{(\varrho^*)^2\cos\alpha}{8} \mp \frac{i(v_0^*)^2}{|\sin\alpha|}\right)|k|^2 + \frac{1}{|\sin\alpha|}\left(\frac{2\sqrt{3}}{9} \pm 6i\right)\left(D_\varphi - \frac{1}{2}\cos\alpha\right)^2.\end{aligned}$$

The first eigenvalue is negative for all the parameters and wave numbers. The other two eigenvalues are oscillating quantities for $\alpha \neq 0$ and they are stable for $D_\varphi > \frac{1}{2}\cos\alpha$ which is the order-disorder transition line we have encountered earlier. As a result, along a transition line that characterizes the onset of the synchronized motion, there are no long wavelength instability mechanisms leading to the formation of a new behavior. The scanning of the regions farther from the transition line with the help of numerical methods shows that there are no other instabilities for this solution too.

5.2.3 *The Synchronized Solution in the Zero Phase Lag Case*

The solution that signifies the onset of collective motion may point to an arbitrary direction. Thus, we write it as $w^* = \|w^*\| e(\varphi)$, where as previous $e(\varphi) = (\cos\varphi, \sin\varphi) \in \mathbb{S}^1 \subset \mathbb{R}^2$ is a unit vector in the direction of $\varphi \in \mathbb{T}$. Without loss of generality, we put $e(\varphi) = (1, 0)$ henceforth.

5.2.3.1 *Longitudinal Perturbations*

We consider the longitudinal perturbations of the form $k = (k_x, 0)^T$, $\delta\hat{w} = (\delta\hat{w}_x, \delta\hat{w}_y)^T$. The matrix coefficients thus read

$$\begin{gathered} M_{11} = 0, M_{12} = iv_0^* k_x, M_{13} = 0,\\ M_{21} = \|w^*\|\left(\frac{1}{2}[1 + j_1(k)]\cos\alpha - 2j_1(k)D_\varphi\right) + \frac{iv_0^*}{2}k_x\left[1 - j_1(k)(\cos\alpha - 2D_\varphi)\cos\alpha\right],\\ M_{22} = -\frac{(v_0^*)^2}{16D_\varphi}k_x^2 - \left(\frac{1}{2}[1 + j_1(k)]\cos\alpha - 2j_1(k)D_\varphi\right) + \frac{iv_0^*}{8D_\varphi}k_x\left[\frac{1}{2} + j_1(k)\right]\|w\|\cos\alpha,\\ M_{23} = \frac{1}{2}j_1(k)\sin\alpha + \frac{iv_0^*}{8D_\varphi}k_x\left[\frac{3}{2} + j_1(k)\right]\|w\|\sin\alpha,\\ M_{31} = -\frac{1}{2}[1 - j_1(k)]\|w^*\|\sin\alpha + \frac{iv_0^*}{2}k_x j_1(k)(\cos\alpha - 2D_\varphi)\sin\alpha,\\ M_{32} = -M_{23},\\ M_{33} = -\frac{(v_0^*)^2}{16D_\varphi}k_x^2 + \frac{1}{2}(j_1(k) - 1)\cos\alpha + \frac{iv_0^*}{8D_\varphi}k_x\left[\frac{1}{2} + j_1(k)\right]\|w^*\|\cos\alpha. \end{gathered}$$

The general form of the dispersion relations given by solving the third order polynomial of the characteristic equation is a complex and uninformative expression. In order to get the insights about the behavior of the perturbations near the order-disorder transition, we consider some simplified cases (Mishra, Baskaran, and Marchetti 2010).

We first analyze the Vicsek model, which is obtained by setting $\alpha = 0$. We see that the dynamics of the perturbations towards the marginal density function decouples from the one towards the momenta, and we have

$$\lambda_1(k) = M_{33}, \quad \lambda_{2,3}(k) \ = \frac{1}{2}\left(M_{22} \pm \sqrt{M_{22}^2 + 4M_{12}M_{21}}\right).$$

In the long wavelength limit $k_x \to 0+0$, two of the above dispersion relations tend to zero and the third one is always negative. The first one up to the fourth order in k_x reads

$$\lambda_1(k_x) = \frac{3iv_0^*}{16D_\varphi}\|w^*\|k_x - \left(\frac{(v_0^*)^2}{D_\varphi} + (\varrho^*)^2\right)\frac{k_x^2}{16} - \frac{iv_0^*(\varrho^*)^2}{64D_\varphi}\|w^*\|k_x^3 + \frac{(\varrho^*)^4}{384}k_x^4 + \mathcal{O}(k_x^5).$$

The real part of the dispersion relation is negative for small k_x. One could find the condition for the instability as $k_x^2 > \frac{24}{(\varrho^*)^4}\left(\frac{(v_0^*)^2}{D_\varphi} + (\varrho^*)^2\right)$. This condition is satisfied provided $k_x \gg 0$, which is however out of the validity of the approximation. The expansion of the other hydrodynamic mode reads

$$\lambda_2(k_x) = iv_0^*\|w^*\|k_x - \frac{(v_0^*)^2}{2}\left(\frac{9}{128D_\varphi} + \frac{1}{1-2D_\varphi} - 1 - \frac{D_\varphi}{2}\left(4 - \frac{3}{8D_\varphi}\right)^2\right)k_x^2 + \mathcal{O}(k_x^3).$$

One can show that the real part of this dispersion relation is always negative for $D_\varphi < 1/2$. Thus, the second dispersion relation is always stable. As a result, for the Vicsek model with $\alpha = 0$, the synchronized homogeneous solution is always stable against long wavelength perturbations.

This result appears as a contradiction to the one obtained for the classical Vicsek model that was shown to exhibit longitudinal long wavelength instability leading to the emergence of the traveling waves. The explanation for this is the type of the continuum limit we derived and the subsequent requirement to have a normalization in the alignment term. In the limit $\frac{N}{L^2} = \text{const}$ for $N, L \to \infty$, they do not use the normalization by the number of particles in time continuous modifications for the Vicsek model. This is not required during the derivation of the continuum limit because of the assumption $\frac{N}{L^2} = \text{const}$, which allows to handle the alignment term. In our case, we do not use such an assumption. Therefore, in order to keep the alignment term finite in the transition $N \to \infty$, we introduce the normalization by the number of particles.

5.2.3.2 *Transversal Perturbations*

We consider the transversal perturbations of the form $k = (0, k_y)^T$, $\delta\hat{w} = (0, \delta\hat{w}_y)$, i.e., orthogonal to the direction of collective motion. The matrix coefficients the read

$$M_{11} = 0, M_{12} = 0, M_{13} = iv_0^*k_y,$$

$$M_{21} = \|w^*\|\left(\frac{1}{2}[1 + j_1(k)]\cos\alpha - 2j_1(k)D_\varphi\right) + \frac{iv_0^*}{2}k_y j_1(k)(\cos\alpha - 2D_\varphi)\sin\alpha,$$

$$M_{22} = -\frac{(v_0^*)^2}{16D_\varphi}k_y^2 - \left(\frac{1}{2}(j_1(k) + 1)\cos\alpha - 2j_1(k)D_\varphi\right) - \frac{iv_0^*}{8D_\varphi}k_y\left[\frac{1}{2} + j_1(k)\right]\|w^*\|\sin\alpha,$$

$$M_{23} = \frac{1}{2}j_1(k)\sin\alpha + \frac{iv_0^*}{8D_\varphi}k_y\left[\frac{3}{2} + j_1(k)\right]\|w^*\|\cos\alpha,$$

$$M_{31} = \frac{iv_0^*}{2}k_y - \frac{1}{2}[1 - j_1(k)]\|w^*\|\sin\alpha + \frac{iv_0^*}{2}k_y j_1(k)(\cos\alpha - 2D_\varphi)\cos\alpha,$$

$$M_{32} = -M_{23},$$
$$M_{33} = -\frac{(v_0^*)^2}{16D_\varphi}k_y^2 + \frac{1}{2}[j_1(k) - 1]\cos\alpha - \frac{iv_0^*}{8D_\varphi}k_y\left[\frac{1}{2} + j_1(k)\right]\|w^*\|\sin\alpha.$$

First, we consider the simplified case of the zero phase lag $\alpha = 0$, which is again equivalent to the linear Vicsek regime.

The two dispersion relations are then given by

$$\lambda_{1,2}(k_y) = \frac{1}{2}\left(M_{33} \pm \sqrt{M_{33}^2 + 4M_{13}M_{31}}\right).$$

Expanding them to the second order in k_y around $k_y = 0$ reveals

$$\lambda_{1,2}(k_y) = \pm iv_0^*\sqrt{1 - D_\varphi}k_y - \left(\frac{(v_0^*)^2}{D_\varphi} + (\varrho^*)^2\right)\frac{k_y^2}{32} + \mathcal{O}(k_y^3).$$

We see that their real part is always negative. Thus, the solution is also stable against transversal perturbations in the linear Vicsek regime $\alpha = 0$.

5.2.4 *The Traveling Wave Solution*

Next, we are going to test the solutions on the matter of stability. We transform Eq. (4.1.4) into the Fourier space with respect to the spatial variables. Most of the terms are transformed as it was described in the previous section, except for the following term arising after the application of the ansatz Eq. (5.1.13):

$$\begin{aligned}\mathcal{F}\{v(r \times \nabla)\rho\}(k,t) &= iv\frac{2\pi}{L}\mathcal{F}\left\{(k \times r)\rho(r,t)\right\}(k,t)\\ &= iv\pi(k_x - k_y)\hat{\rho}(k_x,k_y,t) + \sum_{\substack{q_y\in\mathbb{Z}\\ k_y\neq q_y}}\frac{vk_x}{k_y - q_y}\hat{\rho}(k_x,q_y,t) - \sum_{\substack{q_x\in\mathbb{Z}\\ k_x\neq q_x}}\frac{vk_y}{k_x - q_x}\hat{\rho}(q_x,k_y,t).\end{aligned}$$

The corresponding term of the momentum equation is treated similarly.

The appearance of the couplings to the function values at other wave vectors except for k hinders the subsequent linear stability analysis we have been developing so far. We will not be able to represent the linearized dynamics of the perturbations using the stability matrix $M = (M_{n,m})_{n,m=1,2,3}$ because the time dynamics of $\hat{\rho}(k)$ and $\hat{w}(k)$ is not a closed system anymore. Theoretically, we could map three Fourier indices n, k_x, and k_y into one index and write down the linearized dynamics of all the perturbations with respect to n, k_x, and k_y together. By doing so, first, we would end up with an infinite hierarchy equations again, which we wanted to circumvent on the first place by using the hydrodynamic theory. Second, the solution of the eigenvalue problem would lose the spatial dependence and we would not be able to obtain the results in the form of the dispersion relations. The hydrodynamic equation for the marginal density function would then become

$$\begin{aligned}\partial_t\hat{\rho}(k) &= iv_0\frac{2\pi}{L}[k \cdot \hat{w}(k)] + iv\pi(k_x - k_y)\hat{\rho}(k_x,k_y)\\ &\quad + \sum_{\substack{q_y\in\mathbb{Z}\\ k_y\neq q_y}}\frac{vk_x}{k_y - q_y}\hat{\rho}(k_x,q_y) - \sum_{\substack{q_x\in\mathbb{Z}\\ k_x\neq q_x}}\frac{vk_y}{k_x - q_x}\hat{\rho}(q_x,k_y).\end{aligned}$$

We see that the spatial scale is influenced by v_0. If we introduce the change of variables $k' = v_0 k$, $\hat{\rho}'(k',t) = \hat{\rho}(k,t)$, $\hat{w}'(k',t) = \hat{w}(k,t)$, we rewrite the equation for the marginal density function as

$$\begin{aligned}\partial_t \hat{\rho}'(k') = i\frac{2\pi}{L}[k' \cdot \hat{w}'(k')] + \frac{iv\pi}{v_0}(k'_x - k'_y)\hat{\rho}'(k'_x, k'_y)\\ + \sum_{\substack{q_y \in \mathbb{Z} \\ k'_y \neq v_0 q_y}} \frac{v k'_x}{k'_y - v_0 q_y}\hat{\rho}'(k'_x, v_0 q_y) - \sum_{\substack{q_x \in \mathbb{Z} \\ k'_x \neq v_0 q_x}} \frac{v k'_y}{k'_x - v_0 q_x}\hat{\rho}'(v_0 q_x, k'_y).\end{aligned}$$

If we restrict ourselves only to small values of the particle velocity $v_0 \ll 1$, we see that the first term of the Fourier transform of $v(r \times \nabla)\rho$ would make the major impact. Therefore, we assume that in the limit of small v_0, that Fourier transform is approximated by

$$\mathcal{F}\{v(r \times \nabla)\rho\}(k,t) \approx iv\pi(k_x - k_y)\hat{\rho}(k_x, k_y, t) \tag{5.2.22}$$

and the respective Fourier transform for the momentum field is approximated similarly. In the rest of the discussion, we follow this assumption.

Finally, the hydrodynamic equations Eq. (4.1.4) in the Fourier space with respect to the spatial variables read

$$\begin{aligned}
&\partial_t \hat{\rho}(k) = iv_0^*[k \cdot \hat{w}(k)] + iv\pi(k_x - k_y)\hat{\rho}(k_x, k_y),\\
&\partial_t \hat{w}(k) = \frac{iv_0^*}{2} k\hat{\rho}(k) - C_1\hat{w}(k) - \frac{(v_0^*)^2}{8}C_2|k|^2\hat{w}(k) + iv\pi(k_x - k_y)\hat{w}(k_x, k_y)\\
&\quad + \sum_{q \in \mathbb{Z}^2}\Bigg\{\frac{\hat{\rho}(q)}{2}Q_{-\alpha}K_1(k-q)\\
&\qquad - \frac{1}{4}C_2\Bigg[\hat{w}(q)K_2(k-q) + \frac{iv_0^*}{2}Q_\alpha\Big\{\hat{w}(q)[q \cdot K_1(k-q)] + \hat{w}_\perp(q)[q \cdot K_{1,\perp}(k-q)]\Big\}\\
&\quad + iv_0^* Q_{-\alpha}\Big\{k[\hat{w}(q) \cdot K_1(k-q)] - \hat{w}(q)[k \cdot K_1(k-q)] - [k \cdot \hat{w}(q)]K_1(k-q)\Big\}\Bigg]\Bigg\},
\end{aligned}$$

where $K_{1,\perp} = (-K_{1,y}, K_{1,x})^T$ and we denote $v_0^* = \frac{2\pi}{L}v_0$ and $\varrho^* = \frac{2\pi}{L}\varrho$ as previous. Note that we suppressed the explicit time dependence of $\hat{\rho}$, $\hat{w}$, K_1, and K_2 for compactness.

If we consider the infinitesimal deviations from a stationary (here, in a moving reference frame) spatially homogeneous solution as

$$\begin{aligned}\delta\hat{\rho}(k,t) = \hat{\rho}(k,t) - \hat{\rho}^*(k),\\ \delta\hat{w}(k,t) = \hat{w}(k,t) - \hat{w}^*(k),\end{aligned}$$

their linearized dynamics read

$$
\begin{aligned}
\partial_t \delta\hat{\rho}(k) &= iv\pi(k_x - k_y)\delta\hat{\rho}(k) + iv_0^*[k \cdot \delta\hat{w}(k)],\\
\partial_t \delta\hat{w}(k) &= \Bigg\{ \frac{iv_0^*}{2}k + \frac{1}{2}[1 - j_1(k)]Q_{-\alpha}w^* \\
&\qquad + \frac{1}{4}j_1(k)C_2\left[2\|w^*\|^2 w^* + iv_0^* Q_{-\alpha}\left(\|w^*\|^2 k - 2(k\cdot w^*)w^*\right)\right]\Bigg\}\delta\hat{\rho}(k)\\
&\quad + \Bigg\{ -C_1 - \frac{(v_0^*)^2}{8}C_2|k|^2 + \frac{1}{2}j_1(k)Q_{-\alpha} + iv\pi(k_x - k_y)I \\
&\qquad - \frac{1}{4}C_2\Bigg[\|w^*\|^2 I + 2j_1(k)(w^*\otimes w^*) + \frac{iv_0^*}{2}Q_\alpha\left[(k\cdot w^*)I + (k\cdot w_\perp^*)Q_{\frac{\pi}{2}}\right]\\
&\qquad + iv_0^*[1 + j_1(k)]Q_{-\alpha}\left[(k\otimes w^*) - (w^*\otimes k) - (k\cdot w^*)I\right]\Bigg]\Bigg\}\delta\hat{w}(k),
\end{aligned}
\tag{5.2.23}
$$

where $\otimes$ denotes the outer product, I is the identity matrix, $Q_{\frac{\pi}{2}} = \begin{pmatrix} 0 & -1 \\ 1 & 0 \end{pmatrix}$, and $j_1(k) = 2J_1\left(\varrho^*|k|\right)/\left(\varrho^*|k|\right)$.

Since the direction of collective motion may be arbitrary, we put $\varphi_0 = 0$ without the loss of generality. To solve the eigenvalue problem for the linearized dynamics, we first need to rewrite these equations in the matrix form:

$$
\partial_t \begin{pmatrix} \delta\hat{\rho} \\ \delta\hat{w}_x \\ \delta\hat{w}_y \end{pmatrix} = M \begin{pmatrix} \delta\hat{\rho} \\ \delta\hat{w}_x \\ \delta\hat{w}_y \end{pmatrix}.
$$

The matrix coefficients are found to be

$$
M_{11} = iv\pi(k_x - k_y), \quad M_{12} = iv_0^* k_x, \quad M_{13} = iv_0^* k_y,
$$

$$
\begin{aligned}
M_{21} = {} & \frac{iv_0^*}{2}k_x + \frac{1}{2}[1 - j_1(k)]\|w^*\|\cos\alpha + (\cos\alpha - 2D_\varphi)j_1(k)\|w^*\|\\
& + \frac{iv_0^*}{4D_\varphi}j_1(k)(\cos\alpha - 2D_\varphi)\big[k_x(2D_\varphi\cos\alpha - v\sin\alpha) + k_y(2D_\varphi\sin\alpha + v\cos\alpha)\big]\\
& - \frac{iv_0^*}{2D_\varphi}(\cos\alpha - 2D_\varphi)j_1(k)k_x(2D_\varphi\cos\alpha - v\sin\alpha),
\end{aligned}
$$

$$
\begin{aligned}
M_{22} = {} & -D_\varphi - \frac{(v_0^*)^2}{4(4D_\varphi^2 + v^2)}|k|^2 D_\varphi + \frac{1}{2}j_1(k)\cos\alpha + iv\pi(k_x - k_y)\\
& - \frac{\cos\alpha - 2D_\varphi}{2} - \frac{j_1(k)}{2(4D_\varphi^2 + v^2)}(2D_\varphi w_x^2 + v w_x w_y)\\
& - \frac{iv_0^*}{8(4D_\varphi^2 + v^2)}\big[(2D_\varphi\cos\alpha + v\sin\alpha)(k\cdot w^*) + (-2D_\varphi\sin\alpha + v\cos\alpha)(k\cdot w_\perp^*)\big]\\
& + \frac{iv_0^*[1 + j_1(k)]}{4(4D_\varphi^2 + v^2)}\big[(2D_\varphi\cos\alpha - v\sin\alpha)(k\cdot w^*) - (2D_\varphi\sin\alpha + v\cos\alpha)(k\cdot w_\perp^*)\big],
\end{aligned}
$$

$$
\begin{aligned}
M_{23} = {} & v - \frac{(v_0^*)^2}{8(4D_\varphi^2 + v^2)}|k|^2 v + \frac{1}{2} j_1(k)\sin\alpha \\
& - \frac{\cos\alpha - 2D_\varphi}{4D_\varphi} v - \frac{j_1(k)}{2(4D_\varphi^2 + v^2)}(2D_\varphi w_x w_y + v w_y^2) \\
& + \frac{iv_0^*}{8(4D_\varphi^2 + v^2)}\big[(2D_\varphi\cos\alpha + v\sin\alpha)(k\cdot w_\perp^*) - (-2D_\varphi\sin\alpha + v\cos\alpha)(k\cdot w^*)\big] \\
& + \frac{iv_0^*[1 + j_1(k)]}{4(4D_\varphi^2 + v^2)}\big[(2D_\varphi\cos\alpha - v\sin\alpha)(k\cdot w_\perp^*) + (2D_\varphi\sin\alpha + v\cos\alpha)(k\cdot w^*)\big], \\
M_{31} = {} & \frac{iv_0^*}{2}k_y - \frac{1}{2}[1 - j_1(k)]\|w^*\|\sin\alpha - \frac{\cos\alpha - 2D_\varphi}{2D_\varphi} v j_1(k)\|w^*\| \\
& - \frac{iv_0^*}{4D_\varphi} j_1(k)(\cos\alpha - 2D_\varphi)\big[k_x(v\cos\alpha + 2D_\varphi\sin\alpha) + k_y(v\sin\alpha - 2D_\varphi\cos\alpha)\big] \\
& + \frac{iv_0^*}{2D_\varphi}(\cos\alpha - 2D_\varphi) j_1(k) k_x (v\cos\alpha + 2D_\varphi\sin\alpha), \\
M_{32} = {} & -v + \frac{(v_0^*)^2}{8(4D_\varphi^2 + v^2)}|k|^2 v - \frac{1}{2} j_1(k)\sin\alpha \\
& + \frac{\cos\alpha - 2D_\varphi}{4D_\varphi} v - \frac{j_1(k)}{2(4D_\varphi^2 + v^2)}(-v w_x^2 + 2D_\varphi w_x w_y) \\
& - \frac{iv_0^*}{8(4D_\varphi^2 + v^2)}\big[(-v\cos\alpha + 2D_\varphi\sin\alpha)(k\cdot w^*) + (v\sin\alpha + 2D_\varphi\cos\alpha)(k\cdot w_\perp^*)\big] \\
& - \frac{iv_0^*[1 + j_1(k)]}{4(4D_\varphi^2 + v^2)}\big[(v\cos\alpha + 2D_\varphi\sin\alpha)(k\cdot w^*) + (-v\sin\alpha + 2D_\varphi\cos\alpha)(k\cdot w_\perp^*)\big], \\
M_{33} = {} & -D_\varphi - \frac{(v_0^*)^2}{4(4D_\varphi^2 + v^2)}|k|^2 D_\varphi + \frac{1}{2} j_1(k)\cos\alpha + iv\pi(k_x - k_y) \\
& - \frac{\cos\alpha - 2D_\varphi}{2} - \frac{j_1(k)}{2(4D_\varphi^2 + v^2)}(-v w_x w_y + 2D_\varphi w_y^2) \\
& + \frac{iv_0^*}{8(4D_\varphi^2 + v^2)}\big[(-v\cos\alpha + 2D_\varphi\sin\alpha)(k\cdot w_\perp^*) - (v\sin\alpha + 2D_\varphi\cos\alpha)(k\cdot w^*)\big] \\
& - \frac{iv_0^*[1 + j_1(k)]}{4(4D_\varphi^2 + v^2)}\big[(v\cos\alpha + 2D_\varphi\sin\alpha)(k\cdot w_\perp^*) - (-v\sin\alpha + 2D_\varphi\cos\alpha)(k\cdot w^*)\big].
\end{aligned}
$$

For the subsequent analysis, we consider two simplified cases. Namely, we investigate the longitudinal and transversal perturbations with respect to the direction of collective motion.

5.2.4.1 *Longitudinal Perturbations*

We consider the longitudinal perturbations of the form $k = (k_x, 0)^T$, $\delta\hat{w} = (\delta\hat{w}_x, 0)^T$ for the flow with the momentum field $w^* = (w_x^*, 0)$. The eigenvalues of the resulting eigenvalue problem are

$$\lambda_\pm = \frac{M_{11} + M_{22} \pm \sqrt{D}}{2},$$

where the discriminant is $D = (M_{11} + M_{22})^2 - 4(M_{11}M_{22} - M_{12}M_{21})$ and the required coefficients of the stability matrix read

$$M_{11} = iv\pi k_x, \quad M_{12} = iv_0^* k_x,$$

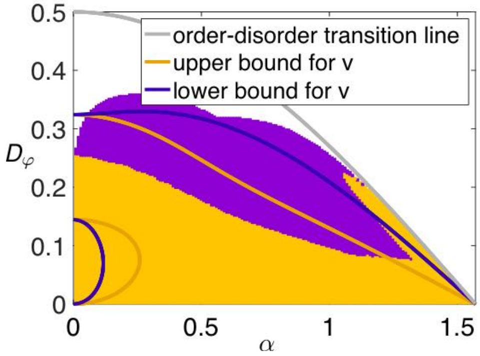

Figure 5.1: Instability regions given by the analysis of the hydrodynamic equations Eq. (4.1.4). The gray line denotes the order-disorder transition line $D_\varphi = \frac{1}{2}\cos\alpha$. The colored lines are found analytically by restricting the analysis to longitudinal perturbations solely. They enclose a line, below which long wavelength perturbations acting on the traveling wave solution appear. The blue (yellow) line is defined by Eq. (5.2.24) with $v = -\sin\alpha$ ($v = -\frac{1}{2}\sin\alpha$). The violet and yellow regions are obtained by numerically solving an eigenvalue problem for Eq. (5.2.23). The violet region includes parameters for which at most one Fourier mode becomes unstable for each wave vector. The yellow region includes parameters for which there are at most two Fourier modes that become unstable for each wave vector. Other parameters are $\tilde{\varrho} = 1$, $\varrho = 0.01$, $v_0 = 0.01$.

$$
\begin{aligned}
M_{21} = {} & \frac{iv_0^*}{2}k_x + \frac{1}{2}(1-j_1)\|w^*\|\cos\alpha \\
& + \frac{\cos\alpha - 2D_\varphi}{4D_\varphi} j_1(k)\Big[4D_\varphi\|w^*\| - iv_0^* k_x(2D_\varphi\cos\alpha - v\sin\alpha)\Big], \\
M_{22} = {} & -D_\varphi - \frac{(v_0^*)^2 k_x^2 D_\varphi}{4(4D_\varphi^2 + v^2)} + \frac{1}{2}j_1(k)\cos\alpha - \left[\frac{1}{2} + j_1(k)\right](\cos\alpha - 2D_\varphi) + iv\pi k_x \\
& - \frac{iv_0^* k_x\|w^*\|}{4(4D_\varphi^2 + v^2)}\left[\frac{1}{2}(2D_\varphi\cos\alpha + v\sin\alpha) - [1 + j_1(k)](2D_\varphi\cos\alpha - v\sin\alpha)\right].
\end{aligned}
$$

One can show that the eigenvalue λ_+ is a hydrodynamic mode since it becomes zero in the limit of small wave numbers, while the other eigenvalue $\lambda_- = -(\cos\alpha - 2D_\varphi)$ is always negative since the condition $D_\varphi < \frac{1}{2}\cos\alpha$ is the existence condition for the given solution. The presence of a hydrodynamic mode might lead to the long wave number instability of the traveling wave solution. It is what we investigate in the following.

Expanding the eigenvalue of the hydrodynamic mode to the second order in k_x around $k_x = 0$, we find

$$
\begin{aligned}
\lambda_+(k_x) = {} & i(v\pi + v_0^*\|w^*\|)k_x \\
& + \frac{(v_0^*)^2}{2}\left[\frac{1}{4D_\varphi}\left(32D_\varphi^2 + D_\varphi\cos\alpha + 8v^2 + \frac{1}{2}v\sin\alpha\right) - \frac{1}{\cos\alpha - 2D_\varphi}\right]k_x^2 + \mathcal{O}(k_x^3).
\end{aligned}
$$

If the long wave length perturbations act on the solution, it is signified by $\mathrm{Re}\lambda_+(k_x) > 0$. Since the group velocity v enters the expression, we cannot draw conclusions about instabilities in the system as such because this parameter is not independent but implicitly depends upon the system parameters. However, we know from the analysis of self-consistent equations Eq. (3.2.17a),Eq. (3.2.17b) that next to the order-disorder transition line the critical group velocity attained along that line is

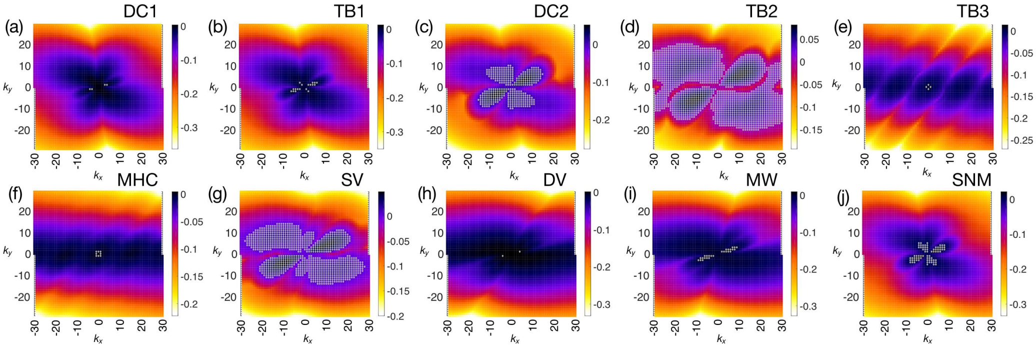

Figure 5.2: Dispersion relations $\lambda(k_x, k_y) = \max\limits_{n \in \mathbb{Z}} \lambda_n(k_x, k_y)$ obtained by solving an eigenvalue problem for Eq. (5.1.19). Grey markers indicate wave vectors, at which there is a Fourier mode with a positive real part. Parameters: $N = 5 \cdot 10^4$, $\tilde{\varrho} = 1$, $v_0 = 0.01$, (a) $\varrho = 0.01, \alpha = 0.78, D_\varphi = 0.2075$, (b) $\varrho = 0.01, \alpha = 0.9, D_\varphi = 0.18$, (c) $\varrho = 0.01, \alpha = 1.3, D_\varphi = 0.06$, (d) $\varrho = 0.01, \alpha = 1.45, D_\varphi = 0.01$, (e) $\varrho = 0.4, \alpha = 1.45, D_\varphi = 0.005$, (f) $\varrho = 0.2, \alpha = 1.36, D_\varphi = 0.005$, (g) $\varrho = 0.01, \alpha = 1.3, D_\varphi = 0.02$, (h) $\varrho = 0.01, \alpha = 1.0, D_\varphi = 0.0375$, (i) $\varrho = 0.01, \alpha = 1.0, D_\varphi = 0.0575$, and (j) $\varrho = 0.01, \alpha = 1.07, D_\varphi = 0.145$.

$v = -\frac{1}{2}\sin\alpha$. Moreover, we know from the analysis of the particle model (see the main text) that the lower bound for the group velocity may be assumed $v = -\sin\alpha$, which is the rate of change of each particles' direction of motion in the case of complete phase synchronization when $D_\varphi \to 0$. Knowing those two bounds, we could guess an approximate boundary of the parameter region, where spatial nonhomogeneities should occur (cf. Fig. 5.1, blue and yellow lines).

The condition for the emergence of the long wave length perturbations in the longitudinal direction (with respect to the direction of collective motion) is given by

$$(\cos\alpha - 2D_\varphi)\left(32D_\varphi^2 + D_\varphi\cos\alpha + 8v^2 + \frac{v}{2}\sin\alpha\right) - 4D_\varphi > 0, \tag{5.2.24}$$

where the group velocity is bounded by $-\sin\alpha < v < -\frac{1}{2}\sin\alpha$ (cf. Fig. 5.1). Recall that the hydrodynamic equations, we are working with, are valid for sufficiently high diffusion levels, i.e., close to the order-disorder transition line. Thus, we see from Fig. 5.1 that the long wavelength perturbations are expected to be observed only for high enough values of α. Moreover, we conclude that the long wavelength perturbations do not arise at the order-disorder transition line.

The last result tells us that there might be the following scenarios for the system behavior. First, at the order-disorder transition line, the traveling wave solution might be stable. Second, at that line, short wavelength perturbations might appear. Third, at that line, long wavelength perturbations transversal to the direction of collective motion might appear. We discard the first case because we know from the kinetic theory that the traveling wave solution is unstable for high enough α at the order-disorder transition line. The analytic confirmation of the existence of short wavelength perturbations seems to be unfeasible since at $D_\varphi = \frac{1}{2}\cos\alpha$, the magnitude of the momentum field, given by Eq. (4.1.5), is proportional $\|w^*\| \propto D_\varphi^{1/2}$ and we cannot perform the respective expansion. Thus, we next look whether we could gain some insight about perturbations transversal to the direction of collective motion.

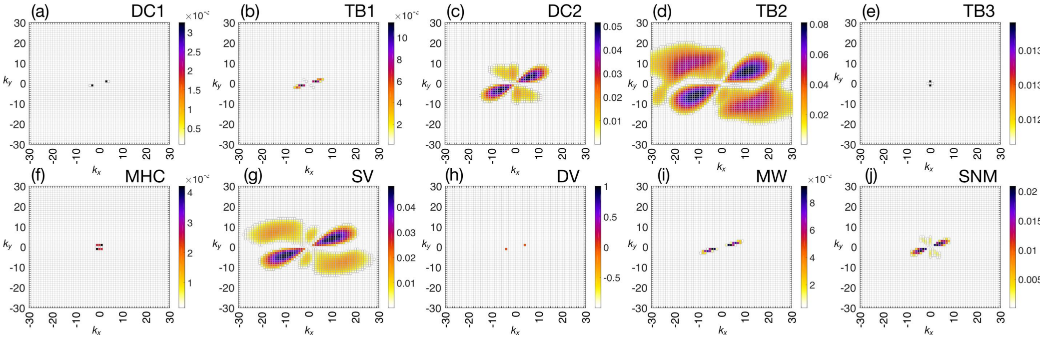

Figure 5.3: Positive real parts of each dispersion relation from Fig. 5.2. Parameters are the same as in Fig. 5.2.

5.2.4.2 *Transversal Perturbations*

We consider the transversal perturbations of the form $k = (0, k_y)^T$, $\delta\hat{w} = (0, \delta\hat{w}_y)$, i.e., orthogonal to the direction of collective motion. The coefficients of the matrix read

$$M_{11} = -iv\pi k_y, \quad M_{13} = iv_0^* k_y,$$

$$\begin{aligned} M_{31} &= \frac{i}{2} v_0^* k_y - \frac{1}{2}[1 - j_1(k)]\|w^*\| \sin\alpha \\ &+ \frac{\cos\alpha - 2D_\varphi}{4D_\varphi} j_1(k)\Big[-2v\|w^*\| + iv_0^* k_y(-v\sin\alpha + 2D_\varphi\cos\alpha)\Big], \end{aligned}$$

$$\begin{aligned} M_{33} = -D_\varphi &- \frac{(v_0^*)^2 k_y^2 D_\varphi}{4(4D_\varphi^2 + v^2)} + \frac{1}{2} j_1(k)\cos\alpha - \frac{1}{2}(\cos\alpha - 2D_\varphi) - iv\pi k_y \\ &+ \frac{iv_0^* k_y \|w^*\|}{4(4D_\varphi^2 + v^2)}\left[\frac{1}{2}(-v\cos\alpha + 2D_\varphi\sin\alpha) - [1 + j_1(k)](v\cos\alpha + 2D_\varphi\sin\alpha)\right]. \end{aligned}$$

The restriction to consider only the perturbations transversal to the direction of collective motion reveals that the dispersion relations are then proportional to the square root of the wave number $\propto \sqrt{k_y}$ in the limit $k_y \to 0$. This fact does not allow us to consider the expansion of the dispersion relations near small wave numbers.

As found previously, close to the order-disorder transition line, we do not observe any instabilities if we restrict ourselves to consider only longitudinal perturbations. However, further away from that line, we have proved that longitudinal perturbations do arise. Because the insight on instability mechanisms of a traveling wave solution is quite limited analytically using the hydrodynamic equations Eq. (4.1.4), we need to solve an eigenvalue problem for the complete system Eq. (5.2.23) numerically. The results of previous analytical studies as well as such a numerical integration can be found in Fig. 5.1. According to the approximation Eq. (5.2.22), we must restrict ourselves to consider small particle velocities. We thus fix $v_0 = 0.01$ and assume $\tilde{\varrho} = 1$ for simplicity. By solving the eigenvalue problem for Eq. (5.2.23) numerically, we obtain dispersion relations $\lambda_n(k_x, k_y) \in \mathbb{C}, n, k_x, k_y \in \mathbb{Z}$. We have considered wave vectors as $k_x, k_y \in [-30, 30]$ without restricting their direction. As a result, in Fig. 5.1, we see that there are indeed spatially nonhomogeneous perturbations acting on Eq. (4.1.5) close to the order-disorder transition line for α sufficiently high. We also see that close to that line, there are two unstable modes. Still, this is quite a limited insight on the structure of the phase diagram. Therefore, at this point, we proceed to the solution of an eigenvalue problem from the kinetic theory, to have a clearer picture of the phase diagram.

5.3 APPLICATION TO SECOND-ORDER ORIENTATIONAL DYNAMICS

In this section, we will derive a Fourier transformed version of Eq. (2.4.23) to be used for the linear stability analysis. First, we introduce the transform with respect to the phase φ. Since it is a periodic variable, i.e., $\varphi \in \mathbb{T}$, this is done via Fourier series

$$f(\varphi, \omega, t) = \sum_{n\in\mathbb{Z}} f_n(\omega, t) e^{-in\varphi},$$

where

$$f_n(\omega, t) = \frac{1}{2\pi} \int_{\mathbb{T}} f(\varphi, \omega, t) e^{in\varphi} \, \mathrm{d}\varphi.$$

By introducing this transform into Eq. (2.4.23) and grouping terms with equivalent exponents, we obtain an infinite hierarchy of evolution equations for Fourier harmonics with respect to phase φ

$$\begin{aligned} \partial_t f_n(\omega, t) &= in\omega f_n(\omega, t) + D_\varphi \partial_{\omega\omega} f_n(\omega, t) \\ &+ \partial_\omega \Big[\xi\omega f_n(\omega, t) + i\sigma\pi e^{-i\alpha} \int_{\mathbb{R}} f_1(\omega', t) \, \mathrm{d}\omega' f_{n-1}(\omega, t) \\ &- i\sigma\pi e^{i\alpha} \int_{\mathbb{R}} f_{-1}(\omega', t) \, \mathrm{d}\omega' f_{n+1}(\omega, t) \Big]. \end{aligned} \tag{5.3.25}$$

Our next step is to perform Fourier transform with respect to angular velocity ω, which is real valued. We introduce the forward transform

$$f_n(k, t) = \frac{1}{\sqrt{2\pi}} \int_{\mathbb{R}} e^{-i\omega k} f_n(\omega, t) \, \mathrm{d}\omega.$$

By applying the forward transform to Eq. (5.3.25), we find the complete Fourier transformed hierarchy of equations to be

$$\begin{aligned} \partial_t f_n(k, t) &= -(n + \xi k) \partial_k f_n(k, t) - k^2 D_\varphi f_n(k, t) \\ &- k\sigma\pi\sqrt{2\pi} \left[e^{-i\alpha} f_1(0, t) f_{n-1}(k, t) - e^{i\alpha} f_{-1}(0, t) f_{n+1}(k, t) \right]. \end{aligned} \tag{5.3.26}$$

The presence of the derivative on the right hand side does not allow to proceed with the linear stability analysis. From now on, we proceed with the goal to perform this analysis numerically. Let us now discretize the Fourier frequency domain as $k_i = i\Delta k, i \in \mathbb{Z}$ with Δk as a small discretization step. By denoting $f_n(k_i, t) = f_{n,i}(t)$, Eq. (5.3.26) reads

$$\begin{aligned} \frac{\mathrm{d}}{\mathrm{d}t} f_{n,i}(t) &= -\frac{n + \xi k_i}{2\Delta k} \left[f_{n,i+1}(t) - f_{n,i-1}(t) \right] - k_i^2 D_\varphi f_{n,i}(t) \\ &- k_i \sigma\pi\sqrt{2\pi} \left[e^{-i\alpha} f_{1,0}(t) f_{n-1,i}(t) - e^{i\alpha} f_{-1,0}(t) f_{n+1,i}(t) \right]. \end{aligned} \tag{5.3.27}$$

Provided that we know a stationary solution $f^*_{n,i}$ to Eq. (5.3.27), we are interested in the behavior of small perturbations towards it. Let $\delta f_{n,i}(t) = f_{n,i}(t) - f^*_{n,i}$ denote such a perturbation. By linearizing Eq. (5.3.27) around the stationary solution $f^*_{n,i}$, we find equations of motion for perturbations to be

$$\begin{aligned} \frac{\mathrm{d}}{\mathrm{d}t} \delta f_{n,i}(t) &\approx -\frac{n + \xi k_i}{2\Delta k} \left[\delta f_{n,i+1}(t) - \delta f_{n,i-1}(t) \right] - k_i^2 D_\varphi \delta f_{n,i}(t) \\ &- k_i \sigma\pi\sqrt{2\pi} \left\{ e^{-i\alpha} \left[f^*_{n-1,i} \delta f_{1,0}(t) + f^*_{1,0} \delta f_{n-1,i}(t) \right] \right. \\ &\left. \qquad - e^{i\alpha} \left[f^*_{n+1,i} \delta f_{-1,0}(t) + f^*_{-1,0} \delta f_{n+1,i}(t) \right] \right\}. \end{aligned} \tag{5.3.28}$$

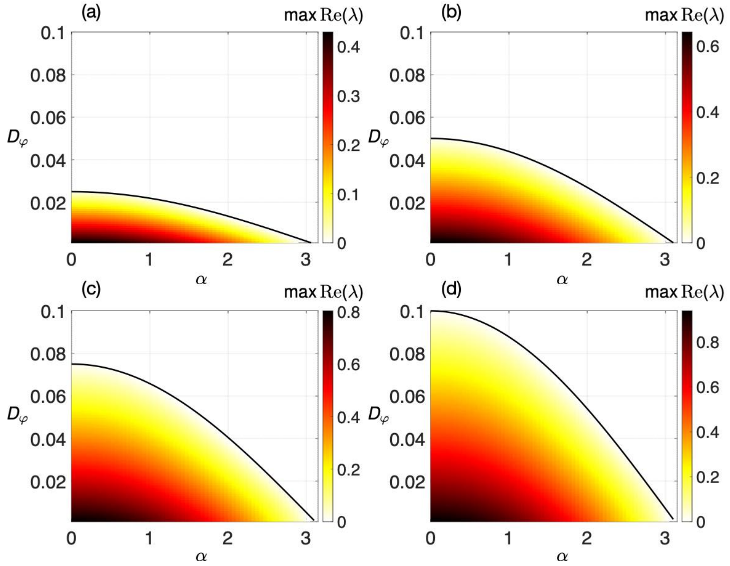

Figure 5.4: Results of the linear stability analysis for the disordered motion Eq. (5.3.29) as a stationary solution to the mean-field PDE. Stability diagrams in the parameter space of the noise strength D_φ and phase lag α show the value of the maximal real part of the strongest unstable mode for (a) $\sigma = 0.5$, (b) $\sigma = 1$, (c) $\sigma = 1.5$, and (d) $\sigma = 2$. The black line denotes the order-disorder transition line $D_\varphi = \frac{1}{2}\sigma\xi\cos(\frac{\alpha}{2})$ found empirically. Other parameters are $\xi = 0.1$, $\sigma = 1$.

5.3.1 *Stability of disordered motion*

For the further analysis, we instantiate stationary solutions. The disordered motion is given by a scaled Gaussian density (see the main text)

$$f(\varphi, \omega) = \frac{1}{(2\pi)^{3/2} s} e^{-\frac{\omega^2}{2s^2}}. \tag{5.3.29}$$

Its Fourier transform with respect to both φ and ω is

$$f^*_{n,i} = f^*_n(k_i) = \frac{1}{(2\pi)^{3/2}} \delta_{n,0} e^{-\frac{s^2 k_i^2}{2}}.$$

Substituting it into Eq. (5.3.28), we observe that both sides of the resulting equations depend on the same Fourier harmonics with respect to the phase, i.e., on the same $n \in \mathbb{Z}$. For example, for $n = 1$ we have

$$\begin{aligned}\frac{\mathrm{d}}{\mathrm{d}t}\delta f_{1,i}(t) \approx &-\frac{1+\xi k_i}{2\Delta k}\left[\delta f_{1,i+1}(t) - \delta f_{1,i-1}(t)\right] \\ &- k_i^2 D_\varphi \delta f_{1,i}(t) - \frac{1}{2} k_i \sigma e^{-i\alpha} e^{-\frac{s^2 k_i^2}{2}}.\end{aligned}$$

We can write this system more compactly as

$$\frac{\mathrm{d}}{\mathrm{d}t}\delta f_{1,i}(t) \approx \sum_{j\in\mathbb{Z}} M_{i,j} \delta f_{1,j}(t),$$

where matrix coefficients are

$$\begin{aligned} M_{i,j} = &-\frac{1+\xi k_i}{2\Delta k}(\delta_{i+1,j}-\delta_{i-1,j}) \\ &- k_i^2 D_\varphi \delta_{i,j} - \frac{1}{2}k_i\sigma e^{-i\alpha} e^{-\frac{s^2 k_i^2}{2}}\delta_{0,j}, \end{aligned}$$

where $\delta_{i,j}$ is the Kronecker delta symbol for $a, b \in \mathbb{Z}$. Similarly, for $n = -1$, the matrix coefficients read

$$\begin{aligned} M_{i,j} = &-\frac{-1+\xi k_i}{2\Delta k}(\delta_{i+1,j}-\delta_{i-1,j}) \\ &- k_i^2 D_\varphi \delta_{i,j} + \frac{1}{2}k_i\sigma e^{i\alpha} e^{-\frac{s^2 k_i^2}{2}}\delta_{0,j} \end{aligned}$$

and for $n \neq \pm 1$ they read

$$M_{i,j} = -\frac{n+\xi k_i}{2\Delta k}(\delta_{i+1,j}-\delta_{i-1,j}) - k_i^2 D_\varphi \delta_{i,j}.$$

Now, we have to solve the eigenvalue problem for the matrix $M = M(n)$ for each mode $n \in \mathbb{Z}$. In practice, we find that the only unstable modes arise for $n = \pm 1$ but for numerical analysis purposes, we take $n = -10, \ldots, 10$. The matrix M is an infinite dimensional matrix and we solve the eigenvalue problem numerically. We restrict the Fourier domain for frequencies to be equal $[-100, 100]$ and take its discretization step $\Delta k = 0.1$. The results can be found in Fig. 5.4 for different values of the coupling strength σ.

6

FINITE VOLUME SCHEMES FOR CONTINUUM LIMIT EQUATIONS

First approaches for the continuum description of active matter were based on symmetry arguments and conservation laws (Bertin, Droz, and Grégoire 2006; Toner, Tu, and Ramaswamy 2005) and described the evolution of hydrodynamic variables, e.g., a marginal density function and a polar order field. This approach allowed to reproduce some of the behavior given by an agent-based description but the resulting equations were not linked to the microscopic parameters, thus, not allowing for the respective analysis of the agent-based behavior. As an alternative, the kinetic theory presents a systematic way to construct a continuum description of an agent system via density functions of agent's positions and velocities (Archer and Rauscher 2004b; Cañizo, J. A. Carrillo, and Rosado 2011; J. A. Carrillo, D'Orsogna, and Panferov 2009; J. A. Carrillo, Fornasier, et al. 2010; J. A. Carrillo, Choi, and Hauray 2014b; J. Carrillo et al. 2014; Lancellotti 2005; Neunzert 1984). Mostly, one is interested in a time evolution of a density function of one agent, which is governed by a nonlinear PDE. As a result, the terms in such a PDE do depend on microscopic parameters from the agent-based model, thus, allowing one to study the continuum limit behavior of a particle system in terms of those parameters.

In this chapter, we are interested in the construction of effective FVMs for numerical integration of PDEs derived as the continuum limit of nonlocally interacting self-propelled particle systems in two dimensions in an overdamped limit (Kruk, J. A. Carrillo, and Koeppl preprint) that takes the following form:

$$\partial_t f(r,\varphi,t) = -v_0 e(\varphi)\cdot\nabla_r f(r,\varphi,t) - \partial_\varphi[w[f](r,\varphi,t) f(r,\varphi,t)] + D_\varphi \partial_{\varphi\varphi} f(r,\varphi,t), \quad (6.0.1)$$

where $r \in \mathbb{R}^2$ is a position vector, $e(\varphi) \in \mathbb{S}^1$ is a unit velocity vector that depends on particle's orientation $\varphi \in \mathbb{R}/(2\pi\mathbb{Z}) =: \mathbb{T}$, $t \in \mathbb{R}_+$ is time, $D_\varphi \in \mathbb{R}_+$ is a rotational diffusion coefficient, $f : \mathbb{R}^2\times\mathbb{T}\times\mathbb{R}_+ \to \mathbb{R}_+$ is a one-particle probability density function which quantifies the probability to find a particle with a position r, orientation φ at time t, w is some functional that represents nonlocal interaction between particles. Besides the high dimensionality of the problem, the presence of the nonlocal interaction requires particular attention to the performance of constructed numerical schemes. Numerical integration of such continuum limit kinetic equations for active matter systems is an ongoing research (Barbaro et al. 2016; J. A. Carrillo, Chertock, and Huang 2015; J. A. Carrillo, Ranetbauer, and Wolfram 2016; Ihle 2013; Pöschel and Schwager 2005; Thüroff, Weber, and Frey 2014). For numerical treatment of general kinetic equations, we refer the reader to (Dimarco and Pareschi 2014).

An important problem in active matter systems is the study of related phase transitions versus model parameters. Its knowledge allows one to analyze, predict, control, and design particle systems with experimentally desirable properties. Depending on the context, one might consider particles of different origins, which in the continuum limit frequently assume polar or nematic representation with polar or nematic interactions (Barbaro et al. 2016; Bertin, Droz, and Grégoire 2009; J. A. Carrillo, Choi, and Pareschi 2019; Degond, Frouvelle, and Liu 2015; Levis, Pagonabarraga, and Liebchen 2019; Nagai et al. 2015; Patelli et al. 2019; Peshkov, Bertin, et al. 2014; Peshkov, Aranson, et al. 2012). Phase transitions are commonly quantified in terms of a polar order parameter. It has been shown that depending on different regimes, one might observe first as well as second order transitions. In the present work, one of our goals is to establish the nature of phase transitions between different states of a model of interest.

6.1 OVERVIEW OF THE CONTINUUM LIMIT FOR A TWO-DIMENSIONAL PARTICLE SYSTEM

When the number of particles becomes large, we look for a continuum description of a particle system. We expect that such a description is more efficient compared to the finite size particle system. The dynamical density functional theory provides a number of ways to derive density functions of particle state variables starting from the Langevin dynamics like Eq. (2.3.13). Even though it is possible to derive continuum limit equations in terms of a joint many-particle density functions, one usually restricts oneself to consider a one-particle density function. For Eq. (2.3.13), we have shown (Kruk, J. A. Carrillo, and Koeppl 2020) using the framework of the FPE (Archer and Rauscher 2004b) that the continuum description of Eq. (2.3.13) with macroscopic scaling (Kipnis and Landim 1998a) is given by a one-particle probability density function evolving according to the Vlasov-Fokker-Planck (Dobrushin 1979; Risken and Frank 1996) equation

$$\partial_t f(r,\varphi,t) = -v_0 e(\varphi)\cdot\nabla_r f(r,\varphi,t) - \partial_\varphi\left[w[f](r,\varphi,t)f(r,\varphi,t)\right] + D_\varphi\partial_{\varphi\varphi}f(r,\varphi,t) \quad (6.1.2)$$

subject to an initial condition:

$$f(r,\varphi,0) = f_0(r,\varphi), \quad f_0(r,\varphi)\geq 0, \quad \int_\Omega f_0(r,\varphi)\,\mathrm{d}r\mathrm{d}\varphi = 1. \quad (6.1.3)$$

The density function $f(r,\varphi,t)$ quantifies the probability to find a particle at a given position $r\in\mathbb{U}^2$ with a given orientation $\varphi\in\mathbb{T}$ at time t. As before, $e(\varphi) = (\cos\varphi,\sin\varphi)\in\mathbb{S}^1$ is a unit vector in the direction of self-propulsion φ. Note that $\nabla_r = (\partial_x,\partial_y)$ denotes a spatial gradient. The rotational velocity or torque exerted by a nonlocal neighborhood is found to be

$$w[f](r,\varphi,t) = \frac{\sigma}{|C(r;\varrho)|}\int_{C(r;\varrho)} f(r',\varphi',t)\sin(\varphi'-\varphi-\alpha)\,\mathrm{d}r'\mathrm{d}\varphi'. \quad (6.1.4)$$

The region of nonlocal interaction is now defined as a cylinder

$$C(r;\varrho) = \left\{(r',\varphi')\in\mathbb{U}^2\times\mathbb{T} \mid \|r-r'\|\leq\varrho\right\}\subset\Omega.$$

The size of the nonlocal neighborhood, which is quantified via $|B^i_\varrho|$ in (2.3.13), is now measured as

$$|C(r;\varrho)| = \int_{C(r;\varrho)} f(r',\varphi',t)\,\mathrm{d}r'\mathrm{d}\varphi'. \quad (6.1.5)$$

One should keep in mind that in general this neighborhood mass is time-dependent but we usually omit this dependence for the sake of compactness.

Eq. (6.1.4) determines the polarization of a particle flow around a given point (up to a phase shift α). This can be formulated by introducing an interaction kernel $K(r,\varphi) = H_\varrho(r)\sin(\varphi+\alpha)$, which is a product of a Heaviside step function $H_\varrho(r) = H(\varrho-\|r\|)$, which ensures that only a particle flow within the distance ϱ is accounted for, and a shifted alignment function. We can therefore express the rotational velocity functional in a more general form as

$$w[f](r,\varphi,t) = -\frac{\sigma}{|C(r;\varrho)|}\left[K(r,\varphi)*f(r,\varphi,t)\right](r,\varphi,t).$$

Whereas this functional form of the angular velocity $w[f](r,\varphi,t)$ does not change the dynamics of the one-particle density function, the convolutional form of the alignment interaction allows for a substantial decrease of temporal complexity of numerical algorithms by means of the discrete Fourier transform (Press et al. 2002).

We observe that by writing the diffusion term as $\partial_{\varphi\varphi} f = \partial_\varphi (f \partial_\varphi \log f)$, we can combine the last two terms in Eq. (6.1.2) in the form of a gradient flow as

$$-\partial_\varphi \{ [w[f](r,\varphi,t) - D_\varphi \partial_\varphi \ln f(r,\varphi,t)] f(r,\varphi,t) \} =: \partial_\varphi [\partial_\varphi \xi[f](r,\varphi,t) f(r,\varphi,t)]. \quad (6.1.6)$$

The new functional ξ denotes the potential function of the flow in the angular direction. However, we cannot extend this form to all the right hand side of Eq. (6.1.2) unless we design a system to be spatially homogeneous. For the latter case, we use a gradient flow structure in the construction of a numerical scheme.

One of the transitions we are interested to investigate is the one in terms of the polarization of a particle flow. This is commonly measured using the global polar order parameter defined as

$$R(t) e^{i\Theta(t)} = \int_\Omega e^{i\varphi} f(r,\varphi,t) \, \mathrm{d}r \mathrm{d}\varphi. \quad (6.1.7)$$

Here, the absolute value R gives the aforementioned measure while the phase Θ can be interpreted as a mean direction of the particle flow. If the flow is completely synchronized so that a φ-marginal of f is a point mass density, the magnitude equals its maximal value $R = 1$. If the flow is uniformly distributed so that $f = \text{const}$, the magnitude equals its minimal value $R = 0$. For any partially synchronized solution with respect to the angular variable φ, the order parameter magnitude assumes intermediate values $R \in (0,1)$. Note that in general the right hand side of (6.1.7) must be normalized but since we consider f as a probability density, the normalization term equals one. In the following, when referring to the order parameter, we will often refer to its magnitude R since it provides the main structural information about the particle flow.

The global polar order parameter Eq. (6.1.7) provides a global information about the momentum field, which is not enough in a spatially nonhomogeneous context. From the continuum PDE Eq. (6.1.2), we see that it is worthwhile to consider a nonlocalized version of Eq. (6.1.7) as

$$R(r,t) e^{i\Theta(r,t)} = \frac{1}{|C(r;\varrho)|} \int_{C(r;\varrho)} e^{i\varphi} f(r,\varphi,t) \, \mathrm{d}r \mathrm{d}\varphi. \quad (6.1.8)$$

One can show that in terms of such a nonlocal polar order field, the PDE Eq. (6.1.2) becomes

$$\begin{aligned} \partial_t f(r,\varphi,t) &= -v_0 e(\varphi) \cdot \nabla_r f(r,\varphi,t) \\ &\quad - \sigma R(r,t) \partial_\varphi \left[\sin(\Theta(r,t) - \varphi - \alpha) f(r,\varphi,t) \right] + D_\varphi \partial_{\varphi\varphi} f(r,\varphi,t). \end{aligned}$$

The presence of the magnitude R in front of the angular flux emphasizes that the rotational rate of change of a particle flow is proportional to the polarization at that point.

6.1.1 *Spatially homogeneous formulation*

It is straightforward to check that any constant function satisfies Eq. (6.1.2). But since we are interested in probability density functions in Ω as its solutions, we find

$$f(r,\varphi,t) = \frac{1}{2\pi}. \quad (6.1.9)$$

In terms of a particle system, this uniform density function corresponds to the chaotic behavior of the system with particles uniformly distributed in $\mathbb{U}^2$ having orientations uniformly distributed in $\mathbb{T}$. One also says that this solution represents a globally disordered or incoherent state.

In order to find solutions except for the trivial one, we note that the model Eq. (6.1.2) admits a major simplification if we assume that the solutions are spatially homogeneous, i.e., $f(r, \varphi, t) = f(\varphi, t)$. Under that assumption, equation Eq. (6.1.2) simplifies to a (1+1)-dimensional PDE, which we can also consider as the continuum Kuramoto-Sakaguchi model (Sakaguchi and Kuramoto 1986) with diffusion:

$$\partial_t f(\varphi, t) = -\partial_\varphi \left[w[f](\varphi, t) f(\varphi, t) \right] + D_\varphi \partial_{\varphi\varphi} f(\varphi, t), \tag{6.1.10}$$

where the nonlocal interaction term Eq. (6.1.4) becomes a global one

$$w[f](\varphi, t) = \sigma \int_{\mathbb{T}} f(\varphi', t) \sin(\varphi' - \varphi - \alpha) \, \mathrm{d}\varphi'$$

with the neighborhood mass omitted since $|C| = \int_{\mathbb{T}} f(\varphi, t) \, \mathrm{d}\varphi = 1$. We shall consider Eq. (6.1.10) with an initial condition:

$$f(\varphi, 0) = f_0(\varphi), \quad f_0(\varphi) \geq 0, \quad \int_{\mathbb{T}} f_0(\varphi) \, \mathrm{d}\varphi = 1. \tag{6.1.11}$$

Note that this equation is of a gradient form $\partial_t f = \partial_\varphi (f \partial_\varphi \xi)$ with the potential $\xi[f](\varphi, t) = -\sigma \int_{\mathbb{T}} \cos(\varphi' - \varphi - \alpha) f(\varphi', t) \, \mathrm{d}\varphi' + D_\varphi \ln f(\varphi, t)$. In the absence of rotations, i.e., $\alpha = 0$, the free energy associated to equation Eq. (6.1.10) is given by (Villani 2003)

$$E[f](t) = -\frac{\sigma}{2} \int_{\mathbb{T}} (\cos * f)(\varphi, t) f(\varphi, t) \, \mathrm{d}\varphi + D_\varphi \int_{\mathbb{T}} f(\varphi, t) \ln f(\varphi, t) \, \mathrm{d}\varphi.$$

We can therefore represent Eq. (6.1.10) in a general gradient flow structure $\partial_t f = \partial_\varphi \left(f \partial_\varphi \frac{\delta E[f]}{\delta f} \right)$. Moreover, one can show that this energy functional decays along solutions of Eq. (6.1.10) according to

$$\frac{\mathrm{d}E}{\mathrm{d}t}[f](t) = -\int_{\mathbb{T}} (\partial_\varphi \xi)^2 f(\varphi, t) \, \mathrm{d}\varphi.$$

However, for chiral interactions with $|\alpha| > 0$, the interaction potential is not symmetric and we cannot write down a respective Liapunov functional. Therefore, we will not consider the free energy dissipation of the constructed numerical schemes as in (J. A. Carrillo, Choi, and Pareschi 2019).

The Kuramoto model is well-known nowadays and it is often used to model synchronization phenomena in various systems (Acebrón et al. 2005; J. A. Carrillo, Gvalani, et al. 2020; Kuramoto 1984; Pikovsky, Rosenblum, and Kurths 2003b). It was discovered in (Kuramoto and Battogtokh 2002) that the addition of a phase lag parameter α to the model allows one to obtain a new type of solutions, termed chimera states (Abrams and S. H. Strogatz 2004), where both synchronized and disordered populations of oscillators coexist. We showed in (Kruk, Maistrenko, and Koeppl 2018) that by extending an oscillator model to a self-propelled particle model, we can obtain such chimera states with and without spatial homogeneity. It appears that for spatially homogeneous states in the continuum limit with noise, we can find a closed form expression for a corresponding density function.

We note that for spatially homogeneous systems nonlocal Eq. (6.1.8) and global Eq. (6.1.7) polar order parameters become equal

$$R(t) e^{i\Theta(t)} = \int_{\mathbb{T}} e^{i\varphi} f(\varphi, t) \, \mathrm{d}\varphi \tag{6.1.12}$$

and one can write the rotational velocity functional Eq. (6.1.4) in terms of this polar order parameter as

$$w[f](\varphi, t) = \sigma R(t) \sin(\Theta(t) - \varphi - \alpha).$$

First, we look for stationary solutions of Eq. (6.1.10). Noting that this equation is invariant under phase translations $f(\varphi, t) \mapsto f(\varphi + \varphi_0, t) \quad \forall \varphi_0 \in \mathbb{T}$, we may put $\Theta = 0$ without loss of generality. Therefore, we find the following condition for stationary solutions

$$D_\varphi \frac{\mathrm{d}^2 f(\varphi)}{\mathrm{d}\varphi^2} = -\sigma R \frac{\mathrm{d}}{\mathrm{d}\varphi} \left[\sin(\varphi + \alpha) f(\varphi)\right]. \tag{6.1.13}$$

To solve this equation, we integrate it once and look for a solution in the form

$$f(\varphi) = c(\varphi) \exp[\gamma \cos(\varphi + \alpha)],$$

where the function $c(\varphi)$ is to be determined from the ODE and $\gamma = \sigma R / D_\varphi$. We find that the solution is

$$f(\varphi) = c_1 \exp[\gamma \cos(\varphi + \alpha)] \left(1 + c_2 \int \exp[-\gamma \cos(\varphi + \alpha)] \mathrm{d}\varphi\right),$$

where c_1, c_2 are constants to be determined. The first constant is given by the periodicity $f(0) = f(2\pi)$, which can be shown to hold if and only if $c_2 = 0$. Next, from the normalization condition $\int_{\mathbb{T}} f(\varphi, t) \, \mathrm{d}\varphi = 1$, we find that $c_1 = (2\pi I_0(\gamma))^{-1}$, where $I_0(\gamma) = 1/(2\pi) \int_{\mathbb{T}} \exp(\gamma \cos \varphi) \mathrm{d}\varphi$ denotes the modified Bessel function of the first kind (Olver et al. 2010). As a result, we have found a nontrivial stationary solution of the form

$$f(\varphi) = \frac{\exp[\gamma \cos(\varphi + \alpha)]}{2\pi I_0(\gamma)}. \tag{6.1.14}$$

In such a form, the solution is not particularly useful since the density function is recursively contained in the definition of the order parameter Eq. (6.1.12). However, we are able to determine the latter the other way. If we multiply Eq. (6.1.14) by $\cos \varphi$ and integrate over the domain $\mathbb{T}$, we find that

$$R = \frac{1}{2\pi I_0(\gamma)} \int_{\mathbb{T}} e^{\gamma \cos(\varphi + \alpha)} e^{i\varphi} \mathrm{d}\varphi = e^{-i\alpha} \frac{I_1(\gamma)}{I_0(\gamma)}.$$

Since we are looking for a nontrivial solution with $R \neq 0$, we conclude that $\alpha = 0$ and the stationary solution is

$$f(\varphi) = \frac{\exp[\gamma \cos \varphi]}{2\pi I_0(\gamma)}, \tag{6.1.15}$$

for which the order parameter magnitude satisfies

$$R = \frac{I_1\left(\frac{\sigma R}{D_\varphi}\right)}{I_0\left(\frac{\sigma R}{D_\varphi}\right)}. \tag{6.1.16}$$

This result tells us that stationary states are possible only in the absence of the phase lag, i.e., in the form of irrotational motion. We refer to (J. A. Carrillo, Choi, and Pareschi 2019) for the detailed analysis of such states.

Our next step is to investigate solutions to Eq. (6.1.3) in the presence of a nonzero phase lag α. By noting that in this case the particle flow moves uniformly either to the left or to the right depending on the sign of α, we are looking for solutions in the form of a traveling wave. We introduce an ansatz $f(\varphi, t) = g(\varphi - vt) = g(\omega)$, where v is the speed of the traveling wave, which is unknown. After this substitution, the compatibility condition Eq. (6.1.13) for stationary solutions becomes

$$D_\varphi \frac{\mathrm{d}^2}{\mathrm{d}\omega^2} g(\omega) = -\frac{\mathrm{d}}{\mathrm{d}\omega}\left\{\left[v + \sigma R \sin(\omega + \alpha)\right] g(\omega)\right\} = 0, \tag{6.1.17}$$

Integrating it with respect to ω yields

$$D_\varphi \frac{\mathrm{d}}{\mathrm{d}\omega} g(\omega) + \left[v + \sigma R \sin(\omega + \alpha)\right] g(\omega) = c_1,$$

where $c_1 \in \mathbb{R}$ is some constant. Solving this equation, we find the solution to be

$$g(\omega) = \exp\left[-\frac{v}{D_\varphi}\omega + \frac{\sigma R}{D_\varphi}\cos(\omega + \alpha)\right]\left(c_1 \int \exp\left[\frac{v}{D_\varphi}\omega' - \frac{\sigma R}{D_\varphi}\cos(\omega' + \alpha)\right] \mathrm{d}\omega' + c_2\right),$$

where $c_2 \in \mathbb{R}$ is some constant. One of the constants is fixed due to the periodicity constraint, i.e., $g(0) = g(2\pi)$. Namely, this implies

$$c_2 = \exp\left(-\frac{v}{D_\varphi}2\pi\right)\left(c_1 \int_{\mathbb{T}} \exp\left[\frac{v}{D_\varphi}\omega' - \frac{\sigma R}{D_\varphi}\cos(\omega' + \alpha)\right] \mathrm{d}\omega' + c_2\right).$$

This subsequently implies

$$c_1 = \frac{c_2\left(\exp\left(\frac{v}{D_\varphi}2\pi\right) - 1\right)}{\int_{\mathbb{T}} \exp\left[\frac{v}{D_\varphi}\omega' - \frac{\sigma R}{D_\varphi}\cos(\omega' + \alpha)\right] \mathrm{d}\omega'}.$$

Next, due to the normalization condition $\int_{\mathbb{T}} g(\omega)\, \mathrm{d}\omega = 1$, we put $c_2 = c_0$ as a normalization constant and find (Gupta, Campa, and Ruffo 2014a)

$$\begin{aligned} g(\omega) = c_0 \exp\left[-\frac{v}{D_\varphi}\omega + \frac{\sigma R}{D_\varphi}\cos(\omega + \alpha)\right] \times& \\ \times \left(1 + \left(e^{2\pi\frac{v}{D_\varphi}} - 1\right)\frac{\int_0^\omega \exp\left[\frac{v}{D_\varphi}\omega' - \frac{\sigma R}{D_\varphi}\cos(\omega' + \alpha)\right] \mathrm{d}\omega'}{\int_{\mathbb{T}} \exp\left[\frac{v}{D_\varphi}\omega' - \frac{\sigma R}{D_\varphi}\cos(\omega' + \alpha)\right] \mathrm{d}\omega'}\right)&. \end{aligned} \tag{6.1.18}$$

This defines a profile of the traveling wave solution $f(\varphi, t) = g(\varphi - vt) = g(\omega)$. One may apply the ansatz backwards in order to obtain the complete form $f(\varphi, t)$ of the solution of Eq. (6.1.10) but for the subsequent numerical analysis, we will use its profile solely. We refer to (Kruk, J. A. Carrillo, and Koeppl 2020) for other forms of this traveling wave solution.

Lemma 6.1.1. *Let f be a smooth solution to Eqs.* (6.1.10) *to* (6.1.11). *Then we have*

$$\begin{aligned} \dot{R}(t) = \sigma R(t)\Big(\cos\alpha \int_{\mathbb{T}} \sin^2(\Theta(t) - \varphi) f(\varphi, t)\, \mathrm{d}\varphi& \\ - \frac{1}{2}\sin\alpha \int_{\mathbb{T}} \sin(2(\Theta(t) - \varphi)) f(\varphi, t)\, \mathrm{d}\varphi\Big)& - D_\varphi R(t). \end{aligned}$$

In particular, if diffusion is higher than a threshold value $D_\varphi \geq D_\varphi^* = \sigma(\cos\alpha + \frac{1}{2}\sin|\alpha|)$ for $|\alpha| \leq \frac{\pi}{2}$, then $\dot{R} \leq 0$ for all $t \geq 0$.

Proof. From the definition of the spatially homogeneous polar order parameter (6.1.12), we can write

$$R(t) = \int_{\mathbb{T}} \cos(\varphi - \Theta(t)) f(\varphi, t)\, \mathrm{d}\varphi, \qquad \int_{\mathbb{T}} \sin(\varphi - \Theta(t)) f(\varphi, t)\, \mathrm{d}\varphi = 0.$$

By differentiating the first equation, we find

$$\begin{aligned}\dot{R}(t) &= \dot{\Theta}(t) \int_{\mathbb{T}} \sin(\varphi - \Theta(t)) f(\varphi, t)\, \mathrm{d}\varphi + \int_{\mathbb{T}} \cos(\varphi - \Theta(t)) \partial_t f(\varphi, t)\, \mathrm{d}\varphi \\ &= \sigma R(t) \int_{\mathbb{T}} \sin(\Theta(t) - \varphi) \sin(\Theta(t) - \varphi - \alpha) f(\varphi, t)\, \mathrm{d}\varphi - D_\varphi R(t) \\ &= \sigma R(t) \Big(\cos\alpha \int_{\mathbb{T}} \sin^2(\Theta(t) - \varphi) f(\varphi, t)\, \mathrm{d}\varphi \\ &\qquad - \frac{1}{2} \sin\alpha \int_{\mathbb{T}} \sin(2(\Theta(t) - \varphi)) f(\varphi, t)\, \mathrm{d}\varphi \Big) - D_\varphi R(t).\end{aligned}$$

□

6.2 PHASE SPACE DISCRETIZATION

Our main goal is to develop a finite volume scheme that reproduces a correct behavior of nonlocally interacting particle flow governed by a 3+1 dimensional integro-differential PDE Eq. (6.1.2). Given that we have much more background on a spatially homogeneous system Eq. (6.1.10), we first introduce a one-dimensional finite volume scheme, i.e., for density functions of an angular variable. We next proceed to the description of a complete three-dimensional scheme that is applied to density functions of spatial and angular variables. For both proposed methods, we prove mass and positivity preservation as well as derive CFL conditions on their stability.

The approach we are going to pursue is the following. First, we perform a phase-space discretization of a PDE of interest, thereby deriving a semidiscrete system of ODE for finite volume cells. We derive the set of equations on uniform meshes but the generalization to nonuniform ones is straightforward. Afterwards, by noting that the dynamics of a velocity field in spatial and angular directions qualitatively differs, we attempt a dimensionality splitting technique in order to effectively cope with the dynamics changes due to spatial and angular fluxes. As a result, we obtain a FVM that is second order accurate both in time and in phase-space variables.

6.2.1 *One-dimensional scheme for spatially homogeneous PDEs*

In this section, we develop a finite volume scheme for continuum limit PDEs under the assumption of spatial homogeneity, i.e., for equation of the form Eq. (6.1.10). Let $\mathbb{T}_L = \{0, \ldots, L-1\}$ denote a discreet one-dimensional torus with L points. We divide a domain $\mathbb{T}$ into finite volume cells $C_k = [\varphi_{k-\frac{1}{2}}, \varphi_{k+\frac{1}{2}}], k \in \mathbb{T}_L$ of a uniform length $\Delta\varphi = 2\pi/L$ with the center of a cell $\varphi_k = k\Delta\varphi$, which correspond to a site k in the torus $\mathbb{T}_L$. Note that since the space is periodic, we have $\varphi_k = \varphi_{k+L}, k \in \mathbb{T}_L$.

We define the cell averages (J. A. Carrillo, Chertock, and Huang 2015) $f_k : \mathbb{T}_L \times \mathbb{R}_+ \to \mathbb{R}$ of a solution to a PDE to be

$$f_k(t) = \frac{1}{\Delta\varphi} \int_{C_k} f(\varphi, t) \mathrm{d}\varphi.$$

The cell averages f_k are functions of time but for the sake of compactness, we will henceforth omit the explicit time dependence of the computed quantities.

The semidiscrete finite volume scheme is obtained by integrating the PDE Eq. (6.1.10) over each cell $C_k, k \in \mathbb{T}_L$. It is consequently formulated as the following system of ODEs for the cell averages:

$$\frac{d}{dt} f_k = -\frac{F^{\varphi}_{k+\frac{1}{2}} - F^{\varphi}_{k-\frac{1}{2}}}{\Delta\varphi}, \tag{6.2.19}$$

where $F^{\varphi}_{k\pm\frac{1}{2}}$ denote angular fluxes. Note that the right hand side of this expression is a second order centered difference of an original flux. In order to find the numerical approximations of the above fluxes at cell interfaces, we need to be able to compute the corresponding values of a solution itself as well as a velocity field. In this paper, we adopt a piecewise linear reconstruction of the numerical solution $f(\varphi, t)$ at each time point. Saying that, we represent a density function in each cell as a first order polynomial as

$$\tilde{f}(\varphi, t) = f_k(t) + (\partial_\varphi f)_k(\varphi - \varphi_k), \quad \varphi \in C_k, \tag{6.2.20}$$

where $(\partial_\varphi f)_k$ is a cell average of a partial derivative with respect to φ, which is to be determined for this reconstruction to work. The knowledge of values of a solution at neighboring cell centers allows us to approximate the slopes $(\partial_\varphi f)_k$ using a second order centered difference method:

$$(\partial_\varphi f)_k = \frac{f_{k+1} - f_{k-1}}{2\Delta\varphi}.$$

Unfortunately, it might occur that this slope approximation might lead to negative values of a reconstructed numerical solution Eq. (6.2.20), which we intent to circumvent. For such cases, we recalculate the slope by imposing a slope limiter that keeps reconstructed values nonnegative. In this paper, we chose to use a generalized minmod limiter

$$(\partial_\varphi f)_k = \operatorname{minmod}\left(\theta\frac{f_{k+1} - f_k}{\Delta\varphi}, \frac{f_{k+1} - f_{k-1}}{2\Delta\varphi}, \theta\frac{f_k - f_{k-1}}{\Delta\varphi}\right),$$

defined as follows

$$\operatorname{minmod}(a, b, c) := \begin{cases} \min(a, b, c) & a > 0, b > 0, c > 0, \\ \max(a, b, c) & a < 0, b < 0, c < 0, \\ 0 & \text{otherwise.} \end{cases} \tag{6.2.21}$$

Note that the values, which are corrected with this slope limiter, are generally of first order. However, in all numerical tests we present in this paper, it is practically not imposed and the numerical scheme stays effectively of second order in $\Delta\varphi$.

At this point, the piecewise linear reconstruction is defined and we can apply Eq. (6.2.20) in the calculation of numerical fluxes, required in Eq. (6.2.19). First, we need to know the values of a solution at each cell interface. They are computed as

$$f^{\mathrm{T}}_k = \tilde{f}(\varphi_{k+\frac{1}{2}}{-0}) = f_k + \frac{\Delta\varphi}{2}(\partial_\varphi f)_k, \quad f^{\mathrm{B}}_k = \tilde{f}(\varphi_{k-\frac{1}{2}}{+0}) = f_k - \frac{\Delta\varphi}{2}(\partial_\varphi f)_k, \tag{6.2.22}$$

where $f(\varphi_{k+\frac{1}{2}}{-0})$ and $f(\varphi_{k-\frac{1}{2}}{+0})$ denote function values at cell interfaces $\varphi_{k+\frac{1}{2}}$ and $\varphi_{k-\frac{1}{2}}$ from inside a cell C_k, respectively. We use the cell interface values to define the numerical fluxes in Eq. (6.2.19) as upwind fluxes as

$$F^{\varphi}_{k+\frac{1}{2}} = w^{+}_{k+\frac{1}{2}} f^{\mathrm{T}}_k + w^{-}_{k+\frac{1}{2}} f^{\mathrm{B}}_{k+1}, \tag{6.2.23}$$

where positive and negative parts of angular velocities are denoted by

$$w^+_{k+\frac{1}{2}} = \max(w_{k+\frac{1}{2}}, 0), \quad w^-_{k+\frac{1}{2}} = \min(w_{k+\frac{1}{2}}, 0). \tag{6.2.24}$$

The exact velocities themselves are given in the PDE Eq. (6.1.10) but need to be numerically approximated at cell interfaces. We note that the PDE is of a gradient flow structure, i.e., we can write $w[f](\varphi, t) = -\partial_\varphi \xi[f](\varphi, t)$ for some potential function ξ, as we showed in Eq. (6.1.6), and we use this fact to define velocities at cell interfaces using a second order centered difference method as

$$w_{k+\frac{1}{2}} = -\frac{\xi_{k+1} - \xi_k}{\Delta\varphi}. \tag{6.2.25}$$

The velocity potential for a homogeneous system is defined as

$$\xi[f](\varphi, t) = -\sigma \int_{\mathbb{T}} f(\varphi', t) \cos(\varphi' - \varphi - \alpha) \mathrm{d}\varphi' + D_\varphi \ln, f(\varphi, t),$$

therefore, it's numerical approximation proceeds as follows

$$\begin{aligned}
&\int_{\mathbb{T}} f(\varphi') \cos(\varphi' - \varphi - \alpha) \mathrm{d}\varphi' \\
&= \sum_{n \in \mathbb{T}_L} \int_{C_n} [f_n + (\partial_\varphi f)_n (\varphi' - \varphi_n)] \cos(\varphi' - \varphi_k - \alpha) \mathrm{d}\varphi' \\
&= \sum_{n \in \mathbb{T}_L} f_n \int_{\varphi_{n-\frac{1}{2}}}^{\varphi_{n+\frac{1}{2}}} \cos(\varphi' - \varphi_k - \alpha) \mathrm{d}\varphi' \\
&\quad + \sum_{n \in \mathbb{T}_L} (\partial_\varphi f)_n \int_{\varphi_{n-\frac{1}{2}}}^{\varphi_{n+\frac{1}{2}}} (\varphi' - \varphi_n) \cos(\varphi' - \varphi_k - \alpha) \mathrm{d}\varphi' \\
&= \sum_{n \in \mathbb{T}_L} f_n \left(2 \sin \frac{\Delta\varphi}{2}\right) \cos(\varphi_n - \varphi_k - \alpha) \\
&\quad + \sum_{n \in \mathbb{T}_L} (\partial_\varphi f)_n \left(\Delta\varphi \cos \frac{\Delta\varphi}{2} - 2 \sin \frac{\Delta\varphi}{2}\right) \sin(\varphi_n - \varphi_k - \alpha).
\end{aligned}$$

As a result, we have obtained the following representation of an approximated velocity potential, which is to be used in Eq. (6.2.25), as

$$\begin{aligned}
\xi_k = -\frac{\sigma}{\sum_{n \in \mathbb{T}_L} f_n} \sum_{n \in \mathbb{T}_L} \Bigg[& f_n \left(\frac{\sin \frac{\Delta\varphi}{2}}{\frac{\Delta\varphi}{2}}\right) \cos(\varphi_n - \varphi_k - \alpha) \\
& + (\partial_\varphi f)_n \sin(\varphi_n - \varphi_k - \alpha) \left(\cos \frac{\Delta\varphi}{2} - \frac{\sin \frac{\Delta\varphi}{2}}{\frac{\Delta\varphi}{2}}\right)\Bigg] + D_\varphi \ln f_k,
\end{aligned}$$

where we have used the fact that since f is a probability density function, its piecewise linear reconstruction yields $\int_{\mathbb{T}} \tilde{f}(\varphi, t) \mathrm{d}\varphi = \sum_{n \in \mathbb{T}_L} f_n \Delta\varphi$. We note that the above approximation of the velocity potential is exact in $\Delta\varphi$ given a piecewise linear reconstruction of a density function.

Theorem 6.2.1. *Consider the IVP Eqs.* (6.1.10) *to* (6.1.11) *with periodic boundaries and the semidiscrete FVM Eq.* (6.2.19) *with a positivity-preserving piecewise linear reconstruction Eq.* (6.2.20). *Assume that the system of ODEs Eq.* (6.2.19) *is discretized by the forward Euler method or by* *a higher-order strong stability preserving (SSP) ODE solver, whose time step can be expressed as a convex combination of several forward Euler steps. Then, computed cell averages remain nonnegative* $f_k(t) \geq 0 \; \forall k \in \mathbb{T}_L \; \forall t > 0$, *provided that the following CFL condition is satisfied:*

$$\Delta t \leq \frac{\Delta\varphi}{2c},$$

where $c = \max_{k \in \mathbb{T}_L} \left\{ w^+_{k+\frac{1}{2}}, -w^-_{k+\frac{1}{2}} \right\}$ *and the velocities at cell interfaces are defined in Eq.* (6.2.25).

Proof. According to the forward Euler method, we discretize Eq. (6.2.19) as

$$f_k(t+\Delta t) = f_k(t) - \frac{\Delta t}{\Delta\varphi}\left(F^{\varphi}_{k+\frac{1}{2}} - F^{\varphi}_{k-\frac{1}{2}}\right).$$

We note that we can express cell averages of a solution as a linear combination of corresponding values at cell interfaces, defined in Eq. (6.2.22), as

$$f_k = \frac{1}{2}\left(f^{\mathrm{T}}_k + f^{\mathrm{B}}_k\right).$$

Using this fact and expressing numerical fluxes as upwind fluxes introduced in Section 6.2.1, we have

$$f_k(t+\Delta t) = \frac{1}{2}\left(f^{\mathrm{T}}_k + f^{\mathrm{B}}_k\right) - \frac{\Delta t}{\Delta\varphi}\left(w^+_{k+\frac{1}{2}} f^{\mathrm{T}}_k + w^-_{k+\frac{1}{2}} f^{\mathrm{B}}_{k+1} - w^+_{k-\frac{1}{2}} f^{\mathrm{T}}_{k-1} - w^-_{k-\frac{1}{2}} f^{\mathrm{B}}_k\right).$$

Now we group the terms according to cell interface values and find

$$f_k(t+\Delta t) = \left(\frac{1}{2} - \frac{\Delta t}{\Delta\varphi} w^+_{k+\frac{1}{2}}\right) f^{\mathrm{T}}_k + \left(\frac{1}{2} + \frac{\Delta t}{\Delta\varphi} w^-_{k-\frac{1}{2}}\right) f^{\mathrm{B}}_k + \frac{\Delta t}{\Delta\varphi} w^+_{k-\frac{1}{2}} f^{\mathrm{T}}_{k-1} - \frac{\Delta t}{\Delta\varphi} w^-_{k+\frac{1}{2}} f^{\mathrm{B}}_{k+1}.$$

The last two terms are always nonnegative. To guarantee positivity preservation of $f_k(t+\Delta t)$, we must require that the values in parentheses of the first two terms remain nonnegative. This yields the following conditions:

$$\frac{\Delta t}{\Delta\varphi} w^+_{k+\frac{1}{2}} \leq \frac{1}{2}, \quad \frac{\Delta t}{\Delta\varphi} w^-_{k-\frac{1}{2}} \geq -\frac{1}{2},$$

the combination of which gives the desired CFL condition. □

Theorem 6.2.2. *Consider the IVP Eqs.* (6.1.10) *to* (6.1.11) *with periodic boundaries. Given the semidiscrete FVM Eq.* (6.2.19) *with a piecewise linear reconstruction Eq.* (6.2.20), *the mass of the discretized system is conserved, i.e.,*

$$\frac{d}{dt}\int_{\mathbb{T}} f(\varphi, t)\mathrm{d}\varphi = 0.$$

Proof. By the piecewise linear reconstruction Eq. (6.2.20), we have

$$\begin{aligned}\frac{d}{dt}\int_{\mathbb{T}} f(\varphi, t)\,\mathrm{d}\varphi &= \frac{d}{dt}\sum_{k\in\mathbb{T}_L}\int_{C_k} \tilde{f}(\varphi, t)\,\mathring{d}\varphi = \frac{d}{dt}\sum_{k\in\mathbb{T}_L}\int_{C_k} f_k + (\partial_\varphi f)_k(\varphi - \varphi_k)\,\mathrm{d}\varphi \\ &= \frac{d}{dt}\sum_{k\in\mathbb{T}_L}\int_{C_k} f_k\,\mathrm{d}\varphi = \frac{d}{dt}\sum_{k\in\mathbb{T}_L} f_k\Delta\varphi = -\sum_{k\in\mathbb{T}_L}\left(F^{\varphi}_{k+\frac{1}{2}} - F^{\varphi}_{k-\frac{1}{2}}\right).\end{aligned}$$

Due to the periodicity of the domain, we have

$$\sum_{k\in\mathbb{T}_L} F^{\varphi}_{k-\frac{1}{2}} = \sum_{k=0}^{L-1} F^{\varphi}_{k-\frac{1}{2}} = \sum_{k=1}^{L} F^{\varphi}_{k+\frac{1}{2}} = \sum_{k=0}^{L-1} F^{\varphi}_{k+\frac{1}{2}} = \sum_{k\in\mathbb{T}_L} F^{\varphi}_{k+\frac{1}{2}}.$$

As a direct consequence, we obtain $\frac{d}{dt}\int_{\mathbb{T}} f(\varphi,t)\mathrm{d}\varphi = 0$ so that the mass of the numerical system is conserved. □

Numerical studies of spatially homogeneous PDEs Eq. (6.1.10) using the finite volume scheme of this section are conducted in Sections 6.4.2-6.4.5. In the following, we generalize the scheme for general spatially nonhomogeneous three-dimensional PDEs Eq. (6.1.2).

6.2.2 *Three-dimensional scheme for spatially nonhomogeneous PDEs*

We start from the discretization of a phase space Ω into finite volume cells. Dimensions corresponding to x, y, and φ variables are divided into N, M, and L cells, respectively. Linear sizes of cells are $\Delta x = 1/N$, $\Delta y = 1/M$, and $\Delta\varphi = 2\pi/L$. Let $\mathbb{U}_N$, $\mathbb{U}_M$, and $\mathbb{T}_L$ denote discreet one-dimensional tori with $N, M, L \in \mathbb{N}$ points, respectively, i.e., $\mathbb{U}_N = \{0,\dots,N-1\}$, $\mathbb{U}_M = \{0,\dots,M-1\}$, $\mathbb{T}_L = \{0,\dots,L-1\}$. We define a uniform grid consisting of cells $C_{i,j,k} = [x_{i-\frac{1}{2}}, x_{i+\frac{1}{2}}] \times [y_{j-\frac{1}{2}}, y_{j+\frac{1}{2}}] \times [\varphi_{k-\frac{1}{2}}, \varphi_{k+\frac{1}{2}}]$ with cell centers $(x_i, y_j, \varphi_k) = (i\Delta x, j\Delta y, k\Delta\varphi), i \in \mathbb{U}_N, j \in \mathbb{U}_M, k \in \mathbb{T}_L$. Due to the periodic boundaries, we have $x_{N+i} = x_i$, $y_{M+j} = y_j$, and $\varphi_{L+k} = \varphi_k$.

The discretization of Ω consists of three-dimensional cells which can be enumerated with a three-dimensional torus as

$$\Omega_{N,M,L} = \{(i,j,k) \mid i \in \mathbb{U}_N, j \in \mathbb{U}_M, k \in \mathbb{T}_L\}.$$

Sites of the torus $(i,j,k) \in \Omega_{N,M,L}$ correspond to the points $(x_i, y_j, \varphi_k) = (i\Delta x, j\Delta y, k\Delta\varphi) \in \Omega$ of the original space. Points of the original space $(x, y, \varphi) \in \Omega$ correspond to the sites $([x/\Delta x], [y/\Delta y], [\varphi/\Delta\varphi]) \in \Omega_{N,M,L}$ of the torus, where [] stands for the integer part.

We define cell averages (J. A. Carrillo, Chertock, and Huang 2015) $f_{i,j,k} : \Omega_{N,M,L} \times \mathbb{R}_+ \to \mathbb{R}$ of solutions to PDEs Eq. (6.1.2) to be

$$f_{i,j,k}(t) = \frac{1}{\Delta x\Delta y\Delta\varphi}\iiint_{C_{i,j,k}} f(x,y,\varphi,t)\mathrm{d}x\mathrm{d}y\mathrm{d}\varphi.$$

As before, for the sake of compactness, we will omit the dependence of most computed quantities on time t henceforth.

The semidiscrete finite volume scheme for a three-dimensional system is obtained by integrating the PDE Eq. (6.1.2) over each cell $C_{i,j,k}$, $(i,j,k) \in \Omega_{N,M,L}$ and is formulated by the following system of ODEs for $f_{i,j,k}$

$$\frac{d}{dt}f_{i,j,k} = -\frac{F^x_{i+\frac{1}{2},j,k} - F^x_{i-\frac{1}{2},j,k}}{\Delta x} - \frac{F^y_{i,j+\frac{1}{2},k} - F^y_{i,j-\frac{1}{2},k}}{\Delta y} - \frac{F^{\varphi}_{i,j,k+\frac{1}{2}} - F^{\varphi}_{i,j,k-\frac{1}{2}}}{\Delta\varphi},$$

for $i \in \mathbb{U}_N$, $j \in \mathbb{U}_M$, and $k \in \mathbb{T}_L$.

In order to define the above fluxes, we extend the same piecewise linear reconstruction method from the previous section. The numerical solution in each cell $C_{i,j,k}$ is thus approximated as a polynomial

$$\tilde{f}(x,y,\varphi) = f_{i,j,k} + (\partial_x f)_{i,j,k}(x-x_i) + (\partial_y f)_{i,j,k}(y-y_j) + (\partial_\varphi f)_{i,j,k}(\varphi-\varphi_k),\ (x,y,\varphi) \in C_{i,j,k}.$$

To be able to use this representation, we need to find each slope $(\partial_x f)_{i,j,k}$, $(\partial_y f)_{i,j,k}$, and $(\partial_\varphi)_{i,j,k}$. To ensure that the solution is second-order accurate, we define the slopes using the centered difference approximations

$$(\partial_x f)_{i,j,k} = \frac{f_{i+1,j,k} - f_{i-1,j,k}}{2\Delta x}, \quad (\partial_y f)_{i,j,k} = \frac{f_{i,j+1,k} - f_{i,j-1,k}}{2\Delta y},$$
$$(\partial_\varphi f)_{i,j,k} = \frac{f_{i,j,k+1} - f_{i,j,k-1}}{2\Delta\varphi}.$$

It might occur that a reconstructed solution becomes negative in some cell $C_{i,j,k}$. In such cases, we recalculate a corresponding slope using a slope limiter. In this paper, we use a generalized minmod limiter Eq. (6.2.21), whose application yields

$$\begin{aligned}
(\partial_x f)_{i,j,k} &= \operatorname{minmod}\left(\theta\frac{f_{i+1,j,k} - f_{i,j,k}}{\Delta x}, \frac{f_{i+1,j,k} - f_{i-1,j,k}}{2\Delta x}, \theta\frac{f_{i,j,k} - f_{i-1,j,k}}{\Delta x}\right),\\
(\partial_y f)_{i,j,k} &= \operatorname{minmod}\left(\theta\frac{f_{i,j+1,k} - f_{i,j,k}}{\Delta y}, \frac{f_{i,j+1,k} - f_{i,j-1,k}}{2\Delta y}, \theta\frac{f_{i,j,k} - f_{i,j-1,k}}{\Delta y}\right),\\
(\partial_\varphi f)_{i,j,k} &= \operatorname{minmod}\left(\theta\frac{f_{i,j,k+1} - f_{i,j,k}}{\Delta\varphi}, \frac{f_{i,j,k+1} - f_{i,j,k-1}}{2\Delta\varphi}, \theta\frac{f_{i,j,k} - f_{i,j,k-1}}{\Delta\varphi}\right),
\end{aligned}$$

We note again that the values, which are corrected with such a limiter, become of first order in a corresponding dimension. But since the number of such points is usually small compared to the total number of grid points, the overall order of the scheme is effectively not reduced. In the numerical tests of this paper, these slope limiters have practically not been triggered.

Now that the piecewise linear reconstruction Section 6.2.2 is completely determined, we are able to compute solution values at each cell interface the following way:

$$\begin{aligned}
f^{\mathrm{E}}_{i,j,k} &= \tilde{f}(x_{i+\frac{1}{2}}-0, y_j, \varphi_k) = f_{i,j,k} + \frac{\Delta x}{2}(\partial_x f)_{i,j,k},\\
f^{\mathrm{W}}_{i,j,k} &= \tilde{f}(x_{i-\frac{1}{2}}+0, y_j, \varphi_k) = f_{i,j,k} - \frac{\Delta x}{2}(\partial_x f)_{i,j,k},\\
f^{\mathrm{N}}_{i,j,k} &= \tilde{f}(x_i, y_{j+\frac{1}{2}}-0, \varphi_k) = f_{i,j,k} + \frac{\Delta y}{2}(\partial_y f)_{i,j,k},\\
f^{\mathrm{S}}_{i,j,k} &= \tilde{f}(x_i, y_{j-\frac{1}{2}}+0, \varphi_k) = f_{i,j,k} - \frac{\Delta y}{2}(\partial_y f)_{i,j,k},\\
f^{\mathrm{T}}_{i,j,k} &= \tilde{f}(x_i, y_j, \varphi_{k+\frac{1}{2}}-0) = f_{i,j,k} + \frac{\Delta\varphi}{2}(\partial_\varphi f)_{i,j,k},\\
f^{\mathrm{B}}_{i,j,k} &= \tilde{f}(x_i, y_j, \varphi_{k-\frac{1}{2}}+0) = f_{i,j,k} - \frac{\Delta\varphi}{2}(\partial_\varphi f)_{i,j,k},
\end{aligned}\tag{6.2.26}$$

where $\tilde{f}(x_{i\pm\frac{1}{2}} \pm 0, y_j, \varphi_k)$, $\tilde{f}(x_i, y_{j\pm\frac{1}{2}} \pm 0, \varphi_k)$, and $\tilde{f}(x_i, y_j, \varphi_{k\pm\frac{1}{2}} \pm 0)$ denote reconstructed solution values at cell interfaces from inside the current cell.

We compute all fluxes in the semidiscrete system of ODEs Section 6.2.2 as upwind fluxes as

$$\begin{aligned}
F^x_{i+\frac{1}{2},j,k} &= u^+_{i+\frac{1}{2},j,k} f^{\mathrm{E}}_{i,j,k} + u^-_{i+\frac{1}{2},j,k} f^{\mathrm{W}}_{i+1,j,k},\\
F^y_{i,j+\frac{1}{2},k} &= v^+_{i,j+\frac{1}{2},k} f^{\mathrm{N}}_{i,j,k} + v^-_{i,j+\frac{1}{2},k} f^{\mathrm{S}}_{i,j+1,k},\\
F^\varphi_{i,j,k+\frac{1}{2}} &= w^+_{i,j,k+\frac{1}{2}} f^{\mathrm{T}}_{i,j,k} + w^-_{i,j,k+\frac{1}{2}} f^{\mathrm{B}}_{i,j,k+1},
\end{aligned}\tag{6.2.27}$$

where $u^\pm_{i+\frac{1}{2},j,k}$, $v^\pm_{i,j+\frac{1}{2},k}$, and $w^\pm_{i,j,k+\frac{1}{2}}$ denote positive and negative parts of velocities defined as before according to Eq. (6.2.24). The definition of upwind fluxes required the knowledge of velocities at cell interfaces. For advection in spatial directions, they are directly obtained from the PDE Eq. (6.1.2) by direct substitution of grid points:

$$u_{i+\frac{1}{2},j,k} = u(x_{i+\frac{1}{2}}, y_j, \varphi_k) = \cos\varphi_k, \quad v_{i,j+\frac{1}{2},k} = v(x_i, y_{j+\frac{1}{2}}, \varphi_k) = \sin\varphi_k. \tag{6.2.28}$$

For the angular direction, we again use the gradient flow structure of the angular subflow and consider the last two terms in the PDE Eq. (6.1.2) as defined by a velocity potential $\xi[f](r,\varphi,t)$ Eq. (6.1.6). One can show, that for a spatially nonhomogenous system, it reads

$$\xi[f](r,\varphi,t) = -\sigma\frac{\iiint_{C(r;\varrho)} f(r',\varphi',t)\cos(\varphi'-\varphi-\alpha)\mathrm{d}r'\mathrm{d}\varphi'}{\iiint_{C(r;\varrho)} f(r',\varphi',t)\mathrm{d}r'\mathrm{d}\varphi'} + D_\varphi \ln f(r,\varphi,t). \tag{6.2.29}$$

We thus determine the angular velocity at cell interfaces from its potential using a second order centered difference scheme

$$w_{i,j,k+\frac{1}{2}} = -\frac{\xi_{i,j,k+1} - \xi_{i,j,k}}{\Delta\varphi}. \tag{6.2.30}$$

Now, we need to perform the discretization of the potential Eq. (6.2.29) using the piecewise linear reconstruction of the solution (6.2.2). First, the numerator for $\xi_{i,j,k}$ is calculated as

$$\begin{aligned}
&\iiint_{C(r_{i,j};\varrho)} \tilde{f}(r',\varphi')\cos(\varphi'-\varphi_k-\alpha)\mathrm{d}r'\mathrm{d}\varphi' = \\
&= \sum_{(l,m,n)\in C_{N,M,L}(r_{i,j};\varrho)} \iiint_{C_{l,m,n}} [f_{l,m,n} + (\partial_x f)_{l,m,n}(x'-x_l) + (\partial_y f)_{l,m,n}(y'-y_m) \\
&\qquad + (\partial_\varphi f)_{l,m,n}(\varphi'-\varphi_n)]\cos(\varphi'-\varphi_k-\alpha)\mathrm{d}x'\mathrm{d}y'\mathrm{d}\varphi' \\
&= \sum_{(l,m,n)\in C_{N,M,L}(r_{i,j};\varrho)} f_{l,m,n}\Delta x\Delta y \int_{\varphi_{n-\frac{1}{2}}}^{\varphi_{n+\frac{1}{2}}} \cos(\varphi'-\varphi_k-\alpha)\mathrm{d}\varphi' \\
&\qquad + \sum_{(l,m,n)\in C_{N,M,L}(r_{i,j};\varrho)} (\partial_\varphi f)_{l,m,n}\Delta x\Delta y \int_{\varphi_{n-\frac{1}{2}}}^{\varphi_{n+\frac{1}{2}}} (\varphi'-\varphi_n)\cos(\varphi'-\varphi_k-\alpha)\mathrm{d}\varphi' \\
&= \sum_{(l,m,n)\in C_{N,M,L}(r_{i,j};\varrho)} f_{l,m,n}\Delta x\Delta y \left(2\sin\frac{\Delta\varphi}{2}\right)\cos(\varphi_n-\varphi_k-\alpha) \\
&\qquad + \sum_{(l,m,n)\in C_{N,M,L}(r_{i,j};\varrho)} (\partial_\varphi f)_{l,m,n}\Delta x\Delta y \left(\Delta\varphi\cos\frac{\Delta\varphi}{2} - 2\sin\frac{\Delta\varphi}{2}\right)\sin(\varphi_n-\varphi_k-\alpha),
\end{aligned}$$

where $r_{i,j} = (x_i, y_j)$ and summations run over $C_{N,M,L}(r_{i,j};\varrho) = \{(l,m,n) \in \Omega_{N,M,L} \mid (x_i - x_l)^2 + (y_j - y_m)^2 \leq \varrho^2\}$. Second, the denominator takes the form

$$\begin{aligned}
\iiint_{C(r_{i,j};\varrho)} f(r',\varphi')\mathrm{d}r'\mathrm{d}\varphi' &= \sum_{(l,m,n)\in C_{N,M,L}(r_{i,j};\varrho)} \iiint_{C_{l,m,n}} f(r',\varphi')\mathrm{d}r'\mathrm{d}\varphi' \\
&= \sum_{(l,m,n)\in C_{N,M,L}(r_{i,j};\varrho)} f_{l,m,n}\Delta x\Delta y\Delta\varphi.
\end{aligned}$$

As a result, we find the discretized velocity potential $\xi_{i,j,k}$, which is to be used in Eq. (6.2.30), to read

$$
\begin{aligned}
\xi_{i,j,k} = &-\frac{\sigma}{\sum_{(l,m,n)\in C_{N,M,L}(r_{i,j};\varrho)} f_{l,m,n}} \times \\
&\times \sum_{(l,m,n)\in C_{N,M,L}(r_{i,j};\varrho)} \Bigg[f_{l,m,n} \left(\frac{\sin\frac{\Delta\varphi}{2}}{\frac{\Delta\varphi}{2}} \right) \cos(\varphi_n - \varphi_k - \alpha) \\
&+ (\partial_\varphi f)_{l,m,n} \sin(\varphi_n - \varphi_k - \alpha) \left(\cos\frac{\Delta\varphi}{2} - \frac{\sin\frac{\Delta\varphi}{2}}{\frac{\Delta\varphi}{2}} \right) \Bigg] + D_\varphi \ln f_{i,j,k},
\end{aligned}
$$

which is exact in Δx, Δy, and $\Delta\varphi$.

Theorem 6.2.3. *Consider the IVP Eqs.* (6.1.2) *to* (6.1.3) *with periodic boundaries and the semidiscrete FVM Section 6.2.2 with a positivity-preserving piecewise linear reconstruction Section 6.2.2. Assume that the system of ODEs Section 6.2.2 is discretized by the forward Euler method or by a higher-order SSP ODE solver, whose time step can be expressed as a convex combination of several forward Euler steps. Then, computed cell averages remain nonnegative* $f_{i,j,k} \geq 0\ \forall i \in \mathbb{U}_N, \forall j \in \mathbb{U}_M, \forall k \in \mathbb{T}_L, \forall t > 0$, *provided that the following CFL condition is satisfied:*

$$\Delta t \leq \min\left\{ \frac{\Delta x}{6a}, \frac{\Delta y}{6b}, \frac{\Delta\varphi}{6c} \right\}$$

with the coefficients $a = \max\limits_{(i,j,k)\in\Omega_{N,M,L}} \left\{ u^{+}_{i+\frac{1}{2},j,k}, -u^{-}_{i+\frac{1}{2},j,k} \right\}$, $b = \max\limits_{(i,j,k)\in\Omega_{N,M,L}} \left\{ v^{+}_{i,j+\frac{1}{2},k}, -v^{-}_{i,j+\frac{1}{2},k} \right\}$, $c = \max\limits_{(i,j,k)\in\Omega_{N,M,L}} \left\{ w^{+}_{i,j,k+\frac{1}{2}}, -w^{-}_{i,j,k+\frac{1}{2}} \right\}$ *and the velocities at cell interfaces are defined in Eqs.* (6.2.28) *to* (6.2.30).

Proof. The proof of this theorem follows the same lines as in Theorem 6.2.1. We only comment that in this case, one should express cell averages of a solution $f_{i,j,k}$ as a linear combination of corresponding values at cell interfaces, defined in Eq. (6.2.26), as

$$f_{i,j,k} = \frac{1}{6}\left(f^{\mathrm{E}}_{i,j,k} + f^{\mathrm{W}}_{i,j,k} + f^{\mathrm{N}}_{i,j,k} + f^{\mathrm{S}}_{i,j,k} + f^{\mathrm{T}}_{i,j,k} + f^{\mathrm{B}}_{i,j,k} \right).$$

□

Theorem 6.2.4. *Consider the IVP Eq.* (6.1.2)*-Eq.* (6.1.3) *with periodic boundaries. Given the semidiscrete FVM Section 6.2.2 with a piecewise linear reconstruction Section 6.2.2, the mass of the discretized system is conserved, i.e.,*

$$\frac{d}{dt}\int_{\Omega} f(r,\varphi,t)\ \mathrm{d}r\mathrm{d}\varphi = 0.$$

Proof. By the periodicity of the domain in all directions, the proof of this theorem follows the same lines as in Theorem 6.2.2. □

Numerical studies of spatially nonhomogeneous PDEs Eq. (6.1.2) using the finite volume scheme of this section are conducted in Sections 6.4.7-6.4.8. Up to now, we have presented the second order discretization of the phase space of the problem keeping the time domain continuous. This way, we have formulated the problems of solving PDEs Eq. (6.1.2) and Eq. (6.1.10) as the problems of solving systems of ODEs Section 6.2.2 and Eq. (6.2.19), respectively. In the next section, we consider approaches to perform time discretization so as to keep the FVM of second order in time as well.

6.3 DIMENSIONALITY SPLITTING

This section considers further discretization approaches for three-dimensional PDEs only. As a result of the phase space discretization from the previous section, we reformulate the IVP for PDEs Eq. (6.1.2)-Eq. (6.1.3) as the IVP for the system of ODEs Section 6.2.2, which we state here for convenience:

$$\frac{d}{dt}f_{i,j,k}(t) = -\frac{F^x_{i+\frac{1}{2},j,k} - F^x_{i-\frac{1}{2},j,k}}{\Delta x} - \frac{F^y_{i,j+\frac{1}{2},k} - F^y_{i,j-\frac{1}{2},k}}{\Delta y} - \frac{F^\varphi_{i,j,k+\frac{1}{2}} - F^\varphi_{i,j,k-\frac{1}{2}}}{\Delta \varphi} \tag{6.3.31}$$

with $f_{i,j,k}(0) = (f_0)_{i,j,k}$ for $(i,j,k) \in \Omega_{N,M,L}$ and the fluxes are as defined in the previous section. From the PDE Eq. (6.1.2) itself and from the derivation of the system of ODEs Eq. (6.3.31), we have seen that the fluxes qualitatively differ for spatial and angular dimensions. Therefore, it might become unreasonable to tackle all of them at once. We will employ this fact in the further construction of our FVM.

The class of methods that allow us to separate dynamics of an autonomous system of ODEs into several subsystems is known as splitting methods (Hairer, Lubich, and G. Wanner 2002). In this paper, we are interested in such splitting methods that lead to the second order accuracy in time. First, we note the following. We can reenumerate the three-dimensional grid of the problem, which is enumerated with three-dimensional indices from $\Omega_{N,M,L}$, with one-dimensional indices ranging from 0 to NML. In other words, the three-dimensional set of indices $\Omega_{N,M,L}$ can be bijectively mapped into a one-dimensional set with NML indices. This allows us to express the above model shortly as

$$\frac{d}{dt}\bar{f}(t) = F(\bar{f}), \quad \bar{f}(0) = \bar{f}_0, \tag{6.3.32}$$

where $\bar{f} = (f_0, \ldots, f_{NML-1}) \in \mathbb{R}^{NML}_+$. We note that we can separate the vector field on the right hand side as

$$\frac{d}{dt}\bar{f}(t) = F^{[1]}(\bar{f}) + F^{[2]}(\bar{f}), \tag{6.3.33}$$

where $F^{[1]}$ and $F^{[2]}$ are defined by spatial and angular fluxes from Eq. (6.3.31), respectively. Now, according to the splitting procedure, instead of the problem Eq. (6.3.33), we consider two subproblems:

$$\frac{d}{dt}\bar{f} = F^{[1]}(\bar{f}) \quad \text{and} \quad \frac{d}{dt}\bar{f} = F^{[2]}(\bar{f}). \tag{6.3.34}$$

Let $\phi^{[i]}_t : \mathbb{R}^{NML}_+ \to \mathbb{R}^{NML}_+, i = 1, 2$ be dynamical flows generated by vector fields $F^{[i]}, i = 1, 2$ (Guckenheimer and Holmes 1990; M. Hirsch, Smale, and Devaney 2004), respectively. If we know exact flows with respect to $F^{[1]}$ and $F^{[2]}$, we could attempt to construct a numerical scheme of the form $\Phi_{\Delta t} = \phi^{[1]}_{\Delta t} \circ \phi^{[2]}_{\Delta t}$, which is known as the Lie-Trotter splitting. However, this formula is only first order accurate. If we also consider the adjoint of the previous method given by $\Phi^*_{\Delta t} = \phi^{[2]}_{\Delta t} \circ \phi^{[1]}_{\Delta t}$ and build the composition of Φ and Φ^* with halved step sizes, we obtain by the theorem of the composition of methods (Hairer, Lubich, and G. Wanner 2002), a new method

$$\Phi_{\Delta t} = \phi^{[1]}_{\Delta t/2} \circ \phi^{[2]}_{\Delta t} \circ \phi^{[1]}_{\Delta t/2},$$

which is known as the Strang (Marchuk) splitting. The Strang splitting formula is of order 2. However, for that technique to work, we must be able to integrate two subproblems Eq. (6.3.34) exactly, which is usually not the case. Therefore, our aim is to obtain a second order method which consists of the composition of approximate direct methods only.

To start with, we consider the case, where one of the flows can be computed exactly, let's say $\phi^{[1]}_{\Delta t}$, and the other one is computed with some p-th order scheme $\Phi^{[2]}_{\Delta t}$. We can state the following

Proposition 6.3.1. *Consider the splitting method and its adjoint defined as*

$$\Phi_{\Delta t} = \phi^{[1]}_{\Delta t} \circ \Phi^{[2]}_{\Delta t}, \quad \Phi^{*}_{\Delta t} = \Phi^{[2]*}_{\Delta t} \circ \phi^{[1]}_{\Delta t}, \tag{6.3.35}$$

where $\phi^{[1]}_{\Delta t}$ *is an exact flow and* $\Phi^{[2]}_{\Delta t}$ *is an approximate numerical flow of order* $p \geq 1$*. For every* $p \geq 1$*, the splitting methods* Φ *and* Φ^* *are first order accurate.*

Proof. Consider the splitting method $\Phi_{\Delta t}$. Let us denote approximate and exact solutions to subproblems Eq. (6.3.34) using respective dynamical flows as $\bar{f}_1(\Delta t) = \Phi^{[2]}_{\Delta t}(\bar{f}_1(0))$ if $\bar{f}_1(0) = \bar{f}_0$ and $\bar{f}_2(\Delta t) = \phi^{[1]}_{\Delta t}(\bar{f}_2(0))$ if $\bar{f}_2(0) = \bar{f}_1(\Delta t)$. On one hand, by Taylor decomposition of the numerical flow around $\Delta t = 0$, we have

$$\bar{f}_1(\Delta t) = \bar{f}_0 + F^{[2]}(\bar{f}_0)\Delta t + \frac{1}{2} F^{[2]'} F^{[2]}(\bar{f}_0)\Delta t^2 + \mathcal{O}(\Delta t^3),$$

where $F^{[2]'}$ is the Jacobian and $\mathcal{O}(\Delta t^3)$ contains higher order terms. Similarly, we find for the exact flow

$$\begin{aligned}
\bar{f}_2(\Delta t) &= \bar{f}_1(\Delta t) + F^{[1]}(\bar{f}_1(\Delta t))\Delta t + \frac{1}{2} F^{[1]'} F^{[1]}(\bar{f}_1(\Delta t))\Delta t^2 + \mathcal{O}(\Delta t^3) \\
&= \bar{f}_0 + \left(F^{[1]}(f_0) + F^{[2]}(\bar{f}_0)\right)\Delta t \\
&+ \frac{1}{2}\left(F^{[1]'} F^{[1]}(\bar{f}_0) + 2F^{[1]'} F^{[2]}(\bar{f}_0) + F^{[2]'} F^{[2]}(\bar{f}_0)\right)\Delta t^2 + \mathcal{O}(\Delta t^3).
\end{aligned}$$

On the other hand, let $\phi_{\Delta t}$ be a flow generated by the exact solution to the original system Eq. (6.3.32) so that $\bar{f}(\Delta t) = \phi_{\Delta t}(\bar{f}_0)$ if $\bar{f}(0) = \bar{f}_0$. The Taylor decomposition of the exact solution gives

$$\begin{aligned}
\bar{f}(\Delta t) &= \bar{f}_0 + F(\bar{f}_0)\Delta t + \frac{1}{2} F' F(\bar{f}_0)\Delta t^2 + \mathcal{O}(\Delta t^3) \\
&= \bar{f}_0 + \left(F^{[1]}(\bar{f}_0) + F^{[2]}(\bar{f}_0)\right)\Delta t \\
&+ \frac{1}{2}\Big(F^{[1]'} F^{[1]}(\bar{f}_0) + F^{[1]'} F^{[2]}(\bar{f}_0) \\
&\qquad + F^{[2]'} F^{[1]}(\bar{f}_0) + F^{[2]'} F^{[2]}(\bar{f}_0)\Big)\Delta t^2 + \mathcal{O}(\Delta t^3).
\end{aligned} \tag{6.3.36}$$

The comparison of two series shows that the splitting method $\Phi_{\Delta t}$ can be of second order if $F^{[1]'} F^{[2]}(\bar{f}_0) = F^{[2]'} F^{[1]}(\bar{f}_0)$, which is generally not true. Therefore, this method is only of first order. The same first order accuracy for the adjoint method $\Phi^*_{\Delta t}$ follows from the fact that adjoint methods always have the same order as their direct counterparts (Hairer, Lubich, and G. Wanner 2002). □

The choice of any integrator of order greater than one does not affect the overall accuracy of a resulting composite scheme of the above form from Proposition 6.3.1. The simplest way to turn any consistent one step method of order one into a second order method is to make the composition with its adjoint with halved step sizes

$$\Psi_{\Delta t} = \Phi^{*}_{\Delta t/2} \circ \Phi_{\Delta t/2} = \Phi^{[2]*}_{\Delta t/2} \circ \phi^{[1]}_{\Delta t} \circ \Phi^{[2]}_{\Delta t/2}. \tag{6.3.37}$$

By the result of Proposition 6.3.1, there is no benefit of making time discretizations of orders ≥ 2. Therefore, already by using Euler methods in Eq. (6.3.37), we achieve the second order approximation in time. However, since the implicit Euler method is adjoint to the explicit one, $\Psi_{\Delta t}$ requires the usage of both of them which is not convenient in practice. Moreover, we want to have a scheme which does not require exact solutions for any of subproblems Eq. (6.3.34). That said, if we consider the composition of only approximate methods without their adjoints, we have the following result

Proposition 6.3.2. *Consider the composition of numerical methods*

$$\Psi_{\Delta t} = \Phi^{[2]}_{\Delta t/2} \circ \Phi^{[1]}_{\Delta t} \circ \Phi^{[2]}_{\Delta t/2}. \tag{6.3.38}$$

If the methods $\Phi^{[1]}$ and $\Phi^{[2]}$ are of second order at least, the resulting composition method Ψ is of second order.

Proof. Let us denote approximate solutions to subproblems Eq. (6.3.34) using numerical flows as $\bar{f}_1(\Delta t/2) = \Phi^{[2]}_{\Delta t/2}(\bar{f}_1(0))$ if $\bar{f}_1(0) = \bar{f}_0$, $\bar{f}_2(\Delta t) = \Phi^{[1]}_{\Delta t}(\bar{f}_2(0))$ if $\bar{f}_2(0) = \bar{f}_1(\Delta t/2)$, and $\bar{f}_3(\Delta t/2) = \Phi^{[2]}_{\Delta t/2}(\bar{f}_3(0))$ if $\bar{f}_3(0) = \bar{f}_2(\Delta t)$. Since the methods $\Phi^{[1]}$ and $\Phi^{[2]}$ are of second order, we perform Taylor decomposition of each solution up to second order around $\Delta t = 0$, and express them in terms of a respective previous solution. We have

$$\begin{aligned}
\bar{f}_1\left(\frac{\Delta t}{2}\right) &= \bar{f}_0 + \frac{1}{2}F^{[2]}(\bar{f}_0) + \frac{1}{8}F^{[2]'}F^{[2]}(\bar{f}_0)\Delta t^2 + \mathcal{O}(\Delta t^3),\\
\bar{f}_2(\Delta t) &= \bar{f}_0 + \left(F^{[1]}(\bar{f}_0) + \frac{1}{2}F^{[2]}(\bar{f}_0)\right)\Delta t\\
&\quad + \frac{1}{2}\left(F^{[1]'}F^{[1]}(\bar{f}_0) + F^{[1]'}F^{[2]}(\bar{f}_0) + \frac{1}{4}F^{[2]'}F^{[2]}(\bar{f}_0)\right)\Delta t^2 + \mathcal{O}(\Delta t^3),\\
\bar{f}_3\left(\frac{\Delta t}{2}\right) &= \bar{f}_0 + \left(F^{[1]}(\bar{f}_0) + F^{[2]}(\bar{f}_0)\right)\Delta t\\
&\quad + \frac{1}{2}\left(F^{[1]'}F^{[1]}(\bar{f}_0) + F^{[1]'}F^{[2]}(\bar{f}_0) + F^{[2]'}F^{[1]}(\bar{f}_0) + F^{[2]'}F^{[2]}(\bar{f}_0)\right)\Delta t^2 + \mathcal{O}(\Delta t^3),
\end{aligned}$$

where $F^{[i]'}, i = 1, 2$ are the Jacobians. The comparison of the last expansion to the Taylor expansion of the exact solution Eq. (6.3.36) shows that $\Psi_{\Delta t}$ is of second order provided that each of the submethods is of second order too. ☐

Corollary 6.3.1. *Consider the composition of numerical methods*

$$\Psi_{\Delta t} = \Phi^{[2]}_{\Delta t/2} \circ \phi^{[1]}_{\Delta t} \circ \Phi^{[2]}_{\Delta t/2}.$$

If the method $\Phi^{[2]}$ is of second order at least and $\phi^{[1]}$ is the exact solution, the resulting composition method Ψ is of second order.

The splitting methods Eq. (6.3.35) from Proposition 6.3.1 were obtained by solving one of subproblems Eq. (6.3.34) with an exact solver and the other one with an approximate method. We now consider the case when both phase space flows cannot be computed exactly so that we use approximations of order p for both of them. We have the following result

Proposition 6.3.3. *Consider the splitting method and its adjoint defined as*

$$\Phi_{\Delta t} = \Phi^{[1]}_{\Delta t} \circ \Phi^{[2]}_{\Delta t}, \quad \Phi^{*}_{\Delta t} = \Phi^{[2]*}_{\Delta t} \circ \Phi^{[1]*}_{\Delta t}, \tag{6.3.39}$$

where $\Phi^{[1]}$ and $\Phi^{[2]}$ are approximate numerical flows of order $p \geq 1$. For every $p \geq 1$, the resulting composition methods Φ and Φ^{*} are first order accurate.

Proof. The proof is analogous to the one in Proposition 6.3.1. $\square$

As before, by the theorem of the composition of methods (Hairer, Lubich, and G. Wanner 2002), a second order scheme is obtained as the composition of a method Φ and its adjoint Φ^* as

$$\Psi_{\Delta t} = \Phi_{\Delta t/2} \circ \Phi^*_{\Delta t/2}.$$

In terms of the splitting methods Eq. (6.3.39), it is expressed as

$$\Psi_{\Delta t} = \Phi^{[1]}_{\Delta t/2} \circ \Phi^{[2]}_{\Delta t/2} \circ \Phi^{[2]*}_{\Delta t/2} \circ \Phi^{[1]*}_{\Delta t/2}. \tag{6.3.40}$$

Note that because in general the numerical flow $\Phi^{[2]}$ does not possess the group property, we cannot combine the middle terms to the form of Eq. (6.3.37). Again, we would like to have a method which does not require the usage of both direct and adjoint steppers as in Eq. (6.3.40). By considering only direct steppers, we have the following result

Proposition 6.3.4. *Consider a composition of numerical methods*

$$\Psi_{\Delta t} = \Phi^{[1]}_{\Delta t/2} \circ \Phi^{[2]}_{\Delta t/2} \circ \Phi^{[2]}_{\Delta t/2} \circ \Phi^{[1]}_{\Delta t/2}.$$

If the methods $\Phi^{[1]}$ and $\Phi^{[2]}$ are of second order at least, the resulting composition method Ψ is of second order.

Proof. Let us denote approximate solutions to subproblems Eq. (6.3.34) using numerical flows as $\bar{f}_1(\Delta t/2) = \Phi^{[1]}_{\Delta t/2}(\bar{f}_1(0))$ if $\bar{f}_1(0) = \bar{f}_0$, $\bar{f}_2(\Delta t/2) = \Phi^{[2]}_{\Delta t/2}(\bar{f}_2(0))$ if $\bar{f}_2(0) = \bar{f}_1(\Delta t/2)$, $\bar{f}_3(\Delta t/2) = \Phi^{[2]}_{\Delta t/2}(\bar{f}_3(0))$ if $\bar{f}_3(0) = \bar{f}_2(\Delta t/2)$, and $\bar{f}_4(\Delta t/2) = \Phi^{[1]}_{\Delta t/2}(\bar{f}_4(0))$ if $\bar{f}_4(0) = \bar{f}_3(\Delta t/2)$. Since the methods $\Phi^{[1]}$ and $\Phi^{[2]}$ are of second order, we perform Taylor decomposition of each solution up to second order around $\Delta t = 0$, and express them in terms of a respective previous solution. We have

$$\begin{aligned}
\bar{f}_1\left(\frac{\Delta t}{2}\right) &= \bar{f}_0 + \frac{1}{2}F^{[2]}(\bar{f}_0)\Delta t + \frac{1}{8}F^{[2]'}F^{[2]}(\bar{f}_0)\Delta t^2 + \mathcal{O}(\Delta t^3),\\
\bar{f}_2\left(\frac{\Delta t}{2}\right) &= \bar{f}_0 + \frac{1}{2}\left(F^{[1]}(\bar{f}_0) + F^{[2]}(\bar{f}_0)\right)\Delta t\\
&\quad + \frac{1}{8}\left(F^{[1]'}F^{[1]}(\bar{f}_0) + 2F^{[1]'}F^{[2]}(\bar{f}_0) + F^{[2]'}F^{[2]}(\bar{f}_0)\right)\Delta t^2 + \mathcal{O}(\Delta t^3),\\
\bar{f}_3\left(\frac{\Delta t}{2}\right) &= \bar{f}_0 + \frac{1}{2}\left(2F^{[1]}(\bar{f}_0) + F^{[2]}(\bar{f}_0)\right)\Delta t\\
&\quad + \frac{1}{8}\left(4F^{[1]'}F^{[1]}(\bar{f}_0) + 4F^{[1]'}F^{[2]}(\bar{f}_0) + F^{[2]'}F^{[2]}(\bar{f}_0)\right)\Delta t^2 + \mathcal{O}(\Delta t^3),\\
\bar{f}_4\left(\frac{\Delta t}{2}\right) &= \bar{f}_0 + \left(F^{[1]}(\bar{f}_0) + F^{[2]}(\bar{f}_0)\right)\Delta t\\
&\quad + \frac{1}{2}\left(F^{[1]'}F^{[1]}(\bar{f}_0) + F^{[1]'}F^{[2]}(\bar{f}_0) + F^{[2]'}F^{[1]}(\bar{f}_0) + F^{[2]'}F^{[2]}(\bar{f}_0)\right)\Delta t^2 + \mathcal{O}(\Delta t^3),
\end{aligned}$$

where $F^{[i]'}, i = 1, 2$ are the Jacobians. The comparison of the last expansion to the Taylor expansion of the exact solution Eq. (6.3.36) shows that $\Psi_{\Delta t}$ is of second order provided that each of the submethods is of second order too. $\square$

To sum the results up, we have derived several dimensionality splitting methods that allow us to decompose system state updates due to velocity fields along different dimensions. Namely, we have represented the system with a total velocity flow Eq. (6.3.32) as the system with two qualitatively different velocity flows Eq. (6.3.33). Performing the splitting, we have considered two subproblems Eq. (6.3.34), each of which deals with only one flow. The main question afterwards is how to combine the solutions to both subproblems in order to preserve the desired order of accuracy of the full solution. Assuming we solve each subproblem Eq. (6.3.34) numerically, we can use the methods of Proposition 6.3.2 or Proposition 6.3.4 in order to achieve the second order in time. However, since Eq. (6.3.38) requires fewer time steppers, we choose it for all the subsequently reported results. For such an FVM, we state similar results about positivity preservation and mass conservation, as in previous sections.

Theorem 6.3.1. *Consider the IVP Eqs.* (6.1.2) *to* (6.1.3) *with periodic boundaries and the semidiscrete FVM Eq.* (6.3.31) *with dimensionality splitting Eq.* (6.3.34),*Eq.* (6.3.38) *with*

$$F^{[1]}_{i,j,k} = -\frac{F^{\varphi}_{i,j,k+\frac{1}{2}} - F^{\varphi}_{i,j,k-\frac{1}{2}}}{\Delta\varphi}, \tag{6.3.41}$$

$$F^{[2]}_{i,j,k} = -\frac{F^{x}_{i+\frac{1}{2},j,k} - F^{x}_{i-\frac{1}{2},j,k}}{\Delta x} - \frac{F^{y}_{i,j+\frac{1}{2},k} - F^{y}_{i,j-\frac{1}{2},k}}{\Delta y}, \tag{6.3.42}$$

where the numerical fluxes $F^{x}_{i\pm\frac{1}{2},j,k}$, $F^{y}_{i,j\pm\frac{1}{2},k}$, $F^{\varphi}_{i,j,k\pm\frac{1}{2}}$ *are defined as in Eq.* (6.2.27) *using a positivity-preserving piecewise linear reconstruction Section 6.2.2. Assume that each system of ODEs Eq.* (6.3.34) *is discretized by a second order method whose time step can be expressed as a convex combination of several forward Euler steps. Then, the computed cell averages remain nonnegative* $f_{i,j,k} \geq 0, (i,j,k) \in \Omega_{N,M,L}$ *for all* $t \geq 0$*, provided that the following CFL condition is satisfied:*

$$\Delta t \leq \min\left\{\frac{\Delta x}{4a}, \frac{\Delta y}{4b}, \frac{\Delta\varphi}{2c}\right\},$$

where $a = \max\limits_{i,j,k}\left\{u^{+}_{i+\frac{1}{2},j,k}, -u^{-}_{i+\frac{1}{2},j,k}\right\}$, $b = \max\limits_{i,j,k}\left\{v^{+}_{i,j+\frac{1}{2},k}, -v^{-}_{i,j+\frac{1}{2},k}\right\}$, *and* $c = \max\limits_{i,j,k}\left\{w^{+}_{i,j,k+\frac{1}{2}}, -w^{-}_{i,j,k+\frac{1}{2}}\right\}$ *and the velocities at cell interfaces are defined in Eq.* (6.2.28), *Eq.* (6.2.30).

Proof. The proof of this theorem follows the same lines as in Theorem 6.2.1 but it should be applied to each subsystem Eq. (6.3.34) separately. By expressing cell averages of a solution $f_{i,j,k}$ of the first subsystem as a linear combination of corresponding values at cell interfaces in angular direction, defined in Eq. (6.2.26), as

$$f_{i,j,k} = \frac{1}{2}\left(f^{\mathrm{T}}_{i,j,k} + f^{\mathrm{B}}_{i,j,k}\right)$$

and a solution of the second subsytem as a linear combination of corresponding values at cell interfaces in spatial directions as

$$f_{i,j,k} = \frac{1}{4}\left(f^{\mathrm{E}}_{i,j,k} + f^{\mathrm{W}}_{i,j,k} + f^{\mathrm{N}}_{i,j,k} + f^{\mathrm{S}}_{i,j,k}\right),$$

the result follows. □

Theorem 6.3.2. *Consider the IVP Eq.* (6.1.2)*-Eq.* (6.1.3) *with periodic boundaries and the semidiscrete FVM with dimensionality splitting as in Theorem 6.3.1. Then, the mass of the discretized system is conserved, i.e.,*

$$\frac{d}{dt}\int_{\Omega} f(r,\varphi,t)\,\mathrm{d}r\mathrm{d}\varphi = 0.$$

Proof. By the periodicity of the domain in all directions, the proof of this theorem follows the same lines as in Theorem 6.2.2. □

We implemented the presented finite volume schemes in C++. To be able to perform numerical analysis of the schemes with meaningful phase space discretizations, we parallelized algorithms using the message passing interface (MPI) standard (Gropp, Lusk, and Skjellum 2014). Our implementation can be found under (`https://github.com/raven91` n.d.).

6.4 NUMERICAL TESTS

In this section, we demonstrate the performance of the developed numerical scheme. As it has been mentioned, the assumption of spatial homogeneity of solutions allows us to greatly simplify the analysis of the system of interest as well as gain theoretical insight on the behavior of its solutions. Therefore, we first conduct numerical experiments under the assumption of spatial homogeneity in Sections 6.4.2-6.4.6, including the study of phase transitions of traveling wave solutions in particular. The phase transitions are quantified with respect to the global polar order parameter that measures the degree of polarization in a particle flow. Next, we test the numerical scheme in a general setup, where nonstationary spatially nonhomogeneous solutions are expected to exist, including the study of related phase transitions as well. These studies are presented in Sections 6.4.7-6.4.8.

6.4.1 *Error norms*

In the following, we will examine the accuracy of numerical schemes in both spatially homogeneous and nonhomogeneous setups. In the former, analytic solutions are known while in the latter, they are not. Therefore, we introduce different norms for different cases. If we know an exact solution, we will use the following norms to quantify convergence errors (Sun, J. A. Carrillo, and Shu 2018):

$$\begin{aligned} e_{L^1} &= \sum_{(i,j,k)\in\Omega_{N,M,L}} \iiint_{C_{i,j,k}} \left|\tilde{f}_h(x,y,\varphi,t) - f(x,y,\varphi,t)\right| \mathrm{d}x\mathrm{d}y\mathrm{d}\varphi, \\ e_{L^2} &= \left(\sum_{(i,j,k)\in\Omega_{N,M,L}} \iiint_{C_{i,j,k}} \left|\tilde{f}_h(x,y,\varphi,t) - f(x,y,\varphi,t)\right|^2 \mathrm{d}x\mathrm{d}y\mathrm{d}\varphi \right)^{\frac{1}{2}}, \\ e_{L^\infty} &= \max_{(i,j,k)\in\Omega_{N,M,L}} \left|\tilde{f}_h(x_i,y_j,\varphi_k,t) - f(x_i,y_j,\varphi_k,t)\right|, \end{aligned} \tag{6.4.43}$$

where $\tilde{f}_h$ is a numerical solution with the reconstruction defined by Eq. (6.2.20) or Section 6.2.2 and phase space discretization h, f is an exact solution, $C_{i,j,k} = [x_{i-\frac{1}{2}}, x_{i+\frac{1}{2}}] \times [y_{j-\frac{1}{2}}, y_{j+\frac{1}{2}}] \times [\varphi_{k-\frac{1}{2}}, \varphi_{k+\frac{1}{2}}]$, $i = 0,\ldots,N-1, j = 0,\ldots,M-1, k = 0,\ldots,L-1$ is a cell on a uniform grid with NML points as defined previously. The integrals in the above expressions are computed using Gauss-Legendre quadrature (Press et al. 2002). Note that in case we use quasiuniform initial conditions, we need to align both solutions in a proper way. In the reported results, we shift an exact solution such that its first moment coincides with the first moment of the reconstructed solution.

In cases where we do not have an exact solution, which is the case when we retrieve spatially nonhomogeneous patterns, we first compute a reference solution with the finest discretization h_1 and compare the rest of the solutions with cruder discretizations h_2 to it using

$$\begin{aligned} e_{L^1} &= \sum_{(i,j,k)\in\Omega_{N,M,L}} \iiint_{C_{i,j,k}} \left|\tilde{f}_{h_1}(x,y,\varphi,t) - \tilde{f}_{h_2}(x,y,\varphi,t)\right| \mathrm{d}x\mathrm{d}y\mathrm{d}\varphi, \\ e_{L^2} &= \left(\sum_{(i,j,k)\in\Omega_{N,M,L}} \iiint_{C_{i,j,k}} \left|\tilde{f}_{h_1}(x,y,\varphi,t) - \tilde{f}_{h_2}(x,y,\varphi,t)\right|^2 \mathrm{d}x\mathrm{d}y\mathrm{d}\varphi\right)^{\frac{1}{2}}, \\ e_{L^\infty} &= \max_{(i,j,k)\in\Omega_{N,M,L}} \left|\tilde{f}_{h_1}(x_i,y_j,\varphi_k,t) - \tilde{f}_{h_2}(x_i,y_j,\varphi_k,t)\right|, \end{aligned} \tag{6.4.44}$$

where the grid size is chosen as a least common denominator in each dimension, i.e. $C_{i,j,k}, i = 0,\ldots,\mathrm{lcd}(N_1,N_2)-1, j = 0,\ldots,\mathrm{lcd}(M_1,M_2)-1, k = 0,\ldots,\mathrm{lcd}(L_1,L_2)-1$. If one needs to compute an error for one and two dimensional domains, it is done straightforwardly by omitting two or one dimensions, respectively, in the above definitions.

6.4.2 *Stationary phase synchronization (1D)*

We start the inspection of performance of constructed numerical schemes by first analyzing the simpler spatially homogeneous systems, whose time evolution is governed by PDEs Eq. (6.1.10). It is known that for sufficiently high diffusion levels D_φ (or equivalently for small coupling coefficients σ), the asymptotic solution consists of chaotically moving particles, whose distribution is given by a uniform density function Eq. (6.1.9). For sufficiently low diffusion levels (or large coupling coefficients), particles self-organize into spatially homogeneous polar groups, which are stationary in the absence of a phase lag, i.e., for $\alpha = 0$, or rotate with constant frequency for $\alpha \neq 0$. In this section, we investigate how the numerical scheme performs in the former case. Namely, we consider a spatially homogeneous version of the continuum limit equation with $\alpha = 0$, also known as the continuum Kuramoto model (J. A. Carrillo, Choi, and Pareschi 2019) with diffusion:

$$\begin{cases} \partial_t f(\varphi,t) = -\partial_\varphi\left[w[f](\varphi,t)f(\varphi,t)\right] + D_\varphi\partial_{\varphi\varphi}f(\varphi,t) & \text{in } \mathbb{T}\times(0,\infty) \\ f(\varphi,0) = a_0 + \sum\limits_{k=1}^{K}\left[a_k\cos(k\varphi) + b_k\sin(k\varphi)\right] & \text{on } \mathbb{T}\times\{t=0\}, \end{cases} \tag{6.4.45}$$

where the angular velocity induced by particles' interactions is $w[f](\varphi,t) = \sigma\int_{\mathbb{T}} f(\varphi',t)\sin(\varphi'-\varphi)\mathrm{d}\varphi'$. The initial condition $f(\varphi,0)$ in the form of a trigonometric series is used to model an irregular but sufficiently smooth function, which is required by the numerical scheme. We shall refer to such initial conditions as quasirandom initial conditions in subsequent discussions. The series coefficients are chosen in such a way that $f(\varphi,0)$ is nonnegative and properly normalized, i.e. $a_0 = \frac{1}{2\pi}$, $a_k, b_k \sim \mathcal{U}(-\varepsilon,\varepsilon), k = 1,\ldots,K,\ K\in\mathbb{N}$. Note that we cannot use a uniform probability density function Eq. (6.1.9) as an initial condition since it is already a solution to the problem Eq. (6.4.45). We also remark that the normalization of the density function is not generally required by the scheme but continuum limit PDEs, we consider in this paper, describe the behavior of probability density functions.

It is well known that the problem Eq. (6.4.45), i.e. the continuum Kuramoto model for identical oscillators with diffusion, exhibits a second-order phase transition with respect to either coupling strength σ or diffusion level D_φ. The phase transition if of second order and occurs at $D_\varphi = \frac{\sigma}{2}$. Its numerical investigation was already described in detail in (J. A. Carrillo, Choi, and Pareschi 2019),

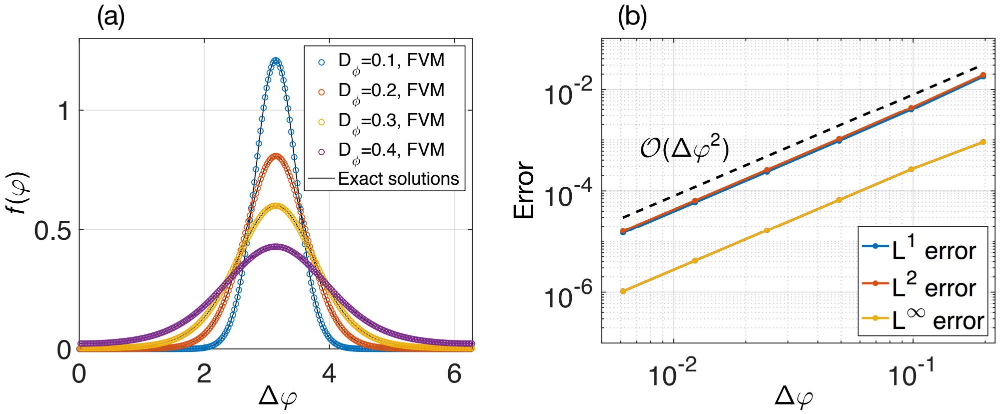

Figure 6.1: (a) Numerical stationary solutions of (1+1)-dimensional Eq. Eq. (6.4.45) with $L = 256$ grid points, compared to respective exact solutions (black lines) in the form of the von Misés density function Eq. (6.4.46). All solutions are centered such that their means coincide. (b) The convergence of error for the same problem Eq. (6.4.45) in L^1, L^2, and L^∞ norms at $t = 100$. The points correspond to grids with 32, 64, 128, 256, 512, and 1024 points. Model parameters are $\sigma = 1$, $D_\varphi = 0.1$.

therefore, we do not consider it here. Instead, we only test how our finite volume scheme performs on the solutions of Eq. (6.4.45) for parameters from the region of stability of a polar order solution. In this case, this solution is a von Misés density function

$$f(\varphi, t) = \frac{\exp\left[\frac{\sigma R}{D_\varphi}\cos(\varphi - \Theta)\right]}{2\pi I_0(\gamma)}, \tag{6.4.46}$$

where $\Theta \in \mathbb{T}$ is the average direction of a particle flow, whose value depends on initial conditions, and I_0 is the modified Bessel function of the first kind. Fig. 6.1(a) illustrates that a numerical solution approximates the exact one very well. Note that since the numerical solution was obtained from quasiuniform initial conditions according to Eq. (6.4.45), it is manually centered so that $\Theta = \pi$, for comparison reasons. The numerical solutions are taken at $t = 200$, when all of them has converged to steady states. However, such a long time is not required for all presented solutions. The time the system takes to converge to a steady state depends on the value of a diffusion coefficient D_φ (or reversely the coupling strength σ). The closer the value to the order-disorder transition point $D_\varphi = \frac{\sigma}{2}$, the longer the time is. This is a well known bottleneck effect near bifurcation points. For the solution with $D_\varphi = 0.4\sigma$, it takes around $t = 200$ simulation time units to converge.

The results of error convergence are presented in Fig. 6.1(b). One can see that in the current setup, the scheme is second order accurate as is guaranteed by its construction. Numerical solutions were compared to the aforementioned von Misés density function Eq. (6.4.46) using error norms defined by Eq. (6.4.43). Initial conditions were again quasiuniform, the time step was $\Delta t = 10^{-5}$, and the errors were computed at $t = 100$, when the steady state has been reached.

6.4.3 *Nonstationary phase synchronization (1D)*

Next, we keep the assumption of spatial homogeneity but assume $\alpha \neq 0$. If the phase lag is added to the particle alignment interaction, a particle flow starts to rotate. Its continuum description in terms of a probability density function becomes skewed and assumes a traveling wave form. A slight

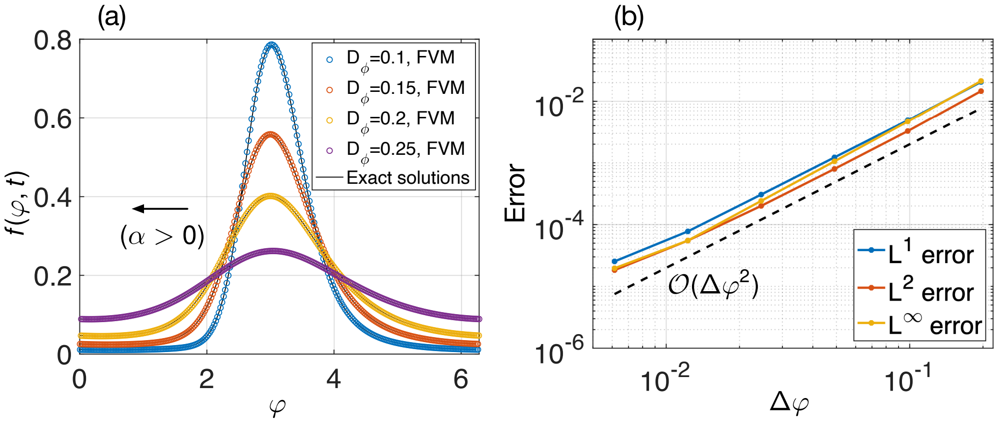

Figure 6.2: (a) Profiles of numerical traveling wave solutions of (1+1)-dimensional Eq. (6.4.47) with $L = 256$ grid points, compared to the respective exact solutions in the form of the skewed circular one-peaked density function Eq. (6.4.48). All solutions are centered such that their means coincide. The black arrow indicates the direction of motion of traveling waves. (b) The convergence of error for the problem Eq. (6.4.47) in L^1, L^2, and L^∞ norms at $t = 100$. The points correspond to grids with 32, 64, 128, 256, 512, and 1024 points. Other parameters are $\sigma = 1$, $\alpha = 1$, $D_\varphi = 0.1$.

generalization to the previous example leads to the following continuum Kuramoto-Sakaguchi model (Sakaguchi and Kuramoto 1986) with diffusion:

$$\begin{cases} \partial_t f(\varphi,t) = -\partial_\varphi \left[w[f](\varphi,t) f(\varphi,t) \right] + D_\varphi \partial_{\varphi\varphi} f(\varphi,t) & \text{in } \mathbb{T} \times (0,\infty) \\ f(\varphi,0) = a_0 + \sum\limits_{k=1}^{K} \left[a_k \cos(k\varphi) + b_k \sin(k\varphi) \right] & \text{on } \mathbb{T} \times \{t = 0\}, \end{cases} \tag{6.4.47}$$

where $w[f](\varphi,t) = \sigma \int_{\mathbb{T}} f(\varphi',t) \sin(\varphi' - \varphi - \alpha) \mathrm{d}\varphi'$ and the choice of an initial condition follows the same considerations as in the previous example. This problem has again two solutions, a uniform density function Eq. (6.1.9) and a skewed unimodal density function Eq. (6.1.18)

$$\begin{aligned} f(\varphi,t) = c_0 \exp &\left[-\frac{v}{D_\varphi}\varphi + \frac{\sigma R}{D_\varphi} \cos(\varphi - vt + \alpha) \right] \times \\ &\times \left(1 + \left(e^{2\pi \frac{v}{D_\varphi}} - 1 \right) \frac{\int_0^{\varphi - vt} \exp\left[\frac{v}{D_\varphi}\varphi' - \frac{\sigma R}{D_\varphi} \cos(\varphi' + \alpha) \right] \mathrm{d}\varphi'}{\int_{\mathbb{T}} \exp\left[\frac{v}{D_\varphi}\varphi' - \frac{\sigma R}{D_\varphi} \cos(\varphi' + \alpha) \right] \mathrm{d}\varphi'} \right), \quad \varphi \in [vt, 2\pi + vt) \end{aligned} \tag{6.4.48}$$

where $c_0 \in \mathbb{R}$ is a normalization constant. The stability of solutions to the problem Eq. (6.4.47) now depends on the values of a phase lag parameter α, diffusion level D_φ, and coupling strength σ. With respect to these parameters, the system exhibits a second order phase transition, which we will investigate later (see Section 6.4.6). The phase transition occurs at $D_\varphi = \frac{\sigma}{2}\cos\alpha$. Here, we illustrate the performance of the scheme for parameter values from the region of stability of the skewed density function Eq. (6.4.48), i.e. for $D_\varphi < \frac{\sigma}{2}\cos\alpha$. Fig. 6.2(a) illustrates that the numerical solution approximates the exact one well. Note that Fig. 6.2(a) shows profiles of actual solutions which have been manually centered for comparison reasons. The numerical solutions were taken at $t = 1000$, which is the time the solution with $\alpha = 1$, $D_\varphi = 0.25$, $\sigma = 1$ takes to converge to the traveling wave form Eq. (6.4.48). This is again because of the critical slowing-down

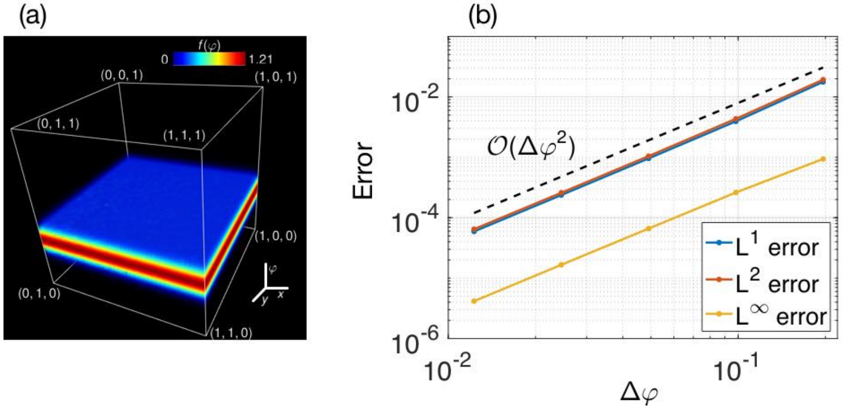

Figure 6.3: (a) Numerical stationary solution of (3+1)-dimensional Eq. Eq. (6.4.49) with $N \times M \times L = 40 \times 40 \times 256$ grid points, whose projection onto φ-axis has the same shape as in Fig. 6.1(a). (b) The convergence of error for the problem Eq. (6.4.49) in L^1, L^2, and L^∞ norms at $t = 100$. The points correspond to grids with 32, 64, 128, 256, and 512 points in φ. The grid contains 40×40 points in spatial variables. Other parameters are $\sigma = 1$, $\varrho = 0.05$, $D_\varphi = 0.1$.

close to the phase transition line (see the discussion in the previous section). In contrast to the zero phase lag case, the phase transition occurs for smaller diffusion levels for fixed α. Moreover, the time the system takes to converge increases exponentially with α even when diffusion is absent (Kruk, Maistrenko, and Koeppl 2018).

We illustrate the error convergence for parameters from the same stability region (cf. Fig. 6.2(b)). One can see that the errors are again of second order as expected. The norms were computed according to Eqs. Eq. (6.4.43) with Eq. Eq. (6.4.48) as a reference solution. The time step was chosen $\Delta t = 10^{-5}$. The norms were computed at $t = 100$, when the system had converged to a traveling wave solution.

6.4.4 *Stationary phase synchronization (3D)*

Spatially homogeneous PDE Eq. (6.1.10) was obtained from the original one Eq. (6.1.2) under the assumption of spatial homogeneity of the system. On one hand, it allowed us to derive analytical results to understand model's behavior but on the other hand, this does not correspond to the original particle flow. We next consider the complete (3+1)-dimensional equation Eq. (6.1.2) but start from the analysis in a parameter region where spatially homogeneous solutions are stable. Again, we first assume a simpler case where the phase lag is not taken into account, i.e. $\alpha = 0$ and consider the following IVP

$$\begin{cases} \partial_t f(r,\varphi,t) = -\nabla_r \cdot [v_0 e(\varphi) f(r,\varphi,t)] \\ \qquad\qquad - \partial_\varphi [w[f](r,\varphi,t) f(r,\varphi,t)] + D_\varphi \partial_{\varphi\varphi} f(r,\varphi,t) & \text{in } \Omega \times (0,\infty) \\ f(r,\varphi,0) = c_0 + \displaystyle\sum_{n,m,l=1}^{K} c_{nml} \sin(2\pi n x - \alpha_{nml}) \sin(2\pi m y - \beta_{nml}) \times & \text{on } \Omega \times \{t=0\}\,, \\ \qquad\qquad \times \sin(l\varphi - \gamma_{nml}) \end{cases} \tag{6.4.49}$$

where $e(\varphi) = (\cos\varphi, \sin\varphi) \in \mathbb{S}^1$ is a unit velocity vector and the angular torque is defined as $w[f](r,\varphi,t) = \frac{\sigma}{|C(r)|} \iiint_{C(r)} f(r',\varphi',t)\sin(\varphi'-\varphi)\mathrm{d}r'\mathrm{d}\varphi'$. Coefficients $c_0, c_{nml} \in \mathbb{R}$ in the initial condition are chosen such that the density function $f(r,\varphi,0)$ is nonnegative and normalized, and the normalization term $|C(r)|$ is defined by Eq. Eq. (6.1.5). The shifts of the arguments are chosen at random $\alpha_{nml}, \beta_{nml}, \gamma_{nml} \sim \mathcal{U}(0, 2\pi)$ in order to approximate a fluctuating density field. One can consider such an initial condition as a generalization of initial conditions from spatially homogeneous examples Eq. (6.4.45),Eq. (6.4.47) to the three-dimensional case.

From the linear stability analysis (Kruk, J. A. Carrillo, and Koeppl 2020), we know that for $\alpha = 0$ the problem Eq. (6.4.49) has the same set of solutions as the spatially homogeneous problem Eq. (6.4.45), i.e. a uniform density function Eq. (6.1.9) and the von Misés density function Eq. (6.4.46). It appears that these solutions are stable against spatially nonhomogeneous perturbations in the absence of phase lag. The reason why spatial patterns, such as traveling bands, do not develop for parameter values close to the order-disorder transition line is because the alignment interaction is normalized in $w[f](r,\varphi,t)$. We remark that in case the normalization term $|C|$ is removed, one actually observes the emergence of such spatial patterns, as is well known for active matter systems with polar interactions (Levis, Pagonabarraga, and Liebchen 2019; Nagai et al. 2015). An exemplary solution to the problem Eq. (6.4.49) is presented in Fig. 6.3(a). One can see that the solution is indeed homogeneous with respect to x and y but has a unimodal symmetric profile in φ. Its projection onto the φ-axis is qualitatively similar to the one in Fig. 6.1(a).

The analysis of solutions for different grid sizes shows the second order convergence in terms of $\Delta\varphi$ (cf. Fig. 6.3(b)). Since the steady state is eventually spatially homogeneous, we cannot test the error convergence in terms of Δx and Δy. The errors were computed using Eq. (6.4.43) with Eq. (6.4.46) as a spatially homogeneous reference solution. The time step was chosen $\Delta t = 5\cdot 10^{-4}$. The errors were computed at $t = 100$, when the numerical solution had converged to the steady state. The model parameters were taken from the region of stability of partially synchronized motion.

6.4.5 *Nonstationary phase synchronization (3D)*

We now proceed by allowing nonzero phase lag $\alpha \neq 0$ in a general three-dimensional system Eq. (6.1.2). We know that in addition to a uniform disordered Eq. (6.1.9) and spatially homogeneous ordered motion Eq. (6.4.48), spatially nonhomogeneous solutions emerge for sufficiently high values of α. Before we proceed to the analysis of such solutions, we would look into performance of our numerical scheme in a parameter region, where a spatially homogeneous skewed unimodal density function Eq. (6.4.48) is stable against spatially nonhomogeneous perturbations in order to be consistent with the previous development. We consider the following IVP

$$\begin{cases} \partial_t f(r,\varphi,t) = -\nabla_r \cdot [v_0 e(\varphi) f(r,\varphi,t)] & \\ \qquad\qquad - \partial_\varphi [w[f](r,\varphi,t) f(r,\varphi,t)] + D_\varphi \partial_{\varphi\varphi} f(r,\varphi,t) & \text{in } \Omega \times (0,\infty) \\ f(r,\varphi,0) = c_0 + \displaystyle\sum_{n,m,l=1}^{K} c_{nml} \sin(2\pi n x - \alpha_{nml}) \sin(2\pi m y - \beta_{nml}) \times & \text{on } \Omega \times \{t=0\}, \\ \qquad\qquad \times \sin(l\varphi - \gamma_{nml}) & \end{cases} \tag{6.4.50}$$

with $w[f](r,\varphi,t) = \frac{\sigma}{|C(r)|} \iiint_{C(r)} f(r',\varphi',t)\sin(\varphi'-\varphi-\alpha)\mathrm{d}r'\mathrm{d}\varphi'$. For α sufficiently small so as to guarantee the stability of spatially homogeneous densities Eq. (6.4.48), an exemplary numerical solution is illustrated in Fig. 6.4(a). One can see that it is indeed homogeneous in x

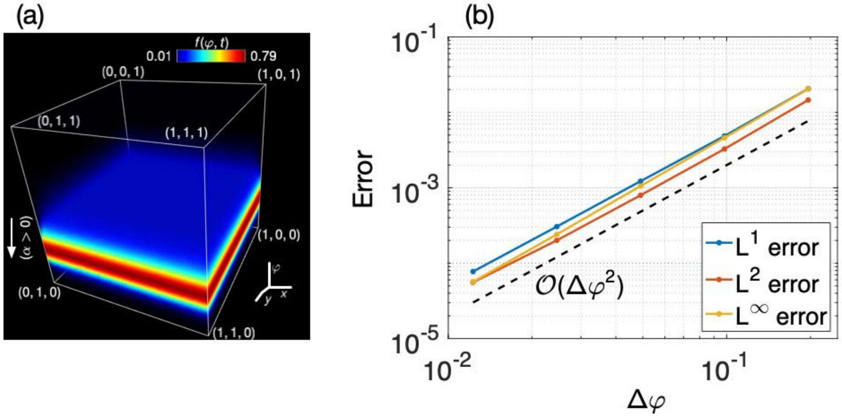

Figure 6.4: (a) Numerical plane wave solution of (3+1)-dimensional Eq. Eq. (6.4.50) with $N \times M \times L = 40 \times 40 \times 256$ grid points, whose projection onto φ-axis has the same shape as in Fig. 6.2(a). The white arrow indicates the direction of motion of the plane wave. (b) The convergence of error for the problem Eq. (6.4.50) in L^1, L^2, and L^∞ norms at $t = 200$. The points correspond to grids with 32, 64, 128, 256, and 512 points in φ. The grid has 40×40 points in spatial variables. Other parameters are $\sigma = 1$, $\varrho = 0.05$, $\alpha = 1$, $D_\varphi = 0.1$.

and y but has a characteristic skewed shape in φ (the blue region is more pronounced above the plane than below). Its projection onto the φ-axis gives a qualitatively similar solitary wave as the one in Fig. 6.2(a). The wave moves transversal to the φ axis with some constant velocity v, the sign of which depends conversely on α. Thus, it has the form of a plane wave in Ω. Such a form of the solution corresponds to a partially synchronized steadily rotating particle flow, which was investigated and termed a nonlocalized self-propelled chimera state in (Kruk, Maistrenko, and Koeppl 2018).

As in the previous example, because of spatial homogeneity of the solution, we are able to determine the order of error convergence versus $\Delta\varphi$ only (cf. Fig. 6.4(b)). The errors were computed with respect to a spatially homogeneous plane wave solution whose φ-profile is given by Eq. (6.4.48) using Eq. (6.4.43). The time step was chosen $\Delta t = 5 \cdot 10^{-4}$. The errors were computed at $t = 200$, when numerical solutions converged to the plane wave form.

6.4.6 *Phase transitions of spatially homogeneous solutions*

In this section, we analyze how phase transitions of spatially homogeneous solutions are captured by the finite volume scheme. Moreover, we concentrate on the nonstationary case with nonzero phase lag and refer the reader to (J. A. Carrillo, Choi, and Pareschi 2019) for the numerical studies of phase transitions of steady states in the continuum Kuramoto model. The phase transitions between spatially homogeneous polar order and disordered motion are commonly quantified with respect to the polar order parameter defined in Eq. (6.1.12), i.e., it is an average orientation on the unit circle with respect to a given density function. Since we know that the continuum Kuramoto-Sakaguchi equation Eq. (6.1.10) has a solution of the traveling wave form, it is enough to study its profile $g(\omega) = f(\varphi - vt, 0) = f(\varphi, t)$ in the analysis of related phase transitions. The polar order parameter can thus be expressed as

$$Re^{i\Theta} = \int_{\mathbb{T}} e^{i\omega} g(\omega) \, \mathrm{d}\omega,$$

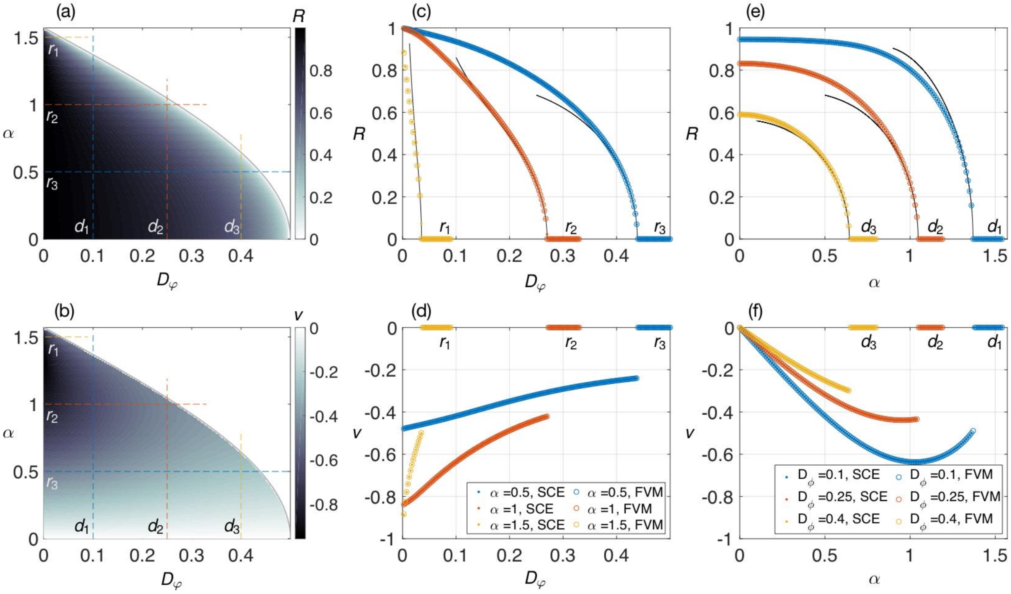

Figure 6.5: (a),(b) Solution of the system of SCEs Eq. (6.4.51) comprising a density function as a traveling wave solution Eq. (6.4.48) and a complex order parameter defined by that solution. The system determines (a) magnitude of the order parameter R and (b) a group velocity v of the traveling wave versus the phase lag α and diffusion coefficient D_φ. The gray line indicates the order-disorder transition line $D_\varphi = \frac{\sigma}{2}\cos\alpha$. The critical group velocity along that line is $v = -\frac{\sigma}{2}\sin\alpha$. The colored lines show intervals of parameter values used in (c)-(f). The marks $r_{1,2,3}$, and $d_{1,2,3}$ denote corresponding lines. (c),(d) Evolution of the order parameter magnitude R and the group velocity v, respectively, versus the diffusion coefficient D_φ for different phase lag values α. (e),(f) Evolution of R and v, respectively, versus α for different diffusion coefficients D_φ. The dots denote values found by solving the system of SCEs Eq. (6.4.51) whereas the circles denote values produced by the FVM with the grid of $L = 256$ points. The black lines show the exact form of R next to the order-disorder transition line, as predicted by the hydrodynamic theory.

where the average direction Θ can be shifted to the origin without loss of generality due to the translation invariance of Eq. Eq. (6.1.10), i.e. $\Theta \equiv 0$. By expanding the above system into the real and imaginary parts, we see that the order parameter must satisfy the following set of self-consistent equations (SCEs)

$$R = \int_{\mathbb{T}} g(\omega)\cos\omega \, \mathrm{d}\omega, \qquad 0 = \int_{\mathbb{T}} g(\omega)\sin\omega \, \mathrm{d}\omega. \tag{6.4.51}$$

This system does not have an analytical solution but we can solve it numerically for polarization R and velocity v. The numerical solution of this system in terms of the model parameters α and D_φ is presented in Figs. 6.5(a) and (b).

Given the above result, we are able to investigate phase transitions related to a spatially homogeneous rotating system Eq. (6.4.50). For each parameter set, we solve it starting from quasiuniform initial conditions, described earlier. We discretize the domain $\mathbb{T}$ into $L = 256$ points and perform all computations of this section with the time step $\Delta t = 10^{-4}$ until $t = 10^4$. The results are presented in Figs. 6.5(c) and (e) for the order parameter magnitude R, and in Figs. 6.5(d) and (f) for the group velocity v. Because either the coupling strength σ or the diffusion coefficient D_φ may be eliminated by an appropriate rescaling of time in Eq. (6.4.50), we fix $\sigma = 1$ without loss of generality and investigate the behavior in terms of α and D_φ. Since a phase transition may happen by changing either the diffusion level D_φ or the phase lag α, we look into both possibilities. First, we fix $\alpha = 0.5, 1.0, 1.5$ and investigate the behavior of $R = R(D_\varphi)$ (cf. Fig. 6.5(c)) and $v = v(D_\varphi)$ (cf. Fig. 6.5(d)). As we expect, the phase transition occurs at $D_\varphi = \frac{\sigma}{2}\cos\alpha$. The black line additionally shows how the order parameter behaves next to the transition line, according to

$$R \approx \sqrt{\frac{4D_\varphi^2 + v^2}{D_\varphi}(\cos\alpha - 2D_\varphi)},$$

which is known from the hydrodynamic description of the particle model Eq. (2.3.13) and derived in (Kruk, J. A. Carrillo, and Koeppl 2020). The grid size for D_φ was chosen 0.0025. For comparison reasons, we show the results obtained with the FVM and those of SCEs Eq. (6.4.51). Next, we fix $D_\varphi = 0.1, 0.25, 0.4$ and investigate the behavior of $R = R(\alpha)$ (cf. Fig. 6.5(e)) and $v = v(\alpha)$ (cf. Fig. 6.5(f)). Again, as expected, the phase transition occurs at $\alpha = \arccos\left(\frac{2D_\varphi}{\sigma}\right)$. The grid size for α was chosen 0.01. The black line and the results of the SCEs Eq. (6.4.51) are obtained as before.

A few remarks on phase transitions between spatially homogeneous states are in order. We quantify them in terms of a polar order parameter magnitude R. Therefore, under the assumption of spatial homogeneity, we observe a second order transition from partially synchronized to disordered state (cf. Fig. 6.5(c) and (e)). However, it is known that for polar active matter systems, the transition from uniform disordered to ordered motion is separated by a region with density-segregated patterns such as traveling bands. It has been established that for the Boltzmann equation for self-propelled particle systems, the respective transitions may be of first and second order depending on a system size (Thüroff, Weber, and Frey 2014). As we mentioned earlier, we do not observe such a spatially nonhomogeneous regime close to the order-disorder transition line because nonlocal alignment interactions in Eq. (6.1.2) are normalized, which makes spatially homogeneous solutions more stable against spatially nonhomogeneous perturbations (Kruk, J. A. Carrillo, and Koeppl 2020).

6.4.7 *Spatially nonhomogeneous solutions*

We have seen that the presented finite volume scheme is capable of reproducing correct behavior under the assumption of spatial homogeneity. Therefore, we proceed to the general PDE Eq. (6.1.2) in a parameter region where spatially nonhomogeneous patterns occur. We consider the same IVP Eq. (6.4.50) from the previous section. From the linear stability analysis of this PDE from the point of view of kinetic theory (Kruk, J. A. Carrillo, and Koeppl 2020), we know that there exists a region in the parameter space of ϱ/v_0, α, and D_φ where the spatially homogeneous skewed unimodal density function Eq. (6.1.18) becomes unstable against spatially dependent perturbations and one observes numerous spatially nonhomogeneous patterns.

In this paper, we would like to concentrate on the analysis of one of such patterns, which we refer to as a localized chimera state (Kruk, Maistrenko, and Koeppl 2018). From the point of view of the particle model Eq. (2.3.13), such a state simultaneously consists of two rather distinct groups of particles. The first group forms a subset of particles that gather into a circular polarized cloud, which rotates in the background of the rest of chaotically moving particles. In the continuum limit, this state is characterized by the formation of a high density skewed ellipsoidal region in Ω (cf. Fig. 6.6(a)) that follows a helical path. We can obtain the aforementioned high density circular cloud as a projection of such a solution into spatial coordinates (cf. Fig. 6.6(b))

$$f(r,t) = \int_{\mathbb{T}} f(r,\varphi,t)\,\mathrm{d}\varphi. \tag{6.4.52}$$

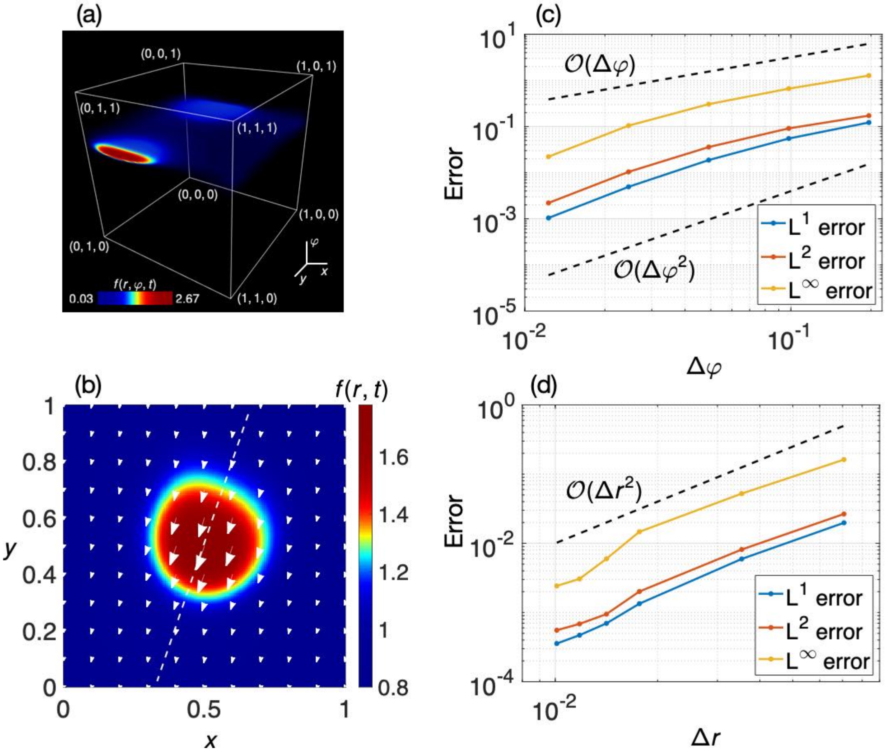

Figure 6.6: (a) Spatially nonhomogeneous solution of Eq. (6.4.50) in the form of localized chimera state. The grid contains $N \times M \times L = 160 \times 160 \times 128$ points. (b) Its projection Eq. (6.4.52) into spatial coordinates. White arrows indicate the momentum field Eq. (6.4.53) generated by the solution. The dashed white line Eq. (6.4.54) passes through the center of maximal density of the projection and is aligned with the momentum field at this point. (c,d) Convergence of error for the same problem and parameter region in L^1, L^2, and L^∞ norms at $t = 1$. The points correspond to grids (c) in φ with 32, 64, 128, 256, and 512 points, and (d) in x, y with 20×20, 40×40, 80×80, 100×100, 120×120, and 140×140 points. Here $\Delta r = \sqrt{\Delta x^2 + \Delta y^2}$. The grid also contains (c) 40×40 points in x, y, (d) 128 points in φ. Other parameters are $v_0 = 1$, $\sigma = 4$, $\varrho = 0.3$, $\alpha = 1.54$, $D_\varphi = 0.01$.

The spatial profile has a form of a bivariate solitary wave which possesses a characteristic front-end asymmetry. This can be observed if we look at the solution profile along the line (cf. Fig. 6.7(b), a white dashed line), centered at the point of maximal density and directed according to the velocity field at this point. We look for the point of maximal spatial density as

$$r_{\max} = \underset{r \in \mathbb{U}^2}{\operatorname{argmax}}\, f(r, t).$$

The velocity field can be retrieved from the momentum field, in turn, obtained as

$$u(r, t) = \int_{\mathbb{T}} e(\varphi) f(r, \varphi, t)\, \mathrm{d}\varphi \qquad (6.4.53)$$

where $e(\varphi) = (\cos\varphi, \sin\varphi) \in \mathbb{S}^1$. Note that the momentum field such defied is isomorphic to the global polar order parameter, we used earlier Eq. (6.1.7). As a result, the line can be parameterized as

$$r(s) = r_{\max} + e(\varphi_{\max})s, \quad s \in \left[-\frac{1}{2}, \frac{1}{2}\right], \tag{6.4.54}$$

where $\varphi_{\max} = \arg(u(r_{\max}))$. Using the piecewise linear reconstruction of the density function Section 6.2.2, we can find the approximate values of the density function at any point on the line (cf. Fig. 6.7(b)). Moreover, for solutions, where the radius of rotation of the localized cluster is sufficiently large so that the cluster does not rotate around a fixed point, the transverse profile of the spatial projection $f(r, t)$ has a symmetric form.

We remark that Eq. (6.4.52),Eq. (6.4.53) constitute a hydrodynamic description of the kinetic PDE Eq. (6.1.2) where polar order is expected to emerge, and is often used to get analytical insights into the dynamics. However, the known drawback of this approach is that it is limited to the regimes close to equilibrium. As opposed to that, our FVMs are applicable to any region in the parameter space, which we will employ in the next following.

In a general spatially nonhomogeneous setup, we are able to calculate error convergence in both angular and spatial variables. Because we do not know any exact solution with spatial dependence, we use Eq. (6.4.44) to compute the norms. The reference solution was the one with $N \times M \times L = 40 \times 40 \times 1024$ grid points. First, we fix $N = 40$, $M = 40$ and vary the angular grid size $\Delta\varphi$. We observe the second order convergence for $\Delta\varphi$ sufficiently small whereas it approaches the first order for largest grid sizes (cf. Fig. 6.6(c)). The reason for the first order behavior is that such discretizations cannot capture high density gradients in φ so that the numerical error is accumulated rather fast. Subsequently, since the dynamics in angular and spatial dimensions are coupled, this results in solutions, diffused away from the correct dynamics. The time step was chosen $\Delta t = 5 \cdot 10^{-4}$. Next, we fix $L = 128$ and vary the spatial grid size $\Delta x, \Delta y$. We again observe the second order error convergence versus $\Delta r = \sqrt{(\Delta x)^2 + (\Delta y)^2}$ even for quite small grid sizes with $N \times M = 20 \times 20$ points (cf. Fig. 6.6(d)). We explain such robustness of the results by the fact that the solutions were computed for quite large $\varrho = 0.3$, resulting in long range interactions. The time step was chosen $\Delta t = 5 \cdot 10^{-4}$. The reference solution was the one with $N \times M \times L = 160 \times 160 \times 128$ grid points.

6.4.8 *Phase transitions of spatially nonhomogeneous solutions*

In Section 6.4.6, we found that in spatially homogeneous systems, the transition between polar order and disorder is of second order. Now that we have an established protocol to generate spatially nonhomogeneous solutions, we are interested to learn about their related phase transitions. By choosing an appropriate scale for the microscopic particle velocity v_0 and interparticle interaction radius ϱ, we find a phase diagram in the (α, D_φ)-parameter space where three distinct solutions are observed, i.e., a spatially homogeneous disordered motion (SHDM), a spatially homogeneous ordered motion (SHOM), and a spatially nonhomogeneous motion (SNM) in the form of a localized chimera state (cf. Fig. 6.7(a)). The figure was obtained from the kinetic linear stability analysis of Eq. (6.1.18), performed in detail in (Kruk, J. A. Carrillo, and Koeppl 2020). We fix $v_0 = 0.25$, $\sigma = 1$, $\varrho = 0.3$. Phase transitions discussed earlier correspond to the transition between SHDM and SHOM, with the bifurcation occurring at $D_\varphi = \frac{\sigma}{2}\cos\alpha$ (a black solid line). In the gray region, starting from quasirandom initial conditions, one observes the formation of spatial structures. The formation happens in two stages. First, the system smooths out initial spatial perturbations but gradually polarizes until the occurrence of a skewed angular profile similar to the one in Fig. 6.2(a). Second, the remaining spatial perturbations start to act on the solution and accumulate eventually

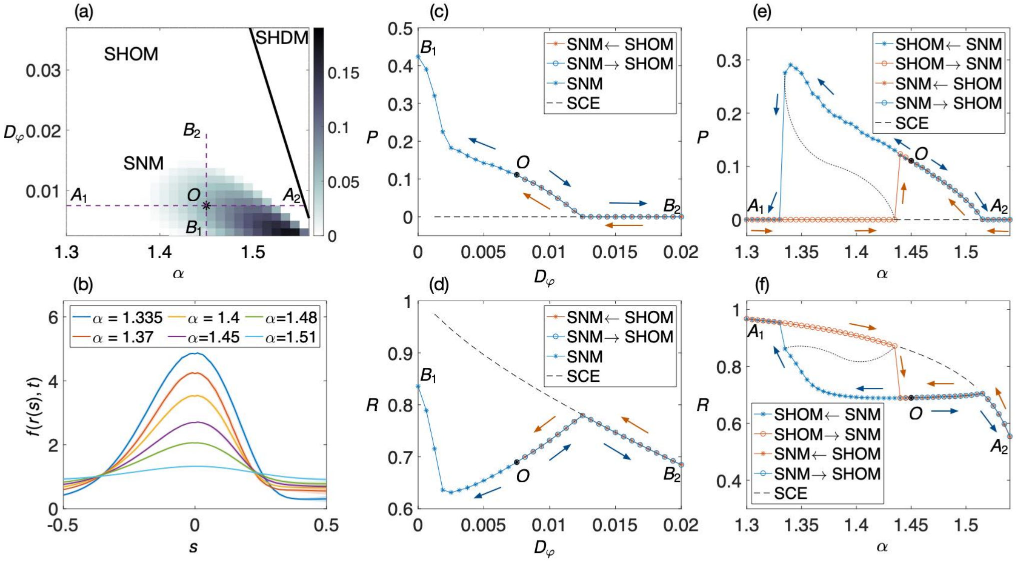

Figure 6.7: Bifurcations scenarios for SNM, represented by localized chimera states. (a) Phase diagram in the parameter space of diffusion D_φ and phase lag α; color shows the maximal real part of the strongest unstable Fourier mode (Kruk, J. A. Carrillo, and Koeppl 2020); the black solid line is the order-disorder transition line $D_\varphi = \frac{\sigma}{2}\cos\alpha$. Black star indicates the initial value $O = (\alpha, D_\varphi) = (1.45, 0.0075)$ used as a starting point for the continuation method (see the text). Purple dashed lines show continuation paths presented in (c,d,e,f). (b) Spatial profiles along the line of nonlocal collective motion in Fig. 6.6(b) for different values of the phase lag taken along the branch of stability of SNM in (e). Solid lines represent averaged densities over 10 time units and shaded regions denote respective standard deviations. (c,d) Localization P Eq. (6.4.55) and polar R Eq. (6.1.7) order parameters versus D_φ, respectively. One observes a second order phase transition between SNM and SHOM with bifurcation at $D_\varphi \approx 0.0125$. Black dashed lines denote unstable branches and have been computed from the system of SCEs Eq. (6.4.51). (e,f) Localization P and polar R order parameters versus α, respectively. One observes two types of phase transitions, namely, the first order one, accompanied with a hysteresis loop, on the path OA_1 with bifurcation points $\alpha \approx 1.33, 1.44$ and the second order one on the path OA_2 with bifurcation at $\alpha \approx 1.515$. Black dashed lines denote unstable branches and have been obtained from Eq. (6.4.51). Black dotted lines are drawn "by hand" in place of unknown unstable branches. Colored lines in (c,d,e,f) indicate directions of bifurcation paths.

into a bivariate unimodal shape. We remark that due to finite numerical precision, the second step might not be triggered for any quasirandom initial conditions given that spatial variations become of order of round-off error $\mathcal{O}(10^{-18})$. To circumvent that, one might either look for such initial conditions that preserve enough spatial perturbations at the time point of maximal synchronization or use multiprecision arithmetic libraries, like the one we used in our implementation.

As one can see in Fig. 6.7(a), the new phase transitions should occur between SHOM and SNM by varying either the diffusion coefficient D_φ or the phase lag parameter α. We inspect each route separately. Before we do that, we need to establish an appropriate order parameter to measure the level of spatial localization induced by a PDE solution as well as be able to detect changes in spatial variation of solutions upon varying model parameters. First, in a similar way as we might consider the global polar order parameter $R(t)$ Eq. (6.1.7) as a measure of angular localization of orientation vectors $e(\varphi)$ belonging to $\mathbb{S}^1$, manifested in a momentum field definition Eq. (6.4.53), we define an order parameter that measures the level of spatial localization of elements belonging to $\mathbb{S}^1 \times \mathbb{S}^1$ in the following way:

$$P(t)e^{i\Psi(t)} = \int_{\Omega} f(r, \varphi, t)e^{i2\pi(x+y)}\,\mathrm{d}r\mathrm{d}\varphi. \tag{6.4.55}$$

This parameter provides the following information. For systems with all the probability mass compressed in one point, i.e., for point measures, the spatial localization is most pronounced and the magnitude of the order parameter attains its maximal value $P = 1$. In the opposite case, for systems with uniform distribution of matter, no spatial localization is observed and the order parameter magnitude attains its minimal value $P = 0$. For partial localization inside a particle flow, we therefore have $P \in (0, 1)$. The phase Ψ is irrelevant to our purposes. Second, to detect changes in spatial structure of solutions while changing model parameters, we introduce the following maximum absolute spatial deviation measure (Thüroff, Weber, and Frey 2014):

$$\delta_r(t) = \max_{(i,j,k)\in\Omega_{N,M,L}} \left\{|f_{i,j,k}(t) - f_k(t)|\right\}, \tag{6.4.56}$$

where spatially averaged solutions are computed as

$$f_k(t) = \frac{1}{NM} \sum_{(i,j)\in\mathbb{U}_N\times\mathbb{U}_M} f_{i,j,k}(t), \quad k \in \mathbb{T}_L.$$

For SHOM, this measure attains values of order $\mathcal{O}(10^{-14})$, when the magnitude of spatial variations is of a round-off error for double precision floating point values.

We now describe the transitions between SNM and SHOM. We start with a parameter point well inside a region where SNM is a stable solution, i.e. $O = (\alpha, D_\varphi) = (1.45, 0.0075)$ (cf. Fig. 6.8(b)), and proceed in a continuation-like manner. First, we fix the phase lag parameter α and increase the diffusion level $D_\varphi \in [0.0075, 0.02]$ with a parameter step size $\Delta D_\varphi = 0.000625$ (cf. Fig. 6.7(a), a vertical path OB_2). Starting from quasirandom initial conditions Eq. (6.4.50), we let the system to converge to a solitary wave form of a localized chimera state and take this solution as an initial condition for a subsequent computation. Then, we change the diffusion level, take as a new initial condition the final solution from a previous parameter, and let the system equilibrate for $T = 100$ time units with $\Delta t = 5\cdot10^{-3}$. Afterwards, we accumulate values of $\delta_r(t)$ Eq. (6.4.56) and continue integration until spatial deviations cease to fluctuate with $\mathrm{d}\delta_r(t)/\mathrm{d}t < 5 \cdot 10^{-5}$. We quantified the rate of change $\mathrm{d}\delta_r(t)/\mathrm{d}t$ as a linear fit to a set of values $\delta_r(t)$ over the last 50 time units. The result of this procedure is shown in Fig. 6.7(c). As we see, the spatial order parameter P assumes a continuous path versus the diffusion constant D_φ. We then start from a point $B_2 = (1.45, 0.02)$ and go in the reverse direction gradually decreasing D_φ with the same step size as before. For each new parameter, we take as an initial condition the final state of the system from a previous parameter and impose small spatial perturbations of the same form as in Eq. (6.4.50) in order to allow spatial perturbations to grow provided that SHOM is unstable. We note that for spatially homogeneous systems, spatial variations are of order of a round-off error, and without such initial spatial perturbations, spatial deviations never grow even for parameter values where SHOM is indeed unstable. During this reverse round of continuation simulations, we integrate the system until $\mathrm{d}\delta_r(t)/\mathrm{d}t < 10^{-6}$. As a result, by varying the diffusion constant D_φ, we observe a supercritical transition between SNM and SHOM on the path OB_2 at $D_\varphi \approx 0.0125$. Additionally, we provide the results of the continuation procedure in terms of the polar order parameter R Eq. (6.1.7) (cf. Fig. 6.7(d)) to make the comparison with SHOM transitions.

As the next step, we study phase transitions between SNM and SHOM versus the phase lag α. There are two ways, they can occur. To begin with, let us follow the right path OA_2 in Fig. 6.7(a). As an initial parameter point, we again set $O = (1.45, 0.0075)$, keep D_φ constant, and vary

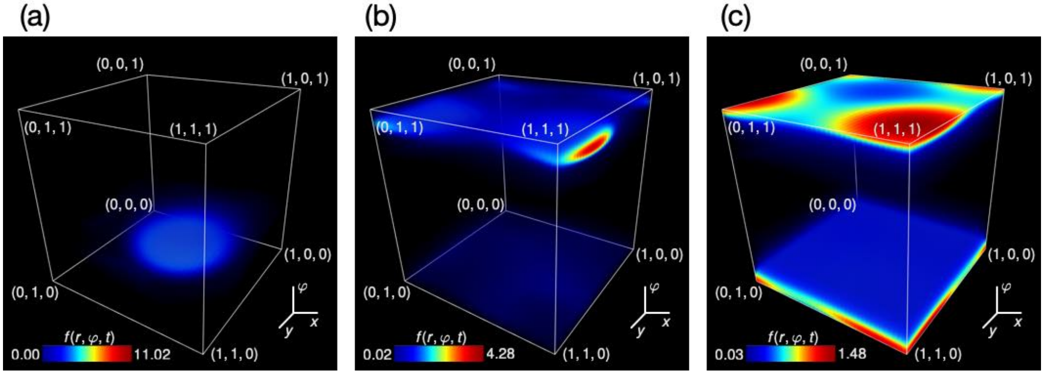

Figure 6.8: Evolution of SNM, represented by localized chimera states, along the bifurcation path A_1A_2 (cf. Fig. 6.7(a)). Snapshots of solutions (a) next to the first order transition at $\alpha = 1.335$, (b) in the middle of the path at $\alpha = 1.45$, and (c) before the second order transition at $\alpha = 1.51$. Other parameters are $v_0 = 0.25$, $\sigma = 1$, $\varrho = 0.3$, $D_\varphi = 0.0075$, $N = 40$, $M = 40$, $L = 256$.

$\alpha \in [1.45, 1.54]$ with a parameter step size $\Delta\alpha = 0.005$. We follow the same continuation protocol as before and report the results in Fig. 6.7(e,f). We see that the transition between SNM and SHOM versus α on this path follows the similar scenario as the previously described transition along OB_2. That is, it is of second order with the bifurcation point $\alpha \approx 1.515$. This comes as no surprise as both bifurcations occur close to the order-disorder transition line $D_\varphi = \frac{\sigma}{2}\cos\alpha$, where the effect of diffusion is substantial. Here, the increase of D_φ is qualitatively similar to the decrease of α. By doing so, a spatially localized region gradually smooths around.

The second way, the transition between SNM and SHOM occurs, is along the left path OA_1 in Fig. 6.7(a). By performing the same continuation procedure for the parameter values $\alpha \in [1.3, 1.45]$, we observe a hysteresis loop (cf. Figs. 6.7(e,f)), characteristic to first order transitions. Along the SNM→SHOM path, we come across a bifurcation point $\alpha \approx 1.33$ of a saddle-node type. Along the SHOM→SNM path, we find a bifurcation point $\alpha \approx 1.44$ of a subcritical type. Apart from the results of the linear stability analysis, which showed us where SNM is observable starting from any initial conditions (except for unstable solutions), we discover the existence of a bistability region where both SHOM and SNM are stable solutions, i.e., $\alpha \in (1.33, 1.44)$ with $D_\varphi = 0.0075$. Moreover, we observe some discrepancy between the results of the linear stability analysis and the continuation method. According to the stability analysis, starting from $\alpha \approx 1.38$, SHOM should become unstable against spatially dependent perturbations while the continuation method provides $\alpha \approx 1.44$. This is because the stability analysis was performed under the assumption of small microscopic particle velocities v_0 in a region of small diffusion, which is not the case here. Therefore, the numerical analysis of the PDE provides us with a better understanding of how solutions behave far from the order-disorder transition line.

Along bifurcation paths with respect to both parameters, SNM undergoes qualitatively similar transformations. Starting from second order transition points ($D_\varphi \approx 0.0125$ in Fig. 6.7(c) and $\alpha \approx 1.515$ in Fig. 6.7(e)), an ellipsoidal shape forms inside a high density layer (cf. Fig. 6.8(c)) but the layer itself does not disappear completely. In Fig. 6.8(b), one can observe coexistence of a localized cluster with such a layer for a parameter point even in the middle of a bifurcation path. By decreasing parameters to minimal values with SNM being stable, the localized cluster is most clearly pronounced and the secondary layer dissolves (cf. Fig. 6.8(a)). The figure demonstrates qualitative changes in SNM with respect to the phase lag α but one obtains similar results by decreasing the diffusion level D_φ towards zero.

7

BACTERIAL SUSPENSIONS AS ACTIVE MATTER SYSTEMS

7.1 EXPERIMENTS ON BACTERIAL SWARMING IN MICROFLUIDIC ENVIRONMENT

One of our goals is to apply active matter theory tools, discussed throughout this thesis, to a genuine system of living agents. One of such systems that are relatively easy to maintain and control are bacterial suspensions (Zhang et al. 2010). We have primarily conducted experiments with *B. subtilis*; however, the same procedures with *E. coli* have also been tested. General bacterial swarming is highly irregular so that in order to observe and extract information of constituent trajectories, we must restrict bacteria to two-dimensional environments. One common way to impose that is to consider the motion in microfluidic channels residing in Polydimethylsiloxane (PDMS) chips Fig. 7.1. We produce such channels with $1\mu m$ height which is enough to prohibit *B. subtilis* from swimming vertically considerably because they are approximately $0.5 - 1\mu m$ in diameter. The width of channels is $200\mu m$, $300\mu m$, and $600\mu m$. Another common approach to observe bacterial swarming in two-dimensions is using agar plates. Even though, bacteria grow considerably larges in lengths on agar plates, their swimming speed is significantly lower compared to microfluidic environments.

We established the protocol to observe the swarming of bacteria in microfluidic environment. Wild type *B. subtilis* is stored in a tip at -80 °C. At the beginning, we scratch a bit of bacterial mass and place it into a reaction tube with yeast extract peptone dextrose (YEPD) medium, prepared in advance. The recipe for this medium is 1% yeast extract, 2% of peptone, and 4% of glucose in distilled water. Additionally, we tested Luria broth and Terrific Broth σ but the motility of *B. subtilis* inside them was considerably lower. The mean for bacterial length with our protocol with YEPD is approximately $3 - 4\mu m$. We tried to control it by adding Ficoll PM 70, polyethylene glycol 4000, and cefalexin, all of which did not prove successful. Next, we take the reaction tube with bacterial suspension into an incubator room with 37 °C and place it on a shaker overnight. In one day, we take the tube and perform a dilution of $1\mu l$ of bacterial suspension and $1600\mu l$ of fresh YEPD. We then take the new culture back to the shaker for the next night. In the morning, after around 14 hours, we take the culture and extract $1ml$ of it into a tip. The tip is then left in a centrifuge for ten minutes with acceleration $1.5g$. Afterwards, 80% of the liquid is removed and the rest of the culture is shaken with a vortex mixer in order to distribute bacteria evenly. At this stage, the culture is ready for experimental observation. We extract the remaining suspension with a syringe and inject it into one of the inlets of a microfluidic channel. Then, bacteria take $0.5 - 1$ hours to pour into the channel depending on its width and required number density. We record the resulting swarming with magnification $100\times$ using oil immersion as a sequence of images taken every $1ms$ during 10 seconds.

7.2 MULTITARGET TRACKING

At this stage, we known the information such as positions, velocities, and orientations of each bacterium at each time point independently. For the analysis of bacterial swarming as a system of interacting particles, we need to know reconstruct trajectories of each bacterium continuously over time. Taking into account that each frame contains several hundreds of bacteria, we would keep the tracking algorithm itself simple. One of the popular choices is the Kalman filter.

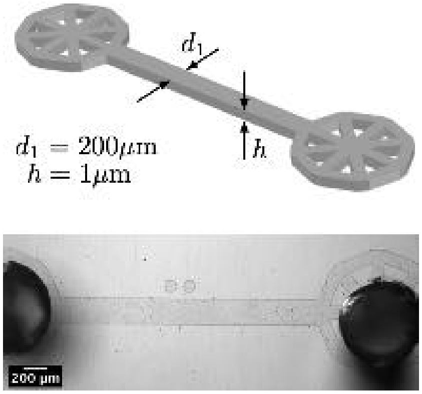

Figure 7.1: The design of a microfluidic chip used for experiments with bacterial swarming.

Let the state of each bacterium be described with two-dimensional position $r_i \in \mathbb{R}^2$ and velocity $v_i \in \mathbb{R}^2$, which we compactly combine into a composite vector $p_i = (r_i, v_i) \in \mathbb{R}^4$. We assume a simple linear update for the state vector

$$p_i(t+1) = Ap_i(t) + w_i(t), \tag{7.2.1}$$

where the state update matrix is

$$A = \begin{pmatrix} 1 & 0 & \Delta t & 0 \\ 0 & 1 & 0 & \Delta t \\ 0 & 0 & 1 & 0 \\ 0 & 0 & 0 & 1 \end{pmatrix}$$

and uncertainty in the state update is accounted for by $w_i(t) \sim \mathcal{N}(0, W), i = 1, \ldots, N$ with the covariance matrix W given. These stochastic variables are independent for all i and all time points.

When a new image is recorded (cf. Section 7.2(a)), we obtain an updated version of the system domain. This must be used to correct the states of all bacteria since they are updated according to simplistic approximated rules. Since by inspecting only one image per time, we can extract only a position of each bacterium, we introduce a measurement variable $z \in \mathbb{R}^2$ that represents our observation over the state of them. We relate state variables introduced above with measurement variables as

$$z_i(t) = Hp_i(t) + q_i(t), \tag{7.2.2}$$

where

$$H = \begin{pmatrix} 1 & 0 & 0 & 0 \\ 0 & 1 & 0 & 0 \end{pmatrix} \tag{7.2.3}$$

and uncertainty in our measurement procedure is accounted for by $q_i(t) \sim \mathcal{N}(0, Q), i = 1, \ldots, N$ with the covariance matrix Q given.

The above procedure assumes that the state p_i is Gaussian distributed. Therefore, it is sufficient to infer how the mean p_i itself and its covariance P_i are updated when new measurements become available. This is solved by applying the Kalman filter (Reich and Cotter 2015). First, we compute prior mean $\hat{p}_i = Ap_i$ and prior covariance $\hat{P}_i = AP_iA^T + W$. Afterwards, we compute posterior mean $p_i = \hat{p}_i + K_i(z_i - H\hat{p}_i)$ and posterior covariance $P_i = (I - K_iH)\hat{P}_i$ where $K_i = \hat{P}_ih^T(H\hat{P}_iH^T + Q)^{-1}$ is the Kalman gain. The major issue is that this method can be

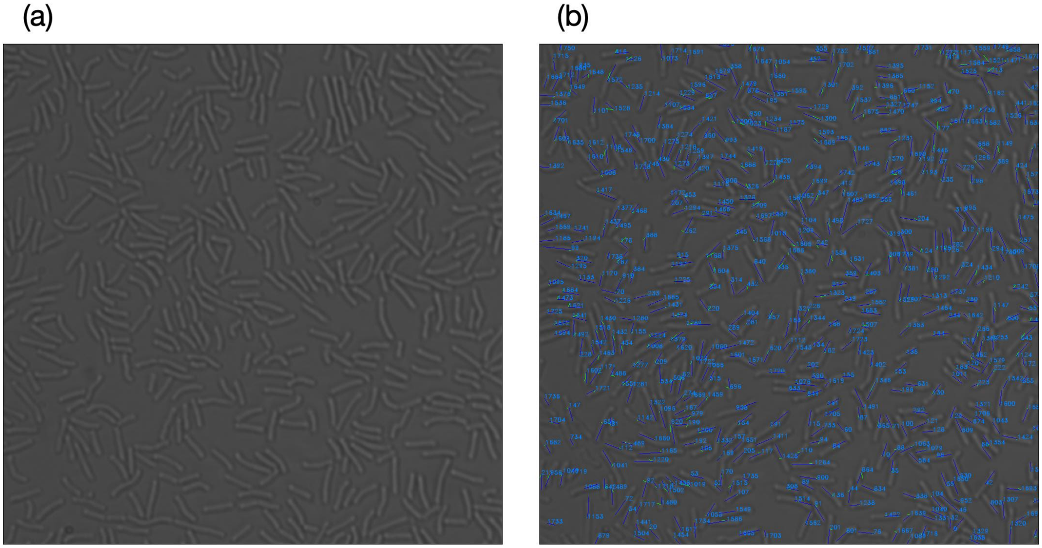

Figure 7.2: A snapshot of swarming of *B. subtilis* in a microfluidic channel. (a) A raw image obtained directly from the microscope. (b) Result of multitarget tracking procedure providing us with positions, velocities, and orientations of most bacteria.

applied for each bacterium separately, i.e., for each i, we must know its position before $r_i(t)$ and after $r_i(t+1)$ the update. However, image segmentation procedures allow us to retrieve positions of the whole group at each next frame irrespective of previous identities. The problem of matching information for each bacterium at current time step to the information for the same bacterium at the next time step is known as the data association. A common approach to solve it is using the Hungarian algorithm, also known as the Kuhn–Munkres algorithm, which solves the maximum weighted matching problem. For the weights between bacterial identities in two consecutive time steps, we used values of the Euclidean distance. The result of the procedure is demonstrated in Fig. 7.2(b), where positions, velocities, and orientation of most bacteria are identified.

7.3 SELF-PROPELLED RODS MODEL

In this section, we introduce a self-propelled rods model with the aim to formalize the observed dynamics of bacterial suspensions in a two-dimensional environment in computationally and mathematically convenient way. We are going to regard each bacterium as a sequence of n connected beads and write down equations of motion for each bead (Kirchhoff, Löwen, and Klein 1996). We assume that every bacterium is able to propel itself. Such models are known as a self-propelled rods (SPR) models (Wensink et al. 2012).

Let us consider a system of N rods that move in a two-dimensional domain of size L with periodic boundaries, which we denote $\Omega := \mathbb{U}^2, \mathbb{U} := \mathbb{R}/(L\mathbb{Z})$. A rod is described with a position $r_\alpha \in \mathbb{U}^2$ and a velocity $u_\alpha \in \mathbb{R}^2$ (cf. Fig. 7.3). It is common to consider rods as having the same magnitude of the velocity, i.e., $\|u_\alpha\| \equiv \text{const}, \alpha = 1, \ldots, N$, but being able to only change their orientation. However, for our purposes, we will assume that rods' velocity magnitudes are constant but nonidentical and sampled from some prior distribution, i.e., $\|u_\alpha\| \sim \pi_u$. From experimental work, we know that the temperature of the microfluidic environment is set $T = 30\,^\circ\text{C} = 303.15\,\text{K}$.

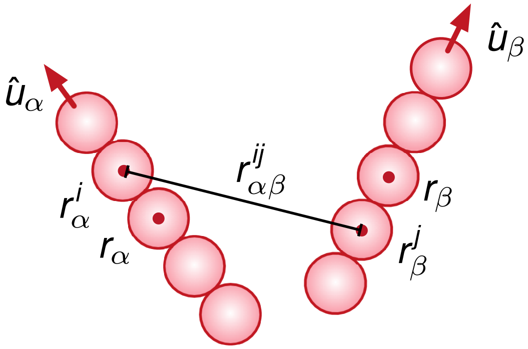

Figure 7.3: Representation of bacteria as self-propelled rods. A rod α is described with a position of the center of mass r_α and unit velocity $\hat{u}_\alpha$. Positions r^i_α of other constituent beads are calculated using the properties of the rods.

We postulate SPRs to obey the following system of SDEs:

$$\begin{aligned} \mathrm{d}r_\alpha &= u_\alpha \,\mathrm{d}t - \frac{1}{k_B T} D^\alpha_T \nabla_{r_\alpha} U \,\mathrm{d}t + \sqrt{2D_\parallel}\, \hat{u}_{\alpha,\parallel}\, \mathrm{d}W^\alpha_1 + \sqrt{2D_\perp}\, \hat{u}_{\alpha,\perp}\, \mathrm{d}W^\alpha_2 \\ \mathrm{d}\hat{u}_\alpha &= -\frac{1}{k_B T} D_R \nabla_{\hat{u}_\alpha} U \,\mathrm{d}t + \sqrt{2D_R}\, \hat{u}_{\alpha,\perp}\, \mathrm{d}W^\alpha_3, \end{aligned} \tag{7.3.4}$$

where k_B is Boltzmann's constant, D^α_T is the diffusion tensor, $\hat{u}_\alpha = \frac{u_\alpha}{\|u_\alpha\|}$ denotes a unit velocity vector, $\hat{u}_{\alpha,\parallel}$ and $\hat{u}_{\alpha,\perp}$ are its longitudinal and transversal components, respectively.

In order to account for the fluctuating environment and for variations in internal structure of bacteria, rods are subject to several stochastic forces modeled with families of independent Wiener processes, i.e., $(W^\alpha_1(t))_{t\geq 0}$, $(W^\alpha_2(t))_{t\geq 0}$, and $(W^\alpha_3(t))_{t\geq 0}, \alpha = 1, \ldots, N$, accounting for longitudinal and transversal perturbations to rods' positions and rotational perturbations to rods' orientations, respectively. Noise strengths for each family are $D_\parallel$, $D_\perp$, and D_R, respectively. The diffusion tensor is defined in terms of longitudinal and transversal noise strengths as

$$D^\alpha_T = \left[D_\perp (I - \hat{u}_\alpha \otimes \hat{u}_\alpha) + D_\parallel \hat{u}_\alpha \otimes \hat{u}_\alpha\right],$$

where I is the identity matrix and $\otimes$ denotes the outer vector product. It has been established (Tirado, Martínez, and Torre 1984) that translational and orientational short-time self-diffusion coefficients for bacterial suspensions can be approximated as

$$\begin{aligned} D_\parallel &= \frac{D_0}{2\pi}\left(\ln a - 0.207 + \frac{0.980}{a} - \frac{0.133}{a^2}\right), \\ D_\perp &= \frac{D_0}{4\pi}\left(\ln a + 0.839 + \frac{0.185}{a} + \frac{0.233}{a^2}\right), \\ D_R &= \frac{3D_0}{\pi l^2}\left(\ln p - 0.662 + \frac{0.917}{a} - \frac{0.050}{a^2}\right), \end{aligned}$$

where $D_0 = \dfrac{k_B T}{\eta_S l}$, η_S is a viscosity coefficient, l is rod's length, and a is rod's aspect ratio. The effective volume fraction of the system is

$$\phi = \frac{N}{A}\left[\lambda(l - \lambda) + \frac{\pi\lambda^2}{4}\right],$$

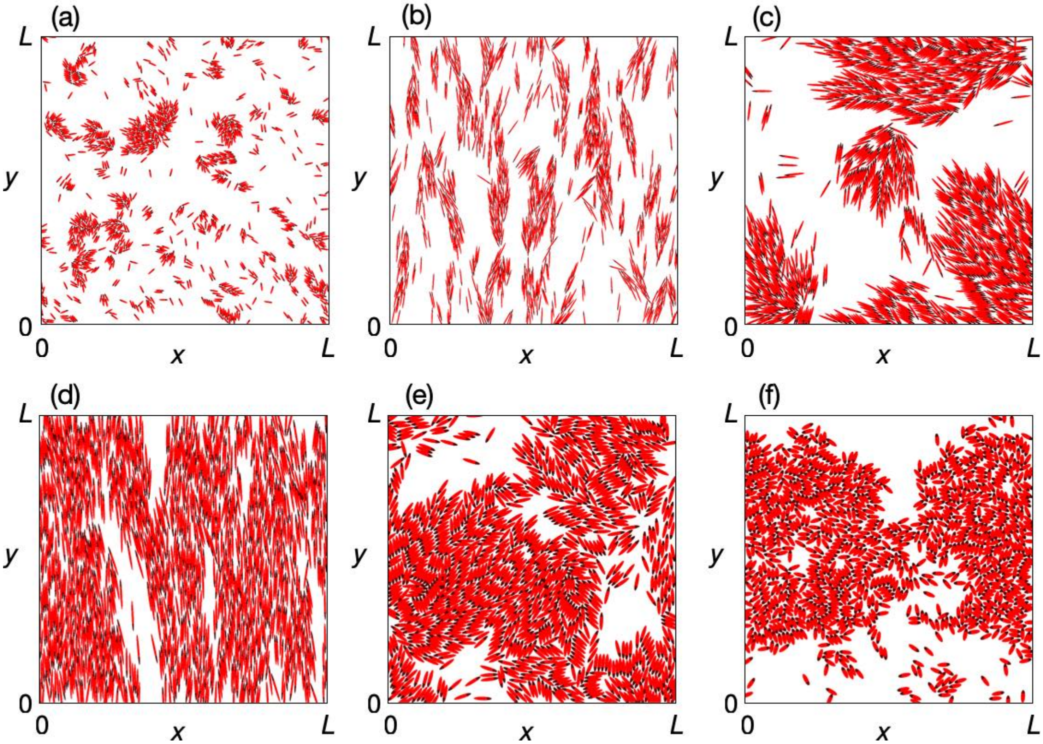

Figure 7.4: Exemplary SPR dynamics due to Eq. (7.3.4) with Yukawa potential for $N = 1000$ rods. (a) Diluted phase with $\phi = 0.17$, $a = 6$, $U_0 = 3e^{-20}$; (b) swarming phase with $\phi = 0.25$, $a = 15$, $U_0 = 1e^{-19}$; (c) bionematic phase with $\phi = 0.5$, $a = 10$, $U_0 = 1e^{-19}$; (d) laning phase with $\phi = 0.75$, $a = 15$, $U_0 = 3e^{-20}$; (e) turbulence phase with $\phi = 0.75$, $a = 5$, $U_0 = 3e^{-20}$; (f) jamming phase with $\phi = 0.6$, $a = 3$, $U_0 = 1e^{-20}$. Rods are displayed as red ellipses with black tips denoting the direction of motion.

where $A = L^2$ denotes the area of the domain.

Interactions between rods are accounted for by an interaction potential U that considers every pairwise bead interaction

$$U = \sum_{\substack{\alpha,\beta \\ \alpha>\beta}} U_{\alpha\beta}.$$

One of the common potentials for systems of SPRs is the Yukawa potential

$$U_{\alpha\beta} = \frac{U_0}{n^2} \sum_{i=1}^{n} \sum_{j=1}^{n} \begin{cases} \frac{e^{-r_{\alpha\beta}^{ij}/\lambda}}{r_{\alpha\beta}^{ij}} & \text{if } r_{\alpha\beta}^{ij} \leq \lambda \\ 0 & \text{if } r_{\alpha\beta}^{ij} > \lambda \end{cases}, \tag{7.3.5}$$

where U_0 is the interaction strength, λ is maximal interaction radius, $r_{\alpha\beta}^{ij}$ is the distance between ith bead of a rod α and jth bead of a rod j, i.e.,

$$r_{\alpha\beta}^{ij} = \left\| (r_\beta + l_j \hat{u}_\beta) - (r_\alpha + l_i \hat{u}_\alpha) \right\|,$$

where

$$l_i = -\frac{l-\lambda}{2} + i\frac{l-\lambda}{n-1}, \; i = 0, \dots, n-1$$

denotes the distance the center r_α of a rod to the centers of each of its beads.

In order to use Eq. (7.3.4), we need to know spatial gradients of the interaction potential with respect to both position and velocity vectors. For the Yukawa potential, they read

$$\begin{aligned}\nabla_{r_\alpha} U &= -\frac{U_0}{n^2}\sum_\beta \sum_{i,j=1}^{n} \frac{\lambda + r_{\alpha\beta}^{ij}}{\lambda} \frac{1}{(r_{\alpha\beta}^{ij})^2} e^{-r_{\alpha\beta}^{ij}/\lambda} \nabla_{r_\alpha} r_{\alpha\beta}^{ij}, \\ \nabla_{\hat{u}_\alpha} U &= -\frac{U_0}{n^2}\sum_\beta \sum_{i,j=1}^{n} \frac{\lambda + r_{\alpha\beta}^{ij}}{\lambda} \frac{1}{(r_{\alpha\beta}^{ij})^2} e^{-r_{\alpha\beta}^{ij}/\lambda} \nabla_{\hat{u}_\alpha} r_{\alpha\beta}^{ij},\end{aligned} \tag{7.3.6}$$

where spatial gradients of interbead distances are

$$\begin{aligned}\nabla_{r_\alpha} r_{\alpha\beta}^{ij} &= -\frac{1}{r_{\alpha\beta}^{ij}} r_{\alpha\beta}^{ij}, \\ \nabla_{\hat{u}_\alpha} r_{\alpha\beta}^{ij} &= -\frac{l_i}{r_{\alpha\beta}^{ij}} r_{\alpha\beta}^{ij}.\end{aligned} \tag{7.3.7}$$

By substituting Eq. (7.3.7) into Eq. (7.3.6), we obtain

$$\begin{aligned}\nabla_{r_\alpha} U &= \frac{U_0}{n^2}\sum_\beta \sum_{i,j=1}^{n} \frac{\lambda + r_{\alpha\beta}^{ij}}{\lambda} \frac{1}{(r_{\alpha\beta}^{ij})^3} e^{-r_{\alpha\beta}^{ij}/\lambda} r_{\alpha\beta}^{ij}, \\ \nabla_{u^\alpha} U &= \frac{U_0}{n^2}\sum_\beta \sum_{i,j=1}^{n} \frac{\lambda + r_{\alpha\beta}^{ij}}{\lambda} \frac{l_i}{(r_{\alpha\beta}^{ij})^3} e^{-r_{\alpha\beta}^{ij}/\lambda} r_{\alpha\beta}^{ij}.\end{aligned}$$

With this, Eq. (7.3.4) is prepared for numerical analysis. Exemplary SPR dynamics resulting from this model is presented in Fig. 7.4.

8

CONCLUSIONS AND OUTLOOK

8.1 SUMMARY OF OUR CONTRIBUTIONS

In this thesis, we concentrated on the analysis of self-organization in systems of SPPs with nonlocal interactions. These are the particles that are able to perform self-propulsion. The interest to study them came from an observation that macroscopic dynamics they exhibit as a whole is different from the dynamics of each constituent particle. Common examples of related self-organization include swarming of bacteria, flocking of birds, schooling of fish, and ensembles of robots, to name a few. Our analysis was two-sided. On one hand, we described particle motion in terms of ODEs or SDEs. This allowed us to design the principles according to which each particle moves and subsequently to investigate how changes in microscale influence the collective behavior. On the other hand, in order to efficiently investigate self-organization phenomena on the large scale, i.e., with $N \to \infty$, we developed continuum descriptions for each SPP model we presented. We considered two different formulations of it, i.e., kinetic and hydrodynamic. The first one describes the distribution of particles over the full phase space while the second one is formulated as a system of conservation laws for the fields that depend on spatial variables only, e.g., particle number densities and momenta.

First, we developed a new SPP model that were able to generate such a novel collective phenomenon as a self-propelled chimera state. In general, chimera states had previously been discovered in systems of network oscillators that were described by the Kuramoto model. There, chimera states signify the separation of an oscillatory ensemble into two groups, one completely synchronized and one chaotic. We found that in an SPP context, there were two such states possible. The first one was spatially homogeneous, i.e., without any localization of particles while the second one was spatially inhomogeneous, i.e., where synchronized particles were additionally able to contract into a high-density cloud. These results held in particle and continuum formulations.

Second, we considered a generalization of the aforementioned model to the active matter setup, i.e., where stochastic perturbations upon the particles are unavoidable. Due to alignment interaction rules subject to a phase lag, our new model was implicitly characterized as chiral. For this model, we rigorously developed the continuum limit description, formalized by a certain PDE. We were able to find new analytical solutions of it which subsequently allowed us to perform linear stability analysis towards them against spatially inhomogeneous perturbations. Such analysis revealed the existence of a large variety of chiral counterparts of such celebrated linear active matter patters as traveling bands, clouds, and vortexes as well as ‘multiheaded’ versions of the aforementioned self-propelled chimera states.

Third, we formulated a new SPP model where orientational dynamics of underlying particles obeyed second order equations. In that work, we primarily concentrated on spatially homogeneous particle configurations, which allowed us to combine theories of active matter and oscillatory networks. We found that an SPP system could also self-organize into a solitary state, where a subset of particles formed a separate frequency-synchronized group. Moreover, we found a cascade of solitary states with different numbers of frequency clusters. In the view of the global coupling imposed in that model, we derived a mean-field limit for spatially homogeneously distributed SPPs and oscillators. The analysis of the mean-field equation confirmed the existence of solitary states in the limit of $N \to \infty$.

Fourth, all aforementioned continuum and mean-field limit descriptions were formalized in terms of nonlinear PDEs with nonlocal integral terms that corresponded to respective nonlocal particle interactions from finite size models. The integration of those equations were not straightforward and in order to able to proceed with such analysis, we put effort in the development of dedicated FVMs. They were constructed with the consideration of positivity preservation of solutions, conservation of mass, and energy dissipation. They were used for the analysis of most of the aforementioned models.

8.2 FUTURE WORK

In Section 4.2, by following the OA reduction procedure, we developed an alternative formulation for hydrodynamic equations for interacting particles that exhibited chimeric motion. This procedure had proved to be useful in the description of the dynamics in oscillatory networks. The resulting equations described particle motion in terms of a system of PDEs for density and polar order fields. The polar order equation appeared to be different from a momentum equation we obtained in Section 4.1. The subsequent analysis of this difference as well as of new equations themselves must be carried out.

The chimera states discussed in this thesis were characteristic for two-dimensional systems. In order to observe them in three dimensions, a new formulation with orientational degrees of freedom must be employed in order to introduce a phase lag into particle alignment interactions. We developed such a model and numerical simulations did reveal three-dimensional analogues of self-propelled chimera states. These results must be analyzed from the point of view of the theory of network oscillators, from where chimera states originate, and from the point of view of the active matter theory.

The chimera states that we reported existed for phase lag values $|\alpha| \leq \frac{\pi}{2}$, i.e., in the so-called in-phase region. It is known for the Kuramoto model that in the opposite case of out-of-phase interactions, other oscillatory collective phenomena arise such as chaotic, rotating, or antiphase chimera states. The latter reminds the nematic order if interpreted from the point of view of the active matter theory. Considering the current attention to active nematics, the further investigation in that direction might prove rewarding.

Our work on solitary states for SPP systems was restricted to spatially homogeneous particle configurations. As the next step to understanding complete dynamics of that second-order system, a similar analysis as the one we performed for chiral active matter should be carried out. It is often the case that one observes nontrivial pattern formation in large scale nonlinear interacting particle systems.

We established a protocol to observe the swarming of *B. subtilis* in microfluidic chips. Afterwards, we were able to extract trajectories of each single bacterium per experimental run by implementing a dedicated multitarget tracking procedure that included image processing and data association. We introduced an SPR model whose variation is in common use for the description of bacterial swarming. As a result, we found that the model did not account for the swarming of *B. subtilis* that we observed. Moreover, such a particle formulation did not allow us to apply the continuum limit studies we developed for the other systems. Therefore, subsequent analysis should first concentrate on the construction of alternative models for bacterial motion. One potential candidate is an SPP model where particles are nematic by construction as well as obey nematic alignment rules. Another promising model is the one where particle's surface is defined by an ellipsoid.

NOTATION

SYMBOL	DESCRIPTION
$\mathbb{N}$	The set of natural numbers.
$\mathbb{Z}$	The set of integer numbers.
$\mathbb{R}$	The set of real numbers.
$\mathbb{R}_+$	The set of positive real numbers.
$\mathbb{C}$	The set of complex numbers.
$\mathbb{T}$	The one dimensional space with periodic boundaries extending from 0 to 2π, i.e., $\mathbb{R}/(2\pi\mathbb{Z})$.
$\mathbb{U}$	The one dimensional space with periodic boundaries extending from 0 to $L > 0$, i.e., $\mathbb{R}/(L\mathbb{Z})$.
$\mathbb{S}^{d-1}$	A unit $d-1$-dimensional sphere in $\mathbb{R}^d$, i.e., $\{x \in \mathbb{R}^d \mid \|x\| = 1\}$.
$\mid A \mid$	The cardinality of a set A.
$\mathcal{O}()$	Big o notation.

ACRONYMS

ABC	Approximate Bayesian Computation
ABP	Active Brownian Particle
BBGKY	Born-Bogolubov-Green-Kirkwood-Yvon
CFL	Courant–Friedrichs–Lewy
CL	Continuum Limit
FVM	Finite Volume Method
IVP	Initial Value Problem
MPI	Message Passing Interface
OA	Ott-Antonsen
ODE	Ordinary Differential Equation
PDE	Partial Differential Equation
PDF	Probability Density Function
PDMS	Polydimethylsiloxane
SDE	Stochastic Differential Equation
SPP	Self-propelled Particle
SPR	Self-propelled Rod
YEPD	Yeast Extract Peptone Dextrose

BIBLIOGRAPHY

Abrams, D. M. and S. H. Strogatz (Oct. 2004). “Chimera States for Coupled Oscillators”. *Phys. Rev. Lett.* 93 (17), p. 174102 (cit. on pp. 9, 18, 22, 26, 84).

Acebrón, J. A., L. L. Bonilla, C. J. Pérez Vicente, F. Ritort, and R. Spigler (Apr. 2005). “The Kuramoto model: A simple paradigm for synchronization phenomena”. *Rev. Mod. Phys.* 77 (1), pp. 137–185 (cit. on p. 84).

Anderson, J. (1995). *Computational Fluid Dynamics*. Computational Fluid Dynamics: The Basics with Applications. McGraw-Hill Education (cit. on p. 6).

Archer, A. J. and M. Rauscher (Sept. 2004a). “Dynamical density functional theory for interacting Brownian particles: stochastic or deterministic?” *Journal of Physics A: Mathematical and General* 37.40, pp. 9325–9333 (cit. on p. 33).

Archer, A. J. and M. Rauscher (Sept. 2004b). “Dynamical density functional theory for interacting Brownian particles: stochastic or deterministic?” *Journal of Physics A: Mathematical and General* 37.40, pp. 9325–9333 (cit. on pp. 38, 81, 82).

Ashwin, P. and O. Burylko (2015). “Weak chimeras in minimal networks of coupled phase oscillators”. *Chaos: An Interdisciplinary Journal of Nonlinear Science* 25.1, p. 013106 (cit. on p. 26).

Barbaro, A. B. T., J. A. Cañizo, J. A. Carrillo, and P. Degond (2016). “Phase transitions in a kinetic flocking model of Cucker-Smale type”. *Multiscale Model. Simul.* 14.3, pp. 1063–1088 (cit. on p. 81).

Bäuerle, T., R. C. Löffler, and C. Bechinger (2020). “Formation of stable and responsive collective states in suspensions of active colloids”. *Nature Communications* 11.1, p. 2547 (cit. on p. 9).

Berner, R., A. Polanska, E. Schöll, and S. Yanchuk (2019). *Solitary states in adaptive nonlocal oscillator networks* (cit. on p. 26).

Bertin, E., M. Droz, and G. Grégoire (Aug. 2006). “Boltzmann and hydrodynamic description for self-propelled particles”. *Phys. Rev. E* 74 (2), p. 022101 (cit. on p. 81).

Bertin, E., M. Droz, and G. Grégoire (Oct. 2009). “Hydrodynamic equations for self-propelled particles: microscopic derivation and stability analysis”. *Journal of Physics A: Mathematical and Theoretical* 42.44, p. 445001 (cit. on pp. 48, 81).

Braun, W. and K. Hepp (1977). “The Vlasov dynamics and its fluctuations in the $1/N$ limit of interacting classical particles”. *Comm. Math. Phys.* 56.2, pp. 101–113 (cit. on p. 40).

Calovi, D. S., U. Lopez, S. Ngo, C. Sire, H. Chaté, and G. Theraulaz (2014). “Swarming, schooling, milling: phase diagram of a data-driven fish school model”. *New Journal of Physics* 16.1, p. 015026 (cit. on p. 9).

Cañizo, J. A., J. A. Carrillo, and J. Rosado (2011). “A WELL-POSEDNESS THEORY IN MEASURES FOR SOME KINETIC MODELS OF COLLECTIVE MOTION”. *Mathematical Models and Methods in Applied Sciences* 21.03, pp. 515–539 (cit. on pp. 33, 81).

Carrillo, J. A., Y.-P. Choi, and M. Hauray (2014a). “The derivation of swarming models: Mean-field limit and Wasserstein distances”. In: *Collective Dynamics from Bacteria to Crowds*. Ed. by A. Muntean and F. Toschi. Vol. 553. CISM International Centre for Mechanical Sciences. Springer Vienna, pp. 1–46 (cit. on p. 20).

Carrillo, J. A., M. R. D’Orsogna, and V. Panferov (2009). “Double milling in self-propelled swarms from kinetic theory”. *Kinet. Relat. Models* 2.2, pp. 363–378 (cit. on p. 81).

Carrillo, J. A., R. S. Gvalani, G. A. Pavliotis, and A. Schlichting (2020). “Long-time behaviour and phase transitions for the Mckean-Vlasov equation on the torus”. *Arch. Ration. Mech. Anal.* 235.1, pp. 635–690 (cit. on p. 84).

Carrillo, J. A., Y.-P. Choi, and L. Pareschi (2019). “Structure preserving schemes for the continuum Kuramoto model: Phase transitions”. *Journal of Computational Physics* 376, pp. 365–389 (cit. on pp. 31, 36, 81, 84, 85, 101, 106).

Carrillo, J. A., A. Chertock, and Y. Huang (2015). “A Finite-Volume Method for Nonlinear Nonlocal Equations with a Gradient Flow Structure”. *Communications in Computational Physics* 17.1, pp. 233–258 (cit. on pp. 81, 87, 91).

Carrillo, J. A., M. Fornasier, G. Toscani, and F. Vecil (2010). “Particle, kinetic, and hydrodynamic models of swarming”. In: *Mathematical modeling of collective behavior in socio-economic and life sciences*. Model. Simul. Sci. Eng. Technol. Birkhäuser Boston, Boston, MA, pp. 297–336 (cit. on p. 81).

Carrillo, J. A., H. Ranetbauer, and M.-T. Wolfram (2016). “Numerical simulation of nonlinear continuity equations by evolving diffeomorphisms”. *Journal of Computational Physics* 327, pp. 186–202 (cit. on p. 81).

Carrillo, J. A., Y.-P. Choi, and M. Hauray (2014b). “The derivation of swarming models: mean-field limit and Wasserstein distances”. In: *Collective dynamics from bacteria to crowds*. Vol. 553. CISM Courses and Lect. Springer, Vienna, pp. 1–46 (cit. on p. 81).

Carrillo, J., Y.-P. Choi, S.-Y. Ha, M.-J. Kang, and Y. Kim (2014). “Contractivity of Transport Distances for the Kinetic Kuramoto Equation”. *Journal of Statistical Physics* 156.2, pp. 395–415 (cit. on pp. 33, 81).

Chaté, H., F. Ginelli, G. Grégoire, F. Peruani, and F. Raynaud (2008). “Modeling collective motion: variations on the Vicsek model”. English. *The European Physical Journal B* 64.3-4, pp. 451–456 (cit. on pp. 7, 9, 10).

Chen, C., S. Liu, X.-q. Shi, H. Chaté, and Y. Wu (Jan. 2017). “Weak synchronization and large-scale collective oscillation in dense bacterial suspensions”. *Nature* 542, 210 EP - (cit. on pp. 9, 25).

Chepizhko, A. A. and V. L. Kulinskii (2009). “The kinetic regime of the Vicsek model”. *AIP Conference Proceedings* 1198.1, pp. 25–33 (cit. on p. 10).

Chepizhko, O. and V. Kulinskii (2014). “The hydrodynamic description for the system of self-propelled particles: Ideal Viscek fluid”. *Physica A: Statistical Mechanics and its Applications* 415, pp. 493–502 (cit. on p. 20).

Coddington, A. and N. Levinson (1955). *Theory of Ordinary Differential Equations*. International series in pure and applied mathematics. McGraw-Hill (cit. on p. 3).

Dean, D. S. (1996). “Langevin equation for the density of a system of interacting Langevin processes”. *Journal of Physics A: Mathematical and General* 29.24, p. L613 (cit. on p. 19).

Degond, P. and S. Motsch (2008). “Continuum limit of self-driven particles with orientation interaction”. *Mathematical Models and Methods in Applied Sciences* 18.supp01, pp. 1193–1215 (cit. on pp. 10, 25).

Degond, P., G. Dimarco, and T. B. N. Mac (2014). “Hydrodynamics of the Kuramoto-Vicsek model of rotating self-propelled particles”. *Mathematical Models and Methods in Applied Sciences* 24.02, pp. 277–325 (cit. on p. 9).

Degond, P., A. Frouvelle, and J.-G. Liu (2015). “Phase Transitions, Hysteresis, and Hyperbolicity for Self-Organized Alignment Dynamics”. *Archive for Rational Mechanics and Analysis* 216.1, pp. 63–115 (cit. on p. 81).

Denk, J., L. Huber, E. Reithmann, and E. Frey (Apr. 2016). “Active Curved Polymers Form Vortex Patterns on Membranes”. *Phys. Rev. Lett.* 116 (17), p. 178301 (cit. on p. 9).

Dimarco, G. and L. Pareschi (2014). “Numerical methods for kinetic equations”. *Acta Numerica* 23, pp. 369–520 (cit. on p. 81).

Dobrushin, R. L. (1979). “Vlasov equations”. *Functional Analysis and Its Applications* 13.2, pp. 115–123 (cit. on pp. 22, 82).

Ērglis, K., Q. Wen, V. Ose, A. Zeltins, A. Sharipo, P. A. Janmey, and A. Cēbers (2007). “Dynamics of Magnetotactic Bacteria in a Rotating Magnetic Field”. *Biophysical Journal* 93.4, pp. 1402–1412 (cit. on p. 9).

Evans, G., J. Blackledge, and P. Yardley (1999). *Analytic Methods for Partial Differential Equations*. Springer Undergraduate Mathematics Series. Springer London (cit. on p. 4).

Evans, L. and A. M. Society (1998). *Partial Differential Equations*. Graduate studies in mathematics. American Mathematical Society (cit. on pp. 4, 5).

Farrell, F. D. C., M. C. Marchetti, D. Marenduzzo, and J. Tailleur (June 2012). “Pattern Formation in Self-Propelled Particles with Density-Dependent Motility”. *Phys. Rev. Lett.* 108 (24), p. 248101 (cit. on p. 7).

Friedrich, B. M. and F. Jülicher (2007). “Chemotaxis of sperm cells”. *Proceedings of the National Academy of Sciences* 104.33, pp. 13256–13261 (cit. on p. 9).

Geyer, D., A. Morin, and D. Bartolo (2018). “Sounds and hydrodynamics of polar active fluids”. *Nature Materials* 17, pp. 789–793 (cit. on p. 9).

Gompper, G., R. G. Winkler, T. Speck, A. Solon, C. Nardini, F. Peruani, H. Löwen, R. Golestanian, U. B. Kaupp, L. Alvarez, T. Kiørboe, E. Lauga, W. C. K. Poon, A. DeSimone, S. Muiños-Landin, A. Fischer, N. A. Söker, F. Cichos, R. Kapral, P. Gaspard, M. Ripoll, F. Sagues, A. Doostmohammadi, J. M. Yeomans, I. S. Aranson, C. Bechinger, H. Stark, C. K. Hemelrijk, F. J. Nedelec, T. Sarkar, T. Aryaksama, M. Lacroix, G. Duclos, V. Yashunsky, P. Silberzan, M. Arroyo, and S. Kale (Feb. 2020). “The 2020 motile active matter roadmap”. *Journal of Physics: Condensed Matter* 32.19, p. 193001 (cit. on p. 7).

Gropp, W., E. Lusk, and A. Skjellum (2014). *Using MPI: Portable Parallel Programming with the Message-Passing Interface*. Scientific and Engineering Computation. MIT Press (cit. on p. 100).

Großmann, R., L. Schimansky-Geier, and P. Romanczuk (Aug. 2013). “Self-propelled particles with selective attraction–repulsion interaction: from microscopic dynamics to coarse-grained theories”. *New Journal of Physics* 15.8, p. 085014 (cit. on p. 57).

Großmann, R., P. Romanczuk, M. Bär, and L. Schimansky-Geier (Dec. 2014). “Vortex Arrays and Mesoscale Turbulence of Self-Propelled Particles”. *Phys. Rev. Lett.* 113 (25), p. 258104 (cit. on pp. 10, 19).

Guckenheimer, J. and P. Holmes (1990). *Nonlinear oscillations, dynamical systems, and bifurcations of vector fields*. Applied mathematical sciences. Springer-Verlag (cit. on p. 95).

Guckenheimer, J. and P. Holmes (2002). *Nonlinear Oscillations, Dynamical Systems, and Bifurcations of Vector Fields*. Applied Mathematical Sciences. Springer New York (cit. on pp. 3, 4).

Gupta, S., A. Campa, and S. Ruffo (2014a). “Kuramoto model of synchronization: equilibrium and nonequilibrium aspects”. *Journal of Statistical Mechanics: Theory and Experiment* 2014.8, R08001 (cit. on pp. 44, 45, 86).

Gupta, S., A. Campa, and S. Ruffo (Feb. 2014b). “Nonequilibrium first-order phase transition in coupled oscillator systems with inertia and noise”. *Phys. Rev. E* 89 (2), p. 022123 (cit. on p. 39).

Hagerstrom, A. M., T. E. Murphy, R. Roy, P. Hovel, I. Omelchenko, and E. Scholl (Sept. 2012). “Experimental observation of chimeras in coupled-map lattices”. *Nat Phys* 8.9, pp. 658–661 (cit. on p. 9).

Hairer, E., C. Lubich, and G. Wanner (2002). *Geometric Numerical Integration: Structure-Preserving Algorithms for Ordinary Differential Equations*. Springer series in computational mathematics. Springer (cit. on pp. 95, 96, 98).

Hale, J. (2009). *Ordinary Differential Equations*. Dover Books on Mathematics Series. Dover Publications (cit. on p. 3).

Han, M., J. Yan, S. Granick, and E. Luijten (2017). "Effective temperature concept evaluated in an active colloid mixture". *Proceedings of the National Academy of Sciences* 114.29, pp. 7513–7518 (cit. on p. 9).

Hellmann, F., P. Schultz, P. Jaros, R. Levchenko, T. Kapitaniak, J. Kurths, and Y. Maistrenko (2020). "Network-induced multistability through lossy coupling and exotic solitary states". *Nature Communications* 11.1, p. 592 (cit. on p. 26).

Hirsch, C. (2006). *Numerical Computation of Internal and External Flows*. Butterworth-Heinemann Limited (cit. on p. 6).

Hirsch, M., S. Smale, and R. Devaney (2004). *Differential Equations, Dynamical Systems, and an Introduction to Chaos*. Pure and Applied Mathematics - Academic Press. Elsevier Science (cit. on p. 95).

https://figshare.com/projects/Traveling_Bands_Clouds_and_Vortices_of_Chiral_Active_Matter/82163 (n.d.) (cit. on pp. 23, 25).

https://github.com/raven91 (n.d.) (cit. on p. 100).

https://www.youtube.com/playlist?list=PLjL7stT6PH4x1qpj_fFa2Rx5bI6EygOuw (n.d.) (cit. on pp. 10, 11, 20).

https://www.youtube.com/playlist?list=PLjL7stT6PH4xdc4X5Ee7xAr2vm49uIHvW (n.d.) (cit. on pp. 23, 25).

https://www.youtube.com/playlist?list=PLjL7stT6PH4z3MFm3uyJFBfduO_yqHLbx (n.d.) (cit. on pp. 26, 34).

Ihle, T. (Oct. 2013). "Invasion-wave-induced first-order phase transition in systems of active particles". *Phys. Rev. E* 88 (4), p. 040303 (cit. on p. 81).

Izhikevich, E. (2007). *Dynamical Systems in Neuroscience*. Computational neuroscience Dynamical systems in neuroscience. MIT Press (cit. on p. 3).

Jaros, P., S. Brezetsky, R. Levchenko, D. Dudkowski, T. Kapitaniak, and Y. Maistrenko (2018). "Solitary states for coupled oscillators with inertia". *Chaos: An Interdisciplinary Journal of Nonlinear Science* 28.1, p. 011103 (cit. on pp. 26–28).

Jaros, P., Y. Maistrenko, and T. Kapitaniak (Feb. 2015). "Chimera states on the route from coherence to rotating waves". *Phys. Rev. E* 91 (2), p. 022907 (cit. on p. 26).

Jordan, D., P. Dominic William Jordan, P. Smith, and S. Jordan (1999). *Nonlinear Ordinary Differential Equations: An Introduction to Dynamical Systems*. Oxford applied and engineering mathematics. Oxford University Press (cit. on p. 3).

Joshi, C. M. and S. K. Bissu (1991). "Some inequalities of Bessel and modified Bessel functions". *Journal of the Australian Mathematical Society. Series A. Pure Mathematics and Statistics* 50.2, pp. 333–342 (cit. on p. 43).

Kaiser, A., A. Snezhko, and I. S. Aranson (2017). "Flocking ferromagnetic colloids". *Science Advances* 3.2, e1601469 (cit. on p. 9).

Kapitaniak, T., P. Kuzma, J. Wojewoda, K. Czolczynski, and Y. Maistrenko (Sept. 2014). "Imperfect chimera states for coupled pendula". *Scientific Reports* 4, p. 6379 (cit. on pp. 9, 26).

Kastberger, G., E. Schmelzer, and I. Kranner (Sept. 2008). "Social Waves in Giant Honeybees Repel Hornets". *PLoS ONE* 3.9, pp. 1–16 (cit. on p. 9).

Katok, A. and B. Hasselblatt (1997). *Introduction to the Modern Theory of Dynamical Systems*. Encyclopedia of Mathematics and its Applications. Cambridge University Press (cit. on p. 3).

Kipnis, C. and C. Landim (1998a). *Scaling Limits of Interacting Particle Systems*. Grundlehren der mathematischen Wissenschaften. Springer Berlin Heidelberg (cit. on pp. 22, 37, 82).

Kipnis, C. and C. Landim (1998b). *Scaling Limits of Interacting Particle Systems*. Grundlehren der mathematischen Wissenschaften. Springer Berlin Heidelberg (cit. on p. 33).

Kirchhoff, T., H. Löwen, and R. Klein (May 1996). "Dynamical correlations in suspensions of charged rodlike macromolecules". *Phys. Rev. E* 53 (5), pp. 5011–5022 (cit. on p. 117).

Kruk, N., J. A. Carrillo, and H. Koeppl (Aug. 2020). "Traveling bands, clouds, and vortices of chiral active matter". *Phys. Rev. E* 102 (2), p. 022604 (cit. on pp. 3, 22, 35, 82, 86, 105, 108, 110, 111).

Kruk, N., J. A. Carrillo, and H. Koeppl (preprint). "A finite volume method for continuum limit equations of nonlocally interacting active chiral particles". *Submitted to Journal of Computational Physics. Preprint is available at https://arxiv.org/abs/2008.08493* (cit. on pp. 3, 34, 36, 81).

Kruk, N., Y. Maistrenko, and H. Koeppl (Sept. 2018). "Self-propelled chimeras". *Phys. Rev. E* 98 (3), p. 032219 (cit. on pp. 3, 10, 13, 19, 22–26, 37, 41, 84, 104, 106, 108).

Kruk, N., Y. Maistrenko, and H. Koeppl (Nov. 2020). "Solitary states in the mean-field limit". *Chaos: An Interdisciplinary Journal of Nonlinear Science* 30.11, p. 111104 (cit. on pp. 3, 25, 27, 29, 34, 36).

Kuramoto, Y. (1984). *Chemical Oscillations, Waves, and Turbulence*. Springer Series in Synergetics. Springer Berlin Heidelberg (cit. on pp. 9, 25, 26, 84).

Kuramoto, Y. and D. Battogtokh (2002). "Coexistence of Coherence and Incoherence in Nonlocally Coupled Phase Oscillators". *Nonlinear Phenomena in Complex Systems* 5.4, pp. 380–385 (cit. on pp. 9, 19, 22, 26, 84).

Kuznetsov, Y. (1998). *Elements of Applied Bifurcation Theory*. Applied Mathematical Sciences. Springer New York (cit. on p. 3).

Lancellotti, C. (2005). "On the Vlasov Limit for Systems of Nonlinearly Coupled Oscillators without Noise". *Transport Theory and Statistical Physics* 34.7, pp. 523–535 (cit. on pp. 22, 33, 81).

Laney, C. (1998). *Computational Gasdynamics*. Computational Gasdynamics. Cambridge University Press (cit. on pp. 6, 40).

Larger, L., B. Penkovsky, and Y. Maistrenko (July 2015). "Laser chimeras as a paradigm for multistable patterns in complex systems". *Nature Communications* 6, p. 7752 (cit. on p. 9).

Lauga, E., W. R. DiLuzio, G. M. Whitesides, and H. A. Stone (2019/11/05 2006). "Swimming in Circles: Motion of Bacteria near Solid Boundaries". *Biophysical Journal* 90.2, pp. 400–412 (cit. on p. 9).

Lei, Q.-L., M. P. Ciamarra, and R. Ni (2019). "Nonequilibrium strongly hyperuniform fluids of circle active particles with large local density fluctuations". *Science Advances* 5.1 (cit. on p. 9).

Lemelle, L., J.-F. Palierne, E. Chatre, and C. Place (2010). "Counterclockwise Circular Motion of Bacteria Swimming at the Air-Liquid Interface". *Journal of Bacteriology* 192.23, pp. 6307–6308 (cit. on p. 9).

Leonard, N. E., T. Shen, B. Nabet, L. Scardovi, I. D. Couzin, and S. A. Levin (2012). "Decision versus compromise for animal groups in motion". *Proceedings of the National Academy of Sciences* 109.1, pp. 227–232 (cit. on p. 10).

Levis, D., I. Pagonabarraga, and B. Liebchen (Sept. 2019). "Activity induced synchronization: Mutual flocking and chiral self-sorting". *Phys. Rev. Research* 1 (2), p. 023026 (cit. on pp. 9, 81, 105).

Liebchen, B. and D. Levis (Aug. 2017). "Collective Behavior of Chiral Active Matter: Pattern Formation and Enhanced Flocking". *Phys. Rev. Lett.* 119 (5), p. 058002 (cit. on p. 9).

Maistrenko, Y., O. Popovych, O. Burylko, and P. A. Tass (Aug. 2004). "Mechanism of Desynchronization in the Finite-Dimensional Kuramoto Model". *Phys. Rev. Lett.* 93 (8), p. 084102 (cit. on p. 29).

Maistrenko, Y., B. Penkovsky, and M. Rosenblum (June 2014). "Solitary state at the edge of synchrony in ensembles with attractive and repulsive interactions". *Phys. Rev. E* 89 (6), p. 060901 (cit. on p. 26).

Marconi, U. M. B. and P. Tarazona (1999). "Dynamic density functional theory of fluids". *The Journal of Chemical Physics* 110.16, pp. 8032–8044 (cit. on p. 41).

Martens, E. A., S. Thutupalli, A. Fourrière, and O. Hallatschek (2013). "Chimera states in mechanical oscillator networks". *Proceedings of the National Academy of Sciences* 110.26, pp. 10563–10567 (cit. on p. 9).

Mishra, S., A. Baskaran, and M. C. Marchetti (June 2010). "Fluctuations and pattern formation in self-propelled particles". *Phys. Rev. E* 81 (6), p. 061916 (cit. on pp. 7, 68).

Moukalled, F., L. Mangani, and M. Darwish (2015). *The Finite Volume Method in Computational Fluid Dynamics: An Advanced Introduction with OpenFOAM® and Matlab*. Fluid Mechanics and Its Applications. Springer International Publishing (cit. on p. 6).

Munyaev, V. O., L. A. Smirnov, V. A. Kostin, G. V. Osipov, and A. Pikovsky (Feb. 2020). "Analytical approach to synchronous states of globally coupled noisy rotators". *New Journal of Physics* 22.2, p. 023036 (cit. on p. 36).

Nagai, K. H., Y. Sumino, R. Montagne, I. S. Aranson, and H. Chaté (Apr. 2015). "Collective Motion of Self-Propelled Particles with Memory". *Phys. Rev. Lett.* 114 (16), p. 168001 (cit. on pp. 7, 10, 81, 105).

Narinder, N., C. Bechinger, and J. R. Gomez-Solano (Aug. 2018). "Memory-Induced Transition from a Persistent Random Walk to Circular Motion for Achiral Microswimmers". *Phys. Rev. Lett.* 121 (7), p. 078003 (cit. on p. 9).

Neunzert, H. (1984). "An introduction to the nonlinear Boltzmann-Vlasov equation". In: *Kinetic Theories and the Boltzmann Equation*. Ed. by C. Cercignani. Berlin, Heidelberg: Springer Berlin Heidelberg, pp. 60–110 (cit. on pp. 33, 81).

Nicholson, D. (1983). *Introduction to plasma theory*. Wiley series in plasma physics. Wiley (cit. on p. 20).

Nourhani, A., V. H. Crespi, and P. E. Lammert (Sept. 2015). "Guiding Chiral Self-Propellers in a Periodic Potential". *Phys. Rev. Lett.* 115 (11), p. 118101 (cit. on p. 9).

O'Keeffe, K. P., H. Hong, and S. H. Strogatz (2017). "Oscillators that sync and swarm". *Nature Communications* 8.1, p. 1504 (cit. on pp. 7, 10).

Øksendal, B. (2003). *Stochastic Differential Equations: An Introduction with Applications*. Hochschultext / Universitext. Springer (cit. on p. 4).

Olmi, S., A. Navas, S. Boccaletti, and A. Torcini (Oct. 2014). "Hysteretic transitions in the Kuramoto model with inertia". *Phys. Rev. E* 90 (4), p. 042905 (cit. on p. 36).

Olver, F. W., D. W. Lozier, R. F. Boisvert, and C. W. Clark (2010). *NIST Handbook of Mathematical Functions*. 1st. New York, NY, USA: Cambridge University Press (cit. on pp. 42, 43, 85).

Omel'chenko, O. E. (Apr. 2018). "The mathematics behind chimera states". *Nonlinearity* 31.5, R121–R164 (cit. on p. 22).

Omel'chenko, O. E., M. Wolfrum, S. Yanchuk, Y. L. Maistrenko, and O. Sudakov (Mar. 2012). "Stationary patterns of coherence and incoherence in two-dimensional arrays of non-locally-coupled phase oscillators". *Phys. Rev. E* 85 (3), p. 036210 (cit. on p. 22).

Omel'chenko, O. E. and E. Knobloch (Sept. 2019). "Chimerapedia: coherence–incoherence patterns in one, two and three dimensions". *New Journal of Physics* 21.9, p. 093034 (cit. on p. 26).

Ott, E. and T. M. Antonsen (2008). “Low dimensional behavior of large systems of globally coupled oscillators”. *Chaos: An Interdisciplinary Journal of Nonlinear Science* 18.3, p. 037113 (cit. on p. 52).

Panaggio, M. J. and D. M. Abrams (Feb. 2015). “Chimera states: coexistence of coherence and incoherence in networks of coupled oscillators”. *Nonlinearity* 28.3, R67–R87 (cit. on p. 26).

Patelli, A., I. Djafer-Cherif, I. S. Aranson, E. Bertin, and H. Chaté (Dec. 2019). “Understanding Dense Active Nematics from Microscopic Models”. *Phys. Rev. Lett.* 123 (25), p. 258001 (cit. on p. 81).

Pearce, P. A. (June 1981). “Mean-field bounds on the magnetization for ferromagnetic spin models”. *Journal of Statistical Physics* 25.2, pp. 309–320 (cit. on p. 43).

Peruani, F., T. Klauss, A. Deutsch, and A. Voss-Boehme (Mar. 2011). “Traffic Jams, Gliders, and Bands in the Quest for Collective Motion of Self-Propelled Particles”. *Phys. Rev. Lett.* 106 (12), p. 128101 (cit. on p. 10).

Peshkov, A., E. Bertin, F. Ginelli, and H. Chaté (2014). “Boltzmann-Ginzburg-Landau approach for continuous descriptions of generic Vicsek-like models”. *The European Physical Journal Special Topics* 223.7, pp. 1315–1344 (cit. on p. 81).

Peshkov, A., I. S. Aranson, E. Bertin, H. Chaté, and F. Ginelli (Dec. 2012). “Nonlinear Field Equations for Aligning Self-Propelled Rods”. *Phys. Rev. Lett.* 109 (26), p. 268701 (cit. on p. 81).

Pikovsky, A., M. Rosenblum, and J. Kurths (2003a). *Synchronization: A Universal Concept in Nonlinear Sciences*. Cambridge Nonlinear Science Series. Cambridge University Press (cit. on p. 14).

Pikovsky, A., M. Rosenblum, and J. Kurths (2003b). *Synchronization: A Universal Concept in Nonlinear Sciences*. Cambridge Nonlinear Science Series. Cambridge University Press (cit. on p. 84).

Platen, E. and N. Bruti-Liberati (2010). *Numerical Solution of Stochastic Differential Equations with Jumps in Finance*. Stochastic Modelling and Applied Probability. Springer Berlin Heidelberg (cit. on pp. 4, 25, 32).

Pöschel, T. and T. Schwager (2005). *Computational Granular Dynamics: Models and Algorithms*. SpringerLink: Springer e-Books. Springer Berlin Heidelberg (cit. on p. 81).

Press, W. H., W. T. Vetterling, S. A. Teukolsky, and B. P. Flannery (2002). *Numerical Recipes in C++: The Art of Scientific Computing*. 2nd. New York, NY, USA: Cambridge University Press (cit. on pp. 83, 100).

Reich, S. and C. Cotter (2015). *Probabilistic Forecasting and Bayesian Data Assimilation*. Cambridge Texts in Applied Mathematics. Cambridge University Press (cit. on p. 116).

Riedel, I. H., K. Kruse, and J. Howard (2005). “A Self-Organized Vortex Array of Hydrodynamically Entrained Sperm Cells”. *Science* 309.5732, pp. 300–303 (cit. on p. 9).

Risken, H. and T. Frank (1996). *The Fokker-Planck Equation: Methods of Solution and Applications*. Springer Series in Synergetics. Springer Berlin Heidelberg (cit. on pp. 33, 38, 82).

Robert L. Devaney, S., M. Hirsch, S. Smale, and R. Devaney (2004). *Differential Equations, Dynamical Systems, and an Introduction to Chaos*. Pure and Applied Mathematics - Academic Press. Elsevier Science (cit. on pp. 3, 4).

Romanczuk, P., M. Bär, W. Ebeling, B. Lindner, and L. Schimansky-Geier (Mar. 2012). “Active Brownian particles”. *The European Physical Journal Special Topics* 202.1, pp. 1–162 (cit. on p. 7).

Sakaguchi, H. and Y. Kuramoto (Sept. 1986). “A Soluble Active Rotator Model Showing Phase Transitions via Mutual Entertainment”. *Progress of Theoretical Physics* 76.3, pp. 576–581 (cit. on pp. 84, 103).

Särkkä, S. and A. Solin (2019). *Applied Stochastic Differential Equations*. Institute of Mathematical Statistics Textbooks. Cambridge University Press (cit. on p. 4).

Schäfer, M. (2006). *Computational Engineering - Introduction to Numerical Methods*. Springer Berlin Heidelberg (cit. on p. 6).

Schmidt, L., K. Schönleber, K. Krischer, and V. García-Morales (2014). “Coexistence of synchrony and incoherence in oscillatory media under nonlinear global coupling”. *Chaos* 24.1, 013102 (cit. on p. 9).

Schöll, E. (2016). “Synchronization patterns and chimera states in complex networks: Interplay of topology and dynamics”. *The European Physical Journal Special Topics* 225.6, pp. 891–919 (cit. on p. 26).

Shima, S.-i. and Y. Kuramoto (Mar. 2004). “Rotating spiral waves with phase-randomized core in nonlocally coupled oscillators”. *Phys. Rev. E* 69 (3), p. 036213 (cit. on p. 54).

Solon, A. P., H. Chaté, and J. Tailleur (Feb. 2015). “From Phase to Microphase Separation in Flocking Models: The Essential Role of Nonequilibrium Fluctuations”. *Phys. Rev. Lett.* 114 (6), p. 068101 (cit. on p. 7).

Souslov, A., B. C. van Zuiden, D. Bartolo, and V. Vitelli (2017). “Topological sound in active-liquid metamaterials”. *Nature Physics* 13.11, pp. 1091–1094 (cit. on p. 9).

Spohn, H. (1991). *Large Scale Dynamics of Interacting Particles*. 1st ed. Springer (cit. on pp. 20, 40).

Strogatz, S. (2007). *Nonlinear Dynamics And Chaos*. Studies in nonlinearity. Sarat Book House (cit. on p. 3).

Sumino, Y., K. H. Nagai, Y. Shitaka, D. Tanaka, K. Yoshikawa, H. Chaté, and K. Oiwa (2012). “Large-scale vortex lattice emerging from collectively moving microtubules”. *Nature* 483.7390, pp. 448–452 (cit. on p. 9).

Sun, Z., J. A. Carrillo, and C.-W. Shu (2018). “A discontinuous Galerkin method for nonlinear parabolic equations and gradient flow problems with interaction potentials”. *Journal of Computational Physics* 352, pp. 76–104 (cit. on p. 100).

Taher, H., S. Olmi, and E. Schöll (Dec. 2019). “Enhancing power grid synchronization and stability through time-delayed feedback control”. *Phys. Rev. E* 100 (6), p. 062306 (cit. on p. 26).

Tanaka, H.-A., A. J. Lichtenberg, and S. Oishi (Mar. 1997a). “First Order Phase Transition Resulting from Finite Inertia in Coupled Oscillator Systems”. *Phys. Rev. Lett.* 78 (11), pp. 2104–2107 (cit. on p. 36).

Tanaka, H.-A., A. J. Lichtenberg, and S. Oishi (1997b). “Self-synchronization of coupled oscillators with hysteretic responses”. *Physica D: Nonlinear Phenomena* 100.3, pp. 279–300 (cit. on p. 36).

Thüroff, F., C. A. Weber, and E. Frey (Nov. 2014). “Numerical Treatment of the Boltzmann Equation for Self-Propelled Particle Systems”. *Phys. Rev. X* 4 (4), p. 041030 (cit. on pp. 81, 108, 112).

Tinsley, M. R., S. Nkomo, and K. Showalter (Sept. 2012). “Chimera and phase-cluster states in populations of coupled chemical oscillators”. *Nat Phys* 8.9, pp. 662–665 (cit. on p. 9).

Tirado, M. M., C. L. Martínez, and J. G. de la Torre (1984). “Comparison of theories for the translational and rotational diffusion coefficients of rod-like macromolecules. Application to short DNA fragments”. *The Journal of Chemical Physics* 81.4, pp. 2047–2052 (cit. on p. 118).

Tociu, L., É. Fodor, T. Nemoto, and S. Vaikuntanathan (Nov. 2019). “How Dissipation Constrains Fluctuations in Nonequilibrium Liquids: Diffusion, Structure, and Biased Interactions”. *Phys. Rev. X* 9 (4), p. 041026 (cit. on p. 9).

Toner, J., Y. Tu, and S. Ramaswamy (2005). “Hydrodynamics and phases of flocks”. *Annals of Physics* 318.1. Special Issue, pp. 170–244 (cit. on p. 81).

Totz, J. F., M. R. Tinsley, H. Engel, and K. Showalter (2020). “Transition from spiral wave chimeras to phase cluster states”. *Scientific Reports* 10.1, p. 7821 (cit. on p. 9).

Vicsek, T., A. Czirók, E. Ben-Jacob, I. Cohen, and O. Shochet (Aug 1995). "Novel Type of Phase Transition in a System of Self-Driven Particles". *Phys. Rev. Lett.* 75 (6), pp. 1226–1229 (cit. on pp. 7, 22).

Vicsek, T. and A. Zafeiris (2012). "Collective motion". *Physics Reports* 517.3–4, pp. 71–140 (cit. on p. 7).

Villani, C. (2003). *Topics in Optimal Transportation*. Graduate studies in mathematics. American Mathematical Society (cit. on p. 84).

Wanner, E., E. Hairer, C. Lubich, G. Wanner, and m. Gerhard Wanner (2002). *Geometric Numerical Integration: Structure-Preserving Algorithms for Ordinary Differential Equations*. Springer series in computational mathematics. Springer (cit. on p. 4).

Wensink, H. H., J. Dunkel, S. Heidenreich, K. Drescher, R. E. Goldstein, H. Löwen, and J. M. Yeomans (2012). "Meso-scale turbulence in living fluids". *Proceedings of the National Academy of Sciences* 109.36, pp. 14308–14313 (cit. on p. 117).

Wiggins, S. (2003). *Introduction to Applied Nonlinear Dynamical Systems and Chaos*. Texts in Applied Mathematics. Springer New York (cit. on p. 3).

Xie, J., E. Knobloch, and H.-C. Kao (Aug. 2014). "Multicluster and traveling chimera states in nonlocal phase-coupled oscillators". *Phys. Rev. E* 90 (2), p. 022919 (cit. on p. 15).

Yates, C. A., R. Erban, C. Escudero, I. D. Couzin, J. Buhl, I. G. Kevrekidis, P. K. Maini, and D. J. T. Sumpter (2009). "Inherent noise can facilitate coherence in collective swarm motion". *Proceedings of the National Academy of Sciences* 106.14, pp. 5464–5469 (cit. on p. 17).

Zauderer, E. (2011). *Partial Differential Equations of Applied Mathematics*. Pure and Applied Mathematics: A Wiley Series of Texts, Monographs and Tracts. Wiley (cit. on pp. 4, 5).

Zhang, H. P., A. Be'er, E.-L. Florin, and H. L. Swinney (2010). "Collective motion and density fluctuations in bacterial colonies". *Proceedings of the National Academy of Sciences* 107.31, pp. 13626–13630 (cit. on p. 115).

CURRICULUM VITÆ

NIKITA KRUK

PERSONAL INFORMATION

DATE OF BIRTH	29 August, 1991
PLACE OF BIRTH	Fastiv, Kyiv Oblast, Ukraine
NATIONALITY	Ukrainian
FAMILY STATUS	Single
HOMEPAGE	https://github.com/raven91

EDUCATION

Master of Science (M.Sc.) 2012-2014
National University of Kyiv-Mohyla Academy, Kyiv, Ukraine

Bachelor of Science (B.Sc.) 2008-2012
National University of Kyiv-Mohyla Academy, Kyiv, Ukraine

WORK EXPERIENCE

Technische Universität Darmstadt 7/2014-
Research Associate, Bioinspired Communication Systems
Darmstadt, Germany

SAPRun Ukraine 2013-2014
Software Developer
Kyiv, Ukraine

December 10, 2020

ERKLÄRUNG LAUT §9 PROMOTIONSORDNUNG

---

§ 8 Abs. 1 lit. c PromO
Ich versichere hiermit, dass die elektronische Version meiner Dissertation mit der schriftlichen Version übereinstimmt.

§ 8 Abs. 1 lit. d PromO
Ich versichere hiermit, dass zu einem vorherigen Zeitpunkt noch keine Promotion versucht wurde. In diesem Fall sind nähere Angaben über Zeitpunkt, Hochschule, Dissertationsthema und Ergebnis dieses Versuchs mitzuteilen.

§ 9 Abs. 1 PromO
Ich versichere hiermit, dass die vorliegende Dissertation selbstständig und nur unter Verwendung der angegebenen Quellen verfasst wurde.

§ 9 Abs. 2 PromO
Die Arbeit hat bisher noch nicht zu Prüfungszwecken gedient.

16.12.2020

Datum und Unterschrift